

**Off-Design Performance Prediction of Gas Turbines  
without the use of Compressor or Turbine Characteristics**

**by**

**Janitha Kanishka Suraweera**

**A thesis submitted to the Faculty of Graduate and Postdoctoral  
Affairs in partial fulfillment of the requirements  
for the degree of**

**Master of Applied Science**

**in**

**Aerospace Engineering**

**Carleton University  
Ottawa, Ontario**

**© 2011**

**Janitha Kanishka Suraweera**



Library and Archives  
Canada

Published Heritage  
Branch

395 Wellington Street  
Ottawa ON K1A 0N4  
Canada

Bibliothèque et  
Archives Canada

Direction du  
Patrimoine de l'édition

395, rue Wellington  
Ottawa ON K1A 0N4  
Canada

*Your file Votre référence*

*ISBN: 978-0-494-87806-4*

*Our file Notre référence*

*ISBN: 978-0-494-87806-4*

#### NOTICE:

The author has granted a non-exclusive license allowing Library and Archives Canada to reproduce, publish, archive, preserve, conserve, communicate to the public by telecommunication or on the Internet, loan, distribute and sell theses worldwide, for commercial or non-commercial purposes, in microform, paper, electronic and/or any other formats.

The author retains copyright ownership and moral rights in this thesis. Neither the thesis nor substantial extracts from it may be printed or otherwise reproduced without the author's permission.

#### AVIS:

L'auteur a accordé une licence non exclusive permettant à la Bibliothèque et Archives Canada de reproduire, publier, archiver, sauvegarder, conserver, transmettre au public par télécommunication ou par l'Internet, prêter, distribuer et vendre des thèses partout dans le monde, à des fins commerciales ou autres, sur support microforme, papier, électronique et/ou autres formats.

L'auteur conserve la propriété du droit d'auteur et des droits moraux qui protègent cette thèse. Ni la thèse ni des extraits substantiels de celle-ci ne doivent être imprimés ou autrement reproduits sans son autorisation.

---

In compliance with the Canadian Privacy Act some supporting forms may have been removed from this thesis.

While these forms may be included in the document page count, their removal does not represent any loss of content from the thesis.

Conformément à la loi canadienne sur la protection de la vie privée, quelques formulaires secondaires ont été enlevés de cette thèse.

Bien que ces formulaires aient inclus dans la pagination, il n'y aura aucun contenu manquant.

Canada

## ABSTRACT

A new method of predicting gas turbine off-design performance is presented. This method, referred to as the core control method, is based on the idea that performance across a gas turbine depends on a single parameter that controls the energy input to the said gas turbine. It is shown that only the design-point performance of a gas turbine is needed to predict its off-design performance, and that neither compressor nor turbine characteristics are required.

A thermodynamic model is developed for predicting the off-design performance of a single-spool turbojet and a two-spool gas generator with a free power turbine. This model is further developed to simulate the effects of handling bleed schedules, performance limiters and performance deterioration.

The core control method is then used to predict the off-design performance of a Rolls-Royce Viper Mark 521 as a proof-of-concept, after which, the new and deteriorated off-design performance of three Rolls-Royce RB211-24GT gas turbines is predicted.

In addition to the discussions on the involved theories and the performance predictions, the process by which the deteriorated RB211-24GT performance data was analyzed, and the sources and propagation of measurement uncertainties are also discussed.

*Eye of the tiger...!*

## ACKNOWLEDGEMENTS

**A**S my first thesis supervisor, I would like to thank Dr. Donald Gauthier of PSM Systems, former professor at Carleton University and my first thesis supervisor, for tolerating my *persistence*, and for trusting in me when only a few others would and giving me a chance to prove myself. His reviews of many drafts of my thesis are also appreciated.

I would also like to thank Prof. Metin Yaras, who became my second thesis supervisor, for his guidance and for reviewing countless drafts of my thesis.

I am also thankful for Prof. Herb Saravanamuttoo, my thesis co-supervisor, for providing me with invaluable guidance with the finer points of gas turbine performance, and for him reviewing several drafts of my thesis. I am also thankful for him letting me borrow rare literature without hesitation, but with threats for my personal safety should I misplace them!

The guidance and supervision provided by Mr. Jerry Blackburn and Mr. Richard Hamby over 15 months during my time as a Graduate Research Student/Performance Specialist at Rolls-Royce Canada is something for which I am truly thankful. In addition to this, the support given to me by the departments of Functional Systems Integration, Combustion and Customer Service Business of Rolls-Royce Canada is also greatly appreciated.

Furthermore, thanks are extended to Mr. Nick Corbett and Mr. Steve Brown of Rolls-Royce UK for providing me with engine data and help with the in-house analysis software, respectively. I am also thankful for Rolls-Royce Canada for providing me with research funding for the first half of my studies.

Finally, I would like to thank my parents for their continuing guidance, encouragement, love and support, without which I would not be here today. I dedicate this work to my parents.

# TABLE OF CONTENTS

<b>ABSTRACT</b>	<b>i</b>
<b>ACKNOWLEDGEMENTS</b>	<b>iv</b>
<b>TABLE OF CONTENTS</b>	<b>vi</b>
<b>LIST OF TABLES</b>	<b>xii</b>
<b>LIST OF FIGURES</b>	<b>xiii</b>
<b>NOMENCLATURE</b>	<b>xviii</b>
<b>1 INTRODUCTION</b>	<b>1</b>
1.1 Overview	3
<b>2 LITERATURE REVIEW</b>	<b>4</b>
2.1 Introduction	4
2.2 Off-Design Performance Simulation Methods	5
2.2.1 Component-Matching Methods	5
2.2.2 Stage Stacking Method	7
2.2.3 Methods based on Gas Path Analysis	9

2.2.4	Methods based on Artificial Intelligence	12
2.2.5	Methods based on Kalman Filtering	16
2.2.6	Methods based on Fuzzy Logic	18
2.2.7	Methods based on Computational Fluid Dynamics	19
2.2.8	Wittenberg's Method	21
2.3	Performance Deterioration in Gas Turbines	27
2.3.1	Deterioration Mechanisms	28
2.3.2	Performance Recovery Methods	32
<b>3</b>	<b>ENGINE DATA ACQUISITION AND ANALYSIS</b>	<b>35</b>
3.1	Introduction	35
3.2	The Rolls-Royce Industrial RB211	36
3.2.1	Introduction	36
3.2.2	Mechanical Configuration	36
3.3	Overview of Engine Data	37
3.3.1	Data Sources	37
3.3.2	Engine Health Monitoring Measurements	37
3.3.3	Data Sampling Frequency	39
3.3.4	Measurement Instruments and Associated Errors	40
3.4	Field Data Analysis Process	45
3.4.1	Pre-Processing of Field Data	45
3.4.2	T <sub>07</sub> Bias Error Correction	45
3.4.3	Instrument Calibration Error Correction	48
3.4.4	Field Dataset Analysis	50

3.4.5	Processing of the Analysis Results	51
3.4.6	Error Propagation	52
<b>4</b>	<b>GAS TURBINE OFF-DESIGN PERFORMANCE PREDICTION USING GASDYNAMICS RELATIONSHIPS</b>	<b>55</b>
4.1	Introduction	55
4.2	An Introduction to the Core Control Method	56
4.3	Single-Spool Turbojet	58
4.3.1	Matching of the Turbine and the Exhaust Nozzle	60
4.3.2	Off-Design Performance Prediction	64
4.4	Simulating the Effect of Bleed Flows	65
4.4.1	Handling Bleeds vs. Cooling Bleeds	65
4.4.2	Effect of Bleed Extraction on Engine Performance	67
4.5	Two-Spool Gas Generator with a Free Power Turbine	71
4.5.1	Matching of the HP, LP and Free Power Turbines	74
4.5.2	Off-Design Performance Prediction	76
4.6	Deteriorated Engine Performance Prediction	79
4.7	Simulating Performance Limiters	81
4.7.1	Simulating the Temperature Limiter	81
4.7.2	Simulating the Speed Limiter	83
<b>5</b>	<b>VALIDATION AND DISCUSSIONS</b>	<b>84</b>
5.1	Introduction	84
5.2	Single-Spool Turbojet	85
5.3	Multi-Spool Gas Turbine – Clean Performance	94

5.4	Multi-Spool Gas Turbine – Deteriorated Performance	102
<b>6</b>	<b>CONCLUSIONS AND RECOMMENDATIONS</b>	<b>111</b>
6.1	Conclusions	111
6.2	Recommendations	113
	<b>REFERENCES</b>	<b>114</b>
	<b>APPENDIX A GAS CHROMATOGRAPH UNCERTAINTY</b>	<b>125</b>
A.1	Overview	126
A.2	The Monte Carlo Method	126
A.3	Monte Carlo Simulation Result	127
	<b>APPENDIX B PROCESSING ANALYSIS RESULTS</b>	<b>129</b>
	<b>APPENDIX C SENSITIVITY ANALYSIS</b>	<b>135</b>
C.1	Overview	136
C.2	Estimated Fuel Flow Rate	137
C.3	LP Compressor Isentropic Efficiency	138
C.4	HP Compressor Isentropic Efficiency	139
C.5	HP Turbine Isentropic Efficiency	140
C.6	LP Turbine Isentropic Efficiency	140
C.7	Power Turbine Isentropic Efficiency	141
C.8	LP Compressor Capacity	141
C.9	HP Compressor Capacity	143
C.10	Core Bleed Flow	144

C.11	Polytropic Compressor Efficiencies	144
C.12	Polytropic Turbine Efficiencies	146
C.13	Uncertainties of the Recoverable Deterioration Factors	148
C.14	Uncertainties of the Site Performance Data	157
C.14.1	LP Compressor Pressure Ratio	157
C.14.2	HP Compressor Pressure Ratio	157
C.14.3	LP Compressor Corrected Mass Flow Rate	158
C.14.4	HP Compressor Corrected Mass Flow Rate	158
C.14.5	Gas Generator Exhaust Pressure	159
C.14.6	Power Turbine Outlet Temperature	159
C.14.7	Fuel Flow Rate	160
C.14.8	Power Output	161

## **APPENDIX D     SOLUTION PROCESSES OF THE CORE CONTROL**

<b>METHOD</b>		<b>162</b>
D.1	Single-Spool Turbojet	163
D.1.1	Introduction	163
D.1.2	Unchoked Turbine	165
D.1.3	Choked Turbine-Unchoked Nozzle	169
D.1.4	Choked Nozzle	170
D.1.5	Post-Solution Process Calculations	172
D.2	Two-Spool Gas Generator with a Free Power Turbine	177
D.2.1	Introduction	177
D.2.2	Unchoked HP Turbine	180

D.2.3	Choked HP Turbine-Unchoked LP Turbine	186
D.2.4	Choked LP Turbine-Unchoked Free Power Turbine	187
D.2.5	Choked Free Power Turbine	188
D.2.6	Post-Solution Process Calculations	189
D.3	Aerodynamic Coupling of the LP and HP Spools	194
D.4	Simulation of Bleed Flows in the Core Control Method	196
D.4.1	Introduction	196
D.4.2	Cooling Bleed Flows	198
D.4.3	Handling Bleed Flows	199
<b>APPENDIX E</b>	<b>DETERIORATED ENGINE PERFORMANCE</b>	<b>204</b>
E.1	Non-Dimensionalizing Predicted and Actual Performance	205
E.2	Predicted and Actual Performance Data at Site	205
<b>APPENDIX F</b>	<b>MATLAB ALGORITHMS</b>	<b>220</b>
F.1	The Monte Carlo Algorithm, chromatograph.m	221
F.2	Core Control Method for a Single-Spool Turbojet, X_1TJ.m	224
F.3	Plotting the Outputs from X_1TJ.m, X_1TJ_PLOTS.m	229
F.4	Core Control Method for a Two-Spool Gas Generator with a Free Power Turbine, X_2TJ.m	233
F.5	Plotting the Outputs from X_2TJ.m, X_2TJ_PLOTS.m	243
F.6	Effect of Handling Bleed Flows, bleedeffect.m	249
F.7	Calculating Gas Turbine Fuel Flow Rate, bleedfuel.m	251
F.8	Turbine Corrected Mass Flow Rate, nozzleflow.m	252
F.9	Turbine Pressure Ratio, nozzlepres.m	253

## **LIST OF TABLES**

Table 1.1	Particulate concentration variation [modified from Upton, 1974]	29
Table C.1	Uncertainties of the recoverable deterioration factors	148

## LIST OF FIGURES

Figure 1.1	Comparison of gas turbine off-design performance simulation methods [modified from Li, 2002]	2
Figure 2.1	Typical requirements for a simple component-matching model	5
Figure 2.2	Comparison between (a) a biological neuron and (b) an artificial neural network [modified from Samarasinghe, 2006]	12
Figure 2.3	A multi-layer perceptron [Zhou and Gauthier, 1999]	13
Figure 2.4	A single-spool turbojet [modified from Wittenberg, 1976a]	22
Figure 2.5	Compressor and turbine-nozzle matching curves for a single-spool turbojet [modified from Wittenberg, 1976a]	24
Figure 2.6	Polytropic efficiencies of actual compressors [modified from Wittenberg, 1976a]	25
Figure 2.7	Actual and predicted off-design performance of the Rolls-Royce Viper [modified from Wittenberg, 1976a]	26

Figure 2.8	Performance deterioration in gas turbines [modified from Gauthier, 2008]	27
Figure 2.9	Result of multiple crank soak washes during a single wash cycle [Taylor and Gotheridge, 2006]	34
Figure 3.1	The Rolls-Royce industrial RB211-24GT DLE RT61 [modified from Broomfield, 2007]	38
Figure 3.2	A schematic illustration of mixing of combustor-discharge and combustor-bypass gases	46
Figure 3.3	Instrument calibration process	49
Figure 3.4	Illustration of the error propagation process	53
Figure 4.1	Single-spool turbojet [modified from Wittenberg, 1976a]	59
Figure 4.2	Matching of the turbine and the exhaust nozzle for a single-spool turbojet [modified from Saravanamuttoo et al., 20010]	60
Figure 4.3	Solution process used by the core control method for a single-spool turbojet	62
Figure 4.4	Effect of handling bleed on the compressor of a single-spool turbojet	66
Figure 4.5	Typical handling bleed schedule	66
Figure 4.6	Bleed flows of a single-spool turbojet	70
Figure 4.7	Two-spool gas generator with a free power turbine and its equivalent two-spool turbojet	72

Figure 4.8	Matching of the HP, LP and free power turbines for a two-spool gas generator with a free power turbine [modified from Saravanamuttoo et al., 2001]	75
Figure 4.9	Core control method for the off-design performance prediction of a two-spool gas generator with a free power turbine	78
Figure 4.10	Typical operating limits for a gas turbine	82
Figure 5.1	Compressor running line of the Viper	87
Figure 5.2	Turbine inlet temperature of the Viper	88
Figure 5.3	Specific fuel consumption of the Viper	89
Figure 5.4	Net thrust of the Viper	90
Figure 5.5	Prediction of the Viper's compressor running line	91
Figure 5.6	Prediction of the Viper's turbine inlet temperature	92
Figure 5.7	Prediction of the Viper's specific fuel consumption and thrust	93
Figure 5.8	The Rolls-Royce industrial RB211-24GT DLE RT61 [modified from Broomfield, 2007]	95
Figure 5.9	LP compressor running line of the industrial RB211	97
Figure 5.10	HP compressor running line of the industrial RB211	98
Figure 5.11	Aerodynamic coupling of the LP and HP spools of the industrial RB211	99
Figure 5.12	Gas generator exhaust temperature of the industrial RB211	100
Figure 5.13	Heat rate and power output of the industrial RB211	101
Figure 5.14	Non-dimensional HP compressor corrected mass flow rate of GT1	103
Figure 5.15	Non-dimensional gas generator exhaust temperature of GT1	104

Figure 5.16	Non-dimensional gas generator exhaust temperature of GT2	106
Figure 5.17	Non-dimensional LP compressor pressure ratio of GT2	106
Figure 5.18	Non-dimensional LP compressor pressure ratio of GT3	108
Figure 5.19	Non-dimensional HP compressor pressure ratio of GT3	108
Figure 5.20	Non-dimensional gas generator exhaust temperature of GT3	109
Figure A.1	Dependency of solution accuracy with the number of guesses	127
Figure A.2	Propagated uncertainty of the fuel lower heating value	128
Figure B.1	Typical deterioration curve of a performance parameter	130
Figure B.2	Initialized recoverable deterioration curves	131
Figure B.3	Arithmetic-averaged recoverable deterioration curve	132
Figure B.4	Refinement of analysis results	133
Figure C.1	Two-spool gas generator with a free power turbine	136
Figure C.2	Recoverable deterioration factor of the LP compressor efficiency	149
Figure C.3	Recoverable deterioration factor of the HP compressor efficiency	150
Figure C.4	Recoverable deterioration factor of the HP turbine efficiency	151
Figure C.5	Recoverable deterioration factor of the LP turbine efficiency	152
Figure C.6	Recoverable deterioration factor of the power turbine efficiency	153
Figure C.7	Recoverable deterioration factor of the LP compressor capacity	154
Figure C.8	Recoverable deterioration factor of the HP compressor capacity	155
Figure C.9	Recoverable deterioration delta of the core bleed flow	156
Figure D.1	Single-spool turbojet [modified from Wittenberg, 1976a]	164
Figure D.2	Matching of the turbine and the exhaust nozzle for a single-spool turbojet [modified from Saravanamuttoo et al., 20010]	164

Figure D.3	Two-spool gas generator with a free power turbine and its equivalent two-spool turbojet	178
Figure D.4	Matching of the HP, LP and free power turbines for a two-spool gas generator with a free power turbine [modified from Saravanamuttoo et al., 2001]	179
Figure D.5	Bleed flows of a single-spool turbojet	197
Figure E.1	Non-dimensional LP compressor pressure ratio of GT1	206
Figure E.2	Non-dimensional HP compressor pressure ratio of GT1	207
Figure E.3	Non-dimensional LP compressor corrected mass flow rate of GT1	208
Figure E.4	Non-dimensional fuel flow rate of GT1	209
Figure E.5	Non-dimensional power output of GT1	210
Figure E.6	Non-dimensional HP compressor pressure ratio of GT2	211
Figure E.7	Non-dimensional LP compressor corrected mass flow rate of GT2	212
Figure E.8	Non-dimensional HP compressor corrected mass flow rate of GT2	213
Figure E.9	Non-dimensional fuel flow rate of GT2	214
Figure E.10	Non-dimensional power output of GT2	215
Figure E.11	Non-dimensional LP compressor corrected mass flow rate of GT3	216
Figure E.12	Non-dimensional HP compressor corrected mass flow rate of GT3	217
Figure E.13	Non-dimensional fuel flow rate of GT3	218
Figure E.14	Non-dimensional power output of GT3	219

## NOMENCLATURE

### *English Symbols*

A	turbine or propelling nozzle throat area
$c_{pa}$	specific heat of air, 1.005 kJ/kgK
$c_{pg}$	specific heat of exhaust gas, 1.148 kJ/kgK
$F_N$	net thrust
f	fuel-to-air ratio
HP	high pressure
$K_{rec}$	recoverable deterioration factor
$K_{nonrec}$	non-recoverable deterioration factor
LP	low pressure
M	Mach number
$\dot{m}$	mass flow rate
$N_H$	high-pressure spool speed
$N_L$	low-pressure spool speed
P	static pressure
$P_o$	ambient pressure (if followed by a number, station total pressure)
PWR	engine power output
Q	fuel heating value

SFC	specific fuel consumption
T	static temperature
T <sub>o</sub>	total temperature

*Greek Symbols*

$\beta$	bleed fraction
$\phi$	spool temperature ratio/core control parameter
$\Gamma$	compressor flow capacity
$\gamma$	gas constant (air = 1.4, exhaust gas = 1.333)
$\eta$	isentropic efficiency
$\eta_{\infty}$	polytropic efficiency
$\eta_B$	combustion efficiency
$\eta_m$	mechanical efficiency

*English Subscripts*

a	air
c	compressor
des	design point
f	fuel
g	gas
HPC	high pressure compressor
HPT	high pressure turbine
LPC	low pressure compressor
LPT	low pressure turbine
max	maximum magnitude
nonrec	non-recoverable
PT	free power turbine
rec	recoverable

t turbine

*Greek Subscripts*

$\beta_C$  cooling bleed

$\beta_H$  handling bleed

*Engine Station Numbering: Single-Spool Turbojet*

1 gas turbine inlet  
2 compressor inlet  
3 compressor outlet  
4 turbine inlet  
5 turbine outlet  
6 propelling nozzle exhaust

*Engine Station Numbering: Two-Spool Gas Generator with a Free Power Turbine*

1 gas turbine inlet  
2 low-pressure compressor inlet  
3 low-pressure compressor outlet  
4 high-pressure compressor outlet  
5 high-pressure turbine inlet  
6 high-pressure turbine outlet  
7 low-pressure turbine outlet  
8 free power turbine outlet  
9 exhaust duct outlet

# 1 INTRODUCTION

**A**N ancient proverb suggests to not to use a cannon to kill a mosquito. If one replaces “cannon” with complex gas turbine off-design performance simulation methods and “mosquito” with the need for gas turbine off-design performance prediction and diagnostics, it can be easily observed that this suggestion has fallen on deaf ears.

The currently available off-design performance simulation methods range from simple component-matching methods to complicated rule-based expert systems. Often, the complex methods are true to their nature that only those who develop these methods and a few others are able to understand their theories. Additionally, even the simple methods lose some of their simplicity when using multiple compressor and turbine characteristics when simulating advanced gas turbine cycles. Interestingly, the accuracy of a given method does not necessarily increase with its complexity.

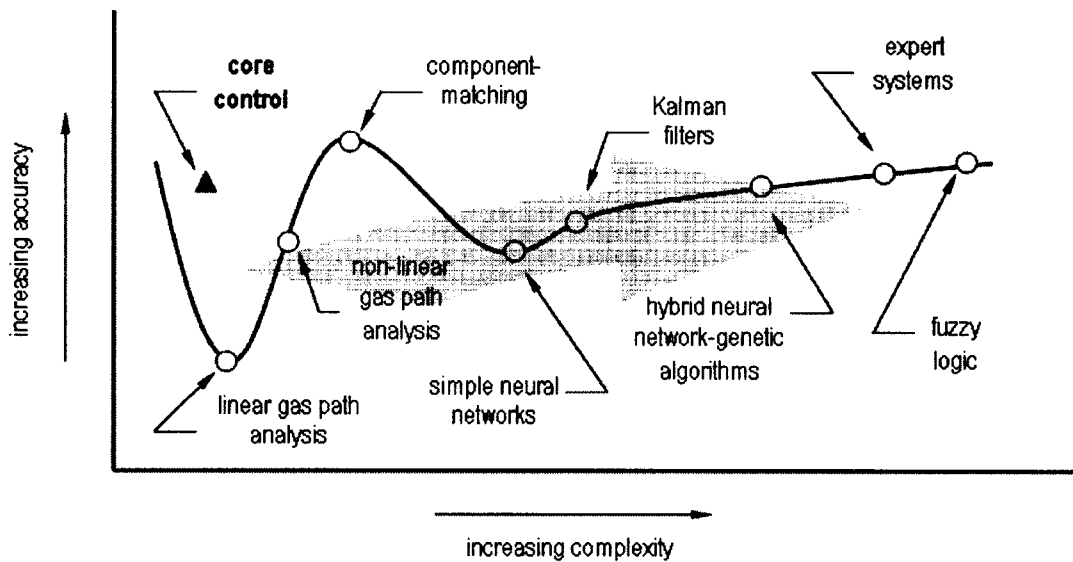


**Figure 1.1** Comparison of gas turbine off-design performance simulation methods  
[modified from Li, 2002]

Therefore, a simple off-design performance simulation method is proposed that is based on fundamental gas turbine gasdynamics relationships. This method, called the *core control method*, is compared from a viewpoint of a typical gas turbine engineer to presently available methods of off-design performance simulation in Figure 1.1.

The core control method is based on the following assumptions: the equilibrium operating point of every component, i.e., compressors and turbines, within a gas turbine is dependent on a single physical variable within the core of the engine; the running line of a given compressor, i.e., the constrained region within which a compressor operates, is dependent on the swallowing capacity of its mechanically-coupled turbine; and, the off-design performance of an engine is related to its on-design performance. This allows the core control method to predict the off-design performance of an engine without using either compressor or turbine characteristics, which are also known as performance maps.

To validate this method, data from three industrial RB211-24GT engines are used. These engines operate at a highly industrial environment, thus exhibit strong deterioration profiles, which is a condition the core control method is expected to simulate successfully.

## **1.1 Overview**

First, a literature review of the currently available gas turbine off-design performance simulation methods, both in the areas of prediction and diagnostics, is presented in Chapter 2. Then, to prepare for the engine data analysis process, the causes and effects of engine performance deterioration are reviewed.

Chapter 3 consists of the engine data analysis process. Here, an overview of the industrial RB211-24GT engine is presented including discussions on engine health monitoring, performance data acquisition process, measurement uncertainties and error propagation, and the data analysis process.

The theory of the core control method is discussed in the Chapter 4. Detailed derivations of the theory discussed herein are available in an appendix.

Chapter 5 includes the validation of the core control method as well as a section on discussion on the validation results. The final chapter, Chapter 6, provides conclusions and suggestions for future work.

## **2 LITERATURE REVIEW**

### **2.1 Introduction**

**A**NY gas turbine currently either in development or in operation has its own off-design performance model. Even the Heinkel series engines – the first ever gas turbines – had off-design performance models, albeit being in the form of a series of plots written on paper (Mattingly, 2005).

The term off-design performance simulation covers the areas of performance prediction as well as performance diagnostics since, without the ability to predict performance, a model cannot diagnose performance. Both of these areas of off-design performance simulation are discussed in this chapter. It can be said that off-design performance models can be categorized into component-matching, stage stacking, variants of gas path analysis, artificial intelligence, fuzzy logic and computational-fluid-dynamics-based methods.

Additionally, the mechanisms of gas turbine performance deterioration will be discussed, which shall aid in the data analysis process.

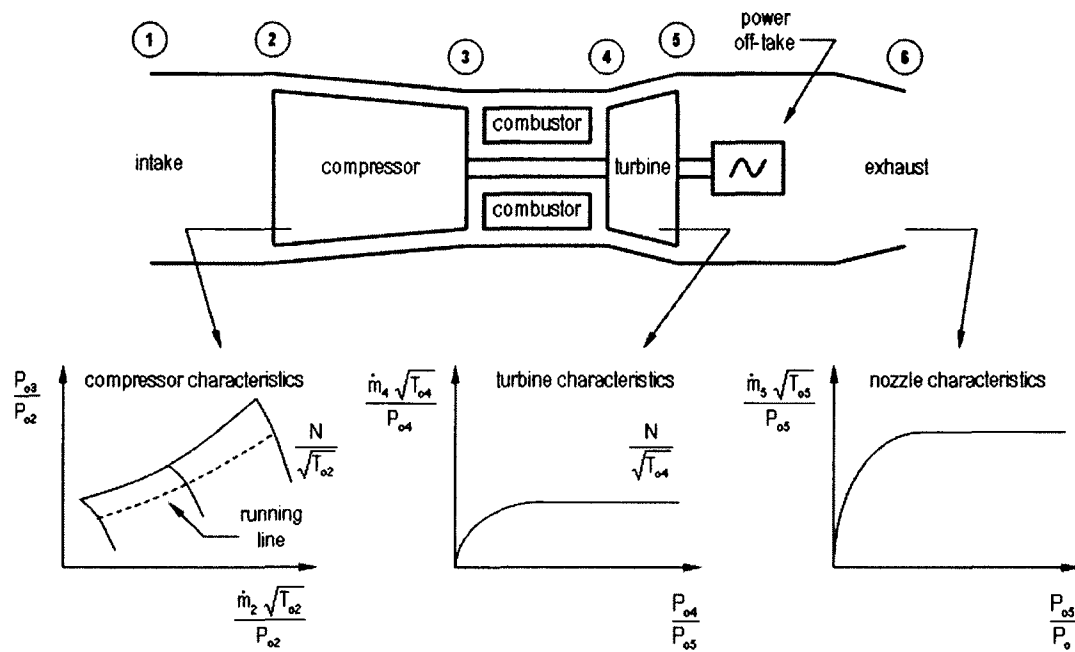


**Figure 2.1** Typical requirements for a simple component-matching model

## 2.2 Off-Design Performance Simulation Methods

### 2.2.1 Component-Matching Methods

Component-matching can be considered as the foundation of off-design performance prediction. In its most simple form, this method requires the knowledge of compressor characteristics, turbine characteristics, and, in the case of a turbojet, nozzle characteristics.

Here, for a required power/thrust output, an operating point on the compressor running line is selected from the compressor characteristic (Figure 2.1). Using this, the operating points of the turbine and the nozzle are calculated. Then, the engine output power/thrust is calculated using flow compatibilities and compressor-turbine work

balance, which then is compared with the required output. If they differ, a different operating point is selected from the compressor characteristics and this process is repeated until convergence is met (Saravanamuttoo et al., 2001). This method of component-matching is referred to as solving via serial-nested loops since, in a detailed scenario, a thermodynamic module is assigned to each of the inlet, compressor, combustor, turbine, exhaust, shaft and cooling flow (Walsh and Fletcher, 1998).

Saravanamuttoo (1963) used component-matching in his pioneering work of transient performance simulation of gas turbines. Many researchers such as Muir et al. (1989), Yin et al. (2001) and Lee et al. (2009), to name a few, have since used component-matching to simulate off-design performance of gas turbines ranging from two-spool industrial gas turbines to generic three-spool mixed-exhaust afterburning turbofan with a con-di variable area nozzle.

Another method of component-matching is referred to as solving via matrix iteration. Here, for a single-spool turbojet, for example, an initial operating point of the compressor and the combustor outlet temperature are assumed (matching guesses) for a given power setting. Then, the operating points of the turbine and propelling nozzle (matching constraints) are calculated. Small variations are then made in the matching guesses and the process is repeated. At the conclusion of this, errors in the matching constraints are available with respect to variations in the matching guesses, which can then be combined to obtain a matrix of partial derivatives. Inverting this matrix and multiplying by the errors in the matching constraints produces a set of values, by which the matching guesses are then varied. This process is repeated until the values produced by the matrix multiplication reaches a convergence limit (Walsh and Fletcher, 1998).

Walsh and Fletcher (1998) suggest that this method rises above the serial nested loops method when solving for off-design performance of advanced gas turbines, i.e., multi-spool engines. Kurzke (2007) uses the matrix iteration method in his well-known GasTurb® software.

It can be said that component-matching is the most popular method of off-design performance simulation due to its ease of implementation. However, this method requires one to know the compressor, turbine (and nozzle) characteristics of the engine in question.

### **2.2.2 Stage Stacking Method**

Stage stacking is a method by which compressor characteristics can be predicted if the characteristics of the first stage of the compressor, and the rotor and stator inlet and outlet angles are known.

Once the inlet axial velocity and blade speed are known for the first stage, gasdynamics equations are used along with the stage characteristics and blade angles to predict the stage performance and the flow conditions at the stage outlet. The first stage outlet flow conditions are then used as the inlet flow conditions for the second stage. The second stage characteristics are calculated from that of the first stage using scaling factors. Thus, the second stage performance is calculated. This procedure is repeated for all stages. Finally, the individual performances are concatenated, or *stacked*, to obtain the performance, i.e., the characteristics, of the full compressor (Steinke, 1982).

Since the accurate prediction of a real compressor characteristic requires real stage characteristics, which are generally unavailable to the public for obvious reasons,

generalized stage characteristics are typically used (Steinke [1982], Saravanamuttoo and Lakshminarasimha [1985]). Surprisingly, comparisons between several real stage characteristics from different engine manufacturers were found by Muir et al. (1989) to fall within a highly constrained scatter band.

Due to the openness of this method which allows one to modify the design of individual stages, stage stacking has found to be popular in simulating compressor performance deterioration due to fouling and erosion (Aker and Saravanamuttoo [1989], Muir et al. [1989], Seddigh and Saravanamuttoo [1990], Tabakoff et al. [1990], Lakshminarasimha et al. [1994] and Hosseini et al. [2009]).

Drummond and Davison ([2009a] and [2009b]) developed a method by which currently-used compressor characteristics are scaled non-linearly (i.e., morphed/twisted rather than linearly scaling) to provide an improved prediction for the characteristics of a compressor in development. This method, which can be considered as an alternative to the stage stacking method, is aimed at reducing the need for *fine tuning* of compressor characteristics otherwise obtained by simply linearly scaling existing compressor characteristics.

Using a database of existing compressor characteristics, the shape variance between similar compressor characteristics is first determined. Then, this is used to morph, rather than scale, an existing characteristic into a new compressor characteristic that could represent the performance of a compressor in development. This predicted compressor characteristic can then be used to determine the off-design performance of a new gas turbine.

This method can also be used to predict the effect of deterioration on gas turbine performance. For this, a database that contains different levels of deterioration on different compressors is required as a reference. Since there are, literally, an infinite number of possible designs for compressors and their possible deteriorations, this method is only as accurate as the vastness of the database available.

Once the compressor characteristics are predicted, one still requires to know the turbine characteristics if engine off-design performance is to be predicted through component-matching. Here, the turbine characteristics are typically generalized turbine characteristics (Aker and Saravanamuttoo, 1989).

### 2.2.3 Methods based on Gas Path Analysis

Gas path analysis methods come in the forms of inverse, non-linear and linear gas path analysis methods; the first of these is a performance prediction method, and the rest are performance diagnostics methods.

The brainchild of Urban (1973), gas path analysis assumes that for small changes in the independent performance parameters of a gas turbine, the dependent performance parameters behave in a linear fashion. Here the independent parameters are efficiencies and flow capacities, and the dependent parameters are pressures, temperatures, etc.

With the independent parameters represented by  $X_i$ , where  $i$  is the  $i^{\text{th}}$  parameter and the dependent parameters represented by  $F(X_i)$ , the change in performance due to a small change in the independent parameters,  $\delta X_i$ , can be expressed as follows.

$$F(X + \delta X_i) \approx F(X_i) + J \delta X_i \quad 2.2.1$$

Here,  $\mathbf{J}$  is a Jacobian, also known as a sensitivity matrix (Walsh and Fletcher, 1998), that contains the partial derivatives of the dependent performance parameters with respect to the independent performance parameters (i.e., power setting parameters), and is obtained using an off-design performance model.

The inverse gas path analysis method involves solving Equation 2.2.1. With estimated changes of independent parameters substituted into  $\delta X_i$ , which then predicts the corresponding engine performance,  $F(X + \delta X_i)$ .

$\mathbf{J}$  typically contains the sensitivities at design-point. These sensitivities do not, however, remain constant for off-design operating points. Therefore, should performance at off-design points be predicted, component sensitivities for those power settings must be used for higher accuracy (Urban [1973], and Ogaji et al. [2002]).

The inverse gas path analysis method can be modified from a performance prediction method to a performance diagnostics method by rearranging Equation 2.2.1 as,

$$\delta X_i \approx \mathbf{J}^{-1} F(\delta X_i) \quad 2.2.2$$

where,

$$F(\delta X_i) = F(X_i + \delta X_i) - F(X_i) \quad 2.2.3$$

thereby laying the foundation for linear gas path analysis. Here, a relatively small change in the dependent performance parameter with respect to a reference point (typically, design-point) is substituted into  $F(\delta X_i)$ . Then, the deviation required of the independent performance parameters,  $\delta X_i$ , can be found (Urban [1973], and Li [2002]).

By introducing an iterative step to the linear gas path analysis, non-linear gas path analysis method is obtained. Here, for a given  $F(\delta X_i)$ , an initial  $\delta X'_i$  is guessed, and the resulting independent parameter,  $X'_i$ , is calculated as,

$$X'_i = X_i + \delta X'_i \quad 2.2.4$$

Then, the deviation in the dependent performance parameter,  $F(\delta X'_i)$ , and  $\delta X'_i$  are calculated by,

$$F(\delta X'_i) = F(X_i + \delta X'_i) - F(X_i) \quad 2.2.5$$

$$\delta X'_i \approx \mathbf{J}^{-1} F(\delta X'_i) \quad 2.2.6$$

respectively. These steps are repeated until convergence (Ogaji et al., 2002).

The gas path analysis method, used for either performance prediction or performance diagnostics is able to provide relatively accurate results, compared to component-matching, within a short amount of time (Mathioudakis et al. [2002], and Simon et al. [2008]).

A setback of this method is that to obtain the sensitivities, one must still have access to another off-design performance model, namely one-based on a component-matching method – which requires one to know compressor and turbine characteristics – using which off-design data can be predicted. Else, off-design data must be obtained from an actual engine. In both cases, the dataset must aptly cover the operating region within which the gas path analysis method is intended to be used.

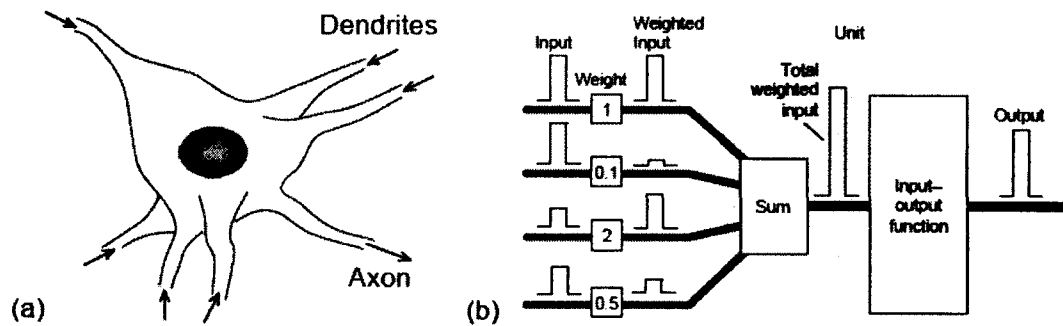


**Figure 2.2** Comparison between (a) a biological neuron and (b) an artificial neural network [modified from Samarasinghe, 2006]

#### 2.2.4 Methods based on Artificial Intelligence

Gas turbine off-design performance simulation through artificial intelligence-based methods is a recent development. These methods may either consist of artificial neural networks or hybrid neural network-genetic algorithms.

Artificial neural networks, or ANNs, are inspired by the interactions of neurons within a biological brain. Just as biological neurons are connected to each other through synaptic pathways, the neurons within an ANN are connected to each other through artificial synaptic pathways known as weights. These weights are a reflection of the synaptic strength between two neurons (Figure 2.2).

To program, or to teach, an ANN, it is repeatedly exposed to a dataset containing a set of inputs and another dataset which contains a set of required outputs. With each exposure, referred to as an epoch, the weights between the neurons adapt such that the ANN-estimated outputs converge with the required outputs. When convergence is met to within the programmer's satisfaction, the learning process is stopped.

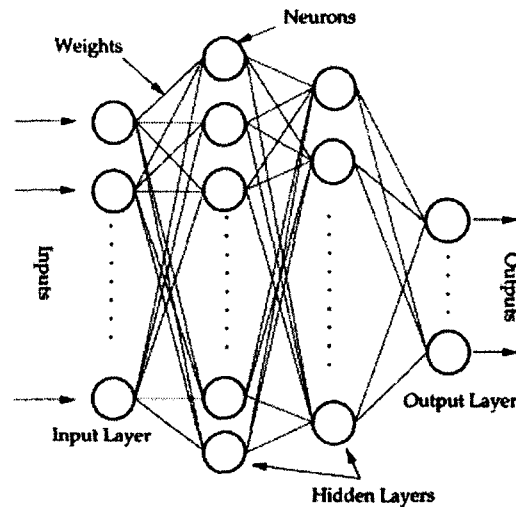


**Figure 2.3** A multi-layer perceptron [Zhou and Gauthier, 1999]

This method of programming an ANN is known as supervised learning. When optimization algorithms are incorporated into the learning process, an ANN is able to complete learning on its own: such method of learning is referred to as unsupervised learning.

The design of an ANN can range from simple single-layer perceptron neural networks to complex multi-layer perceptron (MLP) neural networks (Figure 2.3). Usually ANN-predicted results lose resolution when the number of hidden layers of a MLP increases. An unwritten rule is that MLPs with greater than three hidden layers are often *too smart to learn* (Samarasinghe, 2006).

This can be remedied by employing optimization algorithms during the training process. An optimization algorithm's purpose is to uphold the law of natural selection, also known as survival of the fittest (Sampath et al., 2006). Here, neurons that do not significantly contribute to the output of a neural network are simply discarded with each iteration, thus molding a MLP into a more purpose-built ANN (Samarasinghe, 2006).

From the above discussion, it is evident that ANNs are database-based methods, i.e., they are experts at prediction as long as such scenarios are covered in the learning process. As a result, when used to predict a new scenario, ANNs lose their credibility. In such cases, genetic algorithms (GA) are integrated into a given ANN to provide a hybrid neural network-genetic algorithm, or hybrid ANN-GA. The purpose of a genetic algorithm is to provide some flexibility, within reason, to the weights of an ANN such that optimized predictions can be made in situations where some uncertainty is present in the input data (Kobayashi and Simon, 2001).

Lazaretto and Toffolo (2001) used a MLP with three hidden layers, which was trained using data obtained from non-dimensionalized compressor and turbine characteristics of a LM2500 gas turbine, and an off-design performance model-based on component-matching. Afterwards, only using ambient pressure, ambient temperature, and gas turbine power output as inputs for the ANN, they were able to predict certain internal pressures and temperatures, overall efficiency, inlet air flow and fuel flow rates of the engine to within  $\pm 1\%$  accuracy.

Chiras et al. (2002) used an ANN to simulate the dynamic relationship between the fuel flow rate and the shaft speed of a Rolls-Royce Spey. The ANN was trained with a database of more than 1000 data points (estimated). Upon comparison, the ANN proved superior to existing linear performance prediction methods.

By using a three-layer MLP, Bruner (2002) was able to perform engine data analysis of Raytheon Premier I aircraft in 15 minutes where the conventional method took “several days.” The ANN predictions were found to be within  $\pm 3\%$  of the results obtained from the conventional method.

Kobayashi and Simon (2001) used a hybrid ANN-GA for engine diagnostics. The ANN was used for its ability to predict non-linear relationships and the GA was used as a sensor bias estimator. This method was found to reduce false alarms and missed detections in the diagnostics process.

Artificial-intelligence-based methods are not often used for performance prediction, but for performance diagnostics (Green and Allen, 1997). This may be due to the uncertainty in the prediction of an ANN or a hybrid ANN-GA method when used in an unfamiliar situation, i.e., scenarios not covered in the training dataset. Also, another reason for this may be due to the uneasiness of the gas turbine researcher when accepting a prediction from a method that consists of, essentially, a set of factors, sigmoid functions and simple algebra, and not use any comprehensive equations relating to gas turbine performance.

Green (1998) notes that if an artificial intelligence method is to be held in high regard, it must be able to sense, adapt and reason continuously. Therefore, Green (1998) indirectly recommends not ending a training process after an exposure to a database, but have a continuous training process where an artificial system matures with experience, or learns from experience.

One of the greatest weaknesses of artificial intelligence methods in gas turbine off-design performance simulation is that they are *a posteriori* methods, i.e., they can only “predict” well what is already known, where this knowledge is obtained from either an actual engine or a component-matching model (Sampath et al. [2002], and Samarasinghe [2006]).

### 2.2.5 Methods based on Kalman Filtering

Kalman filtering-based methods assume that a real-life system can be approximated by a linear dynamic system of the form,

$$\dot{\mathbf{x}} = \mathbf{F}\mathbf{x} + \mathbf{G}\mathbf{u} + \mathbf{w} \quad 2.2.7$$

$$\mathbf{z} = \mathbf{H}\mathbf{x} + \mathbf{v} \quad 2.2.8$$

where  $\mathbf{x}$  is a vector containing the states of the system,  $\mathbf{F}$  is the system dynamics matrix,  $\mathbf{u}$  is the control vector,  $\mathbf{H}$  is the measurement matrix,  $\mathbf{w}$  is a white noise process and  $\mathbf{v}$  is the measurement noise.

Kalman filtering is a recursive predictor-corrector-like method which tries to estimate a set of coefficients known as Kalman filter gains, such that the error in the filter prediction is minimized with each iteration. The boundaries within which the filter searches for the optimum filter gains are defined by the user as a white noise process. The Kalman filter gains are calculated using a set of equations known as scalar Riccati equations. Zarchan and Musoff (2005) provide further explanations.

Luppold et al. (1989) used a Kalman filter which utilized a state variable engine model to predict off-design performance of a military turbofan undergoing various levels of deterioration. A similar method was also implemented by Kobayashi et al. (2005).

Litt (2005) attempted to optimize a Kalman filter to predict off-design engine performance using an orthogonal decomposition method. From the presented results, however, only a slight improvement over conventional (Lambert, 1991) Kalman filter-based performance prediction methods was observed.

Since a Kalman filter's predictions are made within a pre-defined noise margin, researchers have attempted to optimize filter predictions by minimizing these margins by introducing constraints. Simon and Simon (2003) assumed that some naturally occurring engine performance deteriorations are quiescent and that they can only worsen with time. Based on this assumption, a set of filter constraints were introduced to *encourage* realistic filter behaviour, which resulted in improved predictions at the expense of increased computing time.

Simon and Garg (2010) used an optimized Kalman filter to perform *a posteriori* data analysis of a gas turbine where the filter was used to predict the unmeasured parameters. Noticeable deviations between the filter predictions and those predicted by component-matching were present for some cases.

Kalman filters, as previously mentioned, are recursive, thus require several iterations to converge to a final value. Depending on the margins of the user-defined-and-estimated process noise and filter initial conditions, this convergence time can be unacceptably long for real-time performance predictions. Additionally, due to the process noise, Kalman filter predictions will not be as accurate as those obtained using component-matching methods.

### **2.2.6 Methods based on Fuzzy Logic**

Fuzzy logic methods are typically used in engine diagnostics when there is a high uncertainty in the measured data. Fuzzy logic is a method of qualitatively expressing a quantity. This reduces any numerical smearing effect that would otherwise be present in a diagnostic due to measurement uncertainty (Martis, 2007). The purpose of fuzzy logic is to be a substitute for an experienced gas turbine engineer (Ganguli, 2002).

Gunetti et al. (2008) suggested a method by which fuzzy logic can be integrated into a conventional, i.e., component-matching-based, method. He used this method for engine health monitoring purposes as well as fault isolation.

Ganguli (2002) used fuzzy logic to diagnose a benchmark two-spool gas turbine fault using only engine exhaust gas temperature, low- and high-pressure spool speeds, and fuel flow rate. He was able to achieve a fault classification accuracy of 89%, and showed that by including pressures and temperatures at compressor inlets and outlets with model inputs, the accuracy in fault diagnosis can be improved to 98%. Comparisons between the fuzzy logic, ANN and Kalman filtering showed that fuzzy logic method had the highest classification accuracy whereas the ANN method had the lowest.

The use of fuzzy logic in off-design performance simulation tends to be the area of performance diagnostics as illustrated through the work of Alexander and Singh (2004), Kyriazis and Mathioudakis (2009), and Li and Korakianitis (2011). Fuzzy logic-based methods show great improvement once the number of measurements used in the diagnostics process is increased (Ganguli, 2002). However, with the availability of many measurements, one would use a direct component-matching scheme to diagnose performance rather than employ a complex method as fuzzy logic.

### **2.2.7 Methods based on Computational Fluid Dynamics**

Computational fluid dynamics, or CFD, is the solving process of real-life fluid flow phenomenon using equations that represent the physics of such fluid flows. These equations are known as Navier-Stokes equations, and are discussed in more detail in any good fluid dynamics/aerodynamics text book (White, 2003).

CFD methods are usually applied to local regions of a gas turbine such as a compressor or a turbine blade, or a combustion chamber. Also, CFD methods are predominantly used during the development process of a concept and used in conjunction with experimental results. A plethora of such applications are presented by researchers in various publications, of which a several recent publications are discussed below.

Tomita et al. (2006) simulated a hypothetical nacelle for an aero- gas turbine at several flight Mach numbers and angles of attack and confirmed that their design was sound. Das et al. (2006) investigated water droplet trajectories in a fan blade passage of a turbofan at off-design conditions and observed that water droplet mass flux increased with the blade radial location.

Blackburn et al. (2007) demonstrated how CFD was used when upgrading the Rolls-Royce industrial Avon. Using CFD, the end-wall contouring within the Avon's axial turbine was optimized, which resulted in a 0.4% of efficiency increase in the turbine.

Since CFD methods are used to represent realistic flow phenomena, every single aspect of the real-life condition-to-be-simulated must be taken into account; otherwise erroneous results would be obtained (Adamczyk et al., 2007).

El-Batsh (2001) simulated fouling build-up on a turbine blade using a moving-boundary-grid and computing a multiphase flow. This CFD simulation was found to be computationally expensive as the fouling build-up demanded significantly higher grid resolution, i.e., increased number of grids, at the boundary.

Morini et al. (2009) and Fouflias et al. (2009) investigated the effect of fouling on compressor blades by varying blade roughness and blade thickness. Gas path blockage due to increased blade thickness was found to be of greater significance to blade efficiency detriment than increased blade roughness.

As can be seen, CFD-based methods applied to an entire gas turbine off-design performance simulation are rare. This is due to the great number of operating conditions experienced by a gas turbine and the even greater number of computational grids and iterations that are required for a CFD method to produce a reasonable result. This discussion does not even consider the computing costs. Additionally, experimental data is always required to validate a CFD prediction.

### 2.2.8 Wittenberg's Method

All previously discussed methods of gas turbine off-design performance simulation require either a thermodynamic method and/or actual engine data for validation purposes, where the thermodynamic method is based on component-matching. However, component-matching requires one to know the compressor and turbine characteristics.

Wittenberg (1976a) developed a method, a simpler form of component-matching, which eliminated the need for compressor and turbine characteristics. Here, one only requires knowledge of the design-point performance of a gas turbine. With a few well-placed assumptions, using gasdynamics relationships, off-design performance of a gas turbine could then be estimated. The reader may refer to either Walsh and Fletcher (1998) or Saravanamuttoo et al. (2001) for detailed discussions of this method. A concise review of this method is presented next.

For a single-spool turbojet, as shown in Figure 2.4, the work compatibility between the compressor and the turbine can be expressed as,

$$\dot{m}_a c_{pa} (T_{o3} - T_{o2}) = \eta_m \dot{m}_g c_{pg} (T_{o4} - T_{o5}) \quad 2.2.9$$

where  $\dot{m}_a$  is the inlet mass flow rate,  $\eta_m$  is the spool mechanical efficiency,  $c_{pa}$  and  $c_{pg}$  are the specific heats for air and exhaust gas, respectively.  $\dot{m}_g$  is the exhaust mass flow rate, which is the sum of the inlet mass flow rate and the fuel flow rate,  $\dot{m}_f$ . Here, the temperatures are total temperatures.

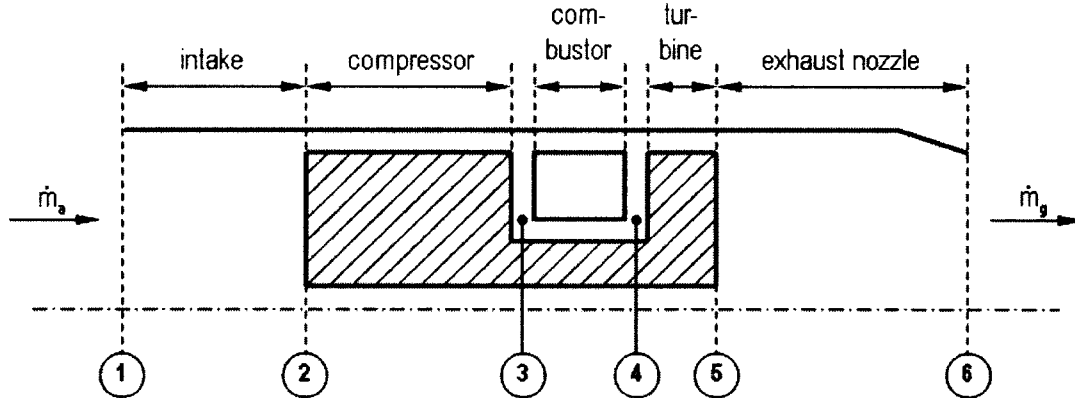


**Figure 2.4** A single-spool turbojet [modified from Wittenberg, 1976a]

Since  $\dot{m}_f$  is typically two orders of magnitude less than  $\dot{m}_a$ ,  $\dot{m}_g$  can be approximated by  $\dot{m}_a$  (Saravanamuttoo et al., 2001). This allows Equation 2.2.9 to be rewritten as,

$$\frac{T_{o3}}{T_{o2}} - 1 = \frac{\eta_m c_{pg}}{c_{pa}} \frac{T_{o4}}{T_{o2}} \left( 1 - \frac{T_{o5}}{T_{o4}} \right) \quad 2.2.10$$

Then, by dividing the terms in Equation 2.2.10 with their respective design-point values and rearranging, Wittenberg arrived at,

$$\frac{T_{o3}}{T_{o2}} = 1 + \phi \left[ \left( \frac{T_{o3}}{T_{o2}} \right)_{des} - 1 \right] \frac{1 - \frac{T_{o5}}{T_{o4}}}{1 - \left( \frac{T_{o5}}{T_{o4}} \right)_{des}}, \quad \text{where } \phi = \frac{\frac{T_{o4}}{T_{o2}}}{\left( \frac{T_{o4}}{T_{o2}} \right)_{des}} \quad 2.2.11$$

Here,  $\phi$  is referred to as the spool temperature ratio.

Similarly, the mass flow compatibility between the compressor and the turbine was expressed as,

$$\frac{\dot{m}_a \sqrt{T_{o2}}}{P_{o2}} = \frac{\dot{m}_a \sqrt{T_{o2}}}{P_{o2}} \bigg|_{\text{des}} \frac{\frac{\dot{m}_g \sqrt{T_{o4}}}{P_{o4}}}{\frac{\dot{m}_g \sqrt{T_{o4}}}{P_{o4}} \bigg|_{\text{des}}} \sqrt{\frac{1}{\phi}} \frac{\frac{P_{o3}}{P_{o2}}}{\frac{P_{o3}}{P_{o2}} \bigg|_{\text{des}}} \quad 2.2.12$$

where the turbine corrected mass flow rate,  $\frac{\dot{m}_g \sqrt{T_{o4}}}{P_{o4}}$ , is assumed to be constant for a

choked turbine, and the combustor pressure loss,  $\frac{P_{o4}}{P_{o3}}$  is assumed to be approximately

constant for all off-design conditions. The compressor pressure and temperature ratios,

$\frac{P_{o3}}{P_{o2}}$  and  $\frac{T_{o3}}{T_{o2}}$ , respectively, are related through,

$$\frac{P_{o3}}{P_{o2}} = \left( \frac{T_{o3}}{T_{o2}} \right)^{\frac{\eta_{\text{comp}} \gamma}{\gamma - 1}} \quad 2.2.13$$

For an unchoked nozzle, the mass flow rate through the nozzle was expressed

using the converging nozzle equation, and the nozzle pressure ratio,  $\frac{P_{o5}}{P_o}$ , was iteratively

found until the compressor pressure ratio converged to produce,

$$\frac{P_{o5}}{P_o} = \frac{P_{o5}}{P_{o4}} \frac{P_{o4}}{P_{o3}} \frac{P_{o3}}{P_{o2}} \frac{P_{o2}}{P_{o1}} \frac{P_{o1}}{P_o} \quad 2.2.14$$

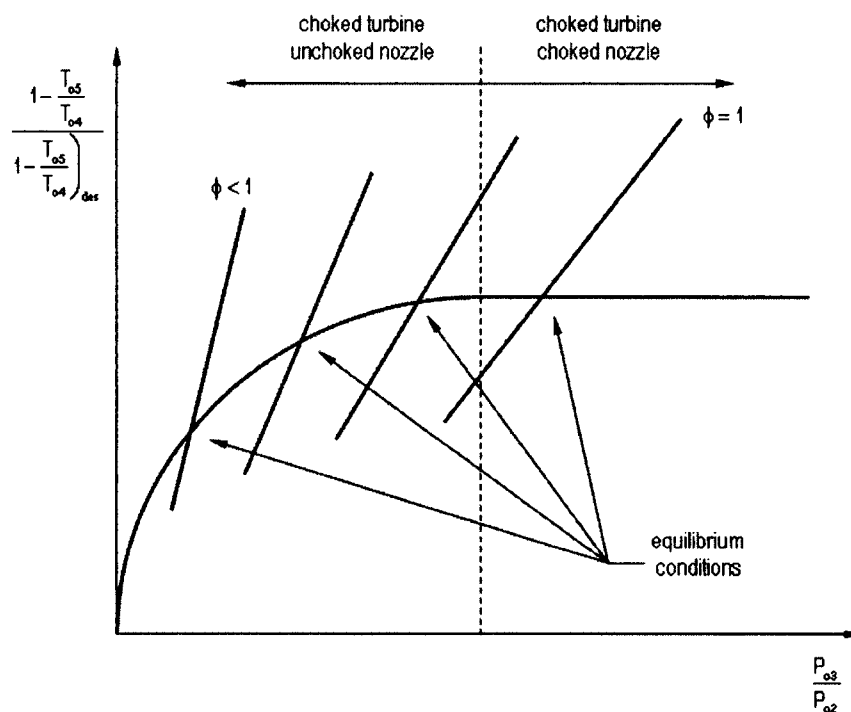


**Figure 2.5** Compressor and turbine-nozzle matching curves for a single-spool turbojet  
[modified from Wittenberg, 1976a]

Thus, Wittenberg demonstrated that the compressor running line can be estimated using the spool temperature ratio and generalized turbine/nozzle characteristics (Figure 2.5).

For multi-spool engines, such as the Rolls-Royce RB211-22 which is a three-spool turbofan, Wittenberg assumed that the high-pressure (HP) and intermediate-pressure (IP) spools remain choked for all off-design conditions. Then, the HP and IP spools were combined together to obtain a hypothetical HP-IP-equivalent spool. This only showed good agreement with engine performance data at high power settings (Wittenberg, 1976a). Mirza-Baig and Saravanamuttoo (1991) used this method to simulate the off-design performance of a Garrett TFE 731-2, a two-spool turbofan.

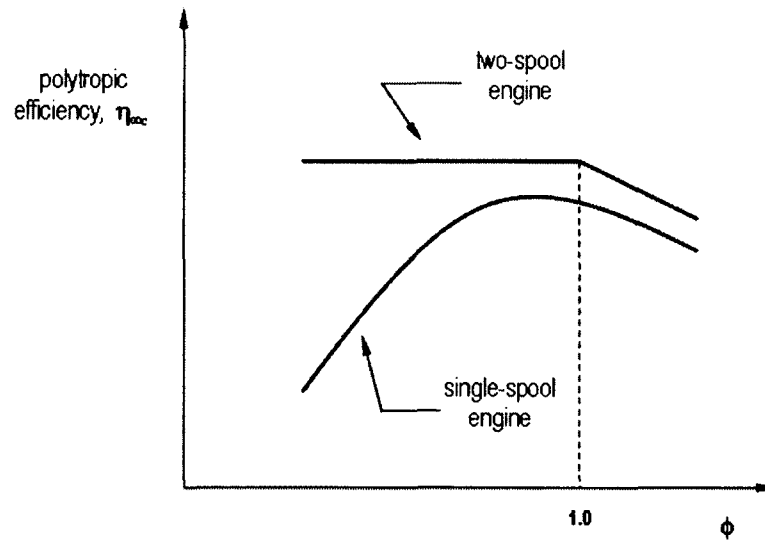


**Figure 2.6** Polytropic efficiencies of actual compressors [modified from Wittenberg, 1976a]

When comparing the spool temperature ratio and the polytropic efficiencies of several compressors (Figure 2.6), Wittenberg observed that for multi-spool engines, the compressor polytropic efficiencies remained constant for a wide range of off-design operating points (Wittenberg, 1976a).

Wittenberg predicted the performance of a Rolls-Royce Viper turbojet assuming constant as well as varying compressor polytropic efficiencies. When compared with the engine data, little variation was found between the two predictions (Figure 2.7).

Puzzlingly, Wittenberg's method has been largely ignored, although it is obvious that it is easy to implement, and possibly the best alternative to the full-scale component-matching methods.

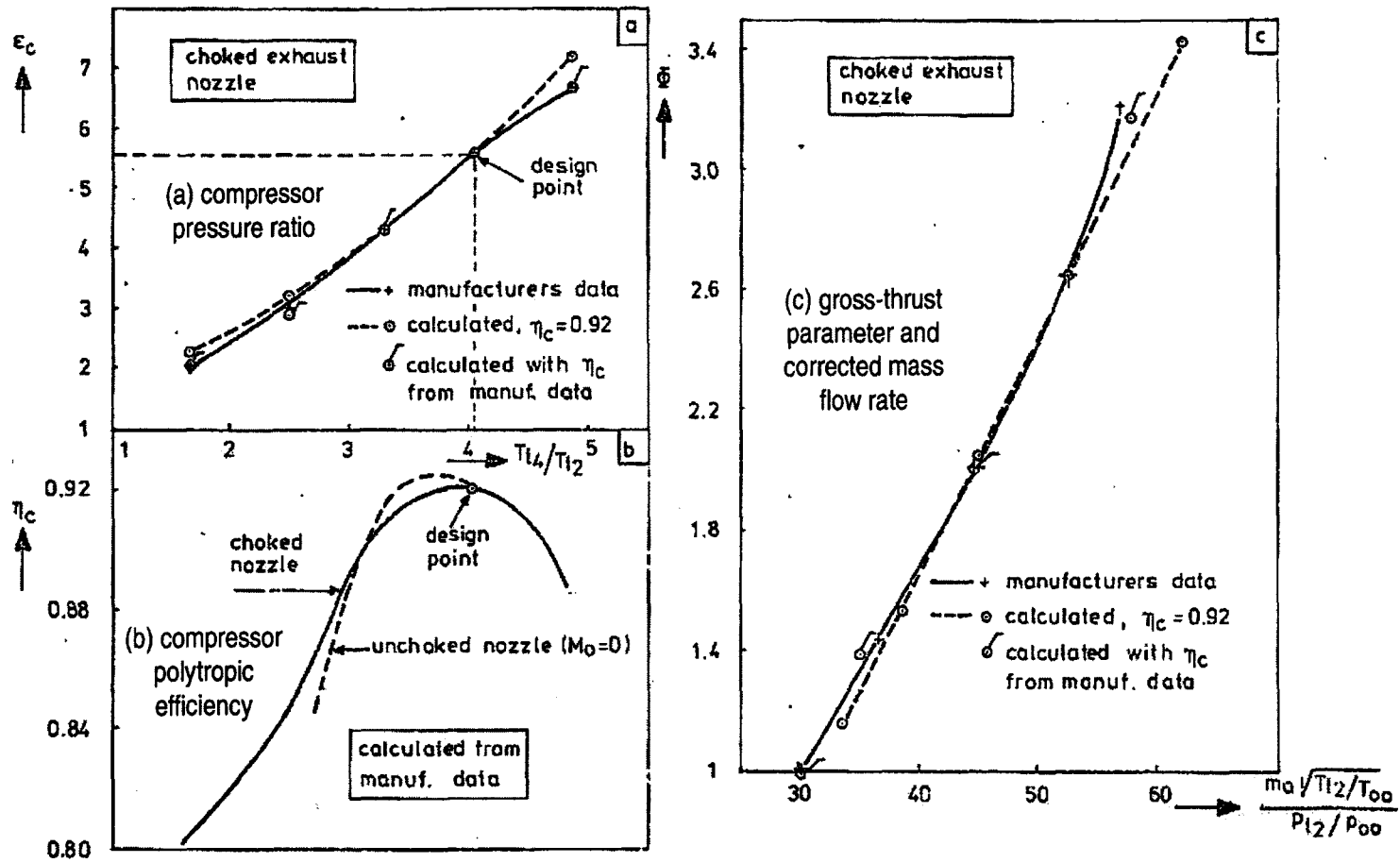
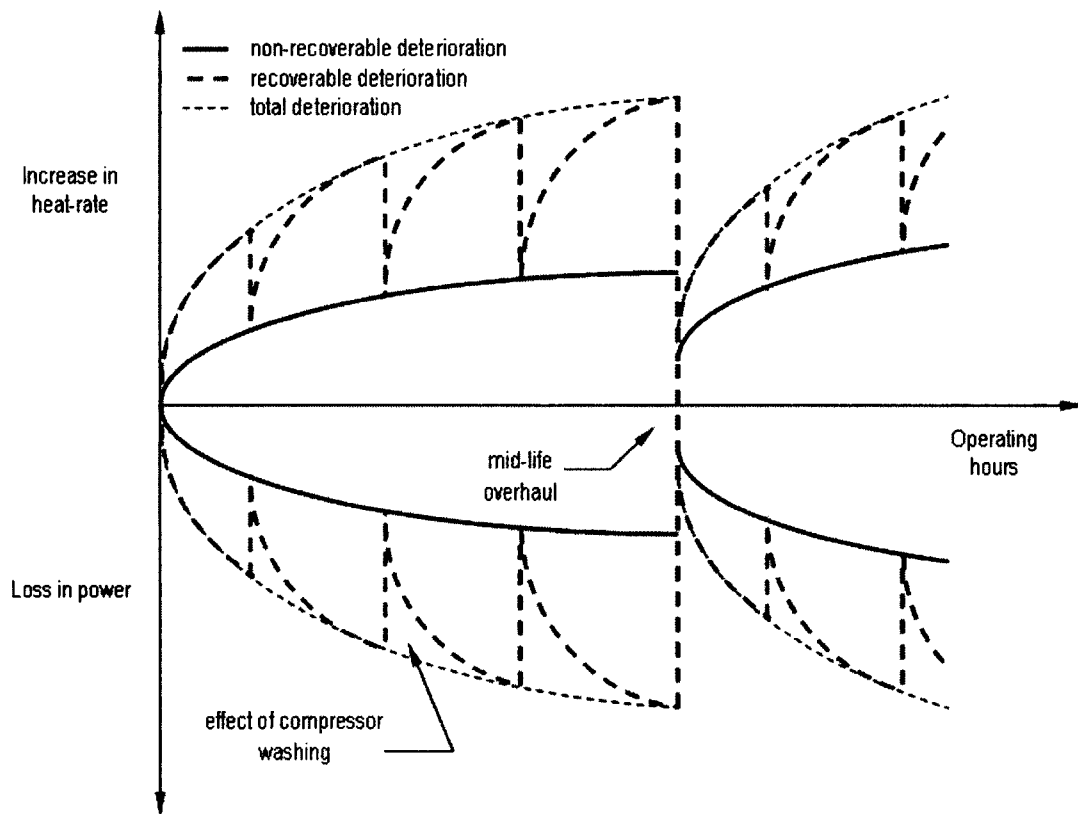


Figure 2.7 Actual and predicted off-design performance of the Rolls-Royce Viper [modified from Wittenberg, 1976a]



**Figure 2.8** Performance deterioration in gas turbines [modified from Gauthier, 2008]

### 2.3 Performance Deterioration in Gas Turbines

In the process of developing a versatile off-design performance simulation method, the need for simulating performance deterioration is also addressed. In the present study, data from deteriorating engines are used to validate the developed model. Therefore, the mechanisms that cause deterioration and their effect on engine performance are reviewed such that the engine data can be skillfully processed.

Performance deterioration is a combination of temporary and permanent deterioration (Figure 2.8). The temporary form, also known as recoverable deterioration,

is due to performance loss resulting from contaminant buildup, i.e., fouling, on engine surfaces exposed to the gas path. Since a majority of these contaminants can be removed by cleaning the affected surfaces, the lost performance can therefore be recovered.

The permanent form, or non-recoverable deterioration, is caused by physical damage resulting from erosion, corrosion and some fouling. Non-recoverable performance deterioration may only be recovered after a complete engine overhaul.

### **2.3.1 Deterioration Mechanisms**

This discussion is weighted towards recoverable deterioration since that is the predominant mode of deterioration observed in the available engine data.

There are many factors that cause engine performance deterioration. They can be categorized into internal and external causes. Internal causes shall cover factors within the engine. This refers to everything related to the engine that is between the inlet and the exhaust filters. External causes cover everything else.

The dominant among internal causes of deterioration are the number of engine starts per year, the number of operating hours, the application of the engine (mechanical drive or power generation), engine operating mode (peak load, baseload or part load) and the type of fuel used. Here, peak load operation refers to an engine that activates whenever extra power (or head increase) is required by the existing power grid. Baseload refers to an engine profile that operates at a constant power setting that is at or above approximately 70% of the engine's design-point. Part load is similar to baseload operation, but the power setting parameter is below the previously-mentioned 70% power limit.

Among external causes, the geographic location of the engine dominates all else. Here, performance deterioration is a result of a combination of ambient temperature and pressure, the relative humidity and the contaminant concentration in the atmosphere.

### **Erosion**

Erosion is a process by which material is removed from a surface resulting in an altered surface geometry due to impaction by particles known as erodent. This is a cause of non-recoverable performance deterioration. Erosion in a gas turbine can be caused by ingestion of sand, fly ash, water droplets, ice, maintenance tools and birds.

Upton (1974) and Saravanamuttoo et al. (2001) suggested that severity of engine erosion is location dependent since atmospheric particulate loading, i.e., solid particles per million by weight (ppmw) varies geographically. The particulate concentrations were classified geographically as follows.

**Table 1.1** Particulate concentration variation [modified from Upton, 1974]

<b>Location</b>	<b>Particulate concentration (ppmw)</b>
Marine	0.01
Rural	0.01 – 0.1
Coastal	0.01 – 0.1
Industrial	0.01 – 0.1
Desert	0.1 – 700

Of all gas turbine components, the compressor is susceptible to most of the erosion damage since it encounters erodent in their original shape, size and almost zero angular velocity. This results in blunted leading edges, sharpened trailing edges and an

increase in overall surface roughness of compressor blades. Erosion in the turbine section is not as severe since the erodent exiting the compressor is typically finer in size than that entering the engine, and in many cases this refined erodent is burned or evaporated in the combustors.

### **Corrosion**

Corrosion is the formation of oxides on a surface. The typical cause of corrosion in gas turbines is the exposure to salts, lead, vanadium and other corrosive chemicals (Kurz and Brun, 2007). Within compressors, highly localized corrosion spots occur. This is known as pitting corrosion. In turbines, once mixed with hot combustion gases, the corrosion inhibitors cause hot corrosion, which tends to be distributed over surfaces exposed to the gas path.

Overall, corrosion increases blade surface roughness and in severe cases, alters blade profiles in gas turbines, thus causing non-recoverable deterioration. The geographic location of an engine has a strong bearing on the severity of corrosion experienced (Kurz and Brun, 2007).

### **Fouling**

Fouling is the buildup of contaminants on engine component surfaces exposed to the gas path such as blades and annulus walls. Fouling is the only recoverable form of deterioration, although if unchecked, can cause non-recoverable deterioration by altering blade geometries as well as increasing blade surface roughness (Saravanamuttoo et al., 2001). Fouling can be the result of the presence of oil or water mists within the ingested

air (Kurz and Brun, 2007), or in the case of extremely small contaminants, electrostatic forces (El-Batsh, 2001). The former is referred to as wet deposition and the latter, dry deposition.

About 80 – 90% of the contaminants that pass through a typical inlet filter are less than 2  $\mu\text{m}$  in size and are the root cause of compressor fouling (Diakunchak, 1992). Fouling within the turbine may also occur as a result of burning liquid fuels or fuels with impurities. However, modern gas turbines generally burn gaseous fuels, qualities of which are set by engine manufacturers, thus experience little fouling. Aker and Saravanamuttoo (1989) indicated that the first stages of axial compressors are the most affected by fouling, and that the number of fouled stages may account for 40 – 50% of the total number of compressor stages. Tarabrin et al. (1998) suggests that fouling affects the first 5 – 6 stages of a compressor and that the contaminant buildup occurs on both the pressure and suction surfaces of the blades. This can be assumed to be ideal fouling locations for dry deposition since such regions experience relatively lower aerodynamic forces. Fouling caused by salt spray tends to build up primarily on the leading edges of the first few compressor stages.

Fouling, just as erosion and corrosion, is location dependent. In rural areas fouling can be caused by insects, pollen and tree sap. Dust and chemical vapours are found to cause fouling in industrial environments; salts in coastal and offshore locations (Saravanamuttoo et al., 2001).

### **2.3.2 Performance Recovery Methods**

Gas turbine maintenance has now become a scheduled task based on engine performance predictions compared to, as Boyce (2002) suggests, breakdown or panic maintenance. Buildup of fouling cannot be prevented since there is no such environment that is without contaminants of some sort. The only methods of combating fouling are by performing a compressor cleaning, by selecting more effective inlet filters, or by applying anti-fouling coating to blade surfaces (Caguiat, 2003). More effective inlet filters tend to be expensive and tend to have a higher head loss. Anti-fouling coating is expensive as well. Therefore, engine operators look towards compressor cleaning as a mean of performance recovery.

#### **Abrasive Cleaning**

Abrasive cleaning is a method where relatively soft materials such as walnut shells, apricot stones, rice husks and spent catalysts are injected into an engine that is either idling or operating at a normal speed. These materials crash on to blade surfaces and break away the deposits. Despite the effectiveness, abrasive cleaning is seldom used since the cleaning materials can lodge themselves within cooling passages, mechanical linkages such as bearing housings and cause severe damage to an engine in the long run. Additionally, the blade coating may experience erosion thus compromising the base metals in addition to increasing surface roughness and losses (Schneider et al., 2010).

## **Compressor Washing**

Compressor washing using de-mineralized water with or without a pH-neutral detergent is another method of performance recovery. Compressor washing can be performed while an engine is running or when it is shutdown. These two scenarios are referred to as online and offline (or crank soak) washing, respectively.

Online washing is attractive to engine operators since this does not require an engine to be shutdown, which, if shutdown, for a heavy frame industrial engine operator may cost up to 24 hours in downtime (Boyce, 2002). During online washing, an engine is brought down to idling speed as water is sprayed into the front of the engine. It is the first few stages of the compressors that are partially cleaned since the water loses sufficient momentum as it impacts blade surfaces while traveling into the compressor. Evaporation also occurs due to high gas temperatures. Coincidentally, only the first few stages are required to be cleaned since they are the most susceptible to fouling (Aker and Saravanamuttoo, 1989). Field experience has shown (Kurz, 2005) that water droplets carry sufficient inertia to cause water erosion on the blade surfaces of the first stage rotor. Therefore, frequent online washing may lead to non-recoverable deterioration.

Offline washing, or crank soak washing, is referred as such since the compressor washing takes place when an engine is shutdown. Here, the engine is rotated by the starter system. Once the compressors are rotating at approximately 50% of the starting speed, the cleaning solution is injected and the starter system is disengaged. The compressor is then allowed to coast to a halt (Boyce, 2002).

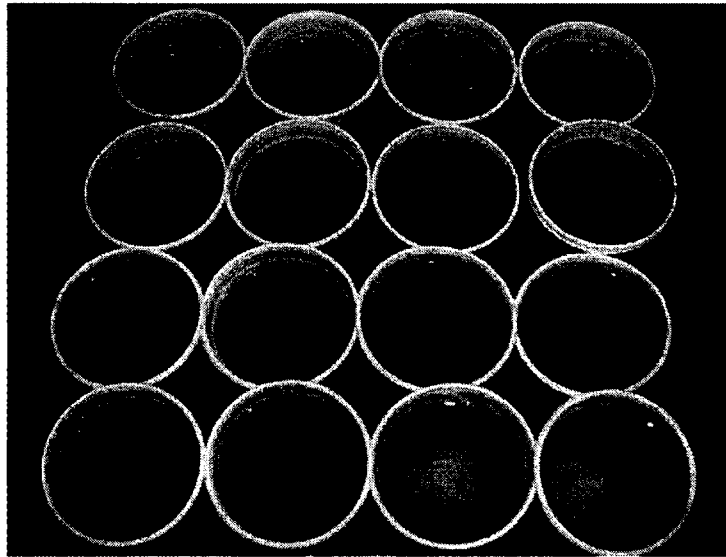


**Figure 2.9** Result of multiple crank soak washes during a single wash cycle [Taylor and Gotheridge, 2006]

Then, the cleaning agent is left to dissolve the contaminants for a few minutes, and rinsed away with de-mineralized water. This process is repeated until water leaving the engine bares evidence of little or no contaminants (Figure 2.9).

Since the engine temperatures and spool speeds are low enough to accommodate liquids into one or two further downstream stages than the online washing procedure, offline washing is more effective than online washing (Boyce [2002], and Saravananuttoo et al. [2001]).

The most effective method of performance recovery after fouling is cleaning by hand. This, however, is only possible if the engine casings can be opened.

## **3 ENGINE DATA ACQUISITION AND ANALYSIS**

### **3.1 Introduction**

A milestone in the development process of any simulation that reflects reality is the validation of the simulation using a set of real-life data. To obtain this validation data, one must first acquire and analyze raw measurements – a process that eventually provides data with an uncertainty margin. If the simulation provides predictions that exist within this uncertainty margin, the simulation is said to be validated.

In this chapter, the source of the validation data for the present study, i.e., three industrial RB211 engines, is first discussed along with a brief introduction to this specific gas turbine. Next, the data acquisition process, the measurement instrumentation and their associated errors are discussed. Finally, a discussion on the data analysis process and the methods by which the measurement errors are propagated into the analysis results is presented.

## **3.2 The Rolls-Royce Industrial RB211**

### **3.2.1 Introduction**

The Rolls-Royce industrial RB211 is one of the world's leading aero-derivative gas turbines used in the power generation and oil-and-gas compression industries.

Introduced in 1975, the industrial RB211 traces its roots to the Rolls-Royce RB211-22 aero- engine, which is a high-bypass, high-efficiency turbofan engine powering aircraft such as the Lockheed L-1011. The latest industrial RB211 is capable of producing up to 33.2 MW of power at 40.5% thermal efficiency (Broomfield, 2007).

### **3.2.2 Mechanical Configuration**

The industrial RB211 consists of a two-spool gas generator and a free power turbine. The low-pressure turbine of the aero- RB211, which powers the fan, is replaced by the free power turbine in the industrial RB211. This free power turbine is used to either drive an electrical generator (for power generation) or a compressor (for gas compression).

The low-pressure (LP) compressor consists of seven stages, and the high-pressure (HP) compressor has six stages. Both HP and LP turbines consist of a single stage each. Depending on the engine variant, the free power turbine has either two or three stages.

The combustors of the Dry, Low Emission (DLE) variant is comprised of nine radial-wise-protruding combustors known as can combustors. These combustors provide improved combustion, thus reduce CO and NO<sub>x</sub> emissions. Additionally, this design allows for combustor design modification while maintaining the core engine dimensions unchanged.

### **3.3 Overview of Engine Data**

#### **3.3.1 Data Sources**

Data were obtained from three industrial RB211 gas turbines, whose exact variant is RB211-24GT DLE RT61 (Figure 3.1). Hereinafter, these three engines are referred to as GT1, GT2 and GT3. A dataset for a given engine includes the engine's performance when new, and performance spanning for a few thousand hours since new.

These engines are used for power generation at a highly industrial environment at Fafen Energia in Camçari, Brazil. As expected (Upton, 1974), heavy performance deterioration on the engines were observed from the data.

#### **3.3.2 Engine Health Monitoring Measurements**

Each production industrial RB211 is equipped with several sensors to measure certain engine performance parameters including pressures and temperatures. These measurements are used by the engine control system to maintain the engine's operation within a pre-specified safety margin.

If an engine owner has agreed to a Long Term Service Contract, some of the measurements used by the engine control system are permanently stored within a database at Rolls-Royce's Customer Service Business division. This stored data is referred to as engine (or unit) health monitoring data, a typical batch of which contains the following performance parameters.

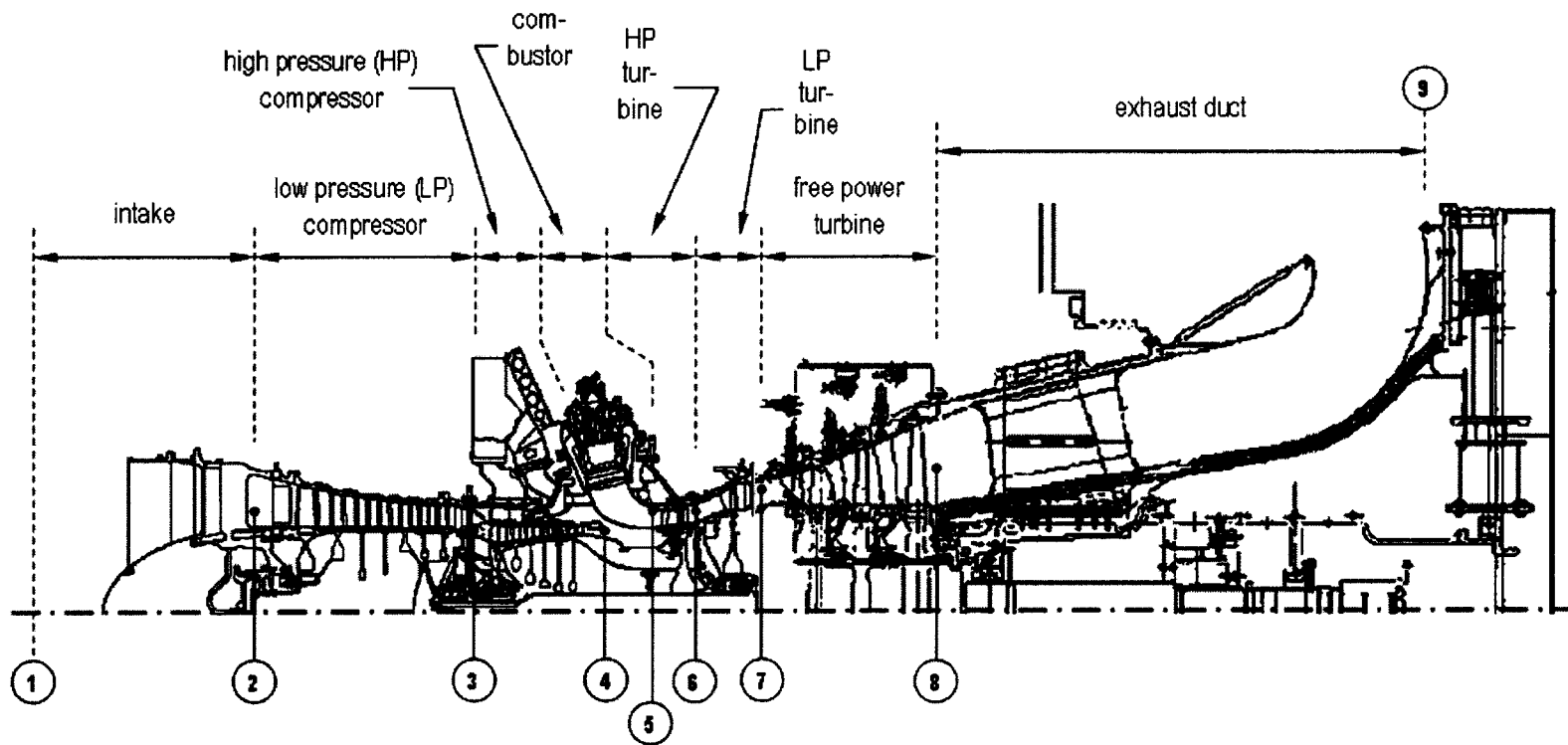


**Figure 3.1** The Rolls-Royce industrial RB211-24GT DLE RT61 [modified from Broomfield, 2007]

Ambient temperature	$T_{o1}$	[K]
Ambient pressure	$P_{o1}$	[kPa]
LP compressor outlet temperature	$T_{o3}$	[K]
LP compressor outlet pressure	$P_{o3}$	[kPa]
HP compressor outlet temperature	$T_{o4}$	[K]
HP compressor outlet pressure <sup>†</sup>	$P_{o4}$	[kPa]
LP turbine outlet temperature	$T_{o7}$	[K]
Fuel flow rate <sup>*</sup>	$\dot{m}_f$	[kg/sec]
Engine power output	PWR	[kW]
LP spool speed	$N_L$	[rpm]
HP spool speed	$N_H$	[rpm]
Fuel composition	-	[-]

<sup>†</sup> the HP compressor outlet pressure is calculated through component-matching

<sup>\*</sup> the fuel flow rate at site is calculated through component-matching

### 3.3.3 Data Sampling Frequency

A dataset for a given site stored under the Long Term Service Contract contains numerous data points spanning thousands of hours. Each data point contains the previously-mentioned parameters, the values of which are measured on the hour every hour. In other words, a dataset for a given site is an hourly log of *instantaneous* engine performance.

### 3.3.4 Measurement Instruments and Associated Errors

In this section, the instruments used to measure the previously-mentioned parameters are discussed. All measurement instruments have been selected by Rolls-Royce based on cost-effectiveness, durability and feasibility. Furthermore, the placements of these instruments within an engine are decided by the engine manufacturer, i.e., Rolls-Royce.

#### Ambient Temperature, $T_{o1}$

A resistive thermal device (RTD) located inside the inlet filter measures the ambient temperature,  $T_{o1}$ . This sensor is manufactured by Rosemount Inc. (Model 0078), and has a temperature cycling uncertainty of  $\pm 0.28$  °C and a stability of  $\pm 0.35$  °C over a temperature range of -200 to +500 °C. At ISO conditions (similar to that observed at site) this device has an accuracy of  $\pm 0.18$  °C (Rosemount, 2010c). Coupled with the data acquisition system uncertainty (arising from signal conditioning) of  $\pm 0.125$  °C (Duminica, 2002) the root sum squared (RSS) uncertainty of  $T_{o1}$  increases to  $\pm 0.50$  °C.

#### LP Compressor Outlet Temperature, $T_{o3}$

Technical details of the  $T_{o3}$  thermocouple are not publicly available. However, Rolls-Royce requires an accuracy of  $\pm 1.5$  °C within an operating range of -50 to +233 °C from this thermocouple. According to Boyce (2002), this requirement would suggest a copper/constantan thermocouple. With the data acquisition system uncertainty of  $\pm 0.75$  °C (Duminica, 2002), the RSS uncertainty of  $T_{o3}$  is  $\pm 1.68$  °C.

The  $T_{o3}$  thermocouple is located approximately 1.5 chord lengths downstream of the stator of the 7<sup>th</sup> LP compressor stage. Due to the location of this sensor, the possible effect of rotor wakes on the measurement was investigated. The data acquisition system has a refresh rate of ~20 milliseconds, during which the  $T_{o3}$  thermocouple may experience at least 30 rotor wakes at design-point rotor speed. Thus, the refresh rate of the data acquisition system is unable to capture the full profile of the temperature fluctuations due to rotor wakes. Instead, the measured fluctuations contribute to the uncertainty of the thermocouple measurements at this location.

Reynolds et al. (1979), Lakshminarayana and Reynolds (1980), and Sullerey and Sayeed Khan (1983) have showed that at this location within a compressor, at least 70% of a rotor wake's intensity is diffused due to turbulence, which is expected to reduce the magnitude of temperature fluctuations caused by the passing rotor wakes.

#### **HP Compressor Outlet Temperature, $T_{o4}$**

The instrument uncertainty required by Rolls-Royce for the  $T_{o4}$  thermocouple is  $\pm 0.4\%$  of reading between 375 to 600 °C. This translates to an uncertainty range increasing from  $\pm 1.5$  °C at 375 °C to  $\pm 2.4$  °C at 600 °C. Therefore, at engine design-point, the  $T_{o4}$  measurement has an estimated instrument uncertainty of  $\pm 1.87$  °C. After accounting for the data acquisition system uncertainty of  $\pm 0.75$  °C (Duminica, 2002), the RSS uncertainty increase to  $\pm 2.01$  °C.

Although technical specifications for this thermocouple are publicly unavailable, the given required temperature hints at a possible iron/constantan or chromel/constantan configuration. Such thermocouples shall have an accuracy of  $\pm 1.0$  °C (Boyce, 2002).

The air used for the  $T_{o4}$  measurement is extracted between two combustor chambers. The air is then channeled into a flow stagnating device similar to a dashpot, where the  $T_{o4}$  measurement is taken. Due to flow diffusion that occurs at the HP compressor outlet prior to entering the combustors, and the additional diffusion that occurs within the flow stagnating device,  $T_{o4}$  temperature fluctuations due to rotor wakes are expected to be negligible.

#### **LP Turbine Outlet Temperature, $T_{o7}$**

The  $T_{o7}$  thermocouple is required by Rolls-Royce to have an uncertainty of  $\pm 0.4\%$  of reading between 375 and 900 °C. At design-point, this produces an uncertainty of  $\pm 3.2$  °C. Accounting for the data acquisition system uncertainty of  $\pm 0.75$  °C (Duminica, 2002), this uncertainty increases to  $\pm 3.3$  °C. Since there are 17  $T_{o7}$  thermocouples, the uncertainty of the overall  $T_{o7}$  measurement is reduced to  $\pm 0.8$  °C with the application of the central limits theorem.

The reason for using 17 thermocouples is that the  $T_{o7}$  measurement is the primary power-setting parameter, i.e., the 'run to' parameter, in an industrial RB211. This renders  $T_{o7}$  a critical measurement, thus requires multiple redundancies and a low measurement uncertainty to ensure safe engine operation.

Considering the operating environment and the required operating range, the thermocouple would be of a chromel/constantan type (Boyce, 2002).

With the data acquisition system refresh period of  $\sim 20$  milliseconds, a single  $T_{o7}$  thermocouple would experience at least 4 rotor wakes, thus is unable to capture the full

temperature fluctuations of the LP turbine rotor wakes. The averaging of the thermocouples would further filter out any fluctuations in the thermocouple readings due to wake passing.

### **Ambient Pressure, $P_{o1}$**

The ambient pressure,  $P_{o1}$ , is measured by a Rosemount pressure gauge (Model 3051 CA1A). This instrument has an uncertainty of  $\pm 0.310$  kPa (Rosemount, 2010b), which increases to (RSS)  $\pm 0.326$  kPa once coupled with the data acquisition system error of  $\pm 0.1$  kPa. This measurement is taken outside the engine housing. Since ambient pressure variation is a quiescent process, this uncertainty can be further reduced by data averaging.

### **LP Compressor Outlet Pressure, $P_{o3}$**

The LP compressor outlet pressure,  $P_{o3}$ , is measured by a Rosemount pressure gauge (Model 3051 PG4A), which has an uncertainty of  $\pm 2.9$  kPa (Rosemount, 2010a). With the data acquisition system error ( $\pm 0.3$  kPa), the RSS uncertainty of the  $P_{o3}$  measurement increases to  $\pm 2.91$  kPa (Duminica, 2002).

$P_{o3}$  is measured through a static port located approximately 1.5 chord lengths downstream of the stators of the 7<sup>th</sup> stage of the LP compressor, and is converted to a total pressure by the engine control system using the LP and HP compressor operating points. Reynolds et al. (1979), Lakshminarayana and Reynolds (1980), and Sullerey and Sayeed Khan (1983) noted that due to the turbulent boundary layer at the annulus walls, blade wakes have negligible effect on the flow profiles within this region. Therefore, the

effects of blade wake passing on the  $P_{03}$  measurement can be considered to be negligible.

### **Low- and High-Pressure Spool Speeds, $N_L$ and $N_H$**

The low- and high-pressure spool speeds,  $N_L$  and  $N_H$ , respectively, are measured by magnetic pulse detectors manufactured by Smiths Aerospace (Model 3602 KGB/1). The speed measurements have an overall uncertainty of  $\pm 0.5$  rpm.

$N_L$  and  $N_H$  are measured by 3 and 2 speed transducers, respectively. These are critical measurements in an industrial RB211 since they are used to perform component matching by the engine control system. Therefore, the usage of multiple instruments is justified. The  $N_L$  and  $N_H$  measurements are the most accurate measurements taken of an industrial RB211 as they have uncertainties less than  $\pm 0.01\%$  of the measured value.

### **Fuel Composition**

The fuel composition is measured by a Daniel Measurement gas chromatograph (Model 500/2350). This measures the mole fraction of the fuel with an overall uncertainty of  $\pm 0.025$  mole fractions. This chromatograph requires four minutes to complete analyzing a fuel sample (Daniel Measurements, 2010).

To determine the effect of the individual uncertainties of each measured compound (i.e.,  $\text{CH}_4$ ,  $\text{C}_2\text{H}_6$ , etc.) on the lower heating value of the fuel, a collective perturbation was performed rather than sequential perturbation. This was accomplished by running a Monte Carlo simulation, and is discussed further in Appendix A. The simulation algorithm is available in Appendix D.1. The lower heating value thus has an uncertainty of  $\pm 43.6$  kJ/kg, which is approximately  $\pm 0.1\%$  of the typical observed value.

## 3.4 Field Data Analysis Process

### 3.4.1 Pre-Processing of Field Data

The data acquisition system records engine performance measurements regardless of an engine's operating status. As a result, the site datasets contained measurements taken while the engine was either shutdown or idling.

Occasional lapses in the functionality of the measurement instrumentation or that of the data acquisition system were also observed. In such a situation, a reading of -5555 was registered in the allocated space within the dataset.

Therefore, a simple data conditioning was performed by discarding data points for which:

- the LP turbine outlet temperature,  $T_{07}$ , dropped below 830 K,
- the LP spool speed,  $N_L$ , dropped below 5000 rpm, and,
- a -5555 reading was registered.

### 3.4.2 $T_{07}$ Bias Error Correction

In an ideal industrial RB211, the combustor-discharge gases and the combustor-bypass gases would fully mix to provide a uniform temperature profile across the annulus at the LP turbine outlet. In other words, all 17  $T_{07}$  measurements would indicate the same temperature.

In reality, however, full mixing of hot and cold gases is rarely achieved. This creates a non-uniform temperature profile at the LP turbine outlet. This results in a few thermocouples indicating 'hot spots' and a few indicating 'cold spots' (Figure 3.2).

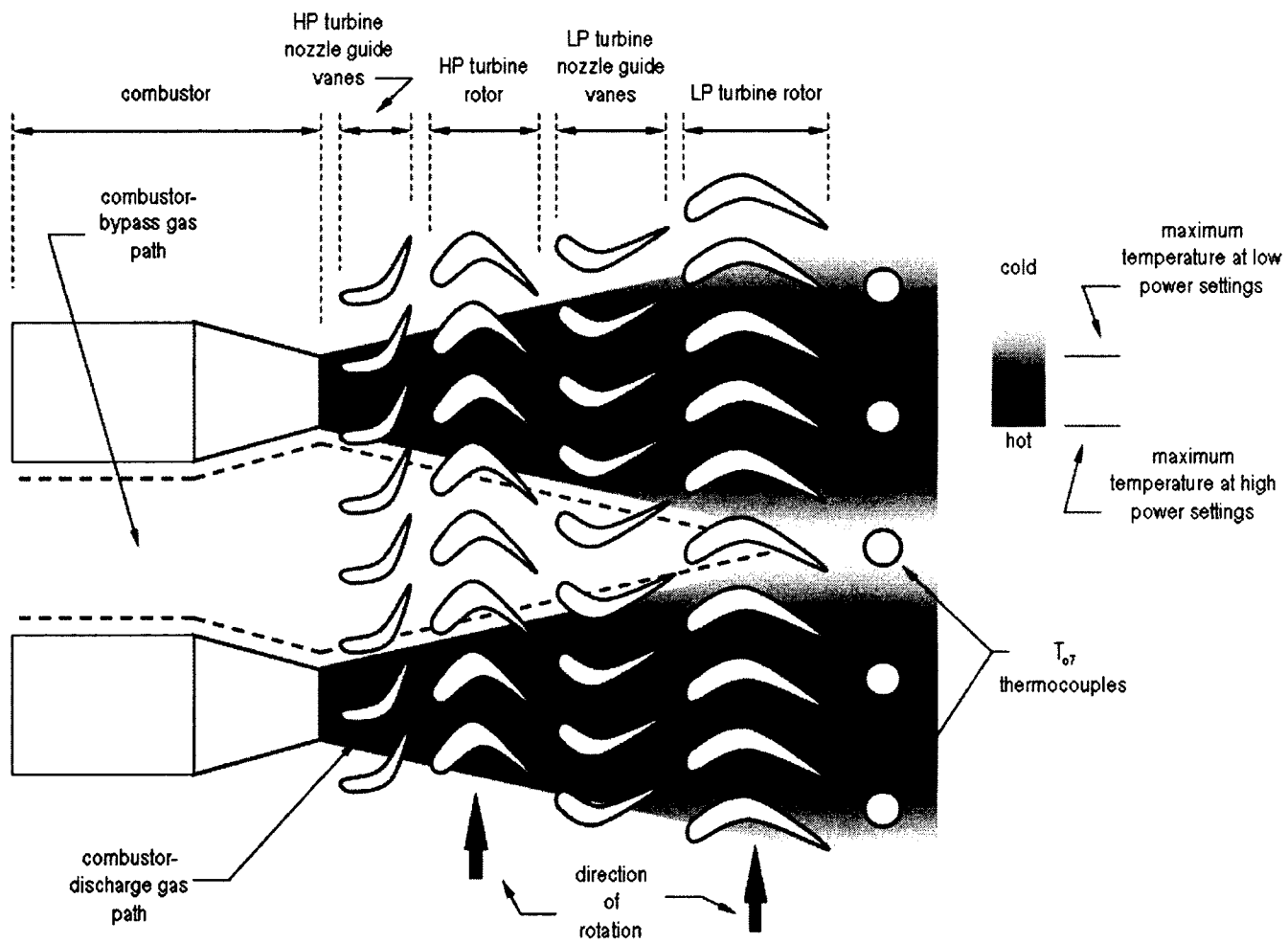


**Figure 3.2** A schematic illustration of mixing of combustor-discharge and combustor-bypass gases

Outliers, i.e., thermocouples indicating extremely high or low temperatures, are excluded from the dataset. These are detected by the industrial RB211's engine control system, which simply discards them while averaging the temperature readings of the remaining thermocouples. Gulen et al. (2000) have followed a similar technique when conducting real-time performance diagnostics on General Electric PG7121EA engines.

Prior to delivery to a customer, each industrial RB211 is put through a pass-off performance test, during which the theoretical and the measured  $T_{o7}$  values are compared. The difference between these two values is considered as the  $T_{o7}$  bias error resulting from the outlier elimination and thermocouple position error. The theoretical  $T_{o7}$  is calculated using component-matching, for which the measured values of the fuel flow rate (only available during the pass-off test) and fuel heating value are used. Saravanamuttoo et al. [2001], and Walsh and Fletcher [2001] present further details.

At different power settings, the amount of mixing between the hot and cold gases, as well as the difference between the temperatures of the hot and cold gases varies (Figure 3.2). As a result, the  $T_{o7}$  bias error is found to vary with the power setting as well.

At low power settings, the error is at its minimum. The error is found to asymptotically reach a maximum with increasing engine power setting. It is observed that approximately above 70% of design-point power setting, the  $T_{o7}$  bias ceases to noticeably change, thus is able to be approximated as constant. Since the engines considered here operate above the 70% power limit, their respective  $T_{o7}$  biases were simply added to their measured  $T_{o7}$  values, thereby compensating for the  $T_{o7}$  bias error.

### 3.4.3 Instrument Calibration Error Correction

Upon reviewing Rolls-Royce practices, it was learned that an engine does not undergo a calibration once delivered to a customer so that any site-specific factors influencing the performance of the engine can be accounted for in the processing of the measurements. This was found to produce faulty analysis results in the form of increasing engine performance with time. Therefore, an *a posteriori* instrument calibration was conducted where the calibration error was minimized by utilizing bias factors (developed by Rolls-Royce) and *experience* of the author and Rolls-Royce engineers (Drosg, 2007). This calibration method revolved around two guidelines described as follows. Figure 3.3 contains a visualization aid.

- the best engine performance with non-recoverable deterioration at site must be less than or equal to the engine performance during the pass-off test
  - o this ensures that when a proper instrument calibration is applied, the engine performance at site will be less than that at pass-off test
  
- the deterioration trend for a performance variable at site (say, for example, the HP compressor efficiency) can be back-extrapolated to zero operating hours. The back-extrapolated value of this performance variable must be the same as that variable's magnitude during the pass-off test
  - o this is applicable for datasets that begin after a several hundred or more operating hours since the pass-off test, i.e., since new. The shape of the extrapolated trend was determined based on experience with

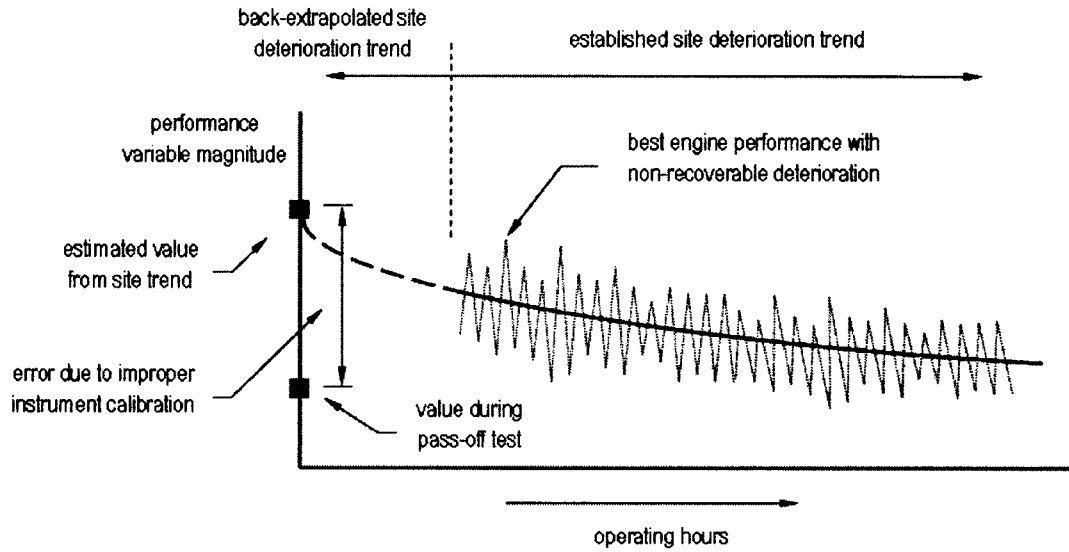


**Figure 3.3** Instrument calibration process

support from literature by Gulen et al. (2000), Kurz and Brun (2001), Veer et al. (2004), and Schneider et al. (2010).

The calibration process involved applying correction factors to the LP and HP compressor outlet pressures and temperatures, and the estimated fuel flow rate. These correction factors were found iteratively using a Rolls-Royce developed software.

### 3.4.4 Field Dataset Analysis

The field datasets were analyzed using a Rolls-Royce-developed proprietary non-linear gas path analysis software. The basic theory on which this software operates was presented in Section 2.2.3.

Through trial and error and using the work of Ogaji et al. (2002) as a guide, the following variables were chosen to be the outputs of the analysis process since they were found to best represent the overall status of engine health.

LP compressor efficiency	$\eta_{LPC}$
HP compressor efficiency	$\eta_{HPC}$
HP turbine efficiency	$\eta_{HPT}$
LP turbine efficiency	$\eta_{LPT}$
Power turbine efficiency	$\eta_{PT}$
LP compressor capacity	$\Gamma_{LPC}$
HP compressor capacity	$\Gamma_{HPC}$
Core bleed flow	$\beta$

Here, the core bleed flow,  $\beta$ , is the sum of the bleed and the leakage flows within the core of the engine. Compressor capacity,  $\Gamma$ , is simply the corrected mass flow rate of a compressor, non-dimensionalized with respect to its design-point value.

The engine measurements mentioned in Section 3.3.2 were used as inputs to obtain the above-mentioned variables.

### 3.4.5 Processing of the Analysis Results

In this step, the recoverable and non-recoverable deterioration data were separated. The purpose of this action was to extract the recoverable deterioration profiles of the analysis results. This was accomplished by expressing a given analysis result, denoted by  $\Omega_{\text{site}}$ , as a function of total engine operating hours, OPHRS, and hours since last wash, WSHRS. Specifically,

$$\Omega_{\text{site}} = K_{\text{rec}}(\text{WSHRS}) \times K_{\text{nonrec}}(\text{OPHRS}) \times \Omega_{\text{nominal}} \quad 3.4.1$$

where  $K_{\text{rec}}(\text{WSHRS})$  is the recoverable deterioration factor,  $K_{\text{nonrec}}(\text{OPHRS})$  is the non-recoverable deterioration factor, and  $\Omega_{\text{nominal}}$  is the nominal magnitude (value when new) of the analysis result at the given power setting.

Each of the recoverable deterioration factors,  $K_{\text{rec}}(\text{WSHRS})$ , were then initialized to their prevailing values at the beginning of their respective wash cycles, thereby eliminating the need to incorporate  $K_{\text{nonrec}}(\text{OPHRS})$  in the remaining calculations.

The deterioration factor for, say, LP compressor efficiency is calculated by first initializing the LP compressor efficiency at a given operating hour (OPHRS) by its nominal efficiency. This factor contains both the recoverable and non-recoverable deterioration factors. Since the number of hours since the last compressor wash (WSHRS) is known from the engine maintenance log, and the trend of the non-recoverable deterioration factor is known from the saw-tooth profile (Figure 2.8) of the complete initialized LP compressor efficiency data,  $K_{\text{rec}}(\text{WSHRS})$  and

$K_{\text{nonrec}}$  (OPHRS) can therefore be separated. The same procedure is followed for the remaining variables mentioned in Section 3.4.4.

At the end of this process, several initialized recoverable deterioration curves would be obtained for a given variable, say, LP compressor efficiency, where each of these curves represents a *tooth* in the saw-tooth profile (Figure 2.8). These curves are then arithmetically-averaged, of which the moving average is found, the process of which is described in detail in Appendix B. The final result was found to be well represented by the following function.

$$K_{\text{rec}})_{\text{average}} = -a(1 - e^{-bt}) + c \quad 3.4.2$$

This function is suggested by Tarabrin et al. (1998). Here,  $a$  is the convergence value,  $b$  is the convergence delay factor, and  $c$  is the initial value, i.e., the value when time,  $t$ , is zero.

### 3.4.6 Error Propagation

The measurement uncertainties were found to propagate to the processed analysis results in three stages (Figure 3.4).

The first stage of error propagation was from the measurement uncertainties to the analysis results prior to processing. Since at this stage, the analysis results are in their unprocessed form, their uncertainties are referred to as raw uncertainties. These uncertainties were calculated through a sensitivity analysis, the method of which is described in Appendix C.

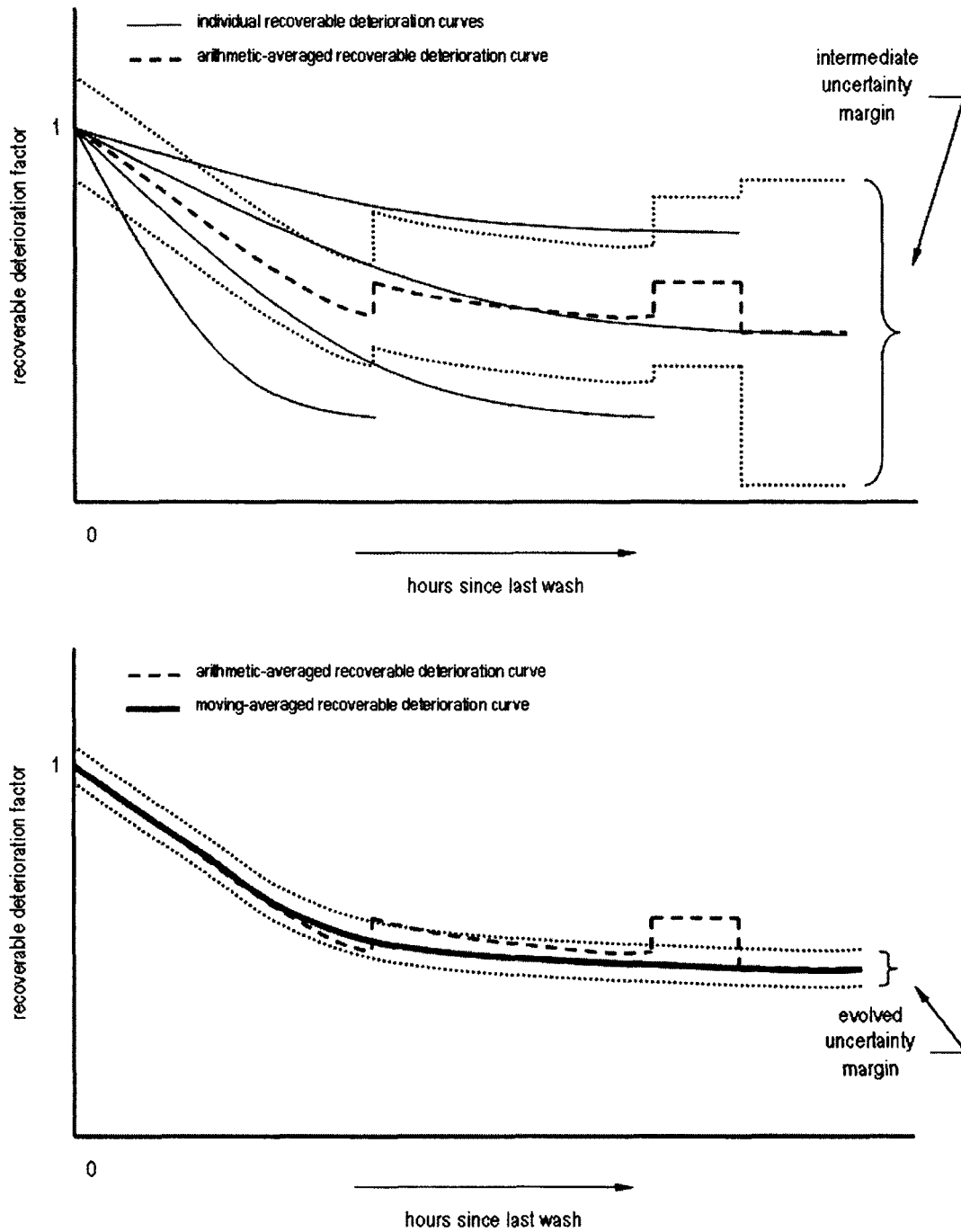


**Figure 3.4** Illustration of the error propagation process

The raw uncertainties were then propagated into the semi-processed analysis results which are the arithmetic average of the recoverable deterioration profiles (Appendix B). These uncertainties are referred to as intermediate uncertainties.

Finally, moving averages were taken of the arithmetic-averaged deterioration profiles. Here, the intermediate uncertainties were first weighted-averaged, and were then applied the central limits theorem (Appendix B). These final uncertainties are referred to as evolved uncertainties.

Appendix C.13 contains the processed recoverable deterioration profiles of the analysis results, as well as the raw and evolved uncertainties.

## **4 GAS TURBINE OFF-DESIGN PERFORMANCE PREDICTION USING GASDYNAMICS RELATIONSHIPS**

### **4.1 Introduction**

**A**S can be recalled from the literature review in Chapter 2, exotic methods such as artificial neural networks and fuzzy logic systems can be used to predict gas turbine off-design performance. However, if one were to step back from these relatively complex approaches, it can be seen without difficulty that fundamental laws of physics that govern everyday life can be manipulated to provide the most simple, yet elegant, solutions to problems that otherwise may seem unconquerable.

In this chapter, such a method for predicting gas turbine off-design performance is presented. An introduction to this method, hereinafter referred to as the *core control method*, is first presented. Then, the application of the core control method for a single-spool turbojet, and a multi-spool gas turbine is discussed. Simulation of bleed flows, independent spool coupling, and gas turbine performance deterioration is also discussed.

## 4.2 An Introduction to the Core Control Method

Wittenberg (1976a) first showed that to predict the off-design performance of a gas turbine, one requires neither compressor nor turbine characteristics, but only the engine design-point performance and a few well-placed assumptions. Based on his research (Section 2.2.8), Wittenberg showed that the polytropic efficiencies of typical gas turbine compressors remain fairly constant over a large operating range. Saravanamuttoo (1968) has shown earlier that with a small error, the polytropic efficiency of a turbine can also be assumed to be constant.

Wittenberg applied his method to a Rolls-Royce Viper Mark 521, which is a single-spool turbojet, where he assumed that the turbine remained choked throughout the turbojet's operating range. In reality, the turbine of the Viper becomes unchoked at low power settings. This produced a noticeable error between the actual and predicted off-design performance at low power levels. Additionally, a handling bleed flow was activated on the Viper at low power settings, which was unaccounted for by Wittenberg. This further contributed to the prediction error.

Wittenberg also simulated the off-design performance of a Rolls-Royce RB211-22 – a three-spool turbofan where he combined the HP and IP (intermediate-pressure) spools to obtain an imaginary HP-IP-equivalent spool. Then, the HP-IP-equivalent turbine was assumed to remain choked throughout the turbofan's operating range.

The RB211-22, however, has an unchoked hot exhaust nozzle at design-point operation, which increased the likelihood of the LP and the IP turbines becoming unchoked at mid-level power settings, during which Wittenberg's HP-IP-equivalent spool assumption would be invalid.

This was proven when the predicted and actual RB211-22 performance deviated for mid- to low-power levels. Therefore, it was decided that Wittenberg's method lacks the resolution to capture detailed gas turbine performance phenomena. This led to the development of the core control method.

When *visualizing* the behaviour of a gas turbine, it was apparent that its performance depends solely on a single independent parameter which has the *power* to control the operating point of every compressor and turbine within the engine. In other words, this parameter was found to be in control of the energy input to the gas turbine.

This input energy was then observed to be absorbed by each spool in succession, starting with the innermost spool, thereby setting an equilibrium operating point for each spool. As a result, a unique equilibrium operating point for the entire gas turbine was found to be present for a given amount of energy input. Since the source of this energy must originate within the core of the engine, this method was thus referred to as the *core control method*.

The core control method operates on similar principles as Wittenberg's method. However, it regards each spool in a multi-spool gas turbine as a separate entity, thus encouraging behaviour similar to that observed in a real gas turbine.

In the proceeding discussions, the core control method, in its simplest form, is first applied to a single-spool turbojet. The discussion then progresses to simulating advanced gas turbine flow phenomena such as bleed flows. Subsequently, off-design performance prediction for a multi-spool gas turbine is discussed, followed by the presentation of an approach which allows deteriorated off-design performance to be predicted.

### 4.3 Single-Spool Turbojet

Figure 4.1 illustrates a schematic of a single-spool turbojet. Performing a work balance between the compressor and the turbine, it can be shown that,

$$\dot{m}_a c_{pa} (T_{o3} - T_{o2}) = \eta_m \dot{m}_g c_{pg} (T_{o4} - T_{o5}) \quad 4.3.1$$

where  $\dot{m}_a$  is the engine inlet air mass flow rate,  $\eta_m$  is the spool mechanical efficiency,  $c_{pa}$  and  $c_{pg}$  are the specific heats for air and exhaust gas, respectively, and  $\dot{m}_g$  is the exhaust gas mass flow rate, where,

$$\dot{m}_g = \dot{m}_a + \dot{m}_f \quad 4.3.2$$

with  $\dot{m}_f$  being the fuel mass flow rate.

Since the typical fuel flow rate,  $\dot{m}_f$ , is approximately two orders of magnitude less than that of the inlet air flow rate,  $\dot{m}_a$ ,  $\dot{m}_g$  can therefore be approximated by  $\dot{m}_a$  (Wittenberg [1976a], Saravanamuttoo et al. [2001], and Walsh and Fletcher [2001]). This allows Equation 4.3.1 to be rearranged as,

$$\frac{T_{o3}}{T_{o2}} - 1 = \frac{\eta_m c_{pg}}{c_{pa}} \frac{T_{o4}}{T_{o2}} \left[ 1 - \frac{T_{o5}}{T_{o4}} \right] \quad 4.3.3$$

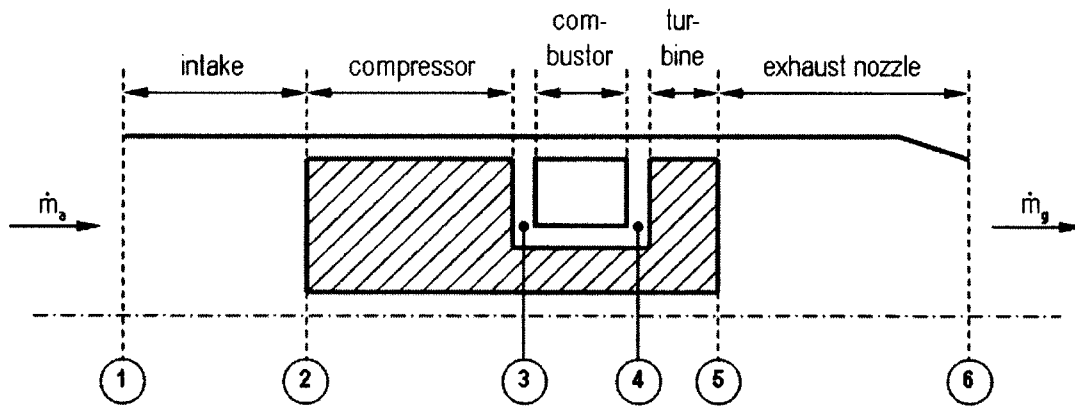


**Figure 4.1** Single-spool turbojet [modified from Wittenberg, 1976a]

If the ratio,  $\frac{\eta_m c_{pg}}{c_{pa}}$ , is assumed to be constant for all on- and off-design operating points, Equation 4.3.3 can be expressed with respect to the design-point values as,

$$\frac{T_{o3}}{T_{o2}} = 1 + \phi \left[ \left( \frac{T_{o3}}{T_{o2}} \right)_{des} - 1 \right] \frac{1 - \frac{T_{o5}}{T_{o4}}}{1 - \left( \frac{T_{o5}}{T_{o4}} \right)_{des}} \quad 4.3.4$$

where  $\phi$  is the spool temperature ratio, i.e., the core control parameter, and,

$$\phi = \frac{\frac{T_{o4}}{T_{o2}}}{\left( \frac{T_{o4}}{T_{o2}} \right)_{des}} \quad 4.3.5$$

where,  $\phi$  represents the temperature rise through the spool, which is a representation of the energy input to the turbojet.

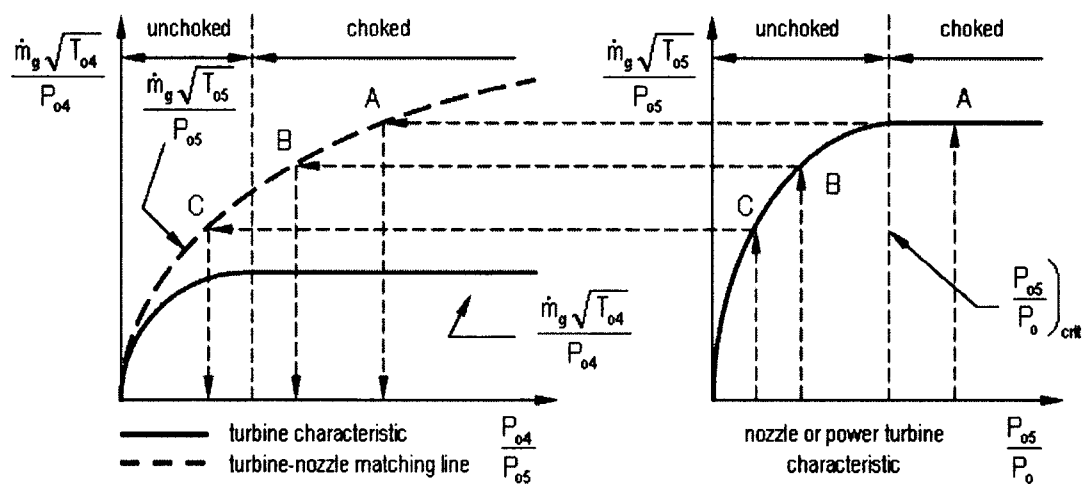


**Figure 4.2** Matching of the turbine and the exhaust nozzle for a single-spool turbojet

[modified from Saravanamuttoo et al., 20010]

Then, to predict the off-design performance of the turbojet, only the correct turbine temperature ratio,  $\frac{T_{05}}{T_{04}}$  for a given  $\phi$  needs to be known. This  $\frac{T_{05}}{T_{04}}$  can be found by determining the operating points of the turbine and the exhaust nozzle using gasdynamics relationships, i.e., component-matching of the turbine and the exhaust nozzle.

#### 4.3.1 Matching of the Turbine and the Exhaust Nozzle

The matching of the turbine and the exhaust nozzle is illustrated in Figure 4.2. This shows three possible operating conditions for the turbine and the nozzle, namely, choked turbine-choked propelling nozzle, choked turbine-unchoked propelling nozzle, and unchoked turbine-unchoked propelling nozzle. Here, choking refers to a sonic throat (Saravanamuttoo et al. [2001], and White [2003]).

When the propelling nozzle is choked (A), a unique condition exists since the turbine pressure ratio,  $\frac{P_{o4}}{P_{o5}}$ , thus the turbine temperature ratio,  $\frac{T_{o4}}{T_{o5}}$ , are fixed at their respective design-point values along with the turbine corrected mass flow rate,  $\frac{\dot{m}_g \sqrt{T_{o4}}}{P_{o4}}$ . Here,

$$\frac{P_{o4}}{P_{o5}} = \left( \frac{T_{o4}}{T_{o5}} \right)^{\frac{\gamma}{\eta_{\text{turb}}(\gamma-1)}} \quad 4.3.6$$

For the choked turbine-unchoked propelling nozzle condition (B), only  $\frac{\dot{m}_g \sqrt{T_{o4}}}{P_{o4}}$  remains at its design-point value. Although the turbine is still choked, due to the unchoked propelling nozzle, its operating point is no longer fixed. Hence,  $\frac{P_{o4}}{P_{o5}}$  exists within the region bounded by the critical pressure ratio,  $\left. \frac{P_{o4}}{P_{o5}} \right)_{\text{crit}}$ , and the design pressure ratio,  $\left. \frac{P_{o4}}{P_{o5}} \right)_{\text{des}}$ . The operating point of the propelling nozzle is dependent on  $\frac{P_{o4}}{P_{o5}}$ , and its corrected mass flow rate,  $\frac{\dot{m}_g \sqrt{T_{o5}}}{P_{o5}}$  is governed by the converging nozzle equation.

Lastly, when the turbine is unchoked (C),  $\frac{\dot{m}_g \sqrt{T_{o4}}}{P_{o4}}$  is determined by the converging nozzle equation, which depends on  $\frac{P_{o4}}{P_{o5}}$ . Once the operating point of the

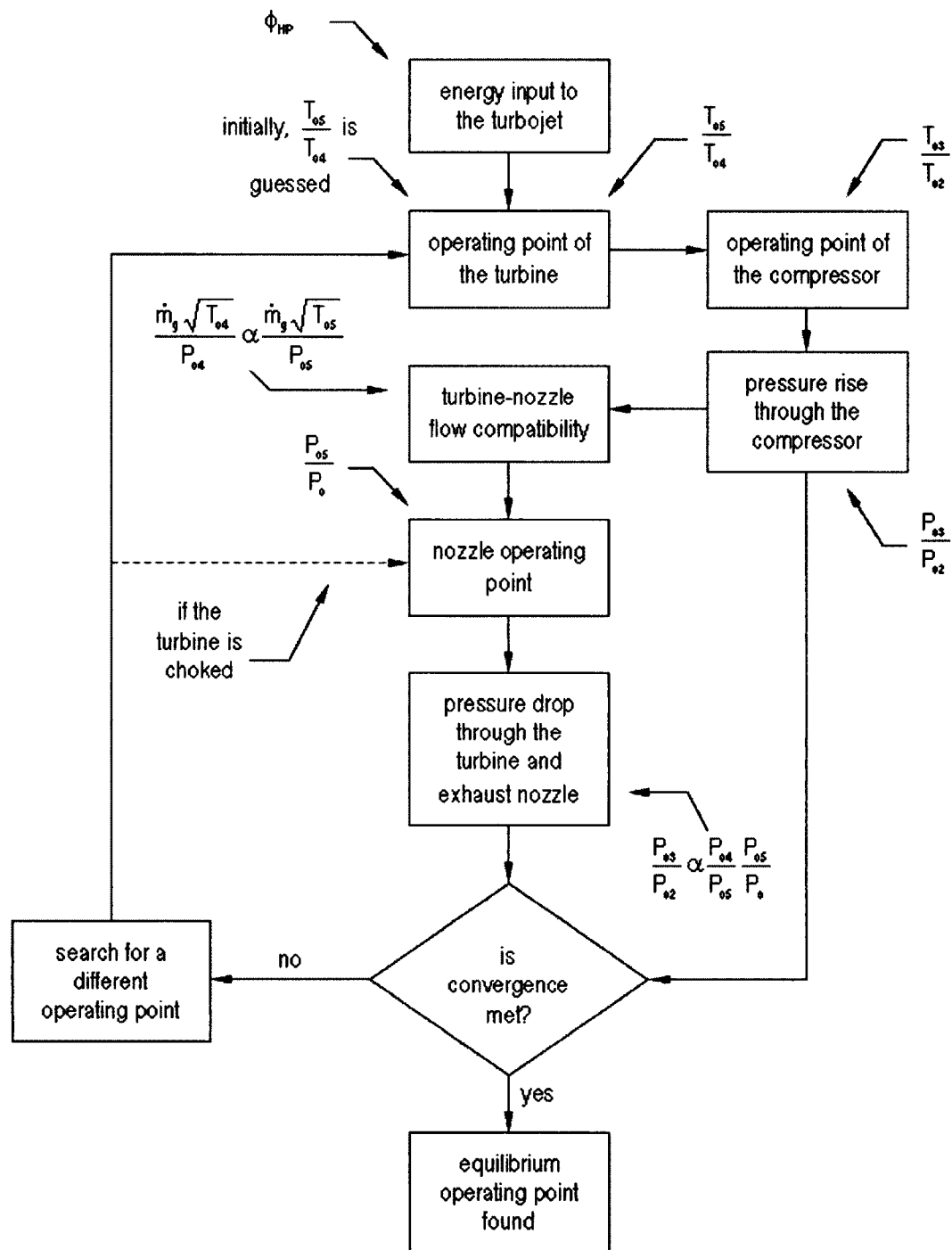


**Figure 4.3** Solution process used by the core control method for a single-spool turbojet

turbine is determined, the operating point of the propelling nozzle can be found through turbine-nozzle flow compatibility.

Based on this turbine-nozzle matching behaviour, a solution process to determine the equilibrium operating point of the turbojet for a given  $\phi$  was developed (Figure 4.3).

Here, for a given core control parameter, an operating point of the turbine is initially assumed, using which the operating point of the propelling nozzle can be found through flow compatibility and the compressor operating point through Equation 4.3.4.

With the operating points of the turbine and the propelling nozzle known, the pressure drop through these components can also be found, which must be the same as the pressure rise through the compressor. Else, the operating point of the turbine is iteratively found until the said pressure drop and pressure rise converge.

Upon convergence, the available information can be used to determine the compressor corrected mass flow rate using,

$$\left. \frac{\dot{m}_a \sqrt{T_{o2}}}{P_{o2}} = \frac{\dot{m}_a \sqrt{T_{o2}}}{P_{o2}} \right)_{des} \left. \frac{\frac{\dot{m}_g \sqrt{T_{o4}}}{P_{o4}} \frac{P_{o3}}{P_{o2}}}{\frac{\dot{m}_g \sqrt{T_{o4}}}{P_{o4}} \left. \frac{P_{o3}}{P_{o2}} \right)_{des}} \right)_{des} \sqrt{\frac{1}{\phi}} \quad 4.3.7$$

Here, the combustor pressure ratio,  $\frac{P_{o4}}{P_{o5}}$ , can be assumed to be constant as per

Saravanamuttoo et al. (2001), and Walsh and Fletcher (2001).

With the compressor pressure ratio and its corresponding compressor corrected mass flow rate found, the compressor operating line can be obtained.

### **4.3.2 Off-Design Performance Prediction**

To predict the off-design performance of a single-spool turbojet, the procedure highlighted in Figure 4.3 can be repeated for different values of the core control parameter. Appendix D.1 contains a more detailed discussion on the solution process. This, in essence, is the core control method.

Although the solution process highlighted by Figure 4.3 can adequately predict the off-design performance of a single-spool turbojet, it still requires further modifications to simulate the effects of bleed flows on overall engine performance.

## 4.4 Simulating the Effect of Bleed Flows

### 4.4.1 Handling Bleeds vs. Cooling Bleeds

There are two types of bleed flows in a gas turbine, namely, handling bleeds and cooling bleeds (Saravanamuttoo et al. [2001], Walsh and Fletcher [2001]).

The purpose of a handling bleed is to prevent a compressor from surging either at low power settings and/or during a transient maneuver. In such scenarios, a compressor's operating point moves towards the surge line (Figure 4.4). If countermeasures are not taken, the compressor may surge, potentially severely damaging an engine (Saravanamuttoo et al., 2001)

There are two types of handling bleeds. One involves bleed extraction within compressor stages, and the other involves bleed extraction from the compressor outlet. The former moves the surge line away from the compressor operating point, thus alters the compressor characteristics. The latter moves the compressor operating point away from the surge line. Both types of handling bleeds increase the surge margin (i.e., the separation between the surge line and the compressor running line), thus prevent surging. The selection of one type of handling bleed over another requires detailed feasibility analysis (Walsh and Fletcher, 2001).

A typical handling bleed valve begins to open at a given compressor corrected speed and linearly increases the bleed flow rate to a maximum at a lower corrected compressor speed (Figure 4.5). In this study, only linear handling bleed extraction from the compressor outlet is considered.

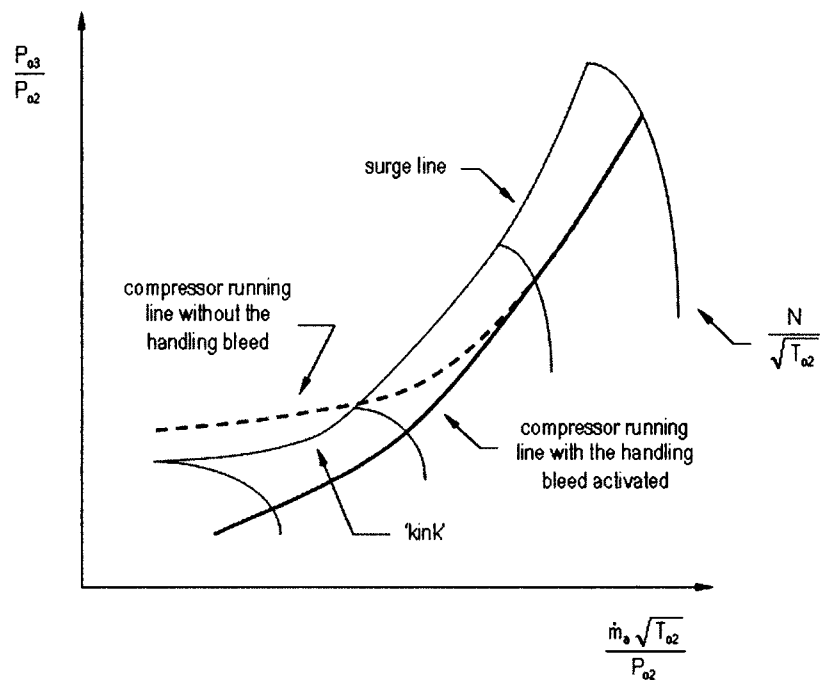


**Figure 4.4** Effect of handling bleed on the compressor of a single-spool turbojet

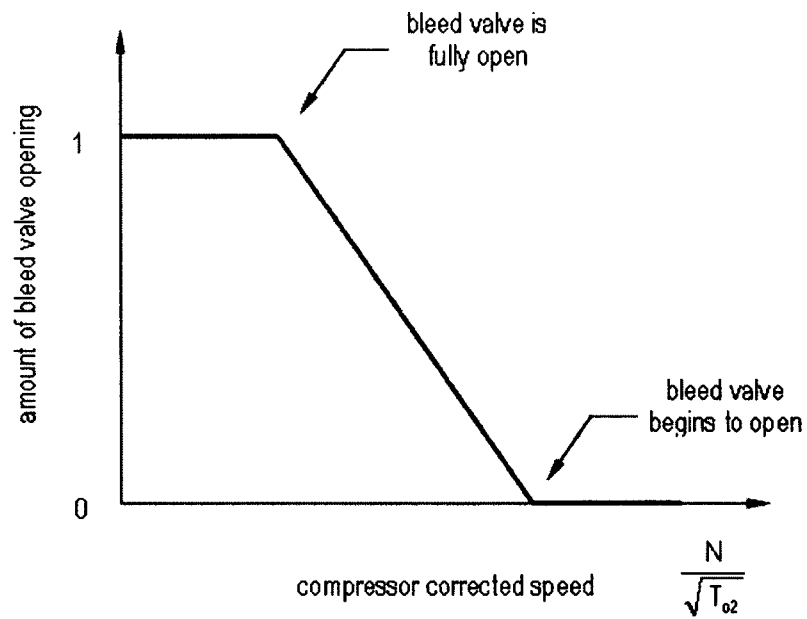


**Figure 4.5** Typical handling bleed schedule

Thermodynamically, cooling bleeds and handling bleeds are indistinguishable. However, unlike handling bleeds, cooling bleed passages are fully open throughout all compressor corrected speeds. Cooling bleeds are used for protecting turbine blades from hot combustor exhaust gases.

In some advanced engines, bleeds are extracted within, or at the outlet of, compressors, where the extracted flow is rerouted to the engine inlet as a technique of inlet flow control. Such bleed flows are not considered in this study.

This leads to the discussion on the thermodynamical aspect of bleed extraction.

#### 4.4.2 Effect of Bleed Extraction on Engine Performance

When bleed is extracted from the compressor-delivered flow, the flow slightly expands thus reducing the compressor outlet pressure,  $P_{o3}$ . This results in a reduction in

the compressor pressure ratio,  $\frac{P_{o3}}{P_{o2}}$ . Since the compressor corrected mass flow rate,

$\frac{\dot{m}_a \sqrt{T_{o2}}}{P_{o2}}$ , is expressed with respect to the compressor inlet conditions, this parameter is

unaffected by bleed extraction.

Apart from the decrease in the compressor pressure rise, the most noticeable effect of bleed extraction is the increase in the engine fuel-to-air ratio,  $f$ , when the fuel flow rate,  $\dot{m}_f$ , is held constant. This happens since,

$$f = \frac{\dot{m}_f}{(1-\beta) \dot{m}_a} \quad 4.4.1$$

where  $\beta$  is the bleed flow coefficient, and,

$$\beta = \frac{\dot{m}_\beta}{\dot{m}_a} \quad 4.4.2$$

where  $\dot{m}_\beta$  is the bleed mass flow rate.

Disregarding this fuel-to-air ratio increase causes a noticeable discrepancy between the actual and predicted turbine inlet temperature values at low power levels, which may result in an erroneous estimation of the fuel consumption.

Although this may not be of much interest to land-based engine simulation, it may be of great interest to aero- engine simulation since such an engine may, at times, spend many hours either idling (while taxiing and delays) and at very low power settings (while on descent).

Figure 4.6 shows a detailed drawing of the bleed extraction system for a single-pool turbojet. As a result of bleed extraction,  $\dot{m}_\beta$ , the compressor delivery mass flow rate,  $\dot{m}'_3$ , compressor outlet pressure,  $P'_{o3}$ , and the compressor exit temperature,  $T'_{o3}$ , change to  $\dot{m}_3$ ,  $P_{o3}$ , and  $T_{o3}$ , respectively, downstream of the bleed valve.

Without bleed extraction, the compressor outlet pressure and temperature ( $P'_{o3}$  and  $T'_{o3}$ ), and the pressure and temperature downstream of the bleed valve are the same. With bleed extraction, the compressor outlet pressure and temperature remains unchanged, although the pressure and temperature downstream of the bleed valve may vary.

Habitually, it is the pressure downstream of the bleed valve that is used to express the compressor pressure ratio (Figure 4.6). This is the reason behind the visible difference between the compressor running lines once a handling bleed valve is activated (Figure 4.4).

Owing to the diffusion caused by bleed extraction, the compressor delivery flow speed decreases, thereby increasing the static temperature. Therefore, the flow Mach number downstream of the handling bleed valve,  $M_3$ , will be less than that of the upstream Mach number,  $M'_3$ . Therefore, one can not assume constant flow conditions before and after the bleed valve, but requires solving for the relevant variables iteratively, the procedure for which is discussed in Appendix D.4.

With the theory of the core control method thus discussed, it is next applied to a multi-spool gas turbine.

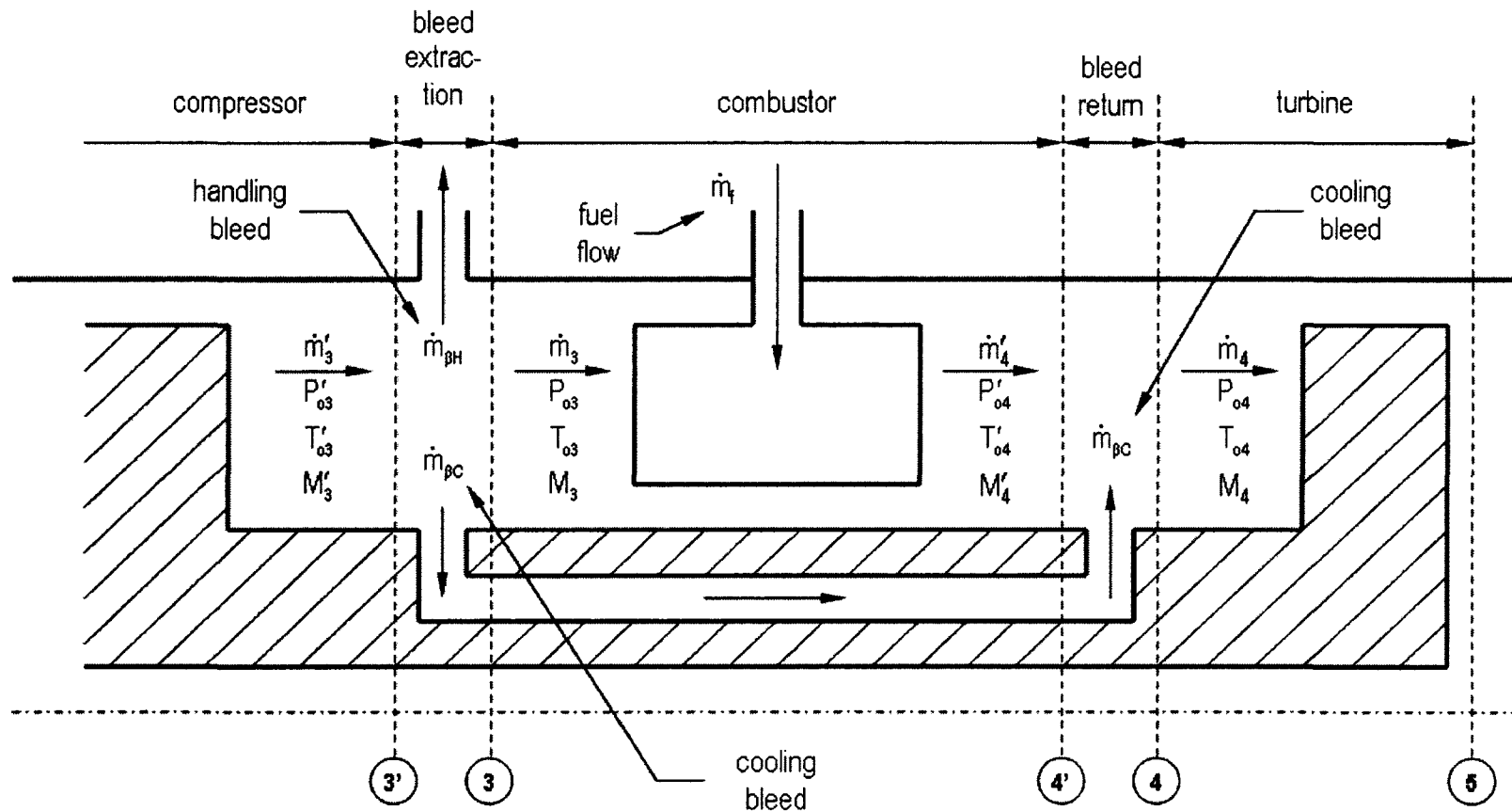


**Figure 4.6** Bleed flows of a single-spool turbojet

## 4.5 Two-Spool Gas Generator with a Free Power Turbine

Here, the core control method is applied to a two-spool gas generator with a free power turbine. This multi-spool gas turbine is of the same configuration as the industrial RB211.

Since the power turbine is a *free* power turbine, i.e., it is not mechanically linked to the gas generator, the power turbine can be replaced by a power-turbine-equivalent converging nozzle. This effectively converts this gas turbine into a two-spool turbojet.

In other words, the exact gasdynamics principles that are applicable to a two-spool gas generator with a free power turbine are applicable to a two-spool turbojet as well (Figure 4.7).

Here, two work balance equations must be used since two spools are present. Based on the principles of the core control method, derivations from these two equations must depend on a single parameter, i.e., the core control parameter.

For the HP spool, the work balance equation gives,

$$\dot{m}_3 c_{pa} (T_{o4} - T_{o3}) = \eta_m \dot{m}_5 c_{pg} (T_{o5} - T_{o6}) \quad 4.5.1$$

where  $\dot{m}_3$  is the HP compressor inlet mass flow rate and  $\dot{m}_5$  is the HP turbine inlet mass flow rate.

Applying the same procedure as for the single-spool turbojet, the ratio  $\frac{\eta_m c_{pg}}{c_{pa}} \frac{\dot{m}_5}{\dot{m}_3}$

is assumed to remain approximately constant for all operating conditions.

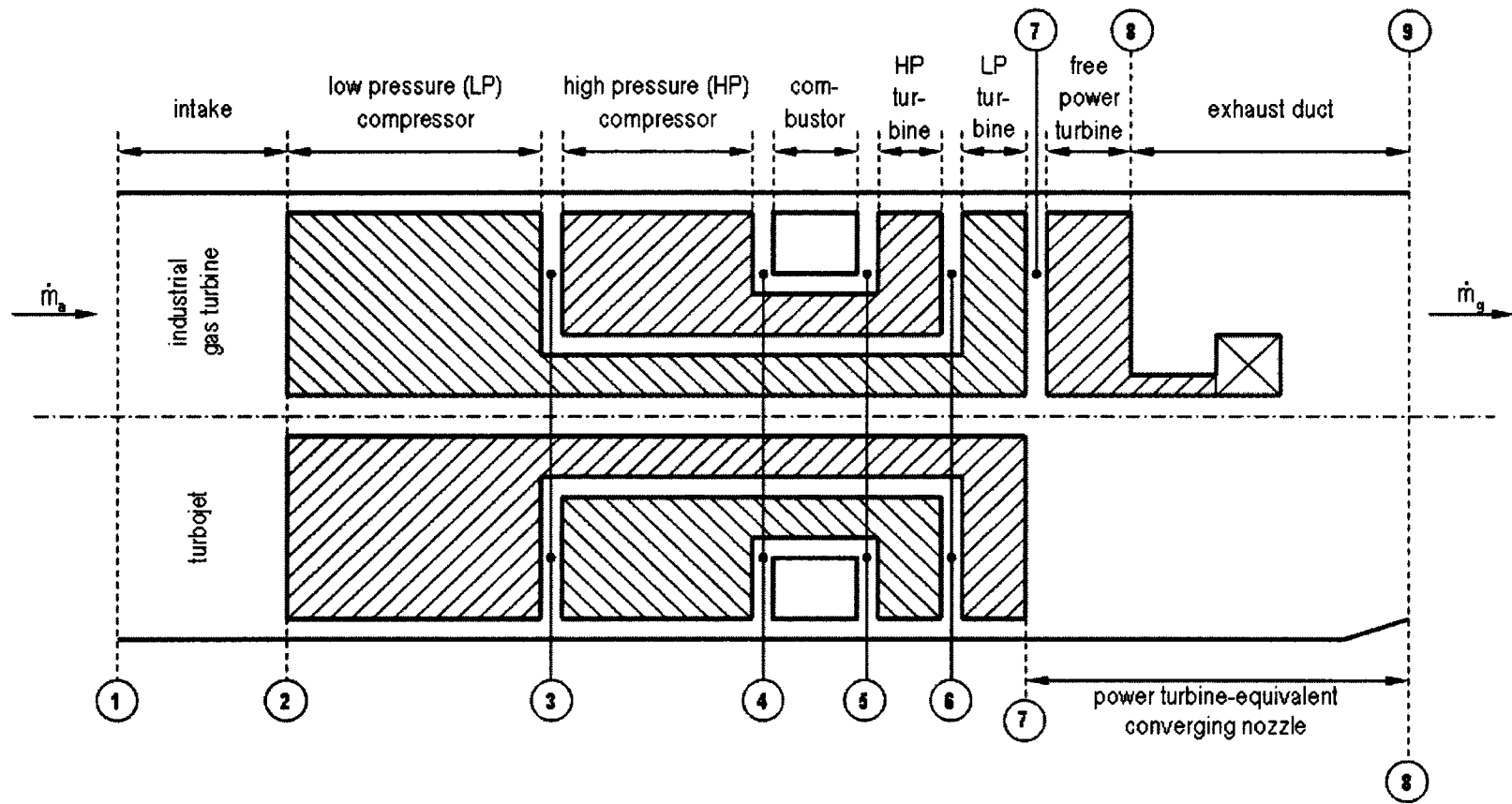


**Figure 4.7** Two-spool gas generator with a free power turbine and its equivalent two-spool turbojet

Then, Equation 4.5.1 can be rewritten as,

$$\frac{T_{o4}}{T_{o3}} = 1 + \phi_{HP} \left[ \left( \frac{T_{o4}}{T_{o3}} \right)_{des} - 1 \right] \frac{1 - \frac{T_{o6}}{T_{o5}}}{1 - \left( \frac{T_{o6}}{T_{o5}} \right)_{des}} \quad 4.5.2$$

where  $\phi_{HP}$  is the core control parameter (also the HP spool temperature ratio) defined as,

$$\phi_{HP} = \frac{\frac{T_{o5}}{T_{o3}}}{\left( \frac{T_{o5}}{T_{o3}} \right)_{des}} \quad 4.5.3$$

Similarly, the work balance of the LP spool,

$$\dot{m}_2 c_{pa} (T_{o3} - T_{o2}) = \eta_m \dot{m}_6 c_{pg} (T_{o6} - T_{o7}) \quad 4.5.4$$

where  $\dot{m}_2$  is the LP compressor inlet mass flow rate and  $\dot{m}_6$  is the LP turbine inlet mass flow rate, which can then be rewritten with respect to  $\phi_{HP}$  as,

$$\frac{T_{o3}}{T_{o2}} = \left[ 1 - \phi_{HP} \left[ \left( 1 - \frac{T_{o2}}{T_{o3}} \right)_{des} \right] \frac{\frac{T_{o6}}{T_{o5}}}{\left( \frac{T_{o6}}{T_{o5}} \right)_{des}} \frac{1 - \frac{T_{o7}}{T_{o6}}}{1 - \left( \frac{T_{o7}}{T_{o6}} \right)_{des}} \right]^{-1} \quad 4.5.5$$

Therefore, Equation 4.5.2 and Equation 4.5.5 can be used to predict the off-design performance of the gas turbine of interest, where only the HP turbine temperature ratio,  $\frac{T_{o6}}{T_{o5}}$ , and the LP turbine temperature ratio,  $\frac{T_{o7}}{T_{o6}}$ , are needed for a given  $\phi_{HP}$ . These two unknowns can be found through flow compatibility between the HP, LP and free power turbines (or the power-turbine-equivalent converging nozzle).

#### 4.5.1 Matching of the HP, LP and Free Power Turbines

For a two-spool gas generator with a free power turbine, there are four possible conditions in which the turbines may operate. Shown in Figure 4.8, these operating conditions are as follows: choked free power turbine; choked HP and LP turbine with unchoked free power turbine; choked HP turbine with unchoked LP and free power turbines; and unchoked HP, LP and free power turbines.

When the free power turbine is choked (A), both HP and LP turbines are choked by default. Since the sonic throat of the free power turbine insulates the HP and LP turbines from external disturbances, the HP and LP turbines operate at a fixed condition (i.e., their respective design-point conditions). Therefore, the pressure and temperature ratios and the corrected mass flow rates of the HP and LP turbine will remain fixed at their design-point values.

At a lower power level, the free power turbine will become unchoked while the HP and LP turbines still remain choked (B). Here, the operating point of the LP turbine is lower than the design-point, yet is greater than or equal to its critical operating point, which is the condition when the LP turbine becomes choked. Shielded by the LP turbine's sonic throat, the HP turbine continues to operate at its (choked) design-point.

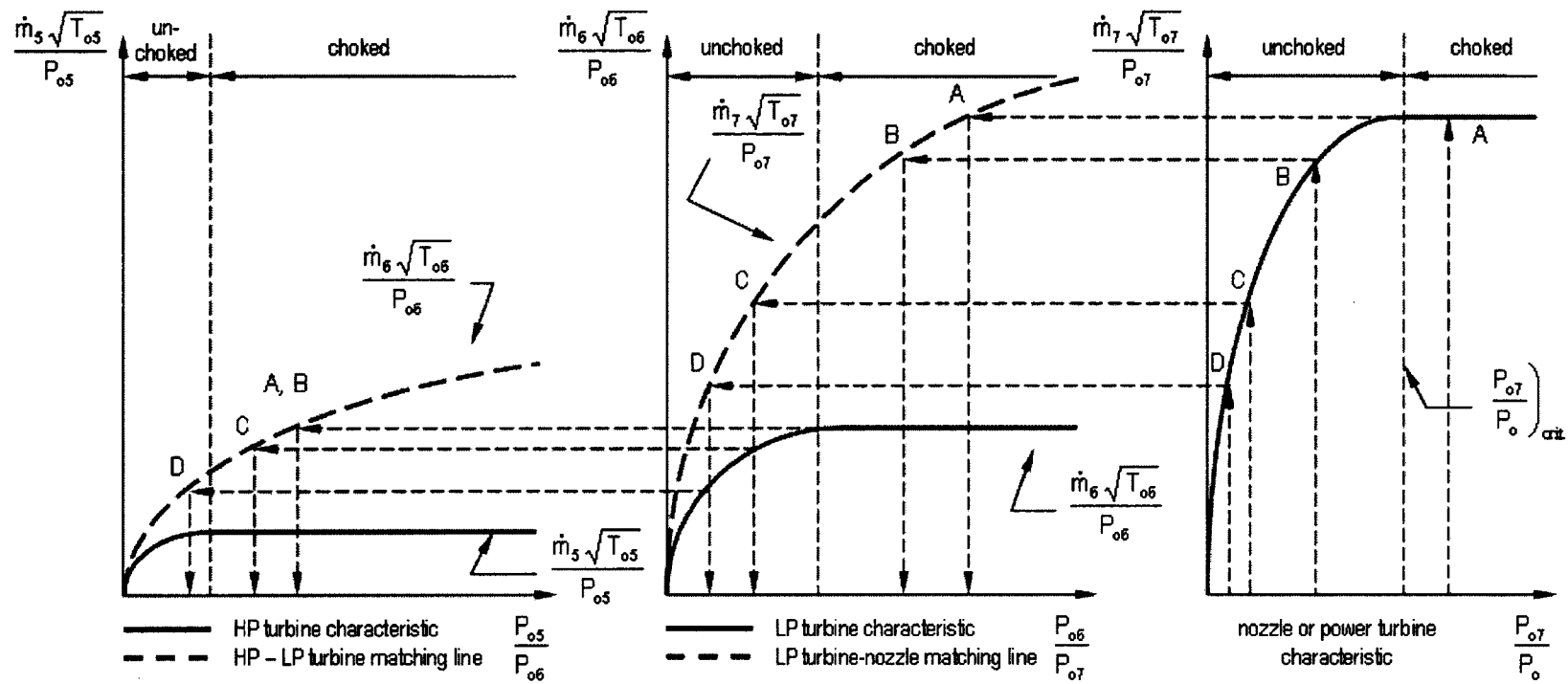


**Figure 4.8** Matching of the HP, LP and free power turbines for a two-spool gas generator with a free power turbine [modified from Saravanamuttoo et al., 2001]

Further lowering the power level shall see the LP turbine becoming unchoked while the HP turbine still remains choked between the design and critical operating points (C). At the lowest power settings, the HP turbine will become unchoked (D).

#### 4.5.2 Off-Design Performance Prediction

Here, the objective is to find the HP and LP turbine temperature ratios that corresponds to a given  $\phi_{HP}$ . A flowchart for this solution process is presented in Figure 4.9.

Here, for a given core control parameter, the operating point of the HP turbine is initially assumed, using which the operating point of the LP turbine and the power turbine (or the power turbine-equivalent converging nozzle) can be calculated through flow compatibility, the HP compressor operating point through Equation 4.5.2, and the LP compressor operating point through Equation 4.5.5.

With the operating points of the turbines (or turbines and converging nozzle) now known, their total pressure drop can be then calculated, which must correspond to the pressure rise through the LP and HP compressors. Else, the operating point of the HP turbine is iteratively found until convergence is met. Appendix D.2 includes further discussion on the solution process.

Upon convergence, the HP compressor corrected mass flow rate can be found by,

$$\frac{\dot{m}_3 \sqrt{T_{o3}}}{P_{o3}} = \frac{\dot{m}_3 \sqrt{T_{o3}}}{P_{o3}} \bigg)_{des} \frac{\frac{\dot{m}_5 \sqrt{T_{o5}}}{P_{o5}} \frac{P_{o4}}{P_{o3}}}{\frac{\dot{m}_5 \sqrt{T_{o5}}}{P_{o5}} \bigg)_{des} \frac{P_{o4}}{P_{o3}} \bigg)_{des}} \sqrt{\frac{1}{\phi_{HP}}} \quad 4.5.6$$

and the LP compressor corrected mass flow rate by,

$$\frac{\dot{m}_2 \sqrt{T_{o2}}}{P_{o2}} = \frac{\dot{m}_2 \sqrt{T_{o2}}}{P_{o2}} \left)_{des} \frac{\frac{\dot{m}_3 \sqrt{T_{o3}}}{P_{o3}} \frac{P_{o3}}{P_{o2}}}{\left)_{des} \frac{\dot{m}_3 \sqrt{T_{o3}}}{P_{o3}} \left)_{des} \frac{P_{o3}}{P_{o2}} \left)_{des} \sqrt{\frac{T_{o3}}{T_{o2}} \left)_{des} \frac{T_{o3}}{T_{o2}}} \quad 4.5.7$$

With the LP and HP compressor pressure ratios and their corresponding corrected mass flow rates known, the compressor running lines can be thus obtained.

Additionally, aerodynamic coupling of the LP and HP spools can also be obtained using,

$$\phi_{LP} = \phi_{HP} \frac{\frac{T_{o6}}{T_{o5}} \frac{T_{o3}}{T_{o2}}}{\left)_{des} \frac{T_{o6}}{T_{o5}} \left)_{des} \frac{T_{o3}}{T_{o2}} \left)_{des}} \quad 4.5.8$$

where  $\phi_{LP}$  is the LP spool temperature ratio.

Aerodynamic coupling, in simplest terms, refers to the equilibrium operating point of the LP spool that corresponds to a given equilibrium operating point of the HP spool. In conventional off-design performance prediction methods, this would require compressor and turbine characteristics, spool moments of inertia, etc., whereas in core control method, one only requires to expand Equation 4.5.4. Further details are presented in Appendix D.3.

Next, the method by which deteriorated engine performance can be simulated is discussed.

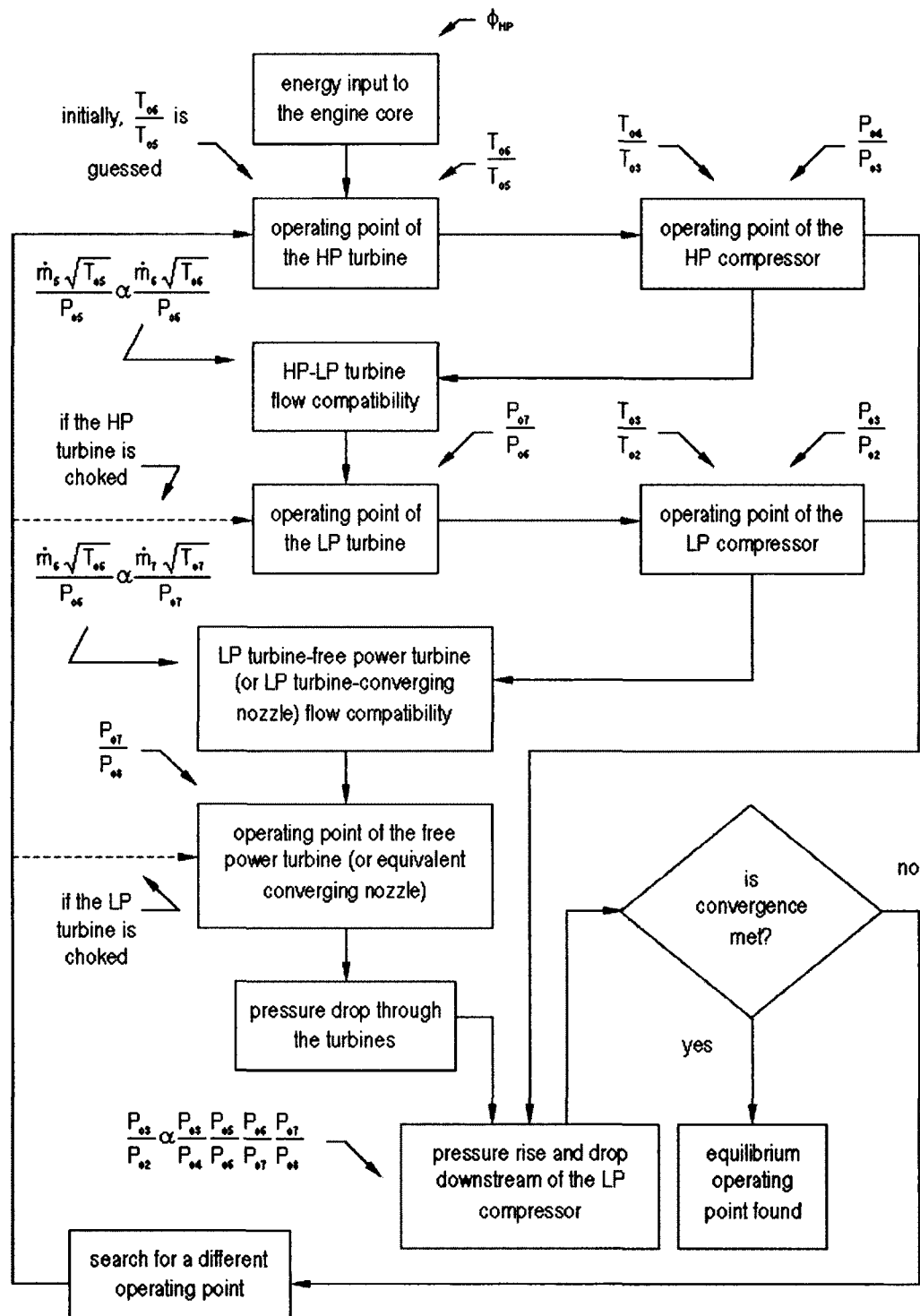


**Figure 4.9** Core control method for the off-design performance prediction of a two-spool gas generator with a free power turbine

## 4.6 Deteriorated Engine Performance Prediction

An advantage of the core control method is that it only utilizes pressure and temperature ratios, and corrected mass flow rates during the solution process. Therefore, only the efficiency drop due to deterioration needs to be implemented during the solution process, where the drop in flow capacities can be calculated *a posteriori*.

The LP compressor pressure ratio change due to recoverable deterioration can be predicted by,

$$\frac{P_{o3}}{P_{o2}} = \left( \frac{T_{o3}}{T_{o2}} \right)^{K_{rec\_ \eta_{\infty}LPC} \cdot \eta_{\infty}LPC \frac{\gamma}{\gamma-1}} \quad 4.6.1$$

where  $K_{rec\_ \eta_{\infty}LPC}$  is the LP compressor polytropic efficiency recoverable deterioration factor and  $\eta_{\infty}LPC$  is the LP compressor design-point polytropic efficiency.

Similarly, the change in HP compressor pressure ratio due to recoverable deterioration can be predicted by,

$$\frac{P_{o4}}{P_{o3}} = \left( \frac{T_{o4}}{T_{o3}} \right)^{K_{rec\_ \eta_{\infty}HPC} \cdot \eta_{\infty}HPC \frac{\gamma}{\gamma-1}} \quad 4.6.2$$

where  $K_{rec\_ \eta_{\infty}HPC}$  is the HP compressor polytropic efficiency recoverable deterioration factor and  $\eta_{\infty}HPC$  is the HP compressor design-point polytropic efficiency.

The drop in LP compressor flow capacity due to recoverable deterioration can be represented by  $\Delta\Gamma_{LPC}$ . Then, the effect of recoverable deterioration on the LP compressor

corrected mass flow rate can be predicted by,

$$\frac{\dot{m}_2 \sqrt{T_{o2}}}{P_{o2}} = (1 - \Delta\Gamma_{LPC}) \left( \frac{\dot{m}_2 \sqrt{T_{o2}}}{P_{o2}} \right)_{des} \frac{\left( \frac{\dot{m}_5 \sqrt{T_{o5}}}{P_{o5}} \right)_{des} \frac{P_{o4}}{P_{o3}} \frac{P_{o3}}{P_{o2}}}{\left( \frac{\dot{m}_5 \sqrt{T_{o5}}}{P_{o5}} \right)_{des} \frac{P_{o4}}{P_{o3}} \frac{P_{o3}}{P_{o2}} \left( \frac{P_{o3}}{P_{o2}} \right)_{des}} \sqrt{\frac{1}{\phi_{HP}}} \sqrt{\frac{T_{o3}}{T_{o2}} \left( \frac{T_{o3}}{T_{o2}} \right)_{des}}$$

4.6.3

The effect of recoverable deterioration on the HP compressor corrected mass flow rate is determined by,

$$\frac{\dot{m}_3 \sqrt{T_{o3}}}{P_{o3}} = \left( \frac{\dot{m}_3 \sqrt{T_{o3}}}{P_{o3}} \right)_{des} \frac{\left( \frac{\dot{m}_2 \sqrt{T_{o2}}}{P_{o2}} \frac{P_{o3}}{P_{o2}} \right)_{des} \sqrt{\frac{T_{o3}}{T_{o2}}}}{\left( \frac{\dot{m}_2 \sqrt{T_{o2}}}{P_{o2}} \right)_{des} \frac{P_{o3}}{P_{o2}} \sqrt{\frac{T_{o3}}{T_{o2}} \left( \frac{T_{o3}}{T_{o2}} \right)_{des}}}$$

4.6.4

In an industrial RB211, non-recoverable deterioration typically causes up to 2% drop in compressor and turbine polytropic efficiencies over 25,000 operating hours. Since the GT1, GT2 and GT3 datasets only span to approximately 7,000 operating hours since new, the drops observed in compressor and turbine efficiencies were within the measurement uncertainty margin.

## 4.7 Simulating Performance Limiters

Performance limiters are installed on gas turbines to protect against extreme aerodynamical, mechanical and thermal stresses. Handling bleeds, discussed earlier, are such a limiter. Typical engine control systems use spool speeds and compressor and/or turbine outlet temperatures as performance limiters as well. The limiters concatenate to produce the typical gas turbine operating limits as shown in Figure 4.10.

Usually, the limiting temperature is monitored at the gas generator (or gas turbine) outlet for a land-based gas turbine, and at the jet pipe outlet for an aero- gas turbine. In the core control method, these performance limiters can be implemented as follows.

### 4.7.1 Simulating the Temperature Limiter

During the solution process, each iteration produces  $\frac{T_{o3}}{T_{o2}}$ ,  $\frac{T_{o4}}{T_{o3}}$ ,  $\frac{T_{o5}}{T_{o6}}$ ,  $\frac{T_{o6}}{T_{o7}}$  and

$\frac{T_{o7}}{T_{o8}}$  for a given  $\phi_{HP}$ . With  $T_{o2}$  known, the following values can then be calculated.

$$T_{o3} = T_{o2} \frac{T_{o3}}{T_{o2}} \quad 4.7.1$$

$$T_{o5} = \left( \phi_{HP} \frac{T_{o5}}{T_{o3}} \right)_{des} T_{o3} \quad 4.7.2$$

$$T_{o6} = T_{o5} \frac{T_{o6}}{T_{o5}} \quad 4.7.3$$

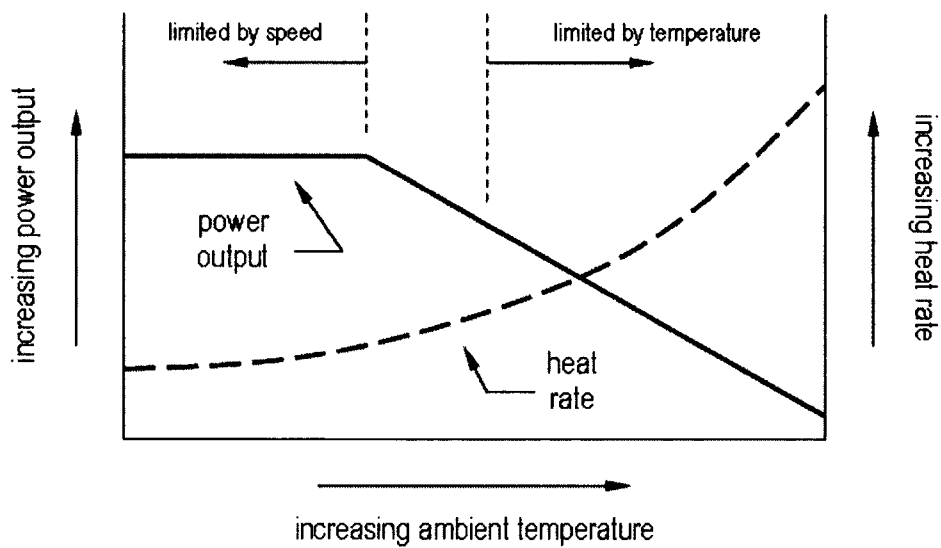


**Figure 4.10** Typical operating limits for a gas turbine

$$T_{o7} = T_{o6} \frac{T_{o7}}{T_{o6}} \quad 4.7.4$$

If  $T_{o7} > T_{o7})_{\max}$ , where  $T_{o7})_{\max}$  is the maximum allowed gas generator exhaust temperature, the effect of the temperature limiter can be propagated through the gas turbine by setting  $T_{o7} = T_{o7})_{\max}$ , and,

$$T_{o6})_{\max} = T_{o7})_{\max} \frac{T_{o6}}{T_{o7}} \quad 4.7.5$$

$$T_{o5})_{\max} = T_{o6})_{\max} \frac{T_{o5}}{T_{o6}} \quad 4.7.6$$

$$T_{o3})_{\max} = \frac{T_{o5})_{\max}}{\left( \phi_{HP} \frac{T_{o5}}{T_{o3}} \right)_{\text{des}}} \quad 4.7.7$$

$$\left. \frac{T_{o3}}{T_{o2}} \right)_{\max} = \frac{T_{o3})_{\max}}{T_{o2}} \quad 4.7.8$$

This new LP compressor temperature ratio can then be used in place of the original LP compressor temperature ratio, thereby forcing the solution process to converge to an equilibrium operating point that guarantees  $T_{o7})_{\max}$  is not exceeded.

#### 4.7.2 Simulating the Speed Limiter

Here, the spool speed cannot be used since the core control method does not use this parameter in the solution process. However, since the gas turbine power output is proportional to the spool speed, it can be used as a substitute.

Continuing from the temperature limiter calculations, the pressures across the gas turbine can be calculated from basic gas turbine performance equations such as Equation 2.2.13 and Equation 4.3.6 for each iteration (refer Appendix D.2 for further details), using which the gas turbine exhaust temperature,  $T_{o8}$ , can be found. Then, with the gas turbine inlet mass flow rate,  $\dot{m}_2$ , found by Equation 4.6.3, the gas turbine power output, PWR, can be determined by,

$$PWR \approx \dot{m}_2 c_{pg} (T_{o7} - T_{o8}) \quad 4.7.9$$

If the power output exceeds the limit,  $PWR_{\max}$ , then  $\phi_{HP}$  can be iteratively reduced until the condition  $PWR \leq PWR_{\max}$  is met.

With the theory of the core control method thus discussed, it is validated in the next chapter.

## **5 VALIDATION AND DISCUSSIONS**

### **5.1 Introduction**

**A**TTTESTATION of the core control method is the purpose of this chapter. First, as a proof of concept, the core control method's ability to predict the off-design performance of a simple single-spool turbojet is validated.

The performance of this turbojet, a Rolls-Royce Viper Mark 521, is compared with the predicted performance for both varying and constant component polytropic efficiencies.

Next, the core control method is applied to predict the off-design performance of three multi-spool gas turbines, the configuration of which is that of the industrial RB211. Here, the off-design performance of the three industrial RB211s at pass-off is first compared with the performance predicted by the core control method. Next, the core control method's ability to predict deteriorated off-design performance is validated.

## 5.2 Single-Spool Turbojet

The performance of a Viper Mark 521 manufactured by Bristol Siddeley, which was later acquired by Rolls-Royce plc., is used for validation. The Viper Mark 521 is an uprating of the Mark 520, and is designed to produce 13.9 kN of thrust at ISA sea level static conditions. With production dating back to 1951, this non-afterburning turbojet is used in light tactical aircraft such as the Hawker Siddeley HS 125 and BAC Provost, and is comparable to the General Electric J85 (Bristol Siddeley, 1964).

The following design-point performance data of this engine are obtained from Bristol Siddeley (1964).

Compressor inlet temperature, $T_{o2}$	288 K
Compressor inlet pressure, $P_{o2}$	101.325 kPa
Compressor pressure ratio, $\frac{P_{o3}}{P_{o2}}$	5.25
Compressor delivery temperature, $T_{o3}$	489.6 K
Turbine inlet temperature, $T_{o4}$	1152 K
Jet pipe temperature, $T_{o5}$	948 K
Jet pipe pressure ratio, $\frac{P_{o5}}{P_{o1}}$	2.02
Compressor polytropic efficiency, $\eta_{\infty_c}$	0.893*
Turbine polytropic efficiency, $\eta_{\infty_t}$	0.844*
Spool mechanical efficiency, $\eta_m$	0.99 <sup>†</sup>
Combustion efficiency, $\eta_B$	0.999 <sup>†</sup>
Nozzle efficiency, $\eta_n$	0.95 <sup>†</sup>

Combustion pressure loss, $\Delta P_b$ %	3.0% <sup>†</sup>
Compressor corrected mass flow rate, $\frac{\dot{m}_2 \sqrt{T_{o2}}}{P_{o2}}$	3.8958 $\frac{\text{kg} \sqrt{\text{K}}}{\text{kPa} \cdot \text{sec}}$
Referred fuel flow rate, $\frac{\dot{m}_f}{P_{o2} \sqrt{T_{o2}}}$	$2.3398 \times 10^{-4} \frac{\text{kg}}{\text{kPa} \cdot \sqrt{\text{K}} \cdot \text{sec}}$
Turbine corrected mass flow rate, $\frac{\dot{m}_4 \sqrt{T_{o4}}}{P_{o4}}$	1.5565 $\frac{\text{kg} \sqrt{\text{K}}}{\text{kPa} \cdot \text{sec}}$
Nozzle corrected mass flow rate, $\frac{\dot{m}_5 \sqrt{T_{o5}}}{P_{o5}}$	3.5597 $\frac{\text{kg} \sqrt{\text{K}}}{\text{kPa} \cdot \text{sec}}$

Assuming choked conditions at design-point,

Turbine inlet area <sup>*</sup> , $A_4$	0.039183 m <sup>2</sup>
Nozzle area, $A_6$	0.088619 m <sup>2</sup>

Note: \* refer to calculated values; † refer to assumed values.

Note: The compressor and turbine efficiencies are calculated from engine data

To improve engine handling at low speeds, an estimated 5.0% of compressor outlet flow is bled overboard for non-dimensional compressor speeds corresponding to

$\frac{N}{N_{des}} \leq 0.75$ , where  $N_{des}$  refers to the design-point compressor speed. It is assumed that

the bleed valve begins to open at  $\frac{N}{N_{des}} = 0.75$ , and linearly increases its opening until

maximum opening is reached at the idling speed of  $\frac{N}{N_{des}} = 0.4$ . The turbine of the Viper

is uncooled due to the relatively low turbine inlet temperature of 1152 K at the design-point. Appendix F.2 contains the Matlab algorithm used for this validation process.

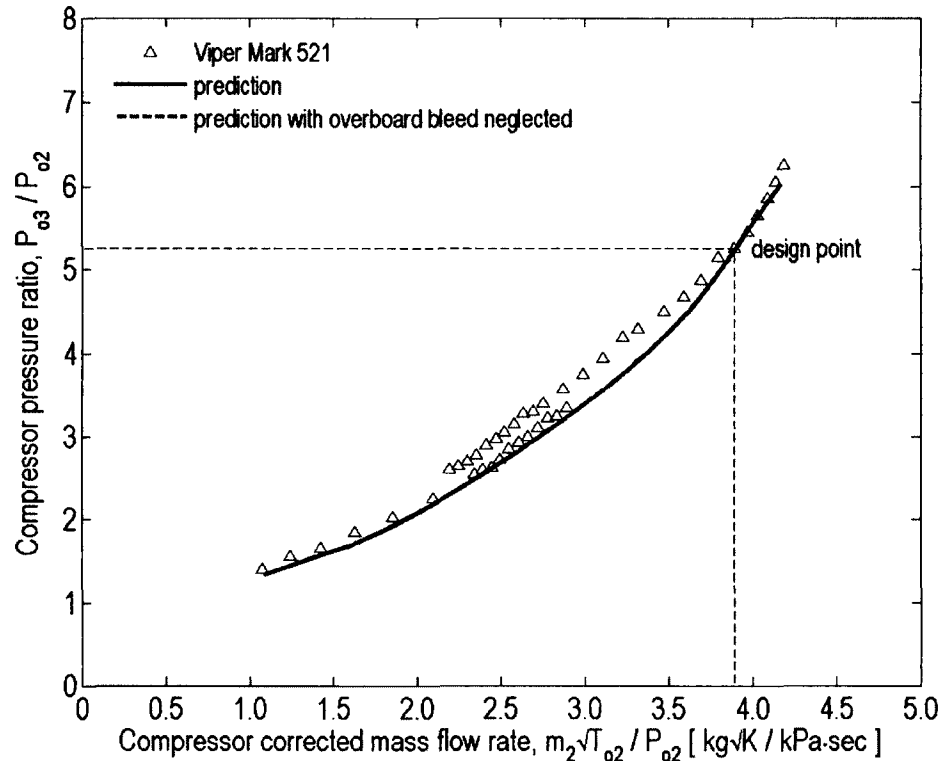


**Figure 5.1** Compressor running line of the Viper

The actual and predicted compressor running lines are presented in Figure 5.1. The discontinuation in the engine data at mid-range power levels is due to the activation of the compressor handling bleed valve. Albeit the presence of a slight deviation for the mid- to high- compressor corrected mass flow rates (hence compressor speeds), good prediction of the compressor running line is made for the remainder.

Very little difference is observed for the predicted compressor running line when the handling bleed flow is neglected. This may lead one to question the necessity of accounting for handling bleed flows in the core control method, an issue, which is addressed in the immediate discussion.

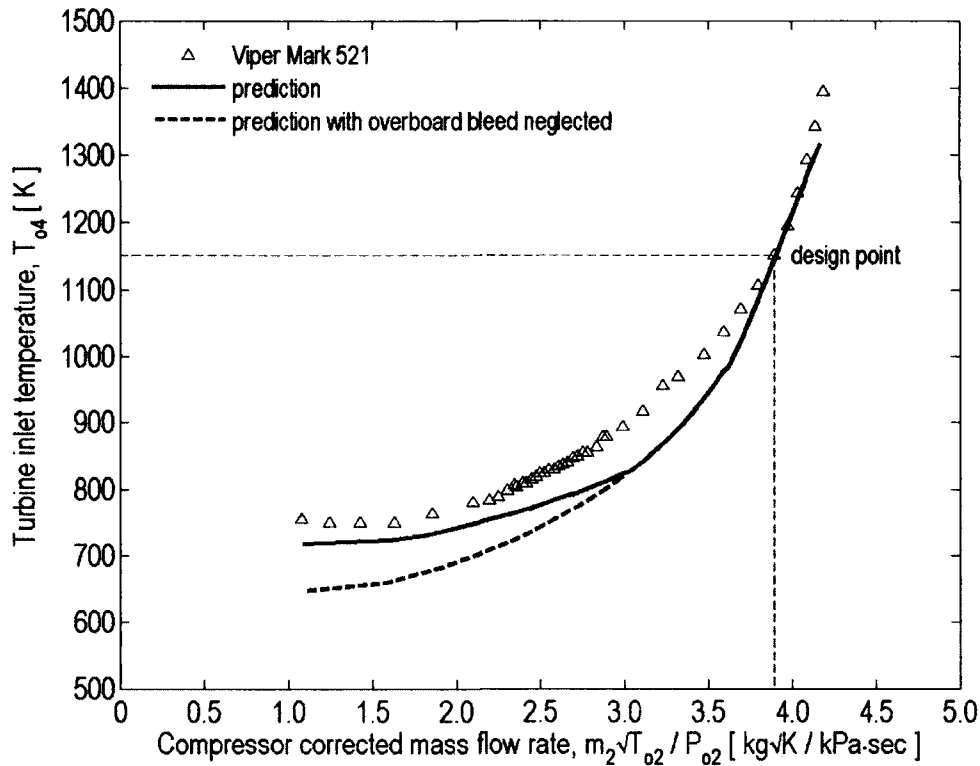


**Figure 5.2** Turbine inlet temperature of the Viper

The effect of neglecting the handling bleed flow on the core control method prediction is illustrated in Figure 5.2. Although neither predictions represent the actual turbine inlet temperature,  $T_{o4}$ , for majority of the Viper's operating range, the prediction that considers the handling bleed is observed to, at least, track the actual temperature variation.

The activation of the handling bleed valve affects both  $T_{o4}$  and the specific fuel consumption, SFC. In the Viper, there is a high likelihood that  $T_{o4}$  is calculated, as turbine inlet temperatures usually are, whereas the fuel flow rate and net thrust are measured. More confidence can be placed in the measured. Thus, the 5.0% handling

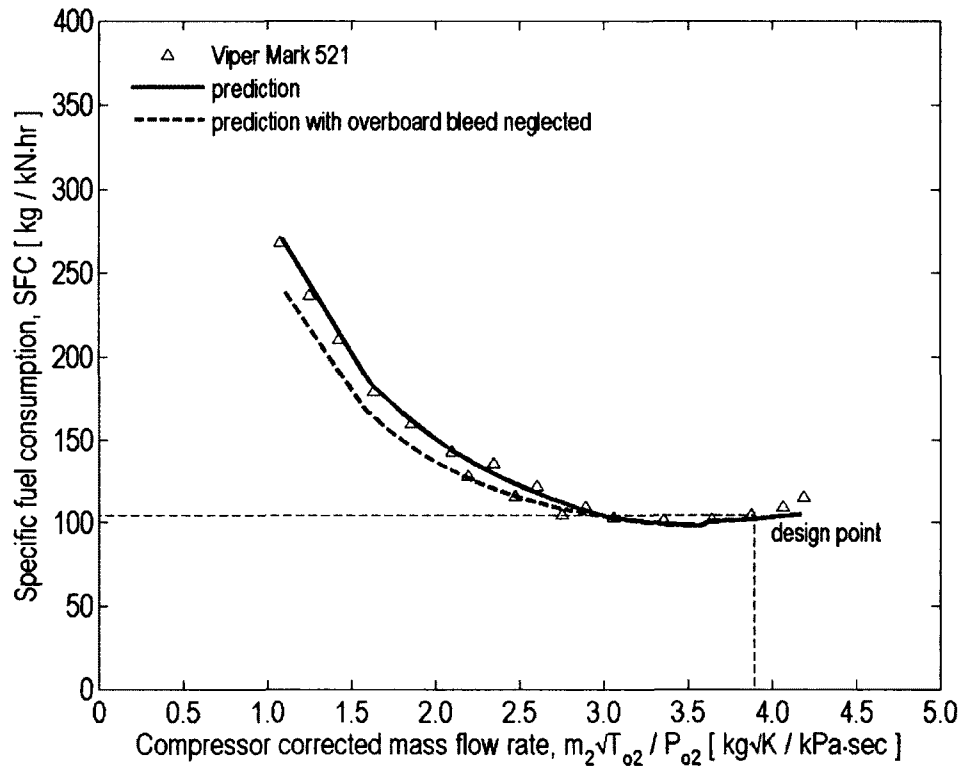


**Figure 5.3** Specific fuel consumption of the Viper

bleed flow was chosen such that a good prediction is made for the SFC (Figure 5.3), rather than for  $T_{04}$ .

Though may appear of little importance, small difference in SFC at low power settings is of great significance. Unlike industrial gas turbines, which mostly operate at high power settings, aero- gas turbines typically spend hours at low power settings while taxiing, held on delays, and while on descent. In such cases, less than a  $\pm 50$  kg/kNhr difference in SFC may translate to more than a tonne of unexpectedly-consumed fuel, which may force an aero- engine operator to experience undesirable occurrences.

Thus, the necessity of accounting for the handling bleed flow is verified.

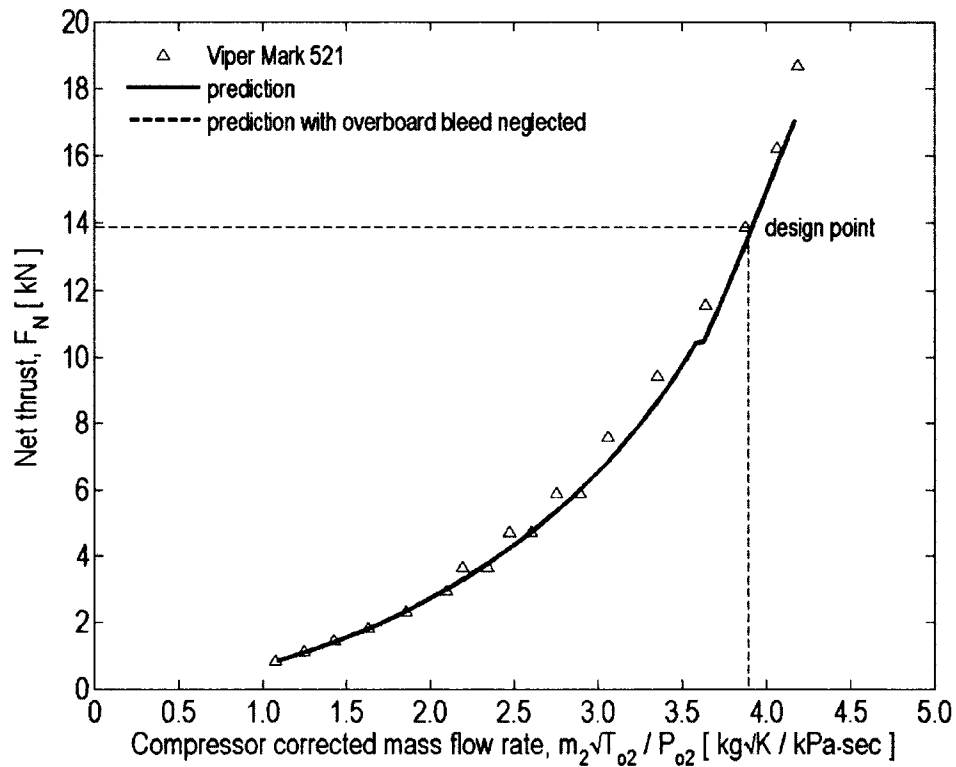


**Figure 5.4** Net thrust of the Viper

Figure 5.4 illustrates the actual and predicted net thrust of the Viper. For any gas turbine, the specific fuel consumption and the thrust output (heat rate and power output for a land-based gas turbine) are the most important performance parameters (Saravanamuttoo et al., 2001). As can be seen, a good prediction is made here.

The minor discontinuity present at approximately  $3.5 \frac{\text{kg}\sqrt{\text{K}}}{\text{kPa}\cdot\text{sec}}$  indicates the choking point of the propelling nozzle.

It can be said that in general, the overall off-design performance has been predicted well.

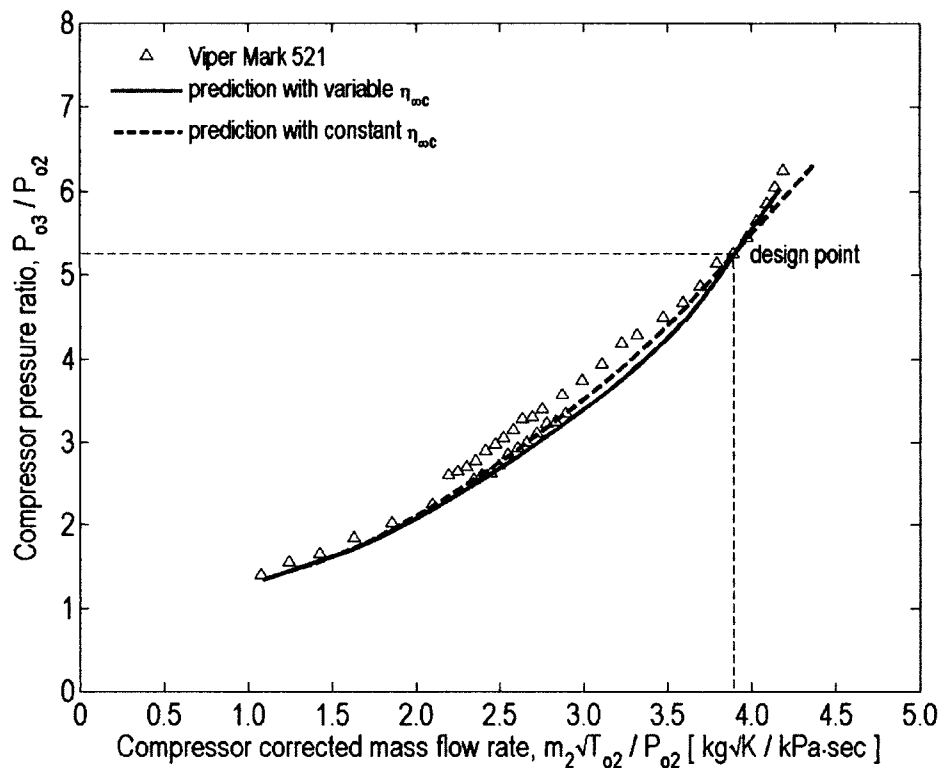


**Figure 5.5** Prediction of the Viper's compressor running line

However, the validation process of the core control method as applied to a single-pool turbojet is not yet complete as the compressor polytropic efficiency was simulated to vary with the compressor speed.

Therefore, the effect of assuming a *constant* compressor polytropic efficiency,  $\eta_{oc}$ , on the predictions was investigated. The resulting plots are presented in Figure 5.5, Figure 5.6, and Figure 5.7, which present the compressor running line, turbine inlet temperature, specific fuel consumption and net thrust, respectively.

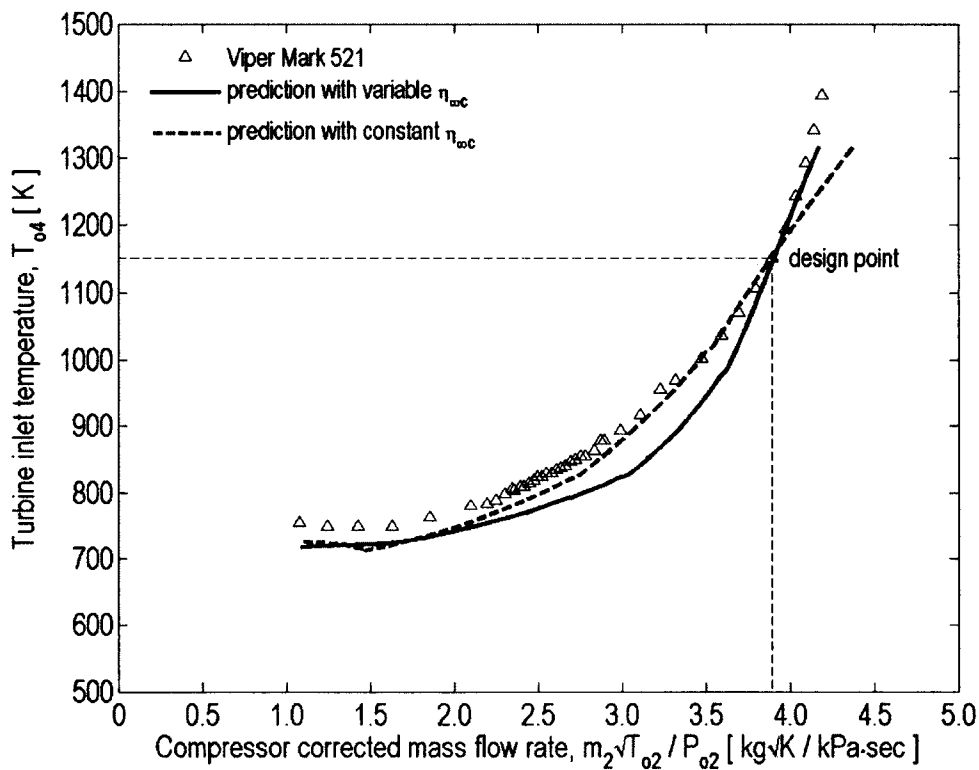


**Figure 5.6** Prediction of the Viper's turbine inlet temperature

In these predictions, the turbine polytropic efficiency was set to its design-point value since Saravanamuttoo (1968) followed the same practice, and since the turbine polytropic efficiency appeared to remain fairly constant throughout the Viper's power range. Since this assumption provided good results, it also validates the work done by Saravanamuttoo (1968) and Wittenberg (1976a).

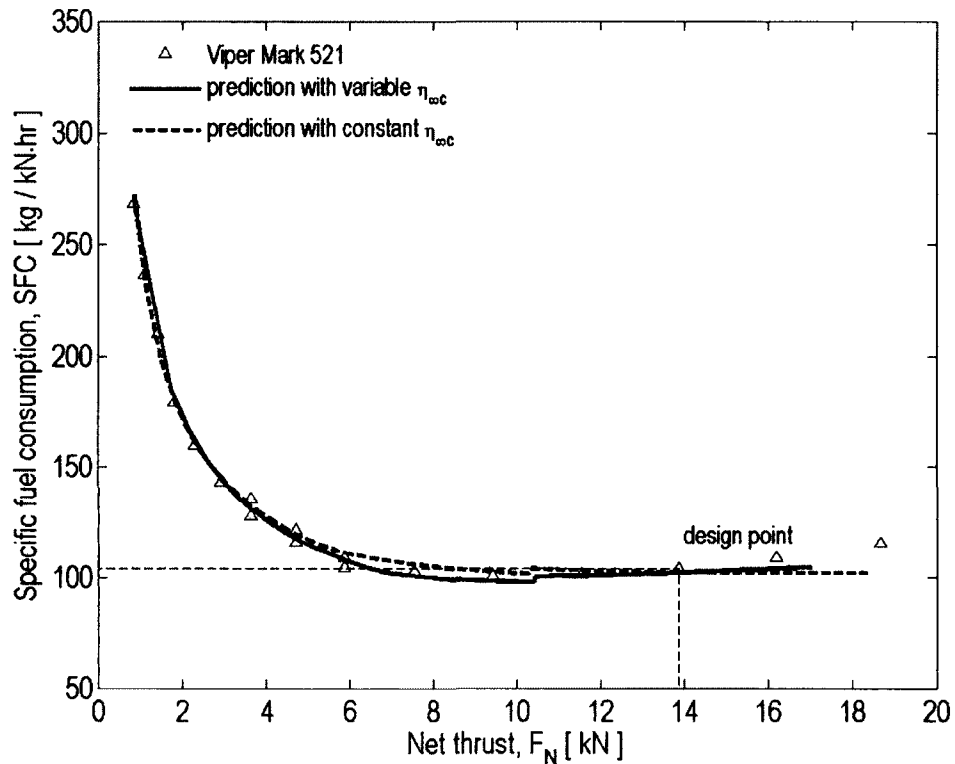


**Figure 5.7** Prediction of the Viper's specific fuel consumption and thrust

Interestingly, when constant compressor polytropic efficiency was assumed, the predictions made were very similar to the variable-efficiency predictions. In some cases, the constant-efficiency predictions were superior to the variable-efficiency predictions (Figure 5.6).

This validates the core control method's ability to accurately predict the off-design performance of a single-spool turbojet engine only using its design-point performance and no compressor or turbine characteristics.

Next, the off-design performance of a multi-spool gas turbine is predicted.

### 5.3 Multi-Spool Gas Turbine – Clean Performance

Here, the pass-off performance data of three Rolls-Royce industrial RB211-24GT engines (Figure 5.8) are used for validating the core control method. New engine performance data (i.e., at zero operating hours) at ISO operating condition was obtained from Broomfield (2007) and the Rolls-Royce products brochure (Rolls-Royce, 2003).

Inlet mass flow rate, $\dot{m}_a$	91.2 kg/sec
Fuel flow rate, $\dot{m}_f$	1.9 kg/sec
Power output, PWR	33.2 MW
HP compressor outlet temperature, $T_{o4}$	740 K
HP compressor outlet pressure, $P_{o4}$	2137.4 kPa
HP turbine inlet temperature, $T_{o5}$	1545 K
LP turbine outlet temperature, $T_{o7}$	1076 K
Power turbine outlet temperature, $T_{o8}$	776 K
Compressor polytropic efficiency, $\eta_{oc}$	0.923 <sup>*</sup>
Combustor pressure drop, $\frac{P_{o5}}{P_{o4}}$	0.97 <sup>§</sup>
Spool mechanical efficiency, $\eta_m$	0.99 <sup>§</sup>
Combustion efficiency, $\eta_{comb}$	0.999 <sup>§</sup>

<sup>\*</sup> calculated from HP compressor outlet pressure and temperature

<sup>§</sup> assumed from Saravanamuttoo et al. (2001)

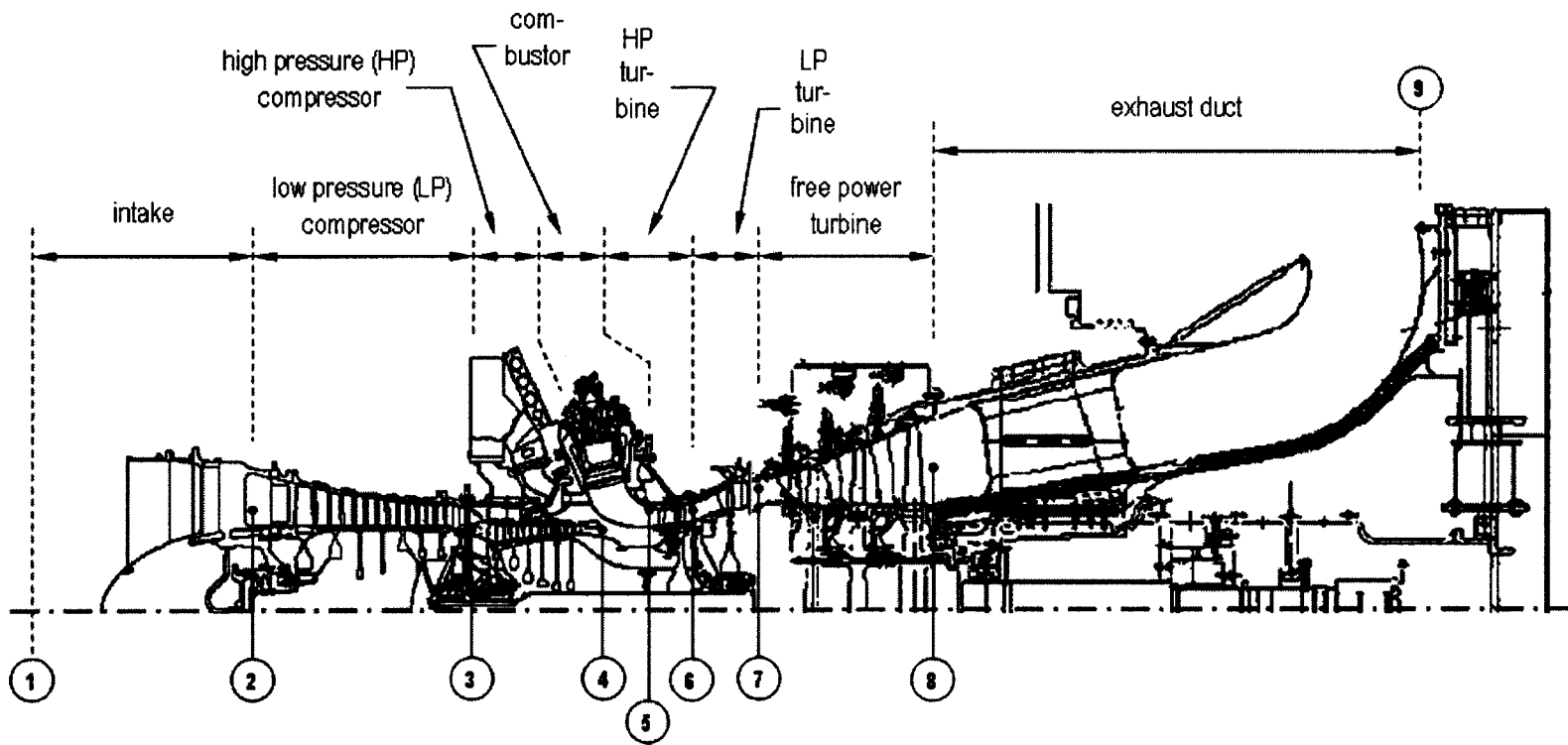


**Figure 5.8** The Rolls-Royce industrial RB211-24GT DLE RT61 [modified from Broomfield, 2007]

First, the core control method is validated against the pass-off, i.e., nominal, data of GT1, GT2 and GT3. Next, the deteriorated performance data is used to establish the core control method's ability to predict deteriorated engine performance.

The uncertainties of the engine performance data are propagated from the measurement uncertainties. These measurement uncertainties at pass-off are assumed to be similar to those observed at site. Since the HP compressor outlet pressure,  $P_{o4}$ , is calculated, its uncertainty is assumed to be similar to that of the LP compressor outlet pressure,  $P_{o3}$ .

The polytropic efficiencies of the compressors and turbines are assumed to remain constant at their design-point values for all on- and off-design operating conditions. If the core control method then produces good predictions, it can be deduced that predictions of similar quality will be made if the actual compressor and polytropic efficiencies are used.

It shall be noted that these pass-off tests are conducted with a power-turbine-equivalent converging nozzle in place of the free power turbine. Therefore, the measurement of the engine's power output is represented by the exhaust gas power. In a gas turbine, the exhaust gas power is the power output of a 100% efficient free power turbine.

It shall also be noted that the figures presented herein are non-dimensionalized due to proprietary reasons.

The reader is referred to Appendix F.4 for the Matlab algorithm used to produce the predictions of the core control method presented herein.

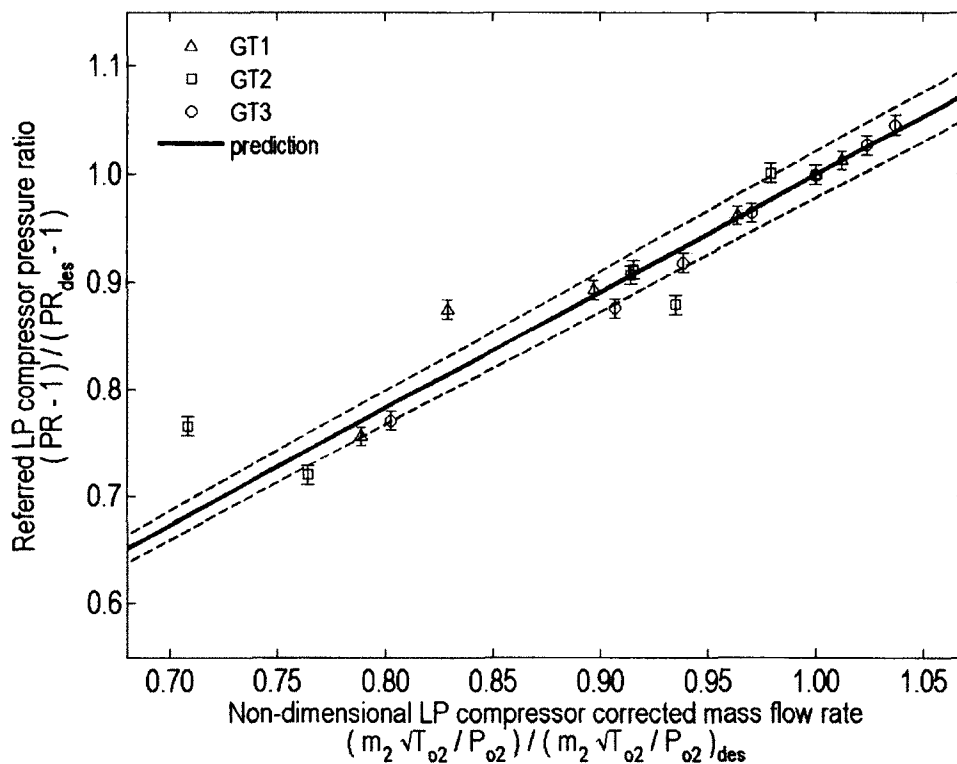


**Figure 5.9** LP compressor running line of the industrial RB211

The predicted LP compressor running line is compared to that of GT1, GT2 and GT3 in Figure 5.9, where the lower end of the engine data represents approximately 50% of design-point power. Here, the uncertainty margin of the prediction is determined by propagating the uncertainties of the compressor and turbine polytropic efficiencies. Apart from a few outliers, the core control method is found to predict the LP compressor running line well.

It shall be noted that the LP compressor of the industrial RB211 employs variable inlet guide vanes. In conventional off-design performance prediction methods, the effect of the variable inlet guide vanes must be simulated. However, since the core control

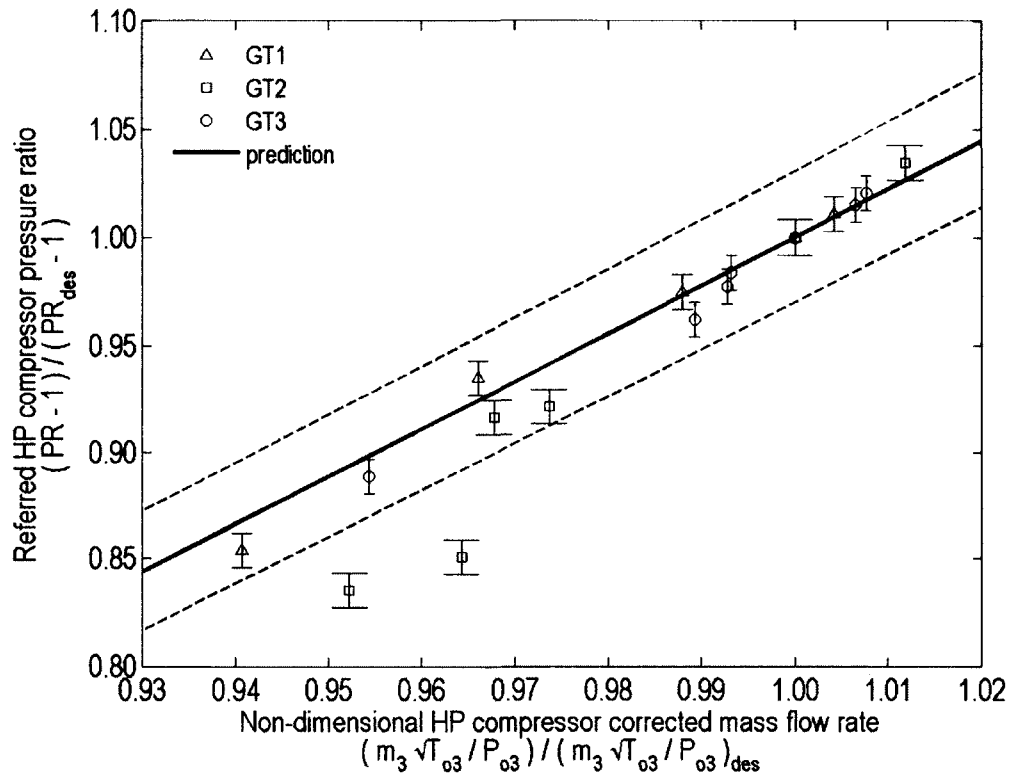


**Figure 5.10** HP compressor running line of the industrial RB211

method only uses pressure ratios, temperature ratios and corrected mass flow rates in its solution process, the variable inlet guide vane was not required to be simulated.

After accounting for the uncertainty of the pass-off data and that of the prediction, it is apparent that the core control method has predicted the HP compressor running line well (Figure 5.10).

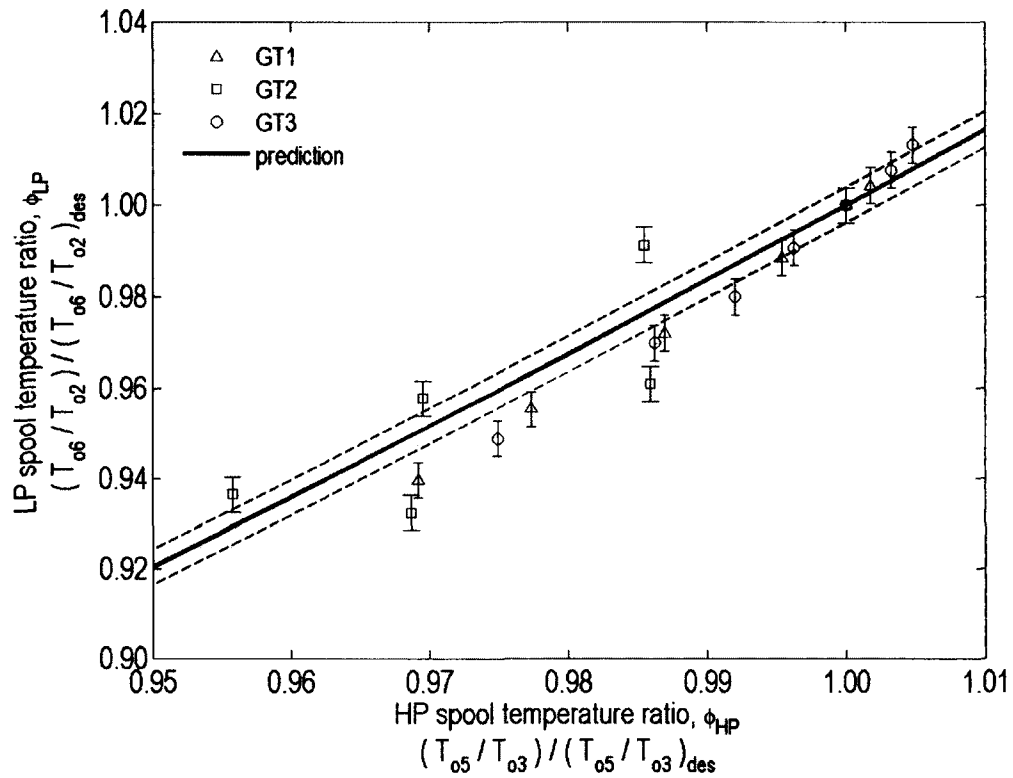


**Figure 5.11** Aerodynamic coupling of the LP and HP spools of the industrial RB211

A milestone in the validation process is the prediction of proper aerodynamic coupling between the two mechanically independent, LP and HP spools (Figure 5.11).

The core control method, was able to predict the aerodynamic coupling of the LP and HP spools of the industrial RB211 using the technique suggested in Section 4.5.2, without using compressor or turbine characteristics.

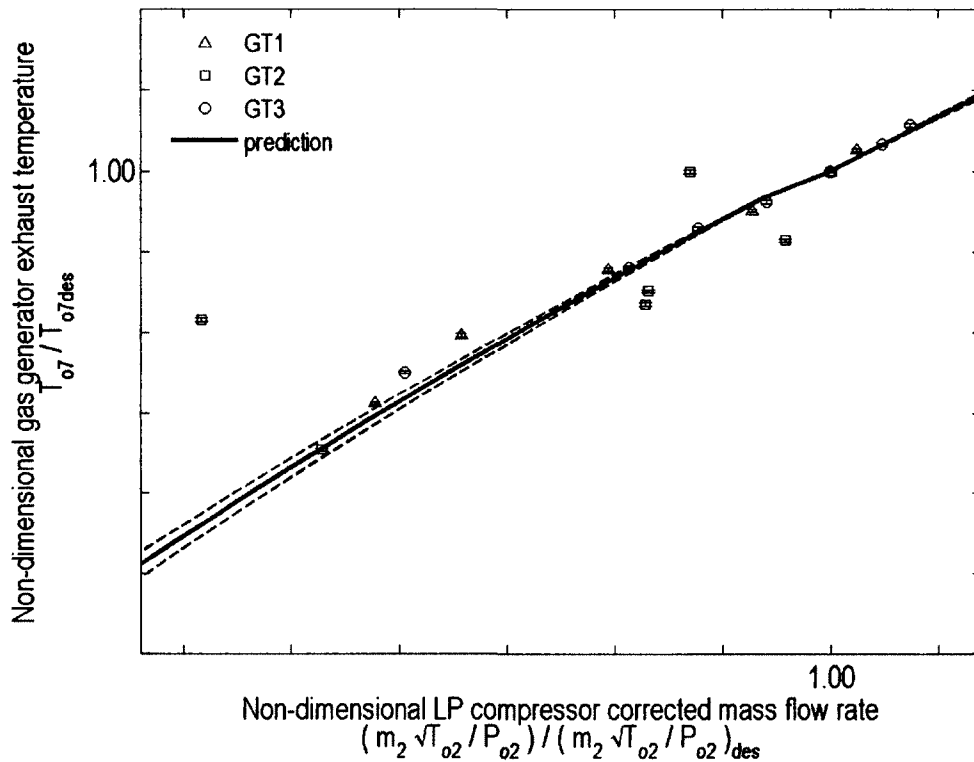


**Figure 5.12** Gas generator exhaust temperature of the industrial RB211

The gas generator exhaust temperature, or the LP turbine outlet temperature,  $T_{o7}$ , is one of the most critical performance parameters of the industrial RB211 as it is an indication of the engine heat rate and the power output. This parameter is well predicted by the core control method (Figure 5.12).

The accurate  $T_{o7}$  prediction suggests that the predicted pressure and temperature ratios of the LP and HP turbines are correct, as reflected by the accurate compressor running line predictions (Figure 5.9 and Figure 5.10). An accurate  $T_{o7}$  prediction also results in an accurately predicted engine heat rate and power output (Figure 5.13).

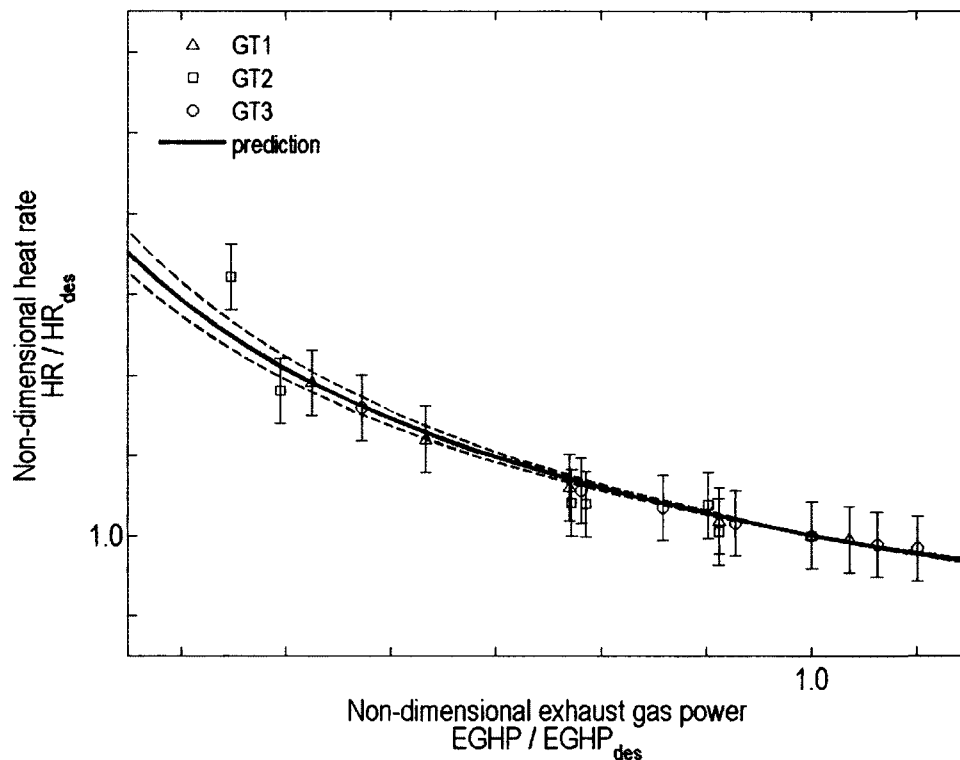


**Figure 5.13** Heat rate and power output of the industrial RB211

All these predictions were made by assuming constant compressor and turbine polytropic efficiencies. Extending from the validation process for the Viper, it can be said that these predictions cannot be further improved by using varying efficiencies.

Therefore, the core control method has been shown to be capable of accurately predicting the off-design performance of a two-spool gas generator with a free power turbine (or an equivalent two-spool turbojet). It shall also be noted that such accurate predictions were made only using the gas turbine's design-point performance. Most importantly, compressor and turbine characteristics were not used.

Next, this method is used to predict deteriorating off-design performance.

## 5.4 Multi-Spool Gas Turbine – Deteriorated Performance

Here, the core control method's ability to predict deteriorating gas turbine off-design performance is investigated.

Specific time periods within the datasets of GT1, GT2 and GT3 were chosen for this procedure. Each chosen time period was found to contain certain deterioration characteristics that possibly could test the limits of the core control method.

The ambient pressure,  $P_{o1}$ , ambient temperature,  $T_{o1}$ , and the core control parameter,  $\phi_{HP}$ , obtained from these datasets were used as control variables. The recoverable deterioration factors, obtained from the data analysis process, were used to simulate the detrimental effect of fouling (Appendix C.13).

Due to the lack of data representing non-recoverable deterioration, no non-recoverable deterioration factors were available. The recoverable deterioration factors alone were incapable of predicting the actual site performance as a bias error was present due to the absence of non-recoverable deterioration factors.

Therefore, to eliminate this bias and to observe the behaviour of the recoverable deterioration prediction aspect of the core control method, the design point polytropic efficiencies were varied within their respective uncertainty margins (Appendix C.11 and Appendix C.12).

The uncertainty margins of the actual site performance were obtained by propagating the measurement uncertainties described in Section 3.3.4, and the related equations are presented in Appendix C.14.

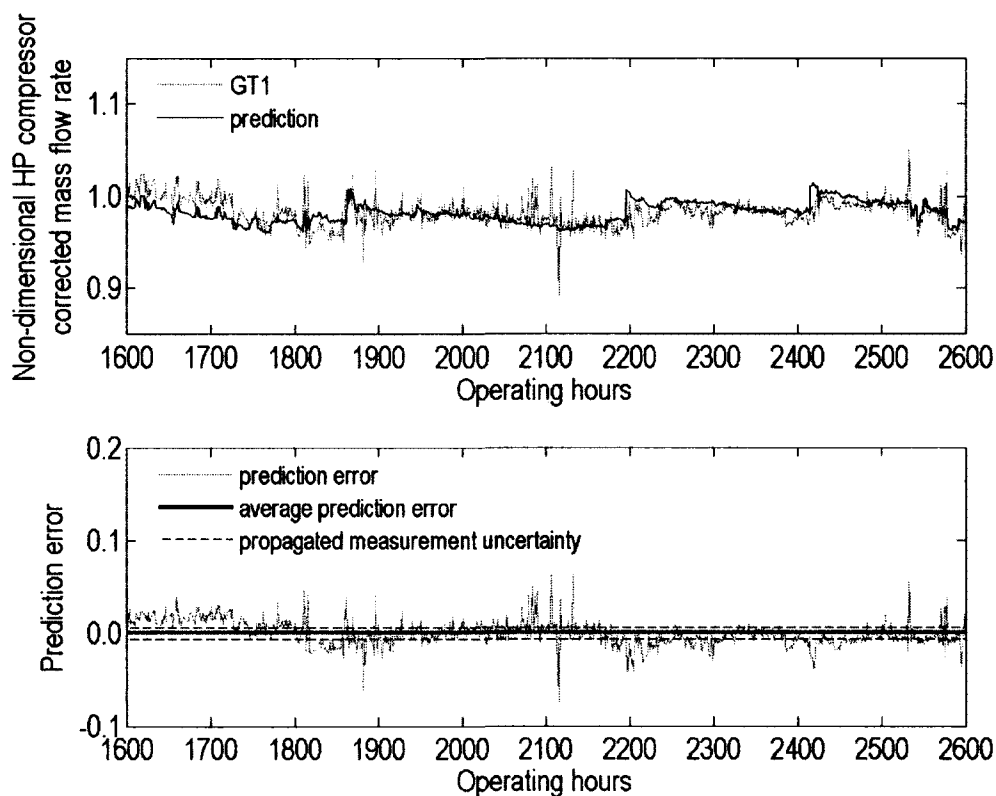


**Figure 5.14** Non-dimensional HP compressor corrected mass flow rate of GT1

The operating profile of GT1 resembled a normal base-load power generation profile. With less than 3,000 operating hours, GT1 was found yet to reach its gas generator exhaust temperature margin, i.e.,  $T_{o7}$  margin. Therefore, the effect of the daily temperature cycle was found to be negligible on GT1's performance.

The core control method was able to predict the effect of compressor washing as per the evidence present at ~1,850, 2,200 and 2,400 operating hours (Figure 5.14). This also validates the hypothesis that the deterioration in the HP compressor corrected mass flow rate is merely an *echo* of the deterioration in the LP compressor corrected mass flow rate. Here, the HP compressor corrected mass flow rate was simply calculated through

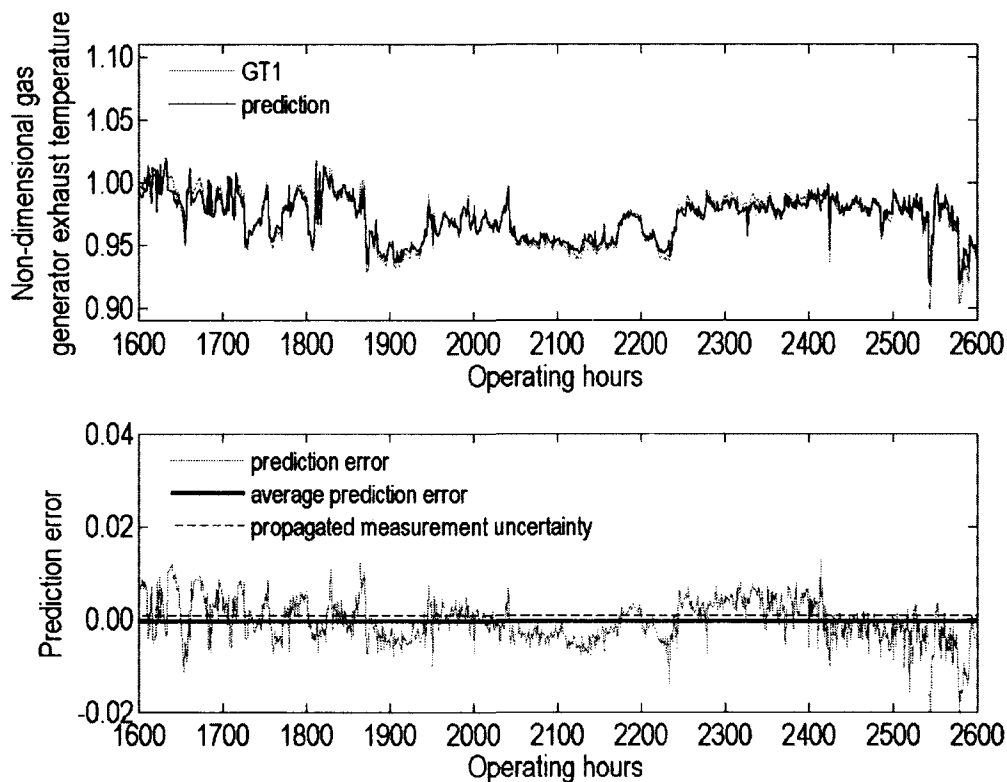


**Figure 5.15** Non-dimensional gas generator exhaust temperature of GT1

the LP and HP compressor mass flow compatibility (Section 4.5).

The corrected mass flow rate predicted by the core control method does not follow every spike observed on the site data. However, the general recoverable deterioration trend is observed to be fairly well predicted. Similar observations can be drawn for  $T_{o,7}$  as well (Figure 5.15). This good  $T_{o,7}$  prediction resulted in similarly well predicted fuel flow rate and power output as well.

The remaining figures of the predictions of GT1 are presented in Appendix E.2.

It is important to note that here, the power output does not reflect the effect of compressor washing either in the site data or the prediction. The reason for which can be

attributed to an ample  $T_{o7}$  margin, which allows the engine control system to maintain a customer-demanded power output by freely increasing the fuel flow, thereby increasing  $T_{o7}$ , in the presence of recoverable deterioration without reaching a performance limit. This ability to produce such diagnostics from the predicted data is an unforeseen, yet mostly welcome, aspect of the core control method.

For GT2, varying the design-point polytropic efficiencies within their uncertainty margins to minimize the prediction errors was fruitless as the core control method under-predicted the LP compressor pressure ratio while over-predicting that of the HP compressor. Therefore, through trial and error, the design-point LP compressor polytropic efficiency was increased by 4.5% of efficiency while that of the HP compressor was reduced by the same amount, which indicated that the HP compressor of GT2 has undergone significant non-recoverable deterioration at site. The shortfall in HP compressor performance is compensated for by the improved performance of the LP compressor. This work-sharing tendency is common in multi-spool gas turbines, and has been captured by the core control method.

Due to the deteriorated HP compressor, GT2 was found to have reached its  $T_{o7}$  margin (Figure 5.16), which prevented the engine control system from compensating for the effects of the daily temperature cycle. As a result, a high-frequency sinusoidal pattern was observed in the predicted and actual GT2 performance variables (Figure 5.17 is one of many which are presented in Appendix E.2).

Since the core control method was able to recognize the  $T_{o7}$  limit and accordingly adjust its predictions, this also validates the performance limiter modification made on the core control method.

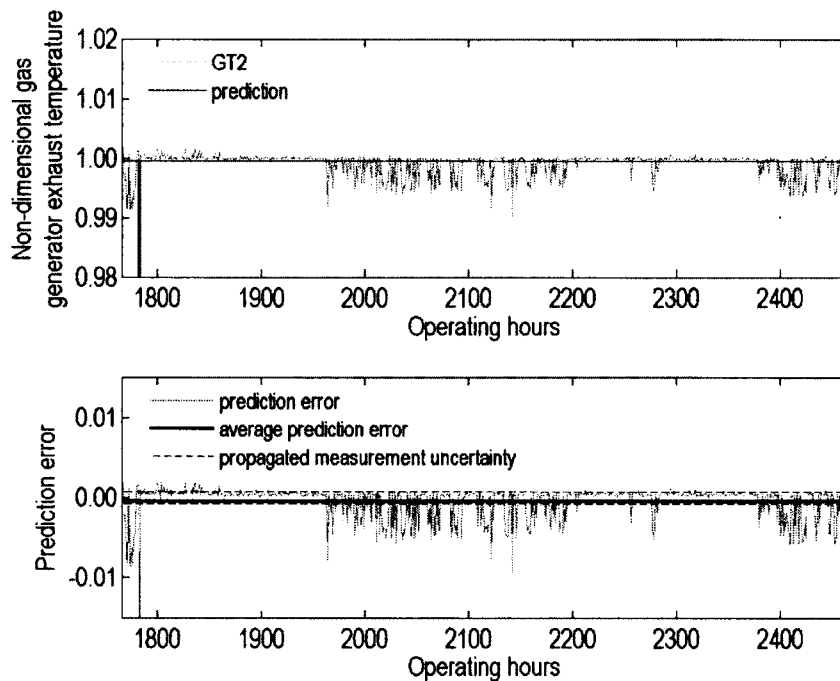


**Figure 5.16** Non-dimensional gas generator exhaust temperature of GT2

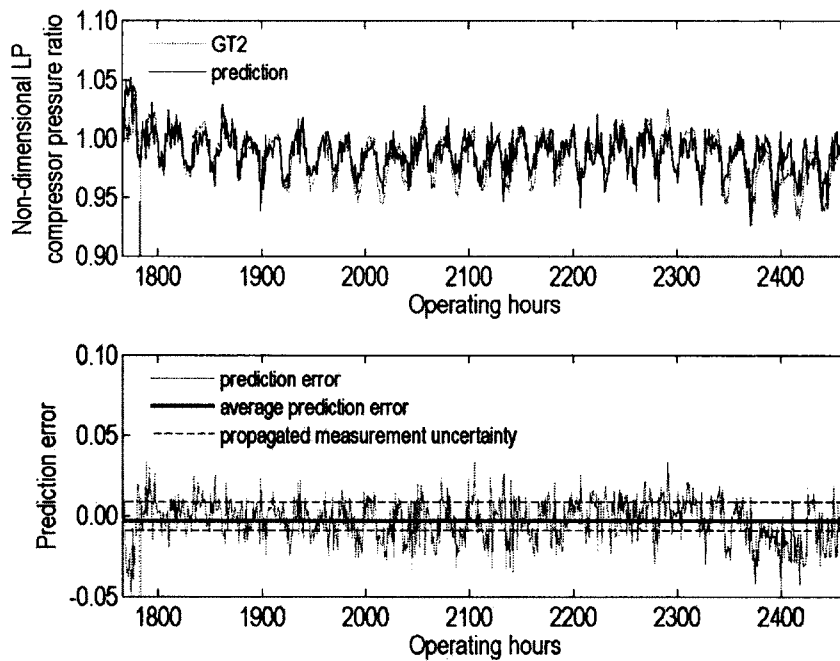


**Figure 5.17** Non-dimensional LP compressor pressure ratio of GT2

The GT3 validation dataset contains a compressor wash, approximately at 6,550 operating hours, and an abrupt reduction in engine performance from 6,800 to 6,900 operating hours. For convenience, the time period from 6,800 to 6,900 operating hours is hereafter referred to as the anomalous period.

Simulation of naturally-occurring deterioration alone, however, was found to be insufficient when predicting the performance within the anomalous period. It was hypothesized that the cause of the performance drop was an instantaneous mechanical failure of a component within GT3.

Upon close observation of the site data, the LP compressor pressure ratio indicated an instantaneous decrease in delivered pressure at approximately 6,800 operating hours – only a few hours prior to the beginning of the anomalous period (Figure 5.18). The HP compressor pressure ratio revealed an instantaneous increase in pressure delivered at the same time (Figure 5.19). The compressor corrected mass flow rates also display instantaneous performance changes at this exact moment (Appendix E.2). A possible explanation for this sudden *spike* is the result of a HP compressor surge.

As GT3 was operating at base-load power at this moment, the possible HP compressor surge was caused by the choking of the rear HP compressor stages. When the HP compressor surged, the compressed gases would have been expelled through GT3's inlet, during which process, the LP compressor handling bleed valve may have been damaged. After a few more hours at base-load power, this handling bleed valve may have failed, thereby allowing maximum rate of flow leakage.

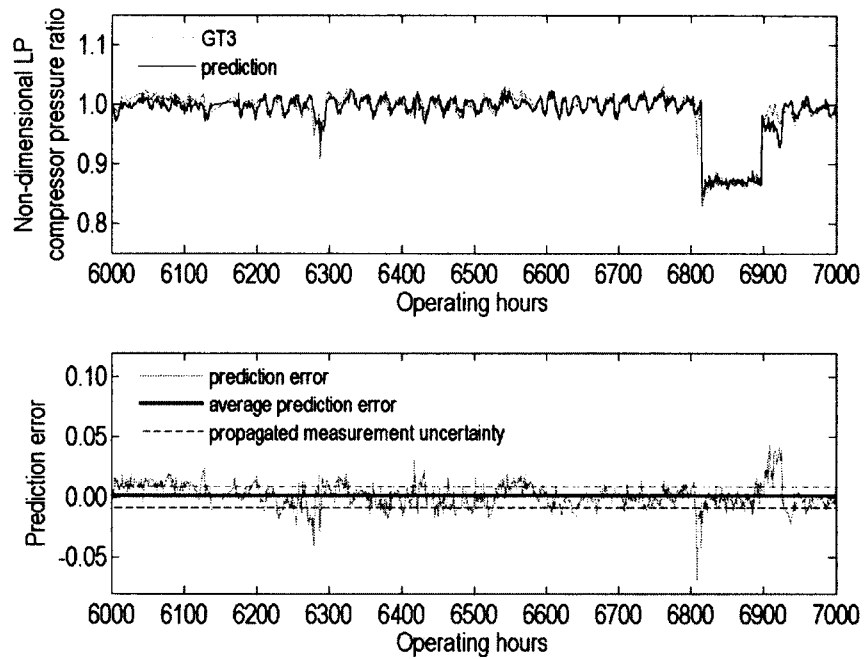


**Figure 5.18** Non-dimensional LP compressor pressure ratio of GT3

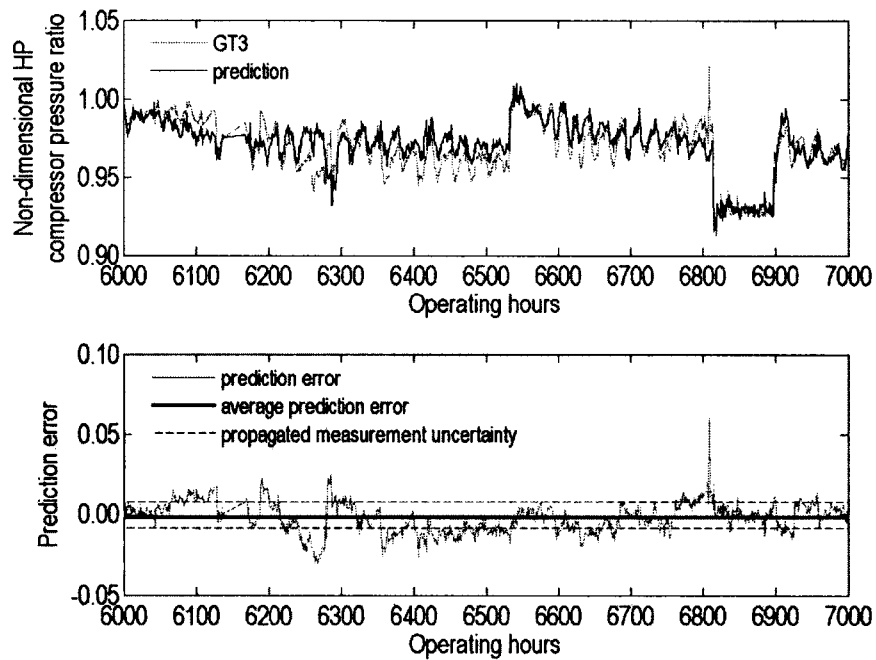


**Figure 5.19** Non-dimensional HP compressor pressure ratio of GT3

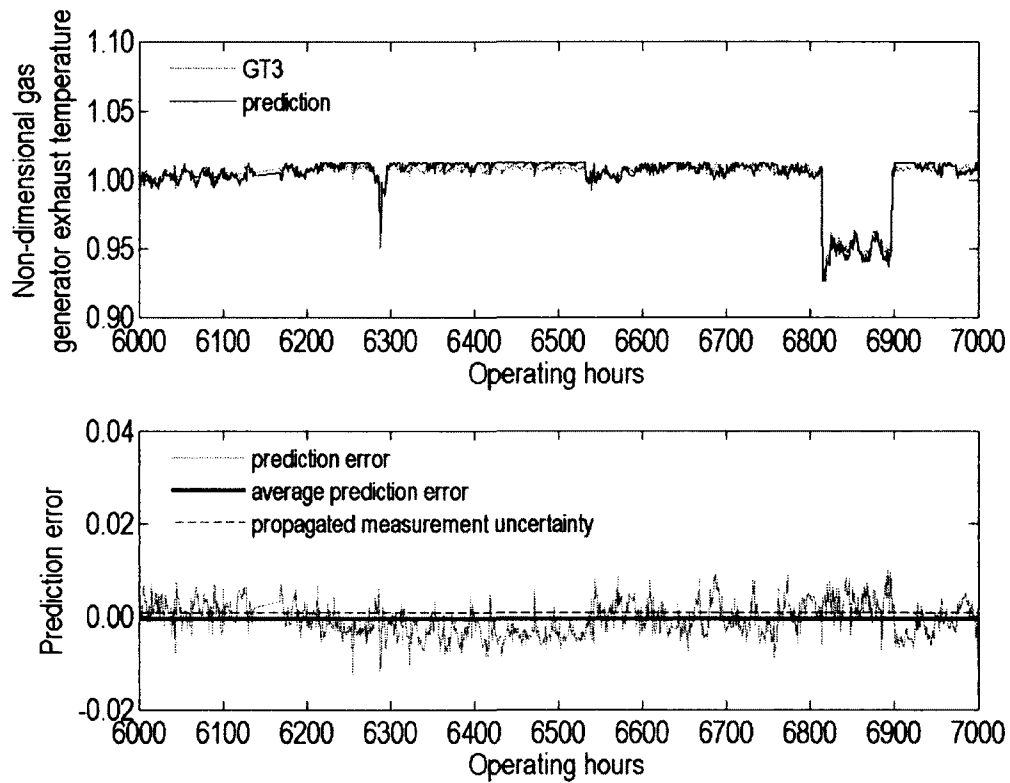


**Figure 5.20** Non-dimensional gas generator exhaust temperature of GT3

Following this thought process, a modified LP compressor handling bleed schedule was implemented, where the bleed schedule was programmed to fully activate (rather than a gradual activation over the engine operating range, as discussed in Section 4.4) within the anomalous period. By trial and error, it was found that a 2.5% bleed flow fraction predicted the performance within the anomalous period well, a sample result of which is presented in Figure 5.20.

It shall be noted that this diagnostic aspect is based on the programmer's experience with the gas turbine being simulated. Therefore, it must be realized that simply achieving alignment between the prediction and the actual data does not

necessarily imply an accurate diagnosis, and that proper engineering judgment must always be applied when drawing conclusions.

The results from the validation process prove that the running line of a compressor can be predicted through the swallowing capacity of its mechanically-coupled turbine. This reveals an unorthodox perspective of the operating behaviour of a gas turbine, namely, that it is the compressor that must satisfy the turbine's *appetite*. This perspective can also be applied when designing new gas turbines.

The usual process of designing a new gas turbine involves scaling of an existing compressor, the performance characteristics of which is then used to design a turbine. Through refinement, the compressor and turbine designs are improved to satisfy predetermined on- and off-design performance of the gas turbine.

However, the capacity of the turbine can be obtained just by using the design-point performance, using which the core control method can be applied to predict the required compressor's running line. This eliminates the guess-work required when scaling a compressor.

The core control method was able to accurately predict the non-deteriorated off-design performance of a single-spool turbojet and a two-spool gas generator with a free power turbine. The core control method was also able to accurately predict the deteriorated performance of three gas turbines with a two-spool gas generator with a free power turbine arrangement. During this process, a performance limiter modification introduced into the core control method was also proven. The core control method is hereby validated.

## **6 CONCLUSIONS AND RECOMMENDATIONS**

### **6.1 Conclusions**

**A**S stated in the Introduction, the purpose of this thesis was to develop a simple performance prediction technique for a multi-spool gas turbine that is able to accurately predict on- and off- design steady-state performance for new and deteriorated gas turbines. Such a technique was developed and its theory was discussed in detail.

The following are the conclusions drawn from this study.

Literature review exposed various methods of off-design performance simulation, which were often complicated, thus understood by very few, and offered a small gain for a large effort. Therefore, a simple, yet versatile, method of predicting gas turbine off-design performance was deemed necessary.

It was hypothesized that all performance parameters of a gas turbine could be represented by a key performance parameter, where this parameter would be within the core of the engine. Thus, the concept of a *core control parameter* was introduced.

The spool temperature ratio,  $\phi$ , which is the ratio between the turbine inlet temperature and the compressor inlet temperature – initialized to their respective design-point values, was chosen as the core control parameter.

The underlying theory of the core control method stated that only the design-point performance was required to predict the off-design performance of a gas turbine, where compressor and turbine characteristics were not required.

Gasdynamics relationships and a solution process were then developed for a generic single-spool turbojet as a proof of concept. This was then used to accurately predict the off-design performance of a nominal Viper Mark 521.

Next, the core control method was applied to a multi-spool gas turbine, which is of a two-spool gas generator with a free power turbine configuration, which was then used to accurately predict the off-design performance of three new industrial RB211 gas turbines. The core control method was further modified to account for performance deterioration, which was then used to accurately predict the deteriorated off-design performance of the same industrial RB211 gas turbines.

The predictions of actual gas turbine performance made by the core control method proved its validity.

During this validation process, proper aerodynamic coupling between the LP and HP spools of the industrial RB211 gas turbines was predicted, and a hidden performance diagnostics aspect of the core control method was revealed.

## 6.2 Recommendations

The technique of core control parameter can be applied for other types of engines such as multi-spool turbojets, multi-spool separate-exhaust turbofans, and multi-spool mixed-exhaust turbofans, as well.

The working fluids used in this method are dry air and exhaust gas. If molecular composition of the working fluid, including that of the fuel, is considered, this technique may produce results with better accuracy.

Although this method only considers steady state performance, this method can also be modified for transient performance prediction as well. However, since transient operation causes a compressor operating line to deviate from optimum efficiency regions due to the temporary flow imbalance between its mechanically-coupled turbine, the validity of the constant component efficiency assumption needs to be examined.

## REFERENCES

- Adamcyk, J. J., Hanses, J. L., and Prahst, P. S., (2007) "A post test analysis of a high-speed two-stage axial flow compressor," *Proceedings of ASME Turbo Expo 2007: Power for Land, Sea and Air*, ASME, Montreal, Canada, GT-2007-28057, May 14-17, 2007
- Aker, G. F., and Saravanamuttoo, H. I. H., (1989) "Predicting gas turbine performance degradation due to compressor fouling using computer simulation techniques," *Journal of Engineering for Power*, Vol. 111, 1989, pp. 343-350
- Alexander P., and Singh, R., (2004) "Gas turbine engine fault diagnostics using fuzzy concepts," *1<sup>st</sup> Intelligent Systems Technical Conference*, AIAA, Chicago, Illinois, USA, AIAA-2004-6223, Sep 20-22, 2004
- Blackburn, J., Frendt, G., Gagné, M., Genest, J. D., Kohler, T., and Nolan, B., (2007) "Performance enhancements of the industrial Avon gas turbine," *Proceedings of ASME Turbo Expo 2007: Power for Land, Sea and Air*, ASME, Montreal, Canada, GT-2007-28315, May 14-17, 2007
- Boyce, M. P., (2002) *Gas Turbine Engineering Handbook*, 2<sup>nd</sup> edition, Gulf Professional Publishing, 2002
- Broomfield, S. P., (2007) "RB211 G-T DLE/RT61 demonstrator experience at TCPL Nordegg," *17<sup>th</sup> Symposium on Industrial Application of Gas Turbines*, Industrial Application of Gas Turbines Committee (IAGTC), Banff, Alberta, Canada, 07-IAGT-3.4, Oct 2007

- Bruner, H. S., (2002) "The analysis of performance flight test data using a neural network," *40<sup>th</sup> AIAA Aerospace Sciences Meeting and Exhibit*, AIAA, Reno, Nevada, USA, AIAA 2002-0989, Jan 14-17, 2002
- Caguiat, D. F., (2003) "Rolls-Royce/Allison 501-K gas turbine antifouling compressor coatings evaluation," *Journal of Turbomachinery*, Vol. 125, Jul 2003, pp. 482-488
- Chiras, N., Evans, C., and Rees, D., (2002) "Nonlinear gas turbine modeling using feedforward neural networks," *Proceedings of ASME Turbo Expo 2002*, ASME, Amsterdam, The Netherlands, GT-2002-30035, Jun 3-6, 2002
- Daniel Measurements, (2010) "Daniel Danalyzer Model 500 Gas Chromatograph," Products Brochure, DAN-PDS-GC-500, May 2010
- Das, K., Hamed, A. A., and Basu, D., (2006) "Droplet trajectories and collection on fan rotor at off-design conditions," *Proceedings of ASME Turbo Expo 2006: Power for Land, Sea and Air*, ASME, Barcelona, Spain, GT-2006-91214, May 8-11, 2006
- Diakunchak, I. S., (1992) "Performance deterioration in industrial gas turbines," *Journal of Engineering for Gas Turbines and Power*, Vol. 114, 1992, pp. 161-168
- Drosg, M., (2007) *Dealing with Uncertainties: A Guide to Error Analysis*, Springer-Verlag Berlin Heidelberg, 2007
- Drummond, C., and Davison, C. R., (2009a) "Capturing the shape variance in gas turbine compressor maps," *Proceedings of the ASME Turbo Expo 2009: Gas Turbine Technical Congress and Exposition*, ASME, Orlando, Florida, USA, GT-2009-60141, Jun 8-12, 2009

- Drummond, C., and Davison, C. R., (2009b) "Improved compressor maps using approximate solutions to the Moore-Greitzer model," *Proceedings of the ASME Turbo Expo 2009: Gas Turbine Technical Congress and Exposition*, ASME, Orlando, Florida, USA, GT-2009-60148, Jun 8-12, 2009
- Duminica, A., (2002) "Industrial RB211 – ECS I/O Requirements – Malpensa Project," *Rolls-Royce Internal Technical Report*, No. GTER 10032, May 2002
- El-Batsh, H., (2001) "Modeling particle deposition on compressor and turbine surfaces," *PhD Thesis*, Institute of Thermal Turbomachines and Powerplants, Vienna University of Technology, Vienna, Sep 2001
- Fouflias, D., Gannan, A., Ramsden, K., Pilidis, P., and Lambart, P., (2009) "CFD predictions of cascade pressure losses due to compressor fouling," *Proceedings of ASME Turbo Expo 2009: Power for Land, Sea and Air*, Orlando, Florida, USA, GT2009-59158, Jun 8-12, 2009
- Ganguli, R., (2002) "Fuzzy logic intelligent system for gas turbine module and system fault isolation," *Journal of Propulsion and Power*, Vol. 18, No. 2, Mar-Apr 2002, pp. 440-447
- Gauthier, J. E. D., (2008) *MECH 5402 Course Notes*, Department of Mechanical and Aerospace Engineering, Carleton University, Ottawa, Ontario, Canada, 2008
- Green, A. J., (1998) "The development of engine health monitoring for gas turbine engine health and life management," *34<sup>th</sup> AIAA/ASME/SAE/ASEE Joint Propulsion Conference and Exhibit*, AIAA, Cleveland, Ohio, USA, AIAA-1998-3544, Jul 13-15, 1998

- Green, A. J., and Allen D. G., (1997) "Artificial intelligence for real time diagnostics and prognostics of gas turbine engines," *33<sup>rd</sup> AIAA/ASME/SAE/ASEE Joint Propulsion Conference and Exhibit*, AIAA, Seattle, Washington, USA, AIAA-1997-2899, Jul 6-9, 1997
- Gulen, S. C., Griffin, P. R., and Paolucci, S., (2000) "Real-time on-line performance diagnostics of heavy-duty industrial gas turbines," *International Gas Turbine & Aeroengine Congress and Exhibition*, ASME, Munich, Germany, 2000-GT-312, May 8-11, 2000
- Gunetti, P., Millis, A., and Thompson, H., (2008) "A distributed intelligent agent architecture for gas-turbine engine health management," *46<sup>th</sup> AIAA Aerospace Science Meeting and Exhibit*, AIAA, Reno, Nevada, USA, AIAA-2008-883, Jan 7-10, 2008
- Hosseini, S. H. R., Khaledi, H., and Soltani, M. R., (2009) "New model based gas turbine fault diagnostics using 1D engine model and nonlinear identification algorithms," *Proceedings of ASME Turbo Expo 2009: Power for Land, Sea and Air*, ASME, Orlando, Florida, USA, GT-2009-59439, Jun 8-12, 2009, pp. 575-585
- Kobayashi, T., and Simon, D. L., (2001) "A hybrid neural network-genetic algorithm technique for aircraft engine performance diagnostics," *37<sup>th</sup> AIAA/ASME/SAE/ASEE Joint Propulsion Conference*, AIAA, Salt Lake City, Utah, USA, AIAA 2001-3763, July 8-11, 2001
- Kobayashi, T., Simon, D. L., and Litt, J. S., (2005) "Application of a constant gain extended Kalman filter for in-flight estimation of aircraft engine performance parameters," *NASA Technical Memorandum*, NASA/TM-2005-213865, Sep 2005
- Kurz, R., (2005) "Gas turbine performance," *Proceedings of the 34<sup>th</sup> Turbomachinery Symposium*, 2005, pp. 131-146

- Kurz, R., and Brun, K., (2001) "Degradation in gas turbine systems," *Journal of Engineering for Gas Turbines and Power*, Vol. 123, Jan 2001, pp. 70-77
- Kurz, R., and Brun, K., (2007) "Gas turbine tutorial – maintenance and operating practices effects on degradation life," *Proceedings of the 36<sup>th</sup> Turbomachinery Symposium*, 2007
- Kurzke, J., (2007) GasTurb 11.0 "A program to calculate design and off-design performance of gas turbines," [www.gasturb.de](http://www.gasturb.de)
- Kyriazis, A., and Mathioudakis, K., (2009) "Gas turbine fault diagnosis using fuzzy-based decision fusion," *Journal of Propulsion and Power*, Vol. 25, No. 2, Mar-Apr 2009, pp. 335-343
- Lakshminarasimha, A. N., Boyce, M. P., and Meher-Homji, C. B., (1994) "Modeling and analysis of gas turbine performance deterioration," *Journal of Engineering for Gas Turbines and Power*, Vol. 166, Jan 1994, pp. 46-52
- Lakshminarayana, B., and Reynolds, B., "Turbulence characteristics in the near wake of a compressor rotor blade," *AIAA Journal*, Vol. 18, No. 11, Nov 1980, pp. 1354-1362
- Lambert, H. H., (1991) "A simulation study of turbofan engine deterioration estimation using Kalman filtering techniques," *NASA Technical Memorandum*, NASA/TM-1991-104233, Jun 1991
- Lazzaretto, A., and Toffolo, A., (2001) "Analytical and neural network models for gas turbine design and off-design simulation," *International Journal for Applied Thermodynamics*, Vol. 4, No. 4, ISSN 1301-9724, Dec 2001, pp. 173-182

- Lee A. S., Singh, R., and Probert, S. D., (2009) "Modelling of the performance of a F100-PW229 equivalent engine under sea-level static conditions," 45<sup>th</sup> *AIAA/ASME/SAE/ASEE Joint Propulsion Conference and Exhibit*, AIAA, Denver, Colorado, USA, AIAA 2009-5018, Aug 2-5, 2009
- Li, Y. G., (2002) "Performance-analysis-based gas turbine diagnostics: a review," *Journal of Power and Energy*, Vol. 216, Part A, Jul 2002, pp. 363-377
- Li, Y. G., and Korikianitis, T., (2011) "Nonlinear weighted-least-squares estimation approach for gas-turbine diagnostic applications," *Journal of Propulsion and Power*, Vol. 27, No. 2, Mar-Apr 2011, pp. 337-345
- Litt, J. S., (2005) "An optimal orthogonal decomposition method for Kalman filter-based turbofan engine thrust estimation," *NASA Technical Memorandum*, NASA/TM-2005-213864, Oct 2005
- Luppold, R. H., Roman, J. R., Gallops, G. W., and Kerr, L. J., (1989) "Estimating in-flight engine performance variations using Kalman filter concepts," 25<sup>th</sup> *AIAA/ASME/SAE/ASEE Joint Propulsion Conference and Exhibit*, AIAA, Monterey, California, USA, AIAA-89-2584, Jul 10-12, 1989
- Martis, D., (2007) "Fuzzy logic estimation applied to Newton methods for gas turbines," *Journal of Engineering for Gas Turbines and Power*, Vol. 129, Jan 2007, 88-96
- Mathioudakis, K., Stamatis, A., and Bonataki, E., (2002) "Allocating the causes of performance deterioration in combined cycle gas turbine plants," *Journal of Engineering for Gas Turbines and Power*, Vol. 124, Apr 2002, pp. 256-262
- Mattingly, J. D., (2005) *Elements of Gas Turbine Propulsion*, 2<sup>nd</sup> edition, AIAA Education Series, 2005

- Mirza-Baig, F. S., and Saravanamuttoo, H. I. H., (1991) "Off-design performance prediction of turbofans using gasdynamics," *International Gas Turbine and Aeroengine Congress and Exposition*, Orlando, Florida, USA, 91-GT-389, Jun 3-6, 1991
- Modest, M. F., (2003) *Radiative Heat Transfer*, 2<sup>nd</sup> edition, Academic Press, 2003
- Moran, M. J., and Shapiro, H. N., (2004) *Fundamentals of Engineering Thermodynamics*, 5<sup>th</sup> edition, John Wiley and Sons, 2004
- Morini, M., Pinellu, M., Spina, P. R., and Venturini, M., (2009) "CFD simulation of fouling on axial compressor stages," *Proceedings of ASME Turbo Expo 2009: Power for Land, Sea and Air*, Orlando, Florida, USA, GT2009-59025, Jun 8-12, 2009
- Muir, D. E., Saravanamuttoo, H. I. H., and Marshall, D. J., (1989) "Health monitoring of a variable geometry gas turbines for the Canadian navy," *Journal of Engineering for Gas Turbines and Power*, Vol. 111, Apr 1989, pp. 244-250
- Ogaji, S. O. T., Sampath, S., Singh, R., and Probert, S. D., (2002) "Parameter selection for diagnosing a gas turbine's performance deterioration," *Applied Energy*, Vol. 73, 2002, pp. 25-46
- Reynolds, B., Lakshminarayana, B., and Ravnidranath, A., (1979) "Characteristics of the near wake of a compressor fan rotor blade," *AIAA Journal*, Vol. 17, No. 9, Sep 1979, pp. 959-967
- Rolls-Royce, (2003) "RN211 gas turbines for oil and gas applications," Products brochure, EO100NA-8/03-3M, 2003

- Rosemount, (2010a) "Rosemount 3051 pressure transmitter," Products brochure, 00813-0100-4001 Rev KA, Aug 2010
- Rosemount, (2010b) "Rosemount 3051 revision 5 pressure transmitter," Products brochure, 00813-0100-4051 Rev BA, Mar 2008
- Rosemount, (2010c) "Temperature sensors and accessories (English)," Products brochure, 00813-0100-2654, Apr 2010
- Samarasinghe, S., (2006) *Neural Networks for Applied Sciences and Engineering: From Fundamentals to Complex Pattern Recognition*, Taylor and Francis Group LLC, 2006
- Sampath, S., Gulati, A., and Singh, R., (2002) "Artificial intelligence techniques for gas turbine engine fault diagnostics," *38<sup>th</sup> AIAA/ASME/SAE/ASEE Joint Propulsion Conference and Exhibit*, AIAA, Indianapolis, Indiana, USA, AIAA 2002-4308, Jul 7-10, 2002
- Saravanamuttoo, H. I. H., (1963) "Analog computer study of the transient performance of the Orenda 600-hp regenerative gas turbine," *Aviation and Space, Hydraulic, and Gas Turbine Conference and Products Show*, ASME, Los Angeles, California, USA, 63-AHGT-38, Mar 3-7, 1963
- Saravanamuttoo, H. I. H., (1968) "Analogue computer simulation of gas turbine performance," PhD Thesis, University of Bristol, 1968
- Saravanamuttoo, H. I. H., and Lakshminarasimha, A. N., (1985) "A preliminary assessment of compressor fouling," *Gas Turbine Conference and Exhibit*, ASME, Huston, Texas, USA, 85-GT-153, Mar 18-21, 1985

- Saravanamuttoo, H. I. H., Rogers G. F. C., and Cohen, H., (2001) *Gas Turbine Theory*, 5<sup>th</sup> edition, Pearsons Education Limited, 2001
- Schneider, E., Bussjaeger, S. D., Franco, S., and Therkorn, D., (2010) "Analysis of compressor on-line washing to optimize gas turbine power plant performance," *Journal of Engineering for Gas Turbines and Power*, Vol. 132, Jun 2010, pp.062001.1-062001.7
- Seddigh, F., and Saravanamuttoo, H. I. H., (1990) "A proposed method for assessing the susceptibility of axial compressors to fouling," *Gas Turbine and Aeroengine Congress and Exposition*, ASME, Brussels, Belgium, 90-GT-348, Jun 11-14, 1990
- Simon, D. L., Bird, J., Davison, C., Volponi, A., and Iverson, R. E., (2008) "Benchmarking gas path diagnostic methods: a public approach," *Proceedings of ASME Turbo Expo 2008: Power for Land, Sea and Air*, Berlin, Germany, GT2008-51360, Jun 9-13, 2008
- Simon, D. L., and Garg, S., (2010) "Optimal tuner selection for Kalman filter-based aircraft engine performance estimation," *NASA Technical Memorandum*, NASA/TM-2010-216076, Jan 2010
- Simon D., and Simon D. L., (2005) "Aircraft turbofan engine health estimation using constrained Kalman filtering," *Journal of Engineering for Gas Turbines and Power*, Vol. 127, Apr 2005, pp. 323-328
- Soares, C., (2008) *Gas Turbines – A Handbook of Air, Land and Sea Applications*, Butterworth-Heinemann, 2008

- Steinke, R. J., (1982) "STGSTK - a computer code for predicting multistage axial-flow compressor performance by a meanline stage-stacking method," *NASA Technical Paper*, NASA, 1982
- Sullerey, R. K., and Sayeed Khan, M. A., (1983) "Freestream turbulence effects on compressor cascade wake," *Journal of Aircraft*, Vol. 20, No. 8, Aug 1983, pp. 733-734
- Tabakoff, W., Lakshminarasimha, A. N., and Pasin, M., (1990) "Simulation of compressor performance deterioration due to erosion," *Journal of Turbomachinery*, Vol. 112, Jan 1990, pp. 78-83
- Tarabrin, A. P., Schurovsky, V. A., Bodrov, A. I., and Stalder, J. P., (1998) "An analysis of axial compressor fouling and blade cleaning method," *Journal of Turbomachinery*, Vol. 120, Apr 1998, pp. 256-261
- Taylor, D. H., and Gotheridge, W. P., "Investigation into surging with RB211 1880-4002 installed in GT2 at Mitra Energy, Batam Island," *Rolls-Royce Internal Technical Report*, No. CS313, Sep 2006
- Tomita, J. T., Bringhenti, C., Barbosa, J. R., and de Jesus, A. B., (2006) "Nacelle design for mixed turbofan engines," *Proceedings of ASME Turbo Expo 2006: Power for Land, Sea and Air*, ASME, Barcelona, Spain, GT-2006-91212, May 8-11, 2006
- Urban, L. A., (1973) "Gas path analysis applied to turbine engine condition monitoring," *Journal of Aircraft*, Vol. 10, No. 7, Jul 1973, pp. 400-406
- Veer, T., Haglerød, K. K., and Bolland, O., (2004) "Measured data correction for improved fouling and degradation analysis of offshore gas turbines," *ASME/IGTI TURBOEXPO Conference 2004*, ASME, Vienna, Austria, GT-2004-53760, Jun 14-17, 2004

Walsh, P. P., and Fletcher, P., (1998) *Gas Turbine Performance*, 1<sup>st</sup> edition, Blackwell Science Ltd, 1998

White, F. M., (2003) *Fluid Mechanics*, 5<sup>th</sup> edition, McGraw-Hill Higher Education, 2003

Wittenberg, H., (1976a) "Prediction of off-design performance of turbojet and turbofan engines based on gasdynamic relationships," Delft University of Technology, Mar 1976

Wittenberg, H., (1976b) "Prediction of off-design performance of turbojet and turbofan engines," *Proceedings on Performance Prediction Methods*, AGARD CP-242-76, 1976

Yin, J., Hales, R., Pilidis, P., and Curnock, B., (2001) "2-shaft high-bypass ratio turbofan performance calculation using a new 2-D fan model," 37<sup>th</sup> *AIAA/ASME/SAE/ASEE Joint Propulsion Conference*, AIAA, Salt Lake City, Utah, USA, AIAA 2001-3302, July 8-11, 2001

Zarchan, P., and Musoff, H., (2005) *Fundamentals of Kalman Filtering: A Practical Approach*, Progress in Aeronautics and Astronautics, Vol. 208, 2005

Zhou, M., and Gauthier, J. E. D., (1999) "A new method for adiabatic flame temperature estimations of hydrocarbon fuels," *Fuel*, Vol. 78, pp. 471-478, 1999

**APPENDIX A      GAS CHROMATOGRAPH  
UNCERTAINTY**

## A.1 Overview

The gas chromatograph used to determine the fuel composition for the industrial RB211 was found to have an overall uncertainty of  $\pm 0.025$  mol fraction. In other words, this uncertainty would effect each molar concentration of the compounds within the fuel.

The molar concentrations can be used to determine the lower heating value of the fuel. Since it would be time consuming to determine the propagated uncertainty of these individual uncertainties as the calculation process involved is lengthy (Moran and Shapiro, 2004), a Monte Carlo simulation was performed.

## A.2 The Monte Carlo Method

Consider a shotgun being used to locate a target. Any number of shotgun shells is available with each shell containing several projectiles, with the total number of projectiles not exceeding, say, 1000. The shells can be in any configuration, ranging from one shell with 1000 projectiles to 1000 shells with one projectile each (Figure A.1).

Then, the shotgun is *vaguely aimed in the direction of the target* and fired.

The probability of a projectile hitting the target increases with the number of shells fired until it reaches a maximum. With a fixed supply of projectiles, increasing the number of shells would not be effective since the number of projectiles within each shell must decrease accordingly, and the time required to shoot the shells increases as well.

After comparing the number of projectiles that hit the target, the number that missed, and the aiming direction, the location of the target can be approximated. This, in essence, is the Monte Carlo method.

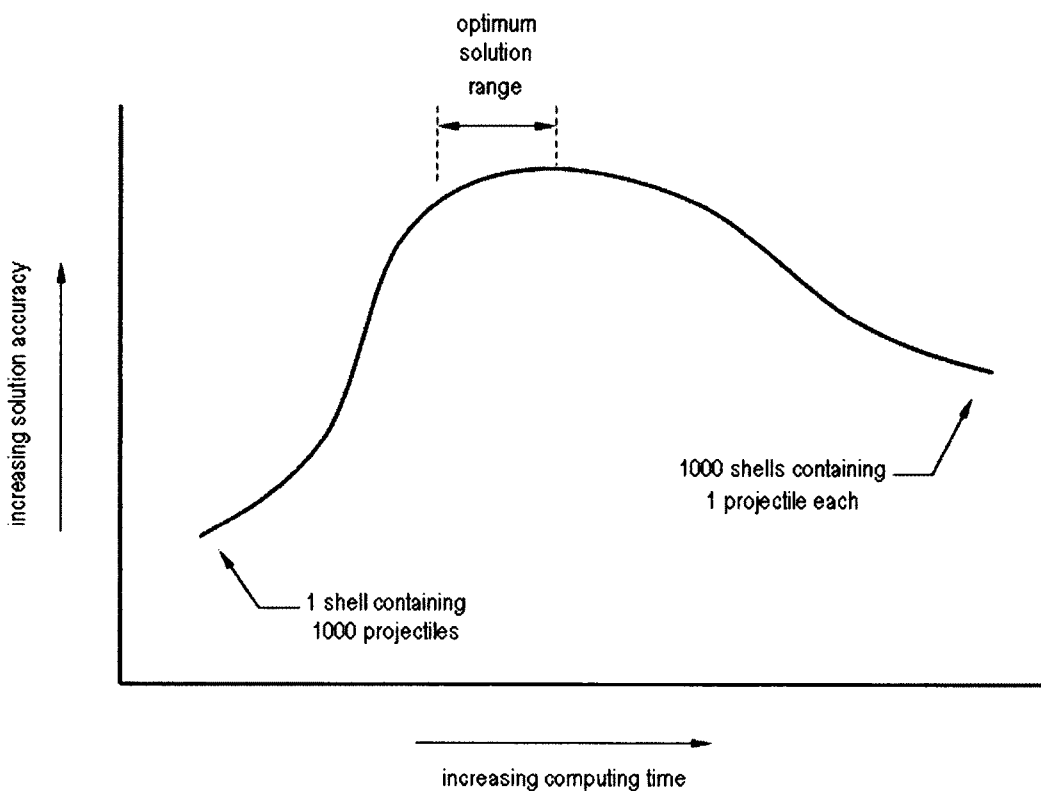


**Figure A.1** Dependency of solution accuracy with the number of guesses

In non-gun related applications of the Monte Carlo method, the 'shell' is referred to as a bundle, and the 'projectiles' are referred to as sub-bundles. For detailed discussions, the reader may refer to Modest (2003).

### A.3 Monte Carlo Simulation Result

A sample result of this simulation is presented in Figure A.2. Due to the random effects, the calculated uncertainty itself had an uncertainty of approximately  $\pm 0.1$  kJ/kg. Since a typical fuel lower heating value is in the order of  $10^4$  kJ/kg, the  $\pm 0.1$  kJ/kg uncertainty was neglected.

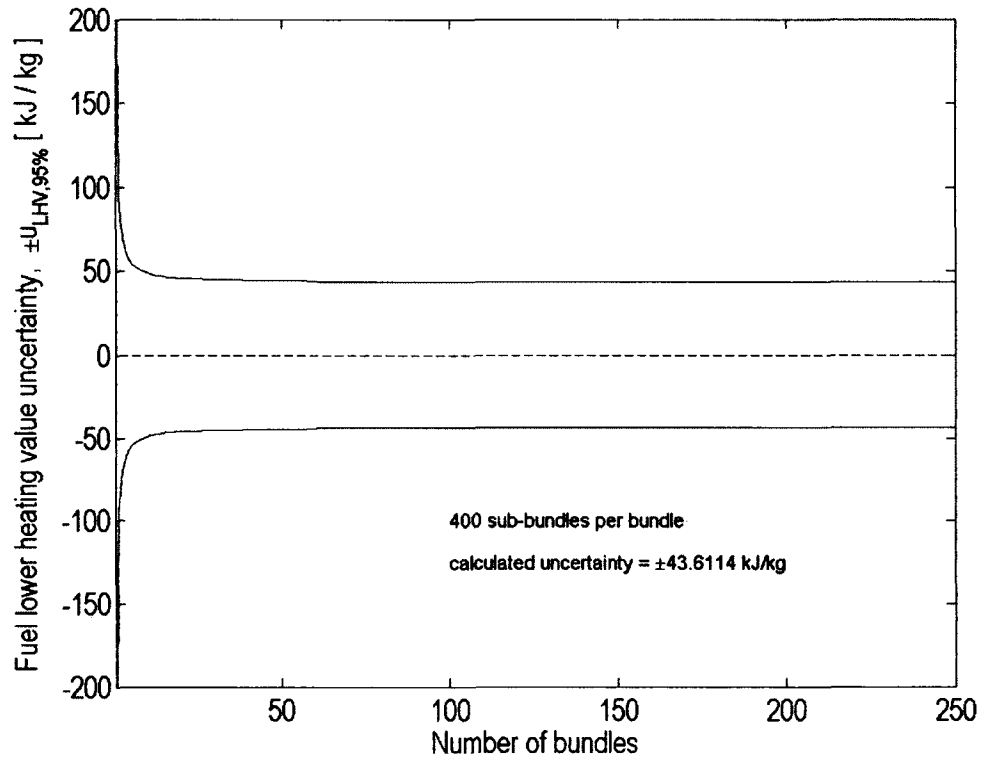


**Figure A.2** Propagated uncertainty of the fuel lower heating value

The reader is referred to Appendix F.1 for the Monte Carlo algorithm used to produce the results illustrated in Figure A.2.

**APPENDIX B      PROCESSING ANALYSIS  
RESULTS**

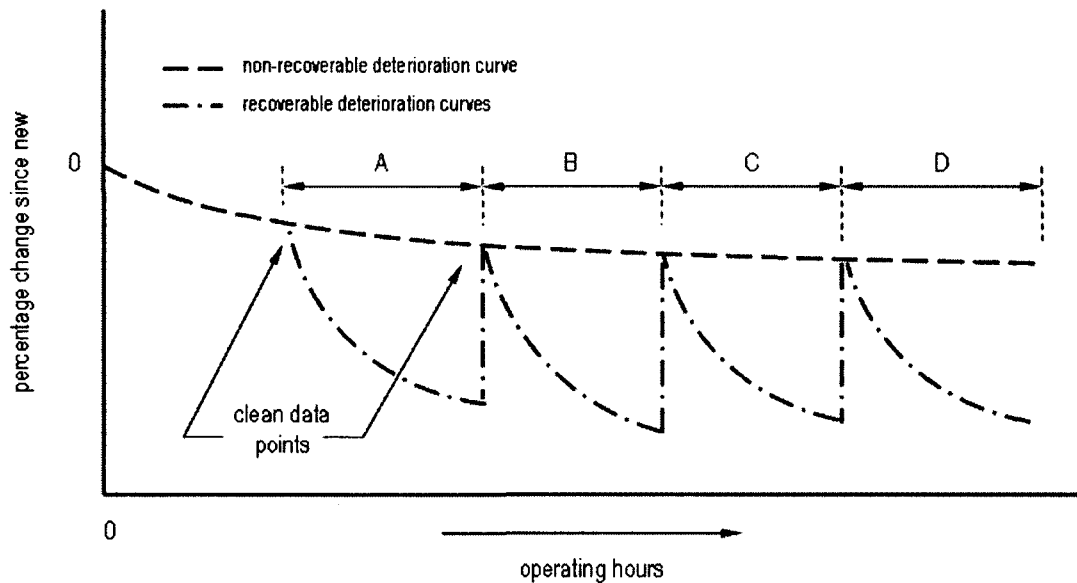


**Figure B.1** Typical deterioration curve of a performance parameter

A typical deterioration curve for a performance parameter, as output by Rolls-Royce's analysis program, is presented in Figure B.1. This is a highly simplified example with only four wash cycles.

This output needs to be conditioned such that two datasets, one containing only the recoverable deterioration and the other non-recoverable deterioration, is obtained.

The recoverable deterioration dataset shall be a function of hours since last wash and the non-recoverable deterioration dataset shall be a function of total operating hours. This allows the total deterioration at a given operating hour and a given hour since last wash to be determined by simply combining the corresponding deterioration factors from the two datasets.

Each of the recoverable deterioration curves A, B, C and D represents a single wash cycle. The first data point in a wash cycle was referred to as a clean data point since it only contains a given performance parameter's non-recoverable deterioration factor.

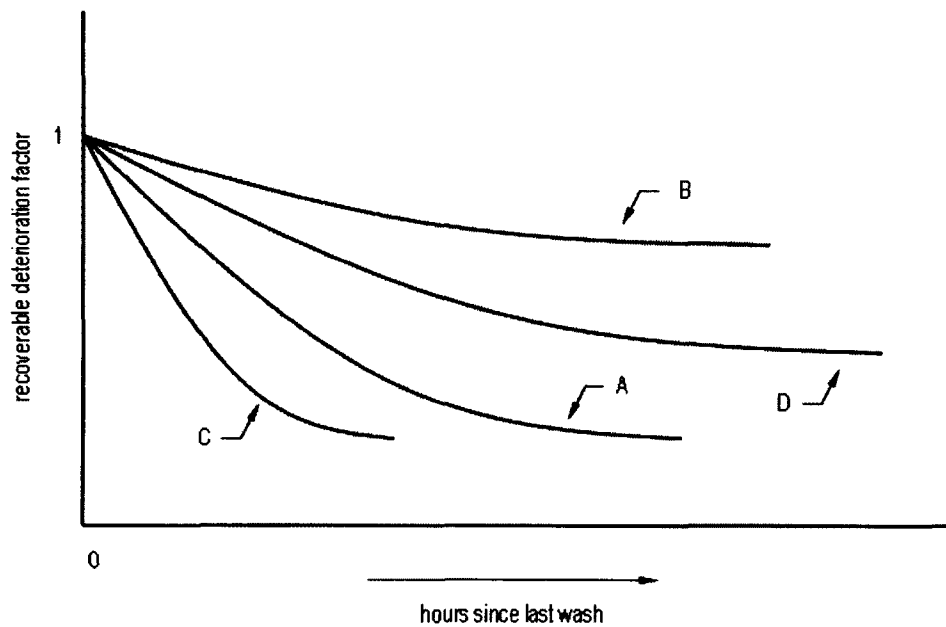


**Figure B.2** Initialized recoverable deterioration curves

It was found that the amount of non-recoverable deterioration occurring within two consecutive clean data points, i.e., a single wash cycle, to fall within the uncertainty margin of that performance parameter.

This allowed the recoverable deterioration curves to be simply initialized to their respective clean data points (Figure B.2).

The uncertainty of these curves is still the raw uncertainty, i.e., the uncertainty propagated directly from the measurement uncertainties. Each of these curves was then combined to produce a single *generalized* recoverable deterioration curve for that performance parameter (Figure B.3).

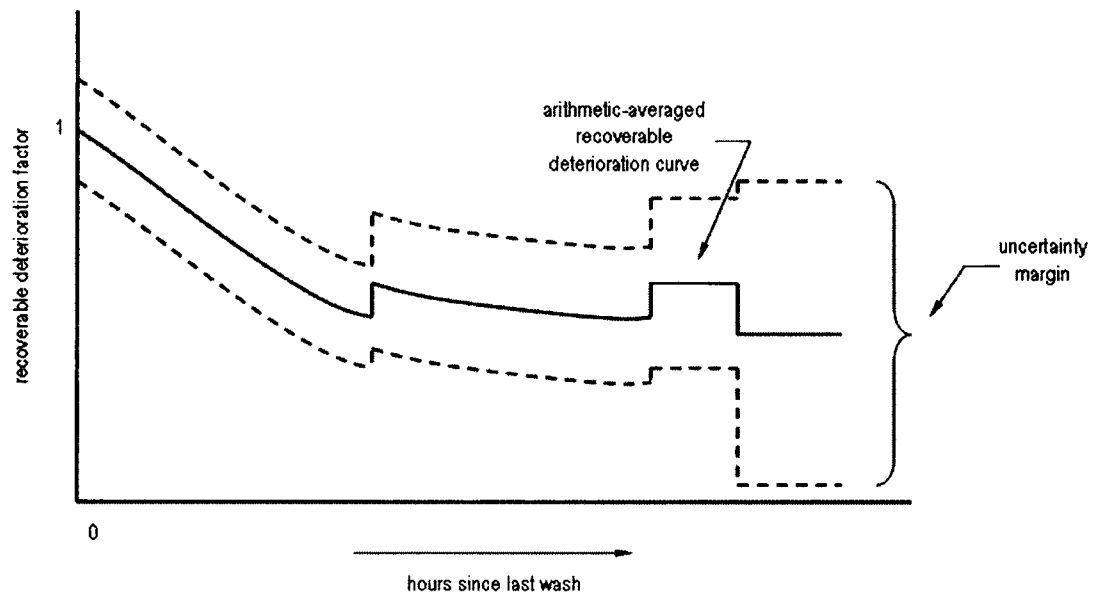


**Figure B.3** Arithmetic-averaged recoverable deterioration curve

A simple arithmetic average alone was found to be insufficient as none of the recoverable deterioration curves were of the same length. As can be seen in Figure B.3, this resulted in discontinuities in the generalized curve as well as the uncertainty margins, which was calculated by,

$$S_{\bar{x}})_{\text{intermediate}} = \frac{S_{x_{\text{raw}}}}{\sqrt{N}} \quad \text{B.1}$$

where  $S_{x_{\text{raw}}}$  is the raw uncertainty, and  $N$  is the number of recoverable deterioration curves of which the arithmetic average was taken.

The increasing intermediate uncertainty,  $S_{\bar{x}})_{\text{intermediate}}$ , with the hours since last wash was of no concern since a deterioration trend established in the early stages of fouling would carry through till the end of the wash cycle (Kurz and Brun, 2001).

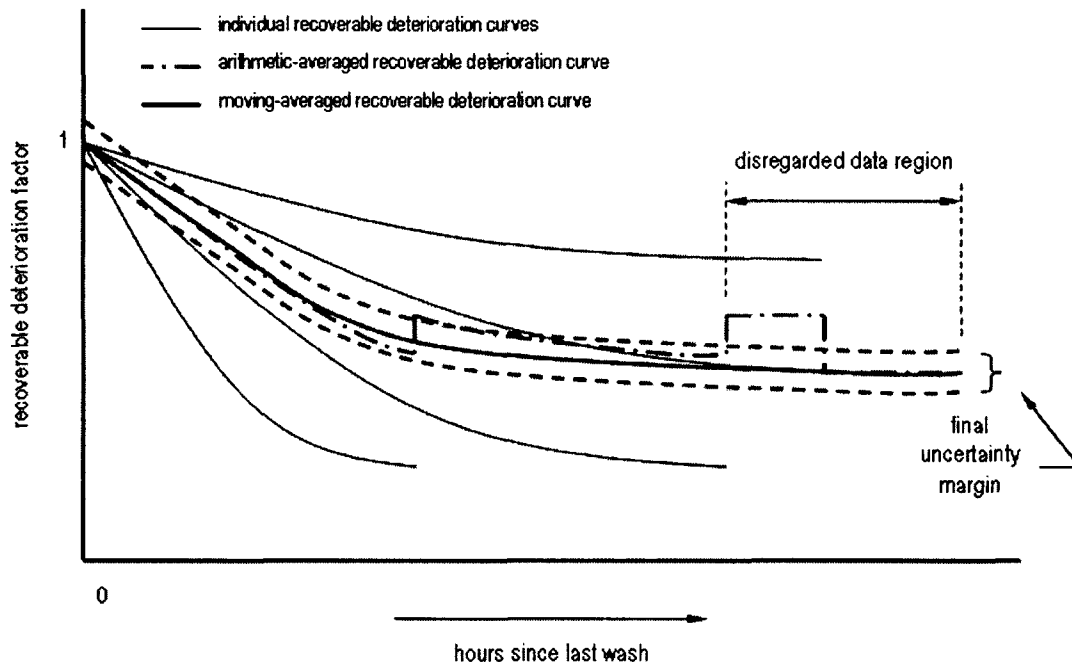


**Figure B.4** Refinement of analysis results

However, to further minimize the uncertainty, the latter portion of the arithmetic-averaged deterioration curve, where the only of a few deterioration curves contributed to the average (less than three), were disregarded (Figure B.4).

The discontinuities and the magnitudes of these intermediate uncertainties were still found to be unsatisfactory. Therefore, a single intermediate uncertainty for a given arithmetic-averaged recoverable deterioration curve was deemed necessary to further process the data.

This new intermediate uncertainty was calculated by taking the weighted average of the individual intermediate uncertainties. A weighted averaging process was chosen since this puts more emphasis on the uncertainties of the regions which were derived from many individual recoverable deterioration curves.

Then, only the discontinuities of the arithmetic-averaged recoverable deterioration curve were required to be addressed. It was observed that the amount of recoverable deterioration occurring within a relatively small time span would exist within the intermediate uncertainty margins. Therefore, a forward-backward moving average of 101 data points was taken of the arithmetic-averaged curve (Figure B.4).

In addition to smoothing the discontinuities, this moving average further reduced the uncertainty of the resulting deterioration curve to,

$$S_{\bar{x}})_{\text{evolved}} = t_{95\%, N=101} \frac{S_{\bar{x}})_{\text{intermediate}}}{\sqrt{101}} \quad \text{B.2}$$

where  $S_{\bar{x}})_{\text{evolved}}$  is the 2-sigma uncertainty margin of 95% confidence and  $t_{95\%, 101}$  is the Student t-distribution for the 95% confidence margin.

## **APPENDIX C      SENSITIVITY ANALYSIS**

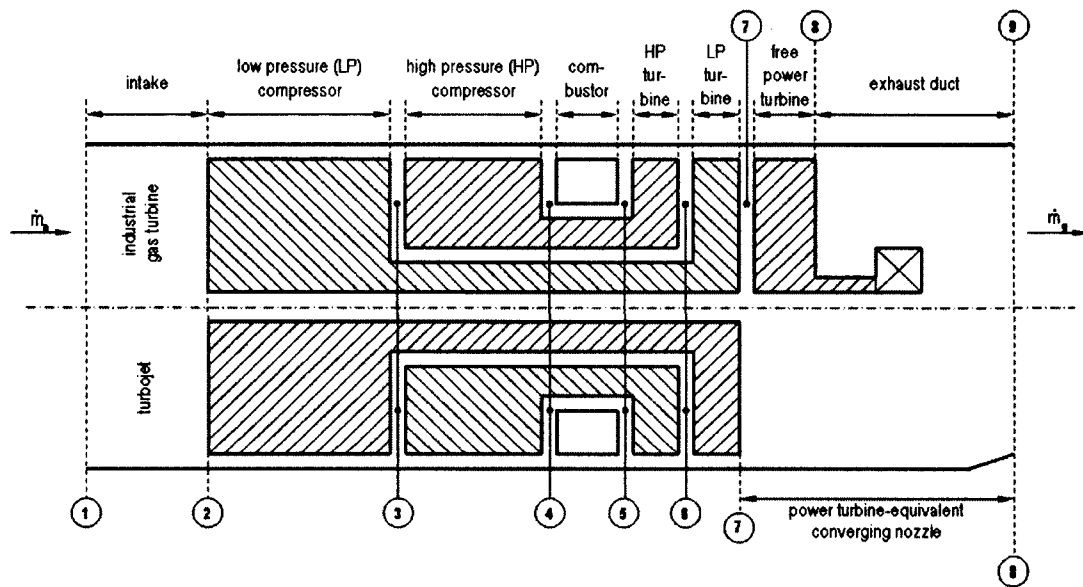


**Figure C.1** Two-spool gas generator with a free power turbine

## C.1 Overview

This section provides the equations that represent the sensitivities of compressor and turbine efficiencies, compressor flow capacities and the core bleed flow. These equations were used to determine the raw uncertainties.

Figure C.1 displays a schematic of the two-spool gas generator with a free power turbine – the stage numbering convention of which is used in this section.

The gas turbine performance equations, from which the presented equations are derived, are given by Saravanamuttoo et al. (2001). A method of converting the isentropic efficiency uncertainties to polytropic efficiency uncertainties is also presented.

First, the method by which the estimated fuel flow rate,  $\dot{m}_f$ , is calculated is briefly discussed after which its propagated uncertainty is calculated.

## C.2 Estimated Fuel Flow Rate

The engine control system of the industrial RB211 estimates the required fuel flow rate using,

$$f = \frac{c_{pg} T_{o5} - c_{pa} T_{o4}}{\eta_B Q}, \text{ with } f = \frac{\dot{m}_f}{\dot{m}_a} \quad \text{C.2.1}$$

where  $f$  is the fuel-to-air ratio,  $\dot{m}_a$  is the inlet mass flow rate,  $T_{o4}$  is the HP compressor outlet temperature,  $T_{o5}$  is the HP turbine inlet temperature,  $Q$  is the lower fuel heating value, and  $\eta_B$  is the combustion efficiency. The uncertainty of the estimated fuel flow,  $u_{\dot{m}_f}$ , can then be calculated by,

$$u_f = \sqrt{\left(\frac{\delta f}{\delta T_{o4}} u_{T_{o4}}\right)^2 + \left(\frac{\delta f}{\delta Q} u_Q\right)^2} \quad \text{C.2.2}$$

where,

$$\frac{\delta f}{\delta T_{o4}} = -\frac{c_{pa}}{\eta_B Q} \quad \text{C.2.3}$$

$$\frac{\delta f}{\delta Q} = \frac{c_{pa} T_{o4} - c_{pg} T_{o5}}{\eta_B Q} \quad \text{C.2.4}$$

This gives a fuel-to-air ratio uncertainty,  $u_f$ , of  $\pm 5.278 \times 10^{-6}$ . Since at design-point,  $\dot{m}_a = 91.2$  kg/sec, the uncertainty of the estimated fuel flow rate,  $u_{\dot{m}_f}$ , was found to be  $\pm 0.005$  kg/sec.

### C.3 LP Compressor Isentropic Efficiency

The raw uncertainty of the LP compressor isentropic efficiency,  $u_{\eta_{LPC}}$ , was found by,

$$u_{\eta_{LPC}} = \sqrt{\left(\frac{\delta\eta_{LPC}}{\delta T_{o2}} u_{T_{o2}}\right)^2 + \left(\frac{\delta\eta_{LPC}}{\delta P_{o2}} u_{P_{o2}}\right)^2 + \left(\frac{\delta\eta_{LPC}}{\delta T_{o3}} u_{T_{o3}}\right)^2 + \left(\frac{\delta\eta_{LPC}}{\delta P_{o3}} u_{P_{o3}}\right)^2} \quad C.3.1$$

where,

$$T_{o3} - T_{o2} = \frac{T_{o2}}{\eta_{LPC}} \left[ \left( \frac{P_{o3}}{P_{o2}} \right)^{\frac{\gamma-1}{\gamma}} - 1 \right] \quad C.3.2$$

$$\frac{\delta\eta_{LPC}}{\delta T_{o2}} = \frac{T_{o3} \left[ \left( \frac{P_{o3}}{P_{o2}} \right)^{\frac{\gamma-1}{\gamma}} - 1 \right]}{(T_{o3} - T_{o2})^2} \quad C.3.3$$

$$\frac{\delta\eta_{LPC}}{\delta T_{o3}} = - \frac{T_{o2} \left[ \left( \frac{P_{o3}}{P_{o2}} \right)^{\frac{\gamma-1}{\gamma}} - 1 \right]}{(T_{o3} - T_{o2})^2} \quad C.3.4$$

$$\frac{\delta\eta_{LPC}}{\delta P_{o2}} = - \frac{\frac{\gamma-1}{\gamma} \frac{P_{o3}}{P_{o2}^2} \left( \frac{P_{o3}}{P_{o2}} \right)^{\frac{\gamma-1}{\gamma}}}{\frac{T_{o3}}{T_{o2}} - 1} \quad C.3.5$$

$$\frac{\delta\eta_{LPC}}{\delta P_{o3}} = \frac{\frac{\gamma-1}{\gamma} \frac{1}{P_{o2}} \left( \frac{P_{o3}}{P_{o2}} \right)^{\frac{\gamma-1}{\gamma}}}{\frac{T_{o3}}{T_{o2}} - 1} \quad C.3.6$$

## C.4 HP Compressor Isentropic Efficiency

The raw uncertainty of the HP compressor isentropic efficiency,  $u_{\eta_{\text{HPC}}}$ , was found by,

$$u_{\eta_{\text{HPC}}} = \sqrt{\left(\frac{\delta\eta_{\text{HPC}}}{\delta T_{03}} u_{T_{03}}\right)^2 + \left(\frac{\delta\eta_{\text{HPC}}}{\delta P_{03}} u_{P_{03}}\right)^2 + \left(\frac{\delta\eta_{\text{HPC}}}{\delta T_{04}} u_{T_{04}}\right)^2} \quad \text{C.4.1}$$

where,

$$T_{04} - T_{03} = \frac{T_{03}}{\eta_{\text{HPC}}} \left[ \left( \frac{P_{04}}{P_{03}} \right)^{\frac{\gamma-1}{\gamma}} - 1 \right] \quad \text{C.4.2}$$

$$\frac{\delta\eta_{\text{HPC}}}{\delta T_{03}} = \frac{T_{04} \left[ \left( \frac{P_{04}}{P_{03}} \right)^{\frac{\gamma-1}{\gamma}} - 1 \right]}{(T_{04} - T_{03})^2} \quad \text{C.4.3}$$

$$\frac{\delta\eta_{\text{HPC}}}{\delta T_{04}} = - \frac{T_{03} \left[ \left( \frac{P_{04}}{P_{03}} \right)^{\frac{\gamma-1}{\gamma}} - 1 \right]}{(T_{04} - T_{03})^2} \quad \text{C.4.4}$$

$$\frac{\delta\eta_{\text{HPC}}}{\delta P_{03}} = - \frac{\frac{\gamma-1}{\gamma} \frac{P_{04}}{P_{03}^2} \left( \frac{P_{04}}{P_{03}} \right)^{\frac{\gamma-1}{\gamma}}}{\frac{T_{03}}{T_{04}} - 1} \quad \text{C.4.5}$$

## C.5 HP Turbine Isentropic Efficiency

The raw uncertainty of the HP turbine isentropic efficiency,  $u_{\eta_{\text{HPT}}}$ , was found by,

$$u_{\eta_{\text{HPT}}} = \sqrt{\left(\frac{\delta\eta_{\text{HPT}}}{\delta T_{o4}} u_{T_{o4}}\right)^2 + \left(\frac{\delta\eta_{\text{HPT}}}{\delta \dot{m}_f} u_{\dot{m}_f}\right)^2} \quad \text{C.5.1}$$

These sensitivities were obtained from the Jacobian of the non-linear gas path analysis program used by Rolls-Royce. Only These sensitivities are used since these are of the two *measured* parameters that have a direct effect on the HP turbine efficiency. The same is true for the efficiency of the LP turbine.

## C.6 LP Turbine Isentropic Efficiency

The raw uncertainty of the LP turbine isentropic efficiency,  $u_{\eta_{\text{LPT}}}$ , was found by,

$$u_{\eta_{\text{LPT}}} = \sqrt{\left(\frac{\delta\eta_{\text{LPT}}}{\delta T_{o4}} u_{T_{o4}}\right)^2 + \left(\frac{\delta\eta_{\text{LPT}}}{\delta \dot{m}_f} u_{\dot{m}_f}\right)^2} \quad \text{C.6.1}$$

These sensitivities were obtained from the Jacobian of the non-linear gas path analysis program used by Rolls-Royce.

## C.7 Power Turbine Isentropic Efficiency

The raw uncertainty of the power turbine isentropic efficiency,  $u_{\eta_{PT}}$ , was found by,

$$u_{\eta_{PT}} = \sqrt{\left(\frac{\delta\eta_{PT}}{\delta T_{o4}} u_{T_{o4}}\right)^2 + \left(\frac{\delta\eta_{PT}}{\delta \dot{m}_f} u_{\dot{m}_f}\right)^2 + \left(\frac{\delta\eta_{PT}}{\delta T_{o7}} u_{T_{o7}}\right)^2} \quad \text{C.7.1}$$

$\frac{\delta\eta_{PT}}{\delta T_{o7}}$  is the power turbine efficiency's sensitivity to the LP turbine outlet temperature,  $T_{o7}$ .

These sensitivities were obtained from the Jacobian of the non-linear gas path analysis program used by Rolls-Royce.

## C.8 LP Compressor Capacity

For a compressor or a turbine, the term capacity refers to that component's relative mass flow rate. For the LP compressor, its capacity,  $\Gamma_{LPC}$ , is,

$$\Gamma_{LPC} = \frac{\dot{m}_2}{\dot{m}_2}_{des} \quad \text{C.8.1}$$

where  $\dot{m}_2$  is the LP compressor inlet mass flow rate and the subscript 'des' denotes the design-point condition.

Since  $\dot{m}_2$  can be calculated from,

$$\dot{m}_2 \approx \frac{\dot{m}_2 \sqrt{T_{o1}}}{P_{o1}} \frac{P_{o1}}{\sqrt{T_{o1}}} \quad \text{C.8.2}$$

the uncertainties in these measurements of  $P_{o1}$  and  $T_{o1}$  will be propagated into the uncertainty of  $\Gamma_{LPC}$ , i.e.,  $u_{\Gamma_{LPC}}$ , which can be calculated by,

$$u_{\Gamma_{LPC}} = \frac{u_{\dot{m}_2}}{(\dot{m}_2)_{des}} \quad \text{C.8.3}$$

where,

$$u_{\dot{m}_2} = \sqrt{\left( \frac{\delta \dot{m}_2}{\delta T_{o1}} u_{T_{o1}} \right)^2 + \left( \frac{\delta \dot{m}_2}{\delta P_{o1}} u_{P_{o1}} \right)^2} \quad \text{C.8.4}$$

$$\frac{\delta \dot{m}_2}{\delta T_{o1}} = \frac{1}{2} \frac{\dot{m}_2 \sqrt{T_{o1}}}{P_{o1}} \frac{P_{o1}}{T_{o1}^{3/2}} \quad \text{C.8.5}$$

$$\frac{\delta \dot{m}_2}{\delta P_{o1}} = \frac{\dot{m}_2 \sqrt{T_{o1}}}{P_{o1}} \frac{1}{\sqrt{T_{o1}}} \quad \text{C.8.6}$$

## C.9 HP Compressor Capacity

Similar to the LP compressor capacity, the uncertainty of the HP compressor capacity,  $u_{\Gamma\_HPC}$ , was found by,

$$u_{\Gamma\_HPC} = \frac{u_{\dot{m}_3}}{\dot{m}_3)_{des}} \quad C.9.1$$

Here,  $\dot{m}_3$  is the compressor inlet mass flow rate, and,

$$u_{\dot{m}_3} = \sqrt{\left(\frac{\delta\dot{m}_3}{\delta T_{o3}} u_{T_{o3}}\right)^2 + \left(\frac{\delta\dot{m}_3}{\delta P_{o3}} u_{P_{o3}}\right)^2} \quad C.9.2$$

$$\frac{\delta\dot{m}_3}{\delta T_{o3}} = \frac{1}{2} \frac{\dot{m}_3 \sqrt{T_{o3}}}{P_{o3}} \frac{P_{o3}}{T_{o3}^{\frac{3}{2}}} \quad C.9.3$$

$$\frac{\delta\dot{m}_3}{\delta P_{o3}} = \frac{\dot{m}_3 \sqrt{T_{o3}}}{P_{o3}} \frac{1}{\sqrt{T_{o3}}} \quad C.9.4$$

## C.10 Core Bleed Flow

The raw uncertainty of the core bleed flow,  $u_{\beta}$ , was found by,

$$u_{\beta} = \sqrt{\left(\frac{\delta\beta}{\delta T_{o4}} u_{T_{o4}}\right)^2 + \left(\frac{\delta\beta}{\delta \dot{m}_f} u_{\dot{m}_f}\right)^2} \quad \text{C.10.1}$$

These sensitivities were obtained from the Jacobian of the non-linear gas path analysis program used by Rolls-Royce.

## C.11 Polytropic Compressor Efficiencies

The polytropic and isentropic efficiencies of the LP compressor,  $\eta_{\infty\text{LPC}}$  and  $\eta_{\text{LPC}}$ , respectively, are related by,

$$\eta_{\infty\text{LPC}} = \frac{\frac{\gamma-1}{\gamma} \ln \frac{P_{o3}}{P_{o2}}}{\ln \frac{\left(\frac{P_{o3}}{P_{o2}}\right)^{\frac{\gamma-1}{\gamma}} - 1}{\eta_{\text{LPC}}} + 1} \quad \text{C.11.1}$$

Then, the LP compressor polytropic efficiency uncertainty can be calculated using,

$$u_{\eta_{\infty\text{LPC}}} = \frac{\delta\eta_{\infty\text{LPC}}}{\delta\eta_{\text{LPC}}} u_{\eta_{\text{LPC}}} \quad \text{C.11.2}$$

where,

$$\frac{\delta\eta_{\infty\text{LPC}}}{\delta\eta_{\text{LPC}}} = \frac{AB}{\eta_{\text{LPC}}(B + \eta_{\text{LPC}})} \left( \ln \frac{B + \eta_{\text{LPC}}}{\eta_{\text{LPC}}} \right)^{-2} \quad \text{C.11.3}$$

$$A = \frac{\gamma - 1}{\gamma} \ln \frac{P_{o3}}{P_{o2}} \quad \text{C.11.4}$$

$$B = \left( \frac{P_{o3}}{P_{o2}} \right)^{\frac{\gamma-1}{\gamma}} - 1 \quad \text{C.11.5}$$

Similarly, the HP compressor polytropic efficiency uncertainty can be calculated using,

$$u_{\eta_{\infty\text{HPC}}} = \frac{\delta\eta_{\infty\text{HPC}}}{\delta\eta_{\text{HPC}}} u_{\eta_{\text{HPC}}} \quad \text{C.11.6}$$

where,

$$\frac{\delta\eta_{\infty\text{HPC}}}{\delta\eta_{\text{HPC}}} = \frac{AB}{\eta_{\text{HPC}}(B + \eta_{\text{HPC}})} \left( \ln \frac{B + \eta_{\text{HPC}}}{\eta_{\text{HPC}}} \right)^{-2} \quad \text{C.11.7}$$

$$A = \frac{\gamma - 1}{\gamma} \ln \frac{P_{o4}}{P_{o3}} \quad \text{C.11.8}$$

$$B = \left( \frac{P_{o4}}{P_{o3}} \right)^{\frac{\gamma-1}{\gamma}} - 1 \quad \text{C.11.9}$$

## C.12 Polytropic Turbine Efficiencies

The polytropic and isentropic efficiencies of the HP turbine,  $\eta_{\infty\text{HPT}}$  and  $\eta_{\text{HPT}}$ , respectively, are related by,

$$\eta_{\infty\text{HPT}} = \frac{\gamma}{\gamma-1} \frac{\ln \left\{ 1 - \eta_{\text{HPT}} \left[ 1 - \left( \frac{P_{06}}{P_{05}} \right)^{\frac{\gamma-1}{\gamma}} \right] \right\}}{\ln \frac{P_{06}}{P_{05}}} \quad \text{C.12.1}$$

Then, the HP turbine polytropic efficiency uncertainty can be calculated using,

$$u_{\eta_{\infty\text{HPT}}} = \frac{\delta \eta_{\infty\text{HPT}}}{\delta \eta_{\text{HPT}}} u_{\eta_{\text{HPT}}} \quad \text{C.12.2}$$

where,

$$\frac{\delta \eta_{\infty\text{HPT}}}{\delta \eta_{\text{HPT}}} = - \frac{A B}{1 - B \eta_{\text{HPT}}} \quad \text{C.12.3}$$

$$A = \frac{\gamma}{\gamma-1} \left( \ln \frac{P_{06}}{P_{05}} \right)^{-1} \quad \text{C.12.4}$$

$$B = 1 - \left( \frac{P_{06}}{P_{05}} \right)^{\frac{\gamma-1}{\gamma}} \quad \text{C.12.5}$$

Similarly, the LP turbine polytropic efficiency uncertainty can be calculated using,

$$u_{\eta_{\infty\_LPT}} = \frac{\delta\eta_{\infty\_LPT}}{\delta\eta_{LPT}} u_{\eta_{LPT}} \quad \text{C.12.6}$$

where,

$$\frac{\delta\eta_{\infty\_LPT}}{\delta\eta_{LPT}} = -\frac{AB}{1 - B\eta_{LPT}} \quad \text{C.12.7}$$

$$A = \frac{\gamma}{\gamma - 1} \left( \ln \frac{P_{o7}}{P_{o6}} \right)^{-1} \quad \text{C.12.8}$$

$$B = 1 - \left( \frac{P_{o7}}{P_{o6}} \right)^{\frac{\gamma - 1}{\gamma}} \quad \text{C.12.9}$$

Finally, the power turbine polytropic efficiency uncertainty can be calculated using,

$$u_{\eta_{\infty\_PT}} = \frac{\delta\eta_{\infty\_PT}}{\delta\eta_{PT}} u_{\eta_{PT}} \quad \text{C.12.10}$$

where,

$$\frac{\delta\eta_{\infty\_PT}}{\delta\eta_{PT}} = -\frac{AB}{1 - B\eta_{PT}} \quad \text{C.12.11}$$

$$A = \frac{\gamma}{\gamma - 1} \left( \ln \frac{P_{o8}}{P_{o7}} \right)^{-1} \quad \text{C.12.12}$$

$$B = 1 - \left( \frac{P_{o8}}{P_{o7}} \right)^{\frac{\gamma - 1}{\gamma}} \quad \text{C.12.13}$$

### C.13 Uncertainties of the Recoverable Deterioration Factors

This section contains the plots of the recoverable deterioration factors. Table C.1 contains the uncertainties.

**Table C.1** Uncertainties of the recoverable deterioration factors

Variable	Raw uncertainties [%]	Evolved uncertainties [%]		
		GT1	GT2	GT3
$\eta_{LPC}$	$\pm 2.37$	$\pm 0.252$	$\pm 0.332$	$\pm 0.524$
$\eta_{\infty LPC}$	$\pm 1.92$	$\pm 0.204$	$\pm 0.269$	$\pm 0.424$
$\eta_{HPC}$	$\pm 2.34$	$\pm 0.249$	$\pm 0.328$	$\pm 0.517$
$\eta_{\infty HPC}$	$\pm 2.00$	$\pm 0.212$	$\pm 0.281$	$\pm 0.442$
$\eta_{HPT}$	$\pm 0.465$	$\pm 0.0494$	$\pm 0.0652$	$\pm 0.103$
$\eta_{\infty HPT}$	$\pm 0.508$	$\pm 0.054$	$\pm 0.0713$	$\pm 0.112$
$\eta_{LPT}$	$\pm 0.747$	$\pm 0.0794$	$\pm 0.105$	$\pm 0.165$
$\eta_{\infty LPT}$	$\pm 0.795$	$\pm 0.0845$	$\pm 0.112$	$\pm 0.176$
$\eta_{PT}$	$\pm 6.64$	$\pm 0.705$	$\pm 0.931$	$\pm 1.47$
$\eta_{\infty PT}$	$\pm 7.43$	$\pm 0.789$	$\pm 1.04$	$\pm 1.64$
$\Gamma_{LPC}$	$\pm 0.337$	$\pm 0.0358$	$\pm 0.0473$	$\pm 0.0745$
$\Gamma_{HPC}$	$\pm 0.624$	$\pm 0.0663$	$\pm 0.0875$	$\pm 0.138$
$\beta$	$\pm 1.148$	$\pm 0.122$	$\pm 0.161$	$\pm 0.254$

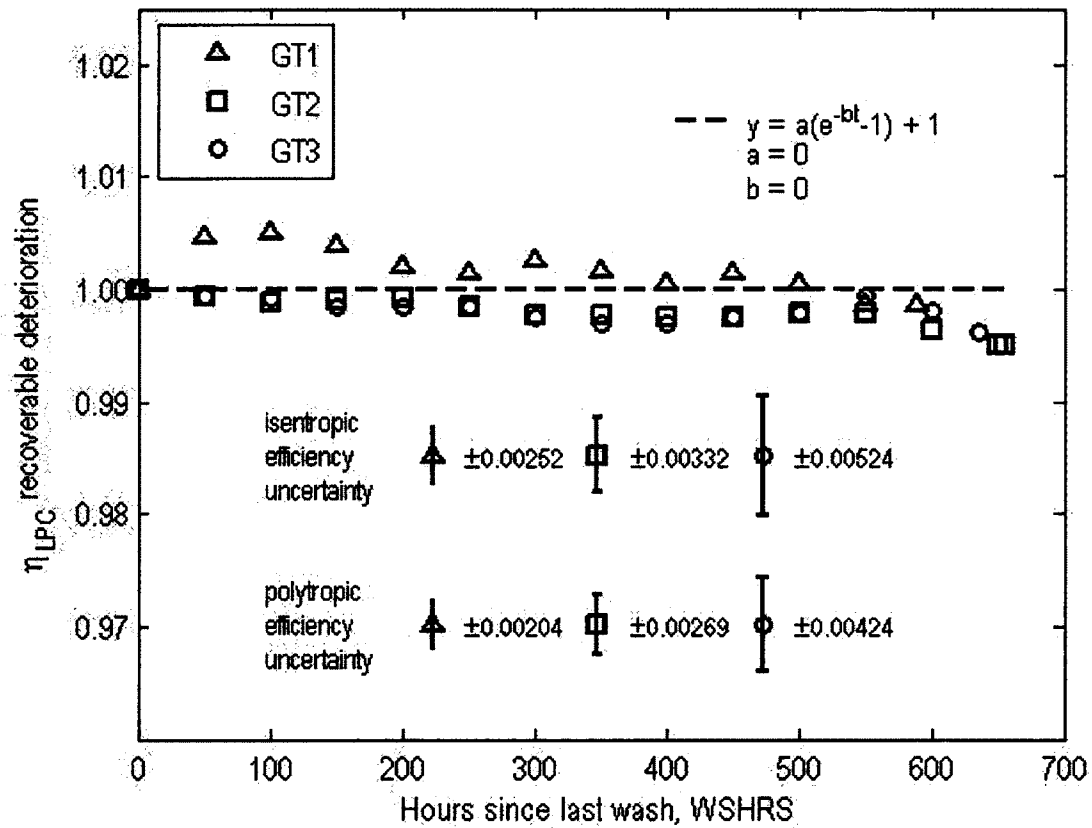


**Figure C.2** Recoverable deterioration factor of the LP compressor efficiency

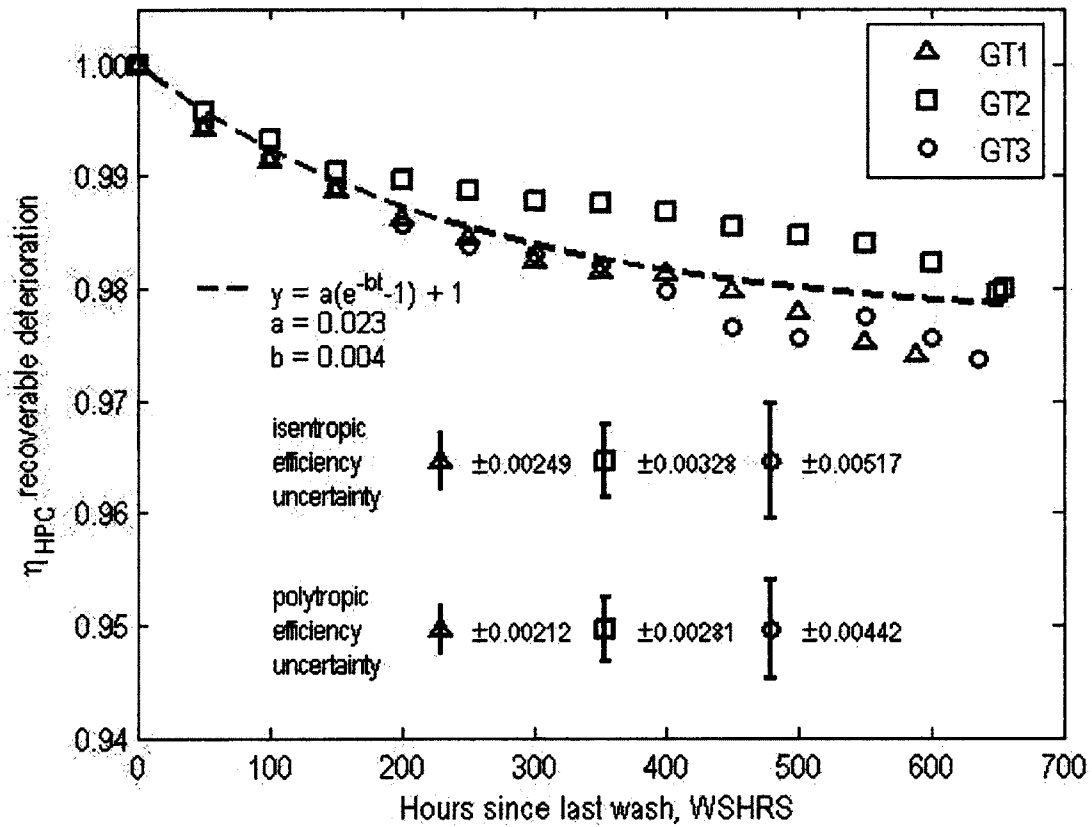


Figure C.3 Recoverable deterioration factor of the HP compressor efficiency

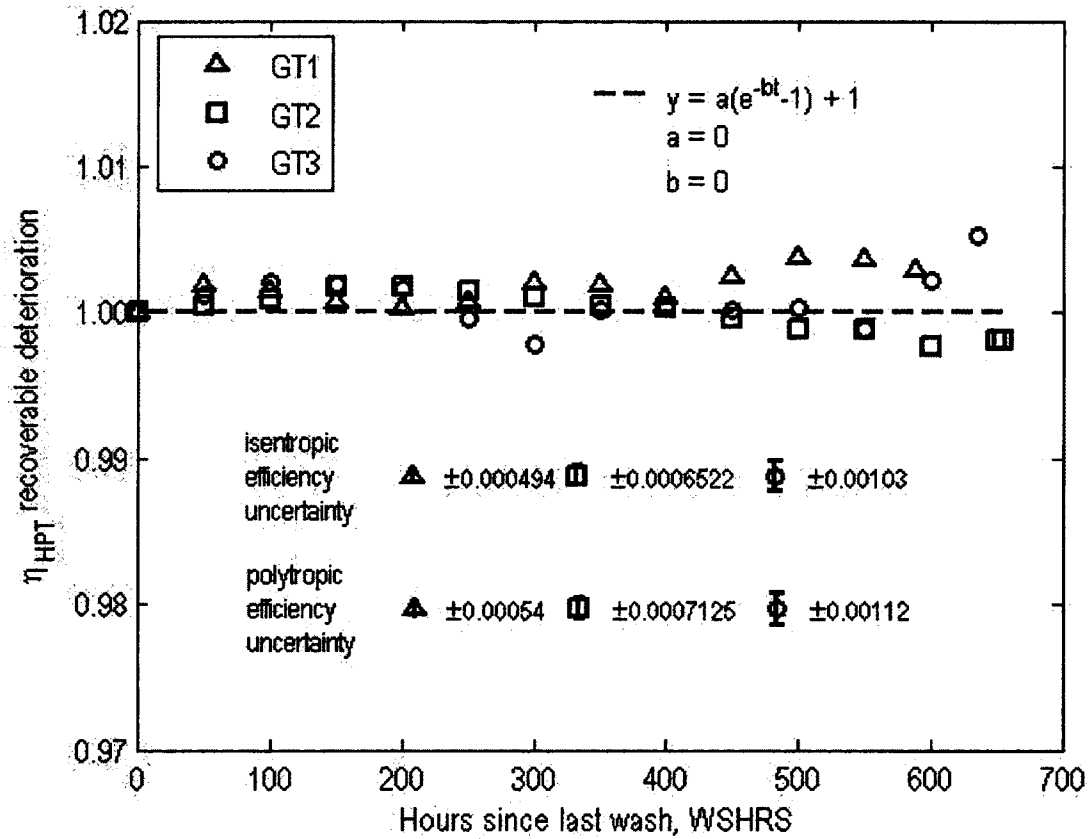


Figure C.4 Recoverable deterioration factor of the HP turbine efficiency

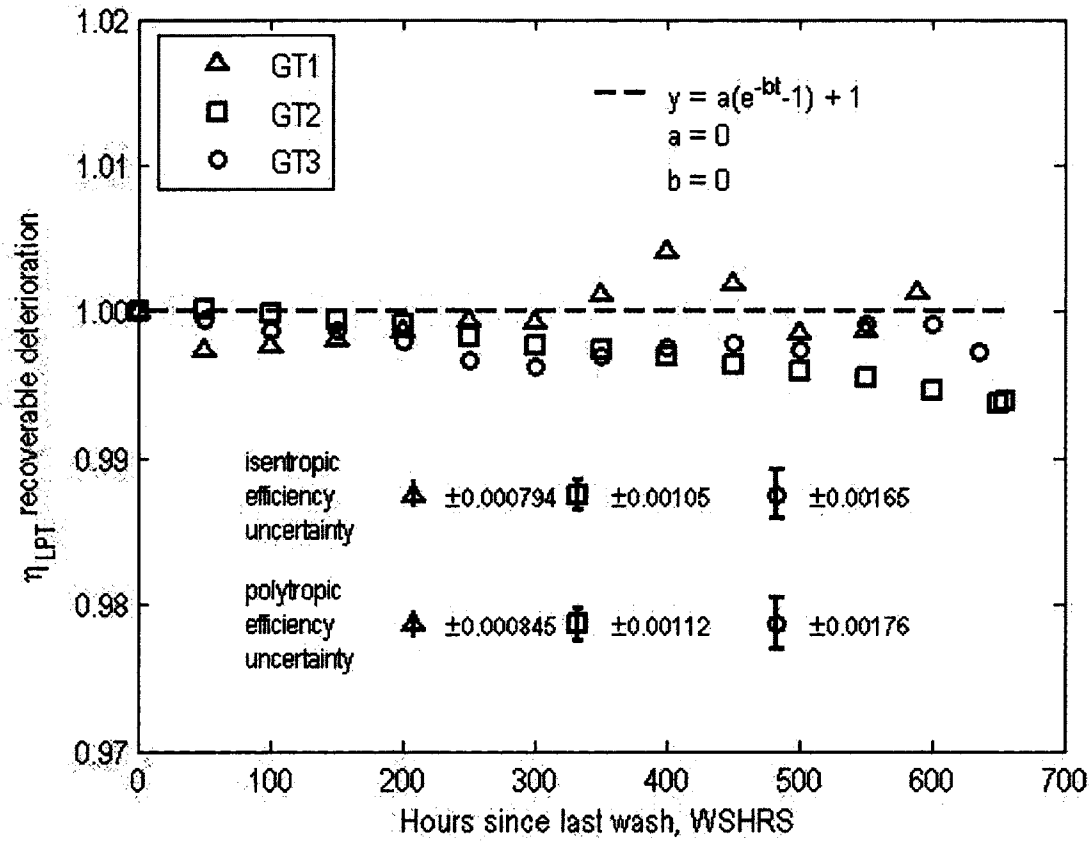


Figure C.5 Recoverable deterioration factor of the LP turbine efficiency

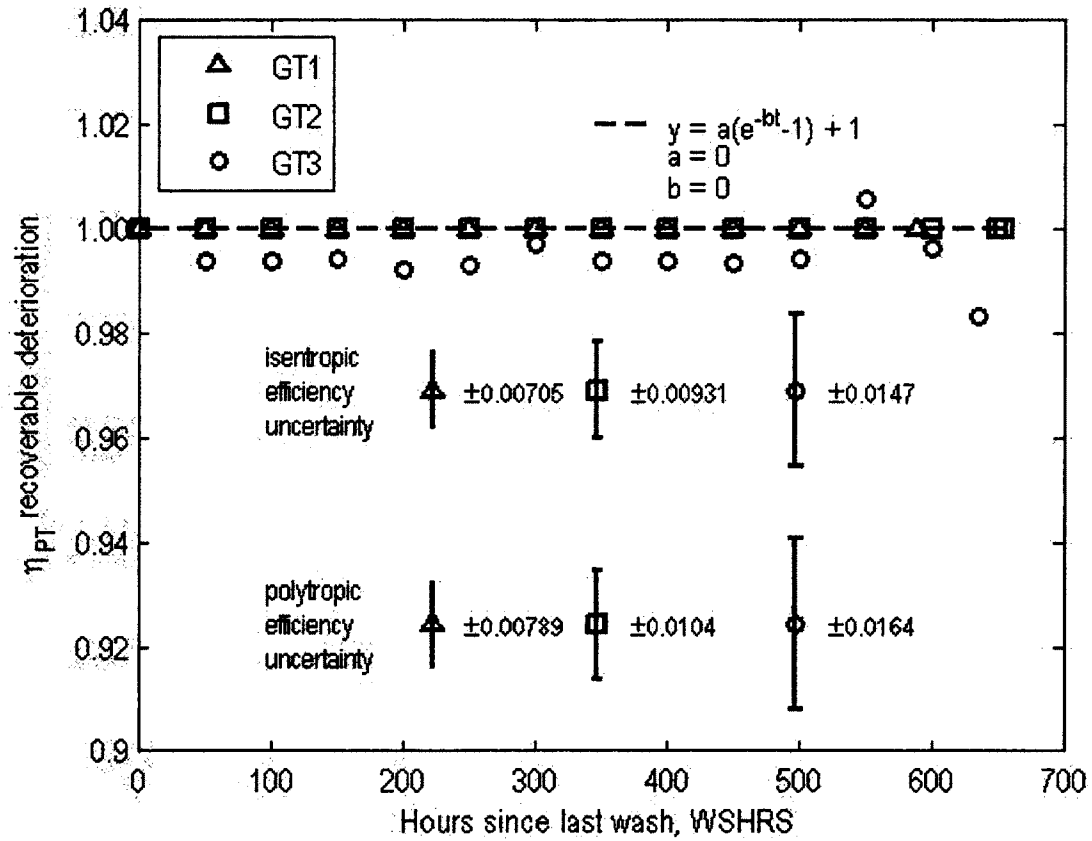


Figure C.6 Recoverable deterioration factor of the power turbine efficiency

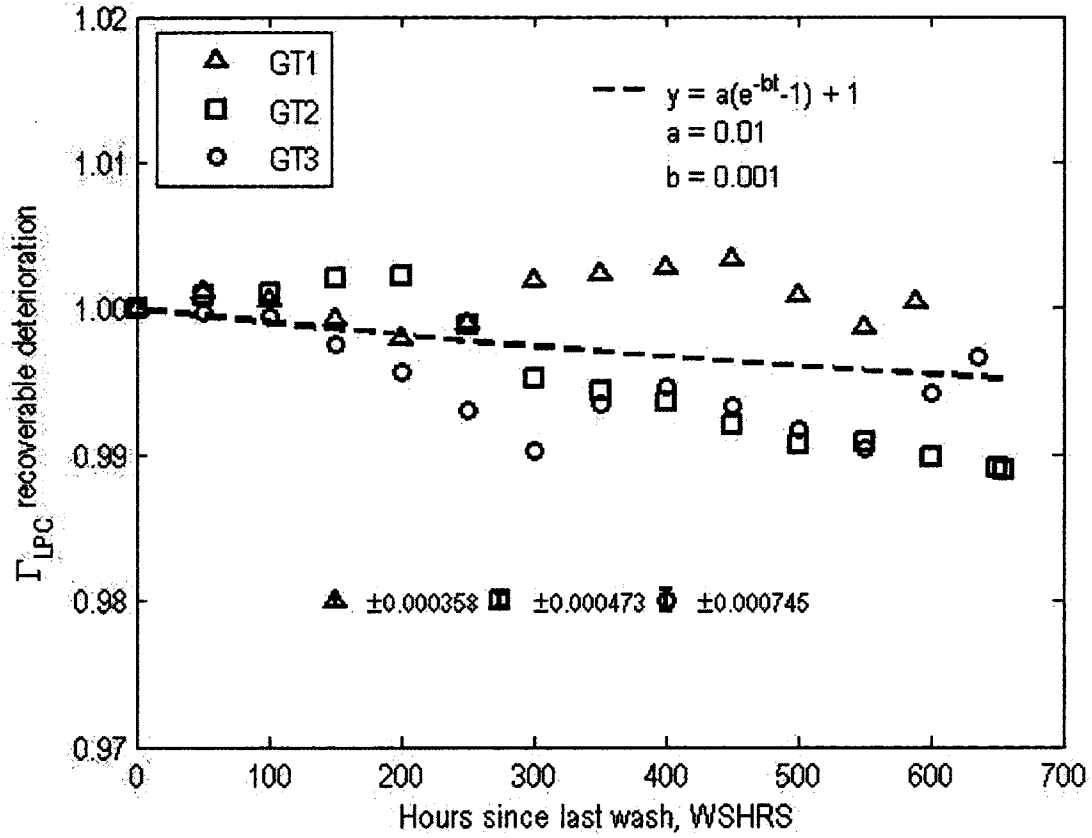
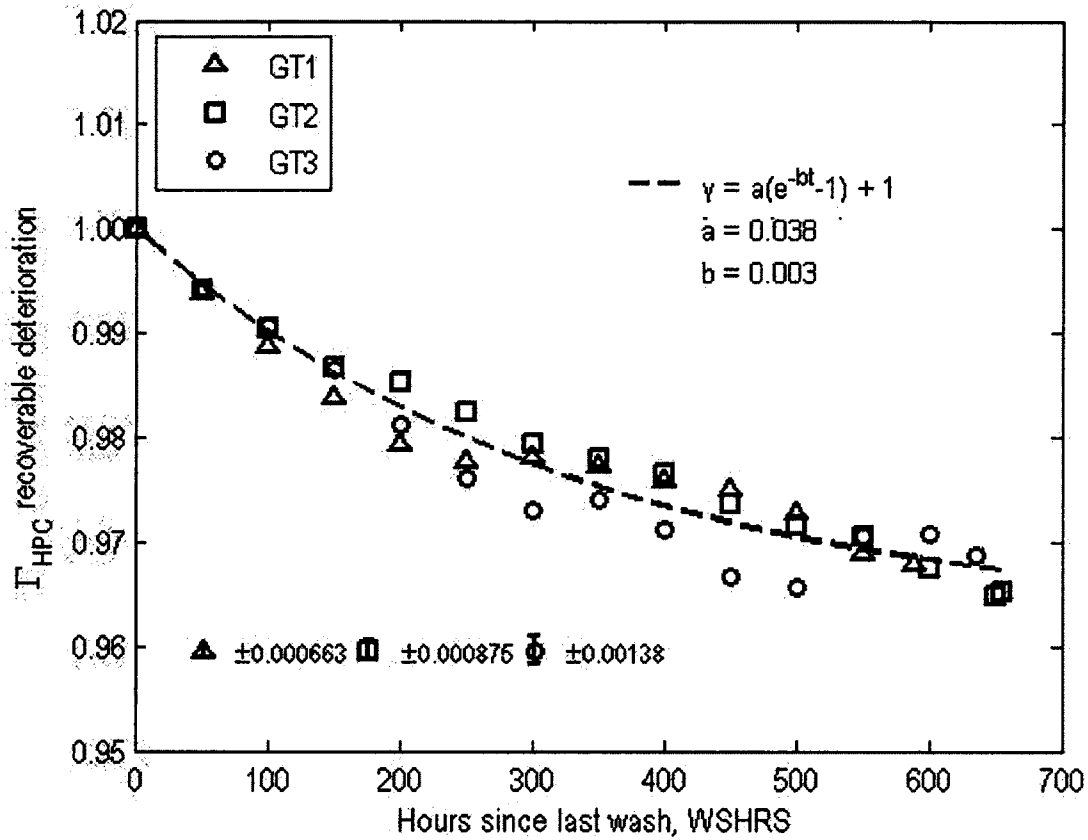


Figure C.7 Recoverable deterioration factor of the LP compressor capacity



**Figure C.8** Recoverable deterioration factor of the HP compressor capacity

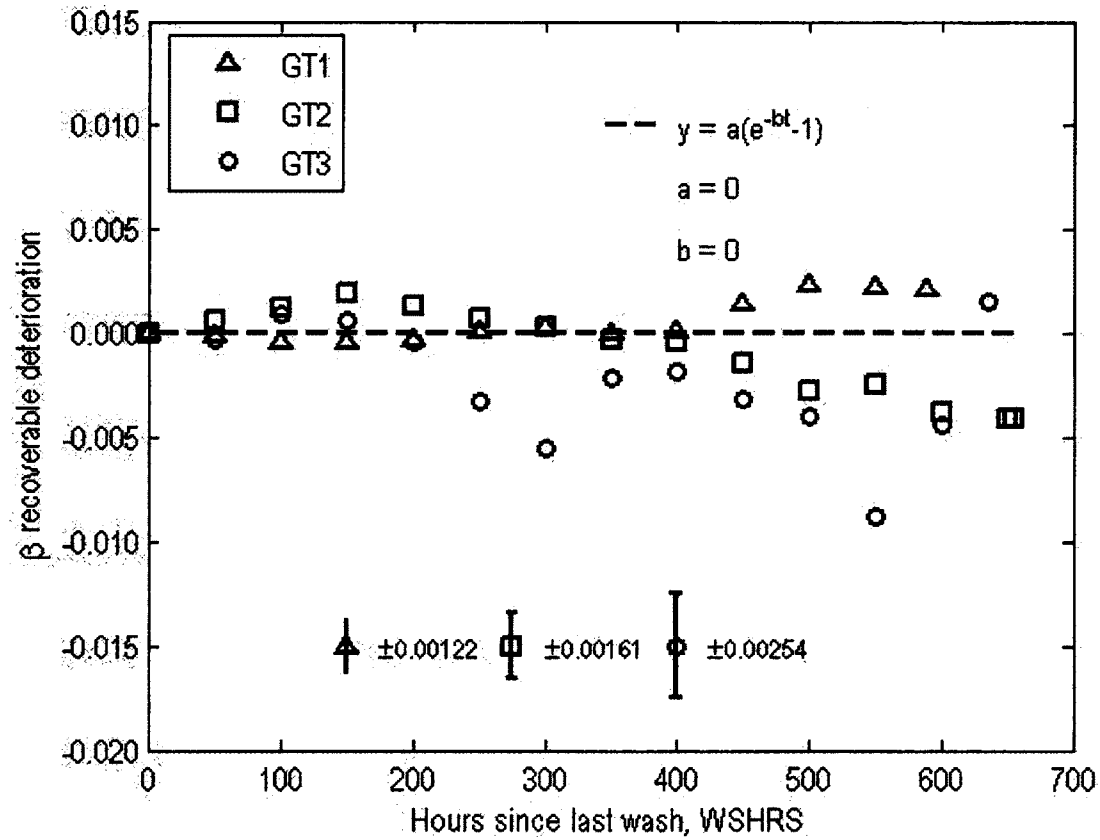


Figure C.9 Recoverable deterioration delta of the core bleed flow

## C.14 Uncertainties of the Site Performance Data

The equations presented herein follow the gas turbine station numbering convention as given by Figure C.1.

### C.14.1 LP Compressor Pressure Ratio

The uncertainty of the LP compressor pressure ratio,  $u_{\frac{P_{o3}}{P_{o2}}}$ , is found by,

$$u_{\frac{P_{o3}}{P_{o2}}} = \sqrt{\left(-\frac{P_{o3}}{P_{o2}^2} u_{P_{o1}}\right)^2 + \left(\frac{1}{P_{o2}} u_{P_{o3}}\right)^2} \quad \text{C.14.1}$$

where  $u_{P_{o1}}$  and  $u_{P_{o3}}$  are the measurement uncertainties of the ambient pressure and the LP compressor outlet pressure, respectively.

### C.14.2 HP Compressor Pressure Ratio

The uncertainty of the HP compressor pressure ratio,  $u_{\frac{P_{o4}}{P_{o3}}}$ , is found by,

$$u_{\frac{P_{o4}}{P_{o3}}} = \sqrt{\left(-\frac{P_{o4}}{P_{o3}^2} u_{P_{o3}}\right)^2 + \left(\frac{1}{P_{o3}} u_{P_{o4}}\right)^2} \quad \text{C.14.2}$$

where  $u_{P_{o4}}$  is the measurement uncertainty of the HP compressor outlet pressure.

Since the HP compressor outlet pressure is calculated, it is assumed to have an uncertainty similar to the LP compressor outlet pressure.

### C.14.3 LP Compressor Corrected Mass Flow Rate

The uncertainty of the LP compressor corrected mass flow rate,  $u_{\frac{\dot{m}_2 \sqrt{T_{o2}}}{P_{o2}}}$ , is calculated by,

$$u_{\frac{\dot{m}_2 \sqrt{T_{o2}}}{P_{o2}}} = \sqrt{\left(-\frac{\dot{m}_2 \sqrt{T_{o2}}}{P_{o2}^2} u_{P_{o1}}\right)^2 + \left(\frac{\dot{m}_2}{2P_{o2} \sqrt{T_{o2}}} u_{T_{o1}}\right)^2} \quad \text{C.14.3}$$

where  $u_{P_{o1}}$  is the measurement uncertainty of the ambient pressure, and  $u_{T_{o1}}$  is the measurement uncertainty of the ambient temperature.

### C.14.4 HP Compressor Corrected Mass Flow Rate

The uncertainty of the HP compressor corrected mass flow rate,  $u_{\frac{\dot{m}_3 \sqrt{T_{o3}}}{P_{o3}}}$ , is calculated by,

$$u_{\frac{\dot{m}_3 \sqrt{T_{o3}}}{P_{o3}}} = \sqrt{\left(-\frac{\dot{m}_3 \sqrt{T_{o3}}}{P_{o3}^2} u_{P_{o3}}\right)^2 + \left(\frac{\dot{m}_3}{2P_{o3} \sqrt{T_{o3}}} u_{T_{o3}}\right)^2} \quad \text{C.14.4}$$

where  $u_{P_{o3}}$  is the measurement uncertainty of the LP compressor outlet pressure, and  $u_{T_{o3}}$  is the measurement uncertainty of the LP compressor outlet temperature.

### C.14.5 Gas Generator Exhaust Pressure

The uncertainty of the gas generator exhaust pressure,  $u_{p_{o7}}$ , is calculated by,

$$u_{p_{o7}} = \sqrt{\left(\frac{\delta P_{o7}}{\delta \frac{P_{o3}}{P_{o2}}} u_{\frac{P_{o3}}{P_{o2}}}\right)^2 + \left(\frac{\delta P_{o7}}{\delta \frac{P_{o4}}{P_{o3}}} u_{\frac{P_{o4}}{P_{o3}}}\right)^2 + \left(\frac{\delta P_{o7}}{\delta P_{o1}} u_{P_{o1}}\right)^2} \quad \text{C.14.5}$$

where,

$$\frac{\delta P_{o7}}{\delta \frac{P_{o3}}{P_{o2}}} = \frac{P_{o7}}{P_{o6}} \frac{P_{o6}}{P_{o5}} \frac{P_{o5}}{P_{o4}} \frac{P_{o4}}{P_{o3}} \frac{P_{o2}}{P_{o1}} P_{o1} \quad \text{C.14.6}$$

$$\frac{\delta P_{o7}}{\delta \frac{P_{o4}}{P_{o3}}} = \frac{P_{o7}}{P_{o6}} \frac{P_{o6}}{P_{o5}} \frac{P_{o5}}{P_{o4}} \frac{P_{o3}}{P_{o2}} \frac{P_{o2}}{P_{o1}} P_{o1} \quad \text{C.14.7}$$

$$\frac{\delta P_{o7}}{\delta P_{o1}} = \frac{P_{o7}}{P_{o6}} \frac{P_{o6}}{P_{o5}} \frac{P_{o5}}{P_{o4}} \frac{P_{o4}}{P_{o3}} \frac{P_{o3}}{P_{o2}} \frac{P_{o2}}{P_{o1}} \quad \text{C.14.8}$$

### C.14.6 Power Turbine Outlet Temperature

The uncertainty of the power turbine outlet temperature,  $u_{T_{o8}}$ , is calculated by,

$$u_{T_{o8}} = \sqrt{\left(\frac{\delta T_{o8}}{\delta T_{o7}} u_{T_{o7}}\right)^2 + \left(\frac{\delta T_{o8}}{\delta P_{o7}} u_{P_{o7}}\right)^2 + \left(\frac{\delta T_{o8}}{\delta P_{o8}} u_{P_{o8}}\right)^2} \quad \text{C.14.9}$$

where  $u_{P_{o8}} \approx u_{P_{o1}}$ , and,

$$\frac{\delta T_{o8}}{\delta T_{o7}} = \left( \frac{P_{o8}}{P_{o7}} \right)^{\frac{\eta_{\infty PT}(\gamma-1)}{\gamma}} \quad \text{C.14.10}$$

$$\frac{\delta T_{o8}}{\delta P_{o7}} = \left[ \frac{\eta_{\infty PT}(1-\gamma)}{\gamma} \right] \left[ P_{o8}^{\frac{\eta_{\infty PT}(\gamma-1)}{\gamma}} \right] \left[ P_{o7}^{\frac{-\eta_{\infty PT}(\gamma-1)}{\gamma}-1} \right] T_{o7} \quad \text{C.14.11}$$

$$\frac{\delta T_{o8}}{\delta P_{o8}} = \left[ \frac{\eta_{\infty PT}(\gamma-1)}{\gamma} \right] \left[ \left( \frac{1}{P_{o7}} \right)^{\frac{\eta_{\infty PT}(\gamma-1)}{\gamma}} \right] \left[ P_{o8}^{\frac{\eta_{\infty PT}(\gamma-1)}{\gamma}-1} \right] T_{o7} \quad \text{C.14.12}$$

### C.14.7 Fuel Flow Rate

The uncertainty of the fuel flow rate,  $u_{\dot{m}_f}$ , is calculated by,

$$u_{\dot{m}_f} = \sqrt{\left( \frac{\delta \dot{m}_f}{\delta T_{o4}} u_{T_{o4}} \right)^2 + \left( \frac{\delta \dot{m}_f}{\delta Q} u_Q \right)^2 + \left( \frac{\delta \dot{m}_f}{\delta \dot{m}_2} u_{\dot{m}_2} \right)^2} \quad \text{C.14.13}$$

where  $u_{\dot{m}_2} \approx u_{\dot{m}_7}$ , and,

$$\frac{\delta \dot{m}_f}{\delta T_{o4}} = -\frac{c_{pa} \dot{m}_2}{\eta_B Q} \quad \text{C.14.14}$$

$$\frac{\delta \dot{m}_f}{\delta Q} = \frac{c_{pg} T_{o5} - c_{pa} T_{o4}}{\eta_B Q} \quad \text{C.14.15}$$

### C.14.8 Power Output

The uncertainty in the power output,  $u_{PWR}$ , can be found by,

$$u_{PWR} = \sqrt{\left(\frac{\delta PWR}{\delta \dot{m}_7} u_{\dot{m}_7}\right)^2 + \left(\frac{\delta PWR}{\delta T_{o7}} u_{T_{o7}}\right)^2 + \left(\frac{\delta PWR}{\delta T_{o8}} u_{T_{o8}}\right)^2} \quad C.14.16$$

where,

$$\frac{\delta PWR}{\delta \dot{m}_7} = c_{pg} (T_{o7} - T_{o8}) \quad C.14.17$$

$$\frac{\delta PWR}{\delta T_{o7}} \approx c_{pg} \dot{m}_2 \quad C.14.18$$

$$\frac{\delta PWR}{\delta T_{o8}} \approx -c_{pg} \dot{m}_2 \quad C.14.19$$

$$u_{\dot{m}_7} \approx \sqrt{\left(\frac{\dot{m}_2 \sqrt{T_{o2}}}{P_{o2}} \frac{1}{\sqrt{T_{o2}}} u_{P_{o2}}\right)^2 + \left(-\frac{\dot{m}_2 \sqrt{T_{o2}}}{2P_{o2}} \frac{P_{o2}}{T_{o2}^{\frac{3}{2}}} u_{T_{o2}}\right)^2} \quad C.14.20$$

**APPENDIX D      SOLUTION PROCESSES OF THE  
CORE CONTROL METHOD**

## **D.1 Single-Spool Turbojet**

### **D.1.1 Introduction**

This appendix discusses the solution process used by the core control method when predicting the off-design performance of a single-spool turbojet (Figure D.1). To focus on the fundamentals of the solution process, advanced flow and control simulations such as handling bleeds and performance limiters are not discussed.

From the discussion in Section 4.3, it can be recalled that the turbine and the nozzle of a single-spool turbojet may operate at three different operating conditions, namely, unchoked turbine-unchoked nozzle, choked turbine-unchoked nozzle, and choked turbine-choked nozzle (Figure D.2). This requires the solution process to have three separate sections, where each is responsible for one of the three operating conditions. The theory required to implement these sections is discussed herein (the figures already available in the main text are presented here for the reader's convenience).

Prior to this discussion, however, it shall be noted that in the core control method, turbine pressure ratios, rather than turbine temperature ratios, are used in the iterative solution process. The reason for this is that pressure ratios provide greater resolution than temperature ratios. For example, in a turbine with a 90% polytropic efficiency, increasing the turbine pressure ratio from 1 to 5 will only result in a temperature ratio increase of 1 to 1.44 (as per Equation D.1.2). Therefore, to avoid numerical instabilities, the turbine pressure ratios are used in the iterative process of the core control method.

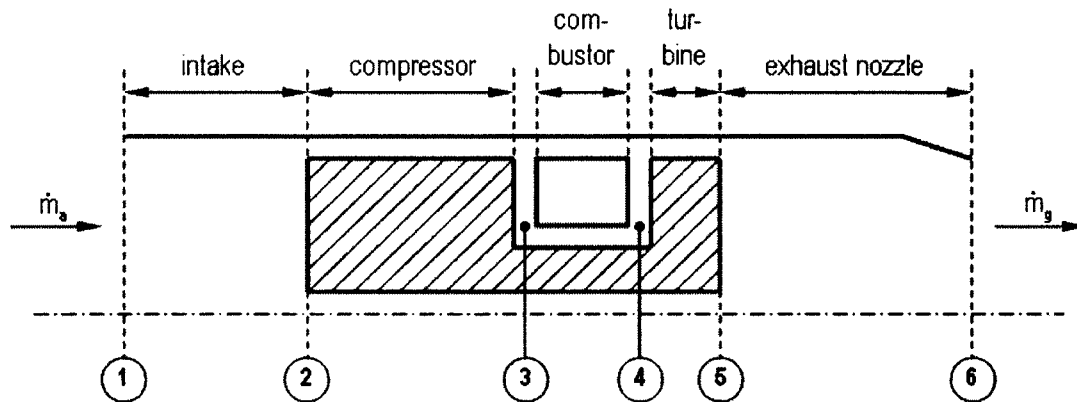


**Figure D.1** Single-spool turbojet [modified from Wittenberg, 1976a]

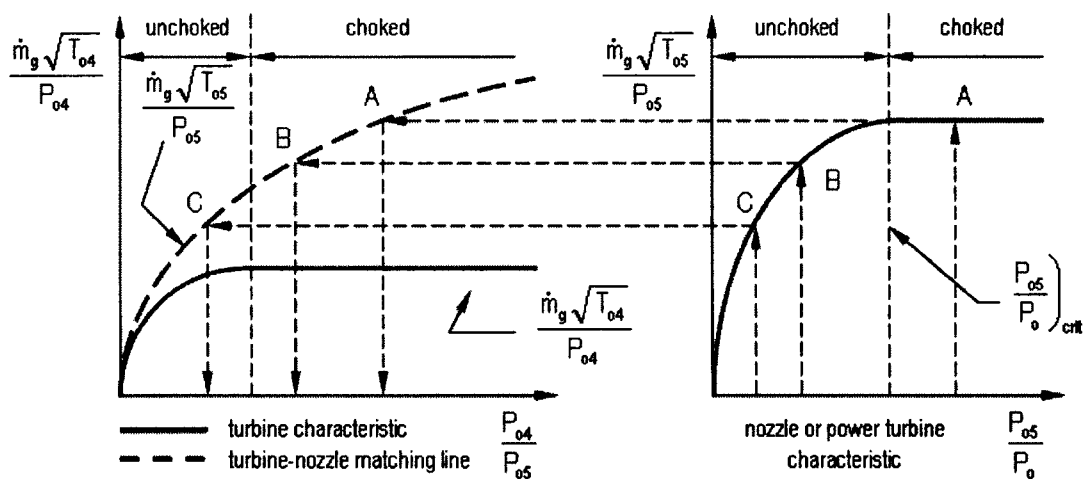


**Figure D.2** Matching of the turbine and the exhaust nozzle for a single-spool turbojet

[modified from Saravanamuttoo et al., 20010]

### D.1.2 Unchoked Turbine

For a given core control parameter,  $\phi$ , the turbine will be unchoked if the turbine pressure ratio,  $\frac{P_{o4}}{P_{o5}}$ , at the turbojet's equilibrium operating point satisfies the condition,

$$1 \leq \frac{P_{o4}}{P_{o5}} < \left( \frac{P_{o4}}{P_{o5}} \right)_{\text{crit}}$$

where  $\left( \frac{P_{o4}}{P_{o5}} \right)_{\text{crit}}$  is the critical pressure ratio, i.e., the pressure ratio at which the turbine

throat becomes choked, where,

$$\left( \frac{P_{o4}}{P_{o5}} \right)_{\text{crit}} = \frac{1}{\left[ 1 - \frac{\gamma-1}{\gamma+1} \right]^{\frac{\gamma}{\gamma-1}}} \quad \text{D.1.1}$$

Then, the turbine temperature ratio,  $\frac{T_{o4}}{T_{o5}}$  can be calculated with the turbine

polytropic efficiency,  $\eta_{\text{out}}$ , by,

$$\frac{T_{o4}}{T_{o5}} = \left( \frac{P_{o4}}{P_{o5}} \right)^{\frac{\eta_{\text{out}}(\gamma-1)}{\gamma}} \quad \text{D.1.2}$$

Next, the turbine corrected mass flow rate,  $\frac{\dot{m}_4 \sqrt{T_{o4}}}{P_{o4}}$ , is calculated from the converging nozzle equation (Saravanamuttoo et al., 2001) as,

$$\frac{\dot{m}_4 \sqrt{T_{o4}}}{P_{o4}} = \frac{A_4}{\sqrt{R}} \sqrt{\frac{2\gamma}{\gamma-1} \left(\frac{P_{o5}}{P_{o4}}\right)^{\frac{2}{\gamma}} \left[1 - \left(\frac{P_{o5}}{P_{o4}}\right)^{\frac{\gamma-1}{\gamma}}\right]} \quad \text{D.1.3}$$

Here,  $A_4$  is the turbine throat area, and  $R$  is the gas constant for air, and is 287 kJ/kgK.

Then, using the mass flow compatibility between the turbine and the propelling nozzle, the propelling nozzle corrected mass flow rate,  $\frac{\dot{m}_5 \sqrt{T_{o5}}}{P_{o5}}$ , can be determined by,

$$\frac{\dot{m}_5 \sqrt{T_{o5}}}{P_{o5}} = \frac{\dot{m}_5 \sqrt{T_{o5}}}{P_{o5}} \bigg)_{\text{des}} \frac{\frac{\dot{m}_4 \sqrt{T_{o4}}}{P_{o4}} \frac{P_{o4}}{P_{o5}} \sqrt{\frac{T_{o4}}{T_{o5}}}}{\frac{\dot{m}_4 \sqrt{T_{o4}}}{P_{o4}} \frac{P_{o4}}{P_{o5}} \bigg)_{\text{des}}} \sqrt{\frac{T_{o4}}{T_{o5}}} \quad \text{D.1.4}$$

where it is assumed that,

$$\frac{\dot{m}_5}{\dot{m}_4} \bigg)_{\text{des}} \approx 1$$

Since the propelling nozzle must be unchoked when the turbine is unchoked

(Figure D.2), the propelling nozzle pressure ratio,  $\frac{P_{o5}}{P_o}$ , is then calculated using,

$$\frac{\dot{m}_5 \sqrt{T_{o5}}}{P_{o5}} = \frac{\frac{A_6}{\sqrt{R}} \sqrt{\frac{2\gamma}{\gamma-1} \left(\frac{P_o}{P_{o5}}\right)^2 \eta_n \left[1 - \left(\frac{P_o}{P_{o5}}\right)^{\frac{\gamma-1}{\gamma}}\right]}}{1 - \eta_n \left[1 - \left(\frac{P_o}{P_{o5}}\right)^{\frac{\gamma-1}{\gamma}}\right]} \quad \text{D.1.5}$$

where  $A_6$  is the propelling nozzle area, and  $\eta_n$  is the propelling nozzle efficiency.

Then, the compressor temperature ratio,  $\frac{T_{o3}}{T_{o2}}$ , is calculated using the expression

derived from the work balance between the compressor and the turbine (see Section 4.3)

as,

$$\frac{T_{o3}}{T_{o2}} = 1 + \phi \left[ \left(\frac{T_{o3}}{T_{o2}}\right)_{\text{des}} - 1 \right] \frac{1 - \frac{T_{o5}}{T_{o4}}}{1 - \left(\frac{T_{o5}}{T_{o4}}\right)_{\text{des}}} \quad \text{D.1.6}$$

where

$$\phi = \frac{\frac{T_{o4}}{T_{o2}}}{\left(\frac{T_{o4}}{T_{o2}}\right)_{\text{des}}} \quad \text{D.1.7}$$

With  $\frac{T_{o3}}{T_{o2}}$  known, the compressor pressure ratio,  $\frac{P_{o3}}{P_{o2}}$ , is calculated next with the

compressor polytropic efficiency,  $\eta_{oc}$ , through,

$$\frac{P_{o3}}{P_{o2}} = \left( \frac{T_{o3}}{T_{o2}} \right)^{\frac{\eta_{oc}\gamma}{\gamma-1}} \quad D.1.8$$

The pressure ratios through the turbojet can be expressed in the form of,

$$\frac{P_{o5}}{P_o} = \frac{P_{o5}}{P_{o4}} \frac{P_{o4}}{P_{o3}} \frac{P_{o3}}{P_{o2}} \frac{P_{o2}}{P_{o1}} \frac{P_{o1}}{P_o} \quad D.1.9$$

where

$$\frac{P_{o1}}{P_o} = \left[ 1 + \frac{\gamma-1}{2} M_o^2 \right]^{\frac{\gamma}{\gamma-1}} \quad D.1.10$$

$$\frac{P_{o2}}{P_{o1}} = \eta_R \quad D.1.11$$

where  $M_o$  is the freestream Mach number, and  $\eta_R$  is the inlet ram recovery efficiency.

Then,  $\frac{P_{o3}}{P_{o2}}$  is recalculated by rearranging Equation D.1.9 as,

$$\frac{P_{o3}}{P_{o2}} = \frac{\frac{P_{o5}}{P_o} \frac{P_{o4}}{P_{o5}}}{\frac{P_{o4}}{P_{o3}} \frac{P_{o3}}{P_{o2}} \frac{P_{o1}}{P_o}} \quad D.1.12$$

If the correct value of  $\frac{P_{o4}}{P_{o5}}$  is found for a given  $\phi$ , then  $\frac{P_{o3}}{P_{o2}}$  calculated by

Equation D.1.8 and Equation D.1.12 shall converge. Else,  $\frac{P_{o4}}{P_{o5}}$  is searched for iteratively.

### D.1.3 Choked Turbine-Unchoked Nozzle

Here, for a given  $\phi$ , at the turbojet's equilibrium operating point,  $\frac{P_{o4}}{P_{o5}}$  satisfies

the condition,

$$\left. \frac{P_{o4}}{P_{o5}} \right)_{\text{crit}} \leq \frac{P_{o4}}{P_{o5}} < \left. \frac{P_{o4}}{P_{o5}} \right)_{\text{des}}$$

where  $\left. \frac{P_{o4}}{P_{o5}} \right)_{\text{des}}$  is the design-point pressure ratio.

Since the turbine is choked, it has a sonic throat. Therefore, the converging nozzle equation as given in Equation D.1.3 is no longer valid. Therefore, the turbine sonic

corrected mass flow rate,  $\left. \frac{\dot{m}_4 \sqrt{T_{o4}}}{P_{o4}} \right)_{\text{crit}}$ , is found by the expression,

$$\left. \frac{\dot{m}_4 \sqrt{T_{o4}}}{P_{o4}} \right)_{\text{crit}} = \sqrt{\frac{\gamma}{R}} \frac{A_4}{\left[ \frac{\gamma+1}{2} \right]^{\frac{\gamma+1}{2(\gamma-1)}}} \quad \text{D.1.13}$$

This expression can be easily obtained using the definition of the Mach number and compressible flow relationships.

Equation D.1.13 can be used to determine the throat area of *any* turbine or converging nozzle given the sonic corrected mass flow rate, and vice versa. Logic

dictates that  $\left. \frac{\dot{m}_4 \sqrt{T_{o4}}}{P_{o4}} \right)_{\text{crit}} = \left. \frac{\dot{m}_4 \sqrt{T_{o4}}}{P_{o4}} \right)_{\text{des}}$ .

With  $\frac{\dot{m}_4 \sqrt{T_{o4}}}{P_{o4}}$  known, and  $\frac{T_{o4}}{T_{o5}}$  calculated from Equation D.1.2, the nozzle

corrected mass flow rate can be calculated using Equation D.1.4.

The remainder of the solution process is identical to that of the unchoked-turbine operating condition.

#### D.1.4 Choked Nozzle

By default, a choked propelling nozzle sets the operating point of the turbine to its design-point. Therefore,

$$\left. \frac{P_{o4}}{P_{o5}} = \frac{P_{o4}}{P_{o5}} \right)_{\text{des}}$$

$$\frac{T_{o4}}{T_{o5}} = \left( \frac{P_{o4}}{P_{o5}} \right)_{\text{des}}^{\frac{\eta_{\text{net}}(\gamma-1)}{\gamma}} \quad \text{D.1.14}$$

and,

$$\left. \frac{\dot{m}_4 \sqrt{T_{o4}}}{P_{o4}} = \frac{\dot{m}_4 \sqrt{T_{o4}}}{P_{o4}} \right)_{\text{des}}$$

Here, note that  $\frac{T_{o4}}{T_{o5}}$  is determined by Equation D.1.14, and not set to  $\frac{T_{o4}}{T_{o5}}_{des}$ ,

since the turbine polytropic efficiency,  $\eta_{\text{tot}}$ , may vary due to deterioration.

Then, for a given  $\phi$ ,  $\frac{T_{o3}}{T_{o2}}$  can be calculated by Equation D.1.6, and  $\frac{P_{o3}}{P_{o2}}$  by

Equation D.1.8. Finally, the nozzle pressure ratio,  $\frac{P_{o5}}{P_o}$ , can be calculated by Equation

D.1.9, which must satisfy the condition,

$$\left. \frac{P_{o5}}{P_o} \right)_{\text{crit}} \leq \frac{P_{o5}}{P_o} < \left. \frac{P_{o5}}{P_o} \right)_{\text{des}}$$

where

$$\left. \frac{P_{o5}}{P_o} \right)_{\text{crit}} = \frac{1}{\left[ 1 - \frac{1}{\eta_j} \left( \frac{\gamma-1}{\gamma+1} \right) \right]^{\frac{\gamma}{\gamma-1}}} \quad \text{D.1.15}$$

No further iterations are required for this operating condition.

The propelling nozzle corrected mass flow rate can then be calculated by,

$$\left. \frac{\dot{m}_5 \sqrt{T_{o5}}}{P_{o5}} \right)_{\text{crit}} = \sqrt{\frac{\gamma}{R}} \frac{A_6}{\left[ \frac{\gamma+1}{2} \right]^{\frac{\gamma+1}{2(\gamma-1)}}} \quad \text{D.1.16}$$

Although it may seem that  $\left. \frac{\dot{m}_5 \sqrt{T_{o5}}}{P_{o5}} \right)_{\text{crit}} = \left. \frac{\dot{m}_5 \sqrt{T_{o5}}}{P_{o5}} \right)_{\text{des}}$ , a propelling nozzle with

a large throat diameter may not necessarily be choked at the design-point, as is the case for the aero- RB211-22 (although this is a turbofan, the concept is transferable to the propelling nozzle of a turbojet). In this case, the design-point will fall under the choked turbine-unchoked nozzle operating condition (Appendix D.1.3).

#### D.1.5 Post-Solution Process Calculations

Once the equilibrium operating point of the turbojet is found, the performance values across the turbojet are determined for a given ambient temperature,  $T_o$ , a given ambient pressure,  $P_o$ , and a given freestream Mach number,  $M_o$ , as follows.

For the inlet nozzle,

$$P_{o1} = P_o \left[ 1 + \frac{\gamma-1}{2} M_o^2 \right]^{\frac{\gamma}{\gamma-1}} \quad \text{D.1.17}$$

$$T_{o1} = T_o \left[ 1 + \frac{\gamma-1}{2} M_o^2 \right] \quad \text{D.1.18}$$

For the compressor inlet,

$$P_{o2} = \eta_R P_{o1} \quad \text{D.1.19}$$

$$T_{o2} = T_{o1} \quad \text{D.1.20}$$

$$\frac{\dot{m}_2 \sqrt{T_{o2}}}{P_{o2}} = \frac{\dot{m}_2 \sqrt{T_{o2}}}{P_{o2}} \left)_{des} \frac{\frac{\dot{m}_4 \sqrt{T_{o4}}}{P_{o4}}}{\frac{\dot{m}_4 \sqrt{T_{o4}}}{P_{o4}}} \left)_{des} \frac{\frac{P_{o3}}{P_{o2}}}{\frac{P_{o3}}{P_{o2}}} \left)_{des} \sqrt{I} \phi \quad \text{D.1.21}$$

$$\dot{m}_2 = \frac{\dot{m}_2 \sqrt{T_{o2}}}{P_{o2}} \frac{P_{o2}}{\sqrt{T_{o2}}} \quad \text{D.1.22}$$

where  $\dot{m}_2$  is the compressor inlet mass flow rate.

For the compressor outlet,

$$P_{o3} = P_{o2} \frac{P_{o3}}{P_{o2}} \quad \text{D.1.23}$$

$$T_{o3} = T_{o2} \frac{T_{o3}}{T_{o2}} \quad \text{D.1.24}$$

$$\dot{m}_3 = \dot{m}_2 \quad \text{D.1.25}$$

For the turbine inlet,

$$P_{o4} = P_{o3} \left)_{des} \frac{P_{o4}}{P_{o3}} \quad \text{D.1.26}$$

$$T_{o4} = T_{o2} \phi \left)_{des} \frac{T_{o4}}{P_{o2}} \quad \text{D.1.27}$$

$$\dot{m}_f = \dot{m}_3 \frac{c_{pg} T_{o4} - c_{pa} T_{o3}}{\eta_B Q} \quad \text{D.1.28}$$

$$\dot{m}_4 = \dot{m}_3 + \dot{m}_f \text{ or } \dot{m}_4 = \frac{\dot{m}_4 \sqrt{T_{o4}}}{P_{o4}} \frac{P_{o4}}{\sqrt{T_{o4}}} \quad \text{D.1.29}$$

where  $\left. \frac{P_{o4}}{P_{o3}} \right)_{des}$  is the design-point combustor pressure loss,  $\dot{m}_f$  is the fuel flow rate,  $\eta_B$  is

the combustion efficiency,  $Q$  is the fuel heating value,  $c_{pa}$  and  $c_{pg}$  are specific heats of air, 1.005 kJ/kgK, and gas, 1.148 kJ/kgK, respectively.

For the turbine outlet,

$$P_{o5} = P_{o4} \frac{P_{o5}}{P_{o4}} \quad \text{D.1.30}$$

$$T_{o5} = T_{o4} \frac{T_{o5}}{P_{o4}} \quad \text{D.1.31}$$

$$\dot{m}_5 = \dot{m}_4 \text{ or } \dot{m}_5 = \frac{\dot{m}_5 \sqrt{T_{o5}}}{P_{o5}} \frac{P_{o5}}{\sqrt{T_{o5}}} \quad \text{D.1.32}$$

For the propelling nozzle,

$$\dot{m}_6 = \dot{m}_5 \quad \text{D.1.33}$$

Then, the turbojet's net thrust,  $F_N$ , can be calculated by,

$$F_N = \dot{m}_6 (V_6 - V_o) + A_6 (P_6 - P_o) \quad \text{D.1.34}$$

where  $V_6$  is the propelling nozzle flow speed,  $V_o$  is the freestream speed, and  $P_6$  is the static pressure at the nozzle throat.

For a choked propelling nozzle,

$$P_6 = P_{o5} \left( \frac{P_o}{P_{o5}} \right)_{\text{crit}} \quad \text{D.1.35}$$

where,

$$\left( \frac{P_{o5}}{P_o} \right)_{\text{crit}} = \frac{1}{\left[ 1 - \frac{\gamma-1}{\gamma+1} \right]^{\frac{\gamma}{\gamma-1}}} \quad \text{D.1.36}$$

$$T_6 = \frac{2}{\gamma+1} T_{o5} \quad \text{D.1.37}$$

$$V_6 = \sqrt{\gamma R T_6} \quad \text{D.1.38}$$

For an unchoked propelling nozzle,

$$P_6 = P_o \quad \text{D.1.39}$$

and,  $M_6$  can be calculated from,

$$\frac{\dot{m}_5 \sqrt{T_{o5}}}{P_{o5}} = \sqrt{\frac{\gamma}{R}} \frac{M_6 A_6}{\left[ 1 + \frac{\gamma-1}{2} M_6^2 \right]^{\frac{\gamma+1}{2(\gamma-1)}}} \quad \text{D.1.40}$$

Then, from the compressible flow relations,  $T_6$  can be found by,

$$T_6 = \frac{T_{o5}}{1 + \frac{\gamma-1}{2} M_6^2} \quad \text{D.1.41}$$

from which,  $V_6$  can be calculated as,

$$V_6 = M_6 \sqrt{\gamma R T_6} \quad \text{D.1.42}$$

Once the net thrust is calculated, the specific fuel consumption, SFC, of the turbojet can be calculated by,

$$\text{SFC} = \frac{\dot{m}_f}{F_N} \quad \text{D.1.43}$$

This is the full solution process of the core control method for a single-spool turbojet.

## **D.2 Two-Spool Gas Generator with a Free Power Turbine**

### **D.2.1 Introduction**

This section discusses the solution process of the core control method as applied to a two-spool gas generator with a free power turbine (Figure D.3).

As discussed in Section 4.5, for this gas turbine configuration, there are four possible operating conditions (Figure D.4). These are, unchoked HP turbine, choked HP turbine-unchoked LP turbine, choked LP turbine-unchoked free power turbine, and choked free power turbine. Note that if a turbine is unchoked, the turbines and/or propelling nozzle situated downstream will also be unchoked.

The figures already available in the main text are presented here for the reader's convenience.

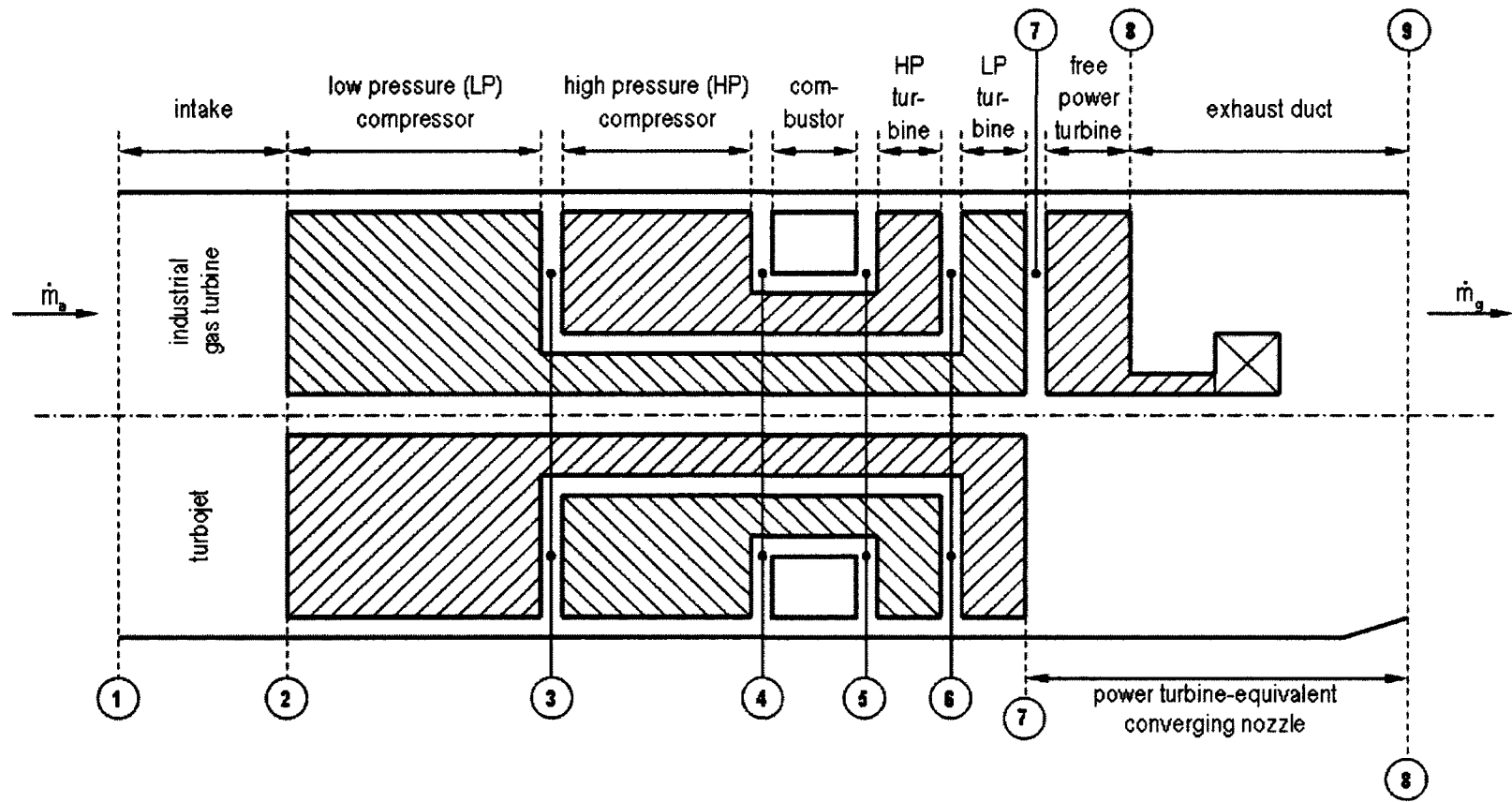


**Figure D.3** Two-spool gas generator with a free power turbine and its equivalent two-spool turbojet

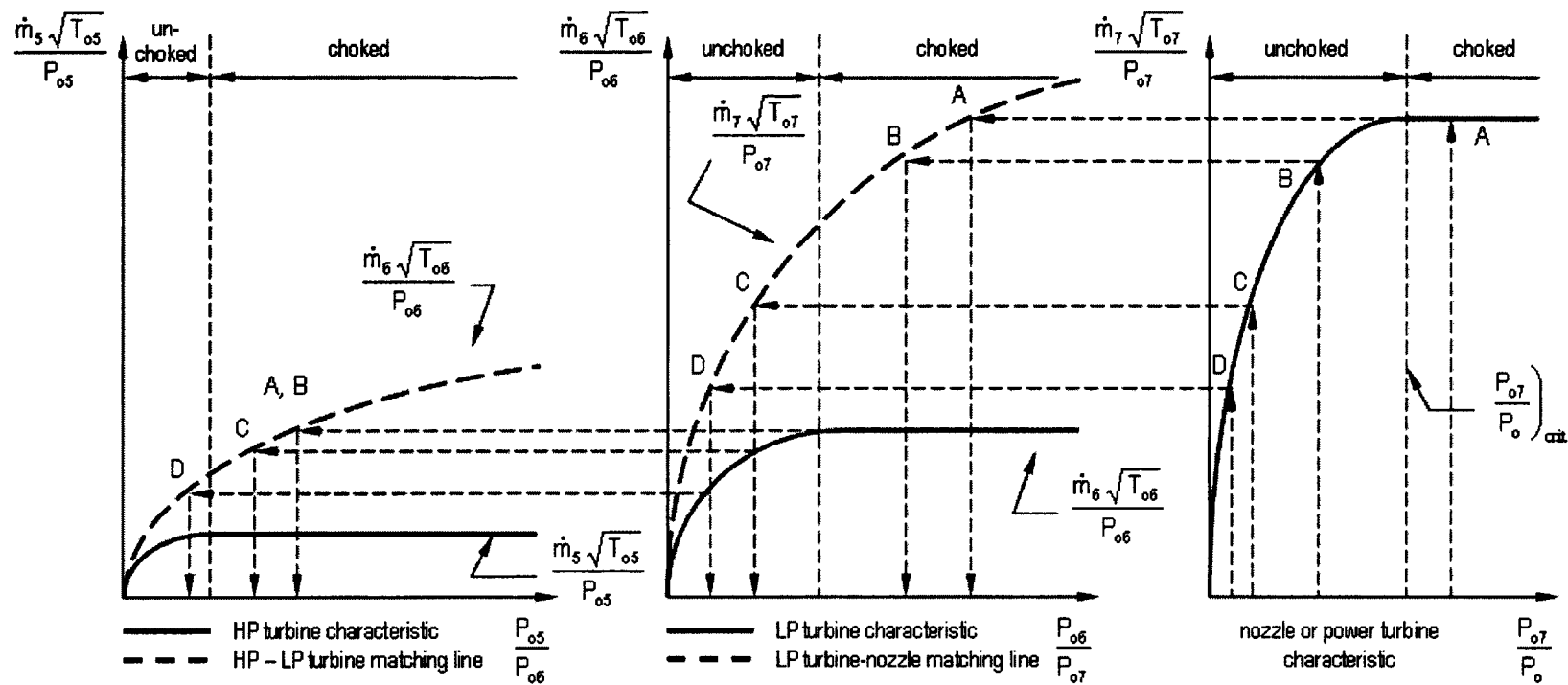


**Figure D.4** Matching of the HP, LP and free power turbines for a two-spool gas generator with a free power turbine [modified from Saravanamuttoo et al., 2001]

### D.2.2 Unchoked HP Turbine

For a given core control parameter,  $\phi_{HP}$ , the HP turbine will be unchoked if the turbine pressure ratio,  $\frac{P_{o5}}{P_{o6}}$ , at the gas turbine's equilibrium operating point satisfies the condition,

$$1 \leq \frac{P_{o5}}{P_{o6}} < \left( \frac{P_{o5}}{P_{o6}} \right)_{crit}$$

where  $\left( \frac{P_{o5}}{P_{o6}} \right)_{crit}$  is the critical pressure ratio, and can be found by Equation D.1.1.

Then, the HP turbine temperature ratio,  $\frac{T_{o5}}{T_{o6}}$  can be calculated with the HP turbine polytropic efficiency,  $\eta_{\infty HPT}$ , by,

$$\frac{T_{o5}}{T_{o6}} = \left( \frac{P_{o5}}{P_{o6}} \right)^{\frac{\eta_{\infty HPT}(\gamma-1)}{\gamma}} \quad D.2.1$$

Next, the HP turbine corrected mass flow rate,  $\frac{\dot{m}_5 \sqrt{T_{o5}}}{P_{o5}}$ , is calculated from the converging nozzle equation, with  $A_5$  as the turbine throat area, using,

$$\frac{\dot{m}_5 \sqrt{T_{o5}}}{P_{o5}} = \frac{A_5}{\sqrt{R}} \sqrt{\frac{2\gamma}{\gamma-1} \left( \frac{P_{o6}}{P_{o5}} \right)^{\frac{2}{\gamma}} \left[ 1 - \left( \frac{P_{o6}}{P_{o5}} \right)^{\frac{\gamma-1}{\gamma}} \right]} \quad D.2.2$$

Then, using the mass flow compatibility between the HP and LP turbines, the LP

turbine corrected mass flow rate,  $\frac{\dot{m}_6 \sqrt{T_{06}}}{P_{06}}$ , can be determined by,

$$\frac{\dot{m}_6 \sqrt{T_{06}}}{P_{06}} = \frac{\dot{m}_6 \sqrt{T_{06}}}{P_{06}} \left( \frac{\dot{m}_5 \sqrt{T_{05}}}{P_{05}} \frac{P_{05}}{P_{06}} \sqrt{\frac{T_{05}}{T_{06}}}_{\text{des}} \right)_{\text{des}} \left( \frac{\dot{m}_5 \sqrt{T_{05}}}{P_{05}} \frac{P_{05}}{P_{06}} \right)_{\text{des}} \sqrt{\frac{T_{05}}{T_{06}}} \quad \text{D.2.3}$$

where it is assumed that,

$$\frac{\dot{m}_6}{\dot{m}_5} \left( \frac{\dot{m}_5}{\dot{m}_6} \right)_{\text{des}} \approx 1$$

Next, using  $\frac{\dot{m}_6 \sqrt{T_{06}}}{P_{06}}$  and the converging nozzle equation, the LP turbine

pressure ratio,  $\frac{P_{06}}{P_{07}}$ , can be calculated by,

$$\frac{\dot{m}_6 \sqrt{T_{06}}}{P_{06}} = \frac{A_6}{\sqrt{R}} \sqrt{\frac{2\gamma}{\gamma-1} \left( \frac{P_{07}}{P_{06}} \right)^{\frac{2}{\gamma}} \left[ 1 - \left( \frac{P_{07}}{P_{06}} \right)^{\frac{\gamma-1}{\gamma}} \right]} \quad \text{D.2.4}$$

This information, along with the LP turbine polytropic efficiency,  $\eta_{\infty\text{LPT}}$ , can then

be used to calculate the LP turbine temperature ratio,  $\frac{T_{o6}}{T_{o7}}$ , as,

$$\frac{T_{o6}}{T_{o7}} = \left( \frac{P_{o6}}{P_{o7}} \right)^{\frac{\eta_{\infty\text{LPT}}(\gamma-1)}{\gamma}} \quad \text{D.2.5}$$

By using the flow compatibility between the LP turbine and the free power

turbine, the free power turbine corrected mass flow rate,  $\frac{\dot{m}_7 \sqrt{T_{o7}}}{P_{o7}}$ , can be determined

by,

$$\frac{\dot{m}_7 \sqrt{T_{o7}}}{P_{o7}} = \frac{\dot{m}_7 \sqrt{T_{o7}}}{P_{o7}} \left)_{\text{des}} \frac{\frac{\dot{m}_6 \sqrt{T_{o6}}}{P_{o6}} \frac{P_{o6}}{P_{o7}} \sqrt{\frac{T_{o6}}{T_{o7}}}}{\left( \frac{\dot{m}_6 \sqrt{T_{o6}}}{P_{o6}} \right)_{\text{des}} \left( \frac{P_{o6}}{P_{o7}} \right)_{\text{des}}} \sqrt{\frac{T_{o6}}{T_{o7}}}}{\frac{T_{o6}}{T_{o7}}} \quad \text{D.2.6}$$

where it is assumed that,

$$\frac{\dot{m}_6}{\dot{m}_7} \left)_{\text{des}} \approx 1$$

Next, using  $\frac{\dot{m}_7 \sqrt{T_{o7}}}{P_{o7}}$  and the converging nozzle equation, the free power turbine

pressure ratio,  $\frac{P_{o7}}{P_{o8}}$ , can be calculated by,

$$\frac{\dot{m}_7 \sqrt{T_{o7}}}{P_{o7}} = \frac{A_7}{\sqrt{R}} \sqrt{\frac{2\gamma}{\gamma-1} \left(\frac{P_{o8}}{P_{o7}}\right)^{\frac{2}{\gamma}} \left[1 - \left(\frac{P_{o8}}{P_{o7}}\right)^{\frac{\gamma-1}{\gamma}}\right]} \quad \text{D.2.7}$$

This information, along with the free power turbine polytropic efficiency,  $\eta_{\infty\text{PT}}$ , can then be used to calculate the free power turbine temperature ratio,  $\frac{T_{o7}}{T_{o8}}$ , as,

$$\frac{T_{o7}}{T_{o8}} = \left(\frac{P_{o7}}{P_{o8}}\right)^{\frac{\eta_{\infty\text{PT}}(\gamma-1)}{\gamma}} \quad \text{D.2.8}$$

If the free power turbine is replaced by a turbine-equivalent converging nozzle, instead of Equation D.2.7, the following is used to determine  $\frac{P_{o7}}{P_{o8}}$ .

$$\frac{\dot{m}_7 \sqrt{T_{o7}}}{P_{o7}} = \frac{\frac{A_8}{\sqrt{R}} \sqrt{\frac{2\gamma}{\gamma-1} \left(\frac{P_{o8}}{P_{o7}}\right)^2 \eta_n \left[1 - \left(\frac{P_{o8}}{P_{o7}}\right)^{\frac{\gamma-1}{\gamma}}\right]}}{1 - \eta_n \left[1 - \left(\frac{P_{o8}}{P_{o7}}\right)^{\frac{\gamma-1}{\gamma}}\right]} \quad \text{D.2.9}$$

where  $A_8$  is the converging nozzle throat area, and  $\eta_n$  is its efficiency.

With these turbine temperature ratios, the HP and LP compressor temperature ratios can be determined using the expressions developed from the work balance relationships of the respective spools (Section 1.5).

Therefore, the HP compressor temperature ratio,  $\frac{T_{o4}}{T_{o3}}$ , is found by,

$$\frac{T_{o4}}{T_{o3}} = 1 + \phi_{HP} \left[ \left( \frac{T_{o4}}{T_{o3}} \right)_{des} - 1 \right] \frac{1 - \frac{T_{o6}}{T_{o5}}}{1 - \left( \frac{T_{o6}}{T_{o5}} \right)_{des}} \quad D.2.10$$

where

$$\phi_{HP} = \frac{\frac{T_{o5}}{T_{o3}}}{\left( \frac{T_{o5}}{T_{o3}} \right)_{des}} \quad D.2.11$$

The HP compressor pressure ratio,  $\frac{P_{o4}}{P_{o3}}$ , can then be calculated with the HP

compressor polytropic efficiency,  $\eta_{\infty\text{-HPC}}$ , through,

$$\frac{P_{o4}}{P_{o3}} = \left( \frac{T_{o4}}{T_{o3}} \right)^{\frac{\eta_{\infty\text{-HPC}} \gamma}{\gamma - 1}} \quad D.2.12$$

The LP compressor temperature ratio,  $\frac{T_{o4}}{T_{o3}}$ , is found by,

$$\frac{T_{o3}}{T_{o2}} = \left\{ 1 - \phi_{HP} \left[ \left( 1 - \frac{T_{o2}}{T_{o3}} \right)_{des} \right] \frac{\frac{T_{o6}}{T_{o5}} - 1 - \frac{T_{o7}}{T_{o6}}}{\left( \frac{T_{o6}}{T_{o5}} \right)_{des} - 1 - \left( \frac{T_{o7}}{T_{o6}} \right)_{des}} \right\}^{-1} \quad D.2.13$$

using which, the LP compressor pressure ratio,  $\frac{P_{o3}}{P_{o2}}$ , can be calculated with the LP

compressor polytropic efficiency,  $\eta_{\text{LPC}}$ , using,

$$\frac{P_{o3}}{P_{o2}} = \left( \frac{T_{o3}}{T_{o2}} \right)^{\frac{\eta_{\text{LPC}} \gamma}{\gamma - 1}} \quad \text{D.2.14}$$

The pressure ratios through the gas turbine can be expressed in the form of,

$$\frac{P_{o9}}{P_o} = \frac{P_{o9}}{P_{o8}} \frac{P_{o8}}{P_{o7}} \frac{P_{o7}}{P_{o6}} \frac{P_{o6}}{P_{o5}} \frac{P_{o5}}{P_{o4}} \frac{P_{o4}}{P_{o3}} \frac{P_{o3}}{P_{o2}} \frac{P_{o2}}{P_{o1}} \frac{P_{o1}}{P_o} \quad \text{D.2.15}$$

where  $\frac{P_{o5}}{P_{o4}}$  is the combustor pressure loss. For a land-based gas turbine,  $\frac{P_{o9}}{P_{o8}}$  is the

exhaust duct pressure loss and  $\frac{P_{o2}}{P_{o1}}$  is the intake pressure loss. For a two-spool turbojet,

$\frac{P_{o9}}{P_{o8}} \approx 1$ , and,

$$\frac{P_{o1}}{P_o} = \left[ 1 + \frac{\gamma - 1}{2} M_o^2 \right]^{\frac{\gamma}{\gamma - 1}} \quad \text{D.2.16}$$

$$\frac{P_{o2}}{P_{o1}} = \eta_R \quad \text{D.2.17}$$

Rearranging Equation D.2.15,  $\frac{P_{o3}}{P_{o2}}$  can be recalculated as,

$$\frac{P_{o3}}{P_{o2}} = \frac{\frac{P_{o9}}{P_o} \frac{P_{o7}}{P_{o8}} \frac{P_{o6}}{P_{o7}} \frac{P_{o5}}{P_{o6}}}{\frac{P_{o9}}{P_{o8}} \frac{P_{o5}}{P_{o4}} \frac{P_{o4}}{P_{o3}} \frac{P_{o2}}{P_{o1}} \frac{P_{o1}}{P_o}} \quad \text{D.2.18}$$

Then,  $\frac{P_{o5}}{P_{o6}}$  is iteratively found until  $\frac{P_{o3}}{P_{o2}}$  calculated from Equation D.2.14 and

Equation D.2.18 converge for a given  $\phi_{HP}$ .

### D.2.3 Choked HP Turbine-Unchoked LP Turbine

Here, for a given  $\phi_{HP}$ ,  $\frac{P_{o5}}{P_{o6}}$  satisfies the condition,

$$\left. \frac{P_{o5}}{P_{o6}} \right)_{\text{crit}} \leq \frac{P_{o5}}{P_{o6}} < \left. \frac{P_{o5}}{P_{o6}} \right)_{\text{des}}$$

Then, the HP turbine temperature ratio can be calculated by Equation D.2.1, and its corrected mass flow rate by,

$$\left. \frac{\dot{m}_5 \sqrt{T_{o5}}}{P_{o5}} \right)_{\text{crit}} = \sqrt{\frac{\gamma}{R}} \frac{A_5}{\left[ \frac{\gamma+1}{2} \right]^{\frac{\gamma+1}{2(\gamma-1)}}} \quad \text{D.2.19}$$

The remaining solution process is identical to that of Appendix D.2.2.

#### D.2.4 Choked LP Turbine-Unchoked Free Power Turbine

Here, the HP turbine is insulated by the LP turbine choking, thus operate at its design-point. Therefore,

$$\left. \frac{P_{o5}}{P_{o6}} = \frac{P_{o5}}{P_{o6}} \right)_{des} \quad \text{and} \quad \left. \frac{\dot{m}_5 \sqrt{T_{o5}}}{P_{o5}} = \frac{\dot{m}_5 \sqrt{T_{o5}}}{P_{o5}} \right)_{des}$$

and,  $\frac{T_{o5}}{T_{o6}}$  is found by Equation D.2.1, as the HP turbine is operating at its design-point.

The LP turbine pressure ratio satisfies the condition,

$$\left. \frac{P_{o6}}{P_{o7}} \right)_{crit} < \frac{P_{o6}}{P_{o7}} < \left. \frac{P_{o6}}{P_{o7}} \right)_{des}$$

at the equilibrium operating point of the gas turbine.

Next, the LP turbine temperature ratio,  $\frac{T_{o6}}{T_{o7}}$ , can be calculated by Equation D.2.5,

and its corrected mass flow rate by,

$$\left. \frac{\dot{m}_6 \sqrt{T_{o6}}}{P_{o6}} \right)_{crit} = \sqrt{\frac{\gamma}{R}} \frac{A_6}{\left[ \frac{\gamma+1}{2} \right]^{\frac{\gamma+1}{2(\gamma-1)}}} \quad \text{D.2.20}$$

The remaining solution process is identical to that of Appendix D.2.2.

### D.2.5 Choked Free Power Turbine

Here, the HP and LP turbines are insulated, thus operate at their respective design-points, due to the choking of the free power turbine. Therefore, for the HP turbine,

$$\left. \frac{P_{o5}}{P_{o6}} = \frac{P_{o5}}{P_{o6}} \right)_{des} \quad \text{and} \quad \left. \frac{\dot{m}_5 \sqrt{T_{o5}}}{P_{o5}} = \frac{\dot{m}_5 \sqrt{T_{o5}}}{P_{o5}} \right)_{des}$$

and for the LP turbine,

$$\left. \frac{P_{o6}}{P_{o7}} = \frac{P_{o6}}{P_{o7}} \right)_{des} \quad \text{and} \quad \left. \frac{\dot{m}_6 \sqrt{T_{o6}}}{P_{o6}} = \frac{\dot{m}_6 \sqrt{T_{o6}}}{P_{o6}} \right)_{des}$$

The temperature ratios of the HP and LP turbines can be calculated by Equation D.2.1 and Equation D.2.5, respectively. At the gas turbine's equilibrium operating point, the free power turbine pressure ratio,  $\frac{P_{o7}}{P_{o8}}$ , satisfies the condition,

$$\left. \frac{P_{o7}}{P_{o8}} \right)_{crit} \leq \frac{P_{o7}}{P_{o8}} < \left. \frac{P_{o7}}{P_{o8}} \right)_{des}$$

Then, its temperature ratio can be calculated using its polytropic efficiency,  $\eta_{\infty PT}$ , as

$$\frac{T_{o7}}{T_{o8}} = \left( \frac{P_{o7}}{P_{o8}} \right)^{\frac{\eta_{\infty PT}(\gamma-1)}{\gamma}} \quad \text{D.2.21}$$

and its corrected mass flow rate can be calculated by,

$$\left. \frac{\dot{m}_7 \sqrt{T_{o7}}}{P_{o7}} \right)_{\text{crit}} = \sqrt{\frac{\gamma}{R}} \frac{A_7}{\left[ \frac{\gamma+1}{2} \right]^{\frac{\gamma+1}{2(\gamma-1)}}} \quad \text{D.2.22}$$

The remaining solution process is identical to that of Appendix D.2.2.

### D.2.6 Post-Solution Process Calculations

Once the equilibrium operating point is found for a given  $\phi_{\text{HP}}$ , the performance across the gas turbine can be calculated as follows. Note that for a land-based gas turbine,

$P_{o1} = P_o$ ,  $T_{o1} = T_o$ , and *hopefully*,  $M_o \approx 0$ .

Then, for the LP compressor inlet,

$$P_{o2} = P_{o1} \frac{P_{o2}}{P_{o1}} \quad \text{D.2.23}$$

$$T_{o2} \approx T_{o1} \quad \text{D.2.24}$$

$$\left. \frac{\dot{m}_2 \sqrt{T_{o2}}}{P_{o2}} = \frac{\dot{m}_2 \sqrt{T_{o2}}}{P_{o2}} \right)_{\text{des}} \frac{\left. \frac{\dot{m}_5 \sqrt{T_{o5}}}{P_{o5}} \right)_{\text{des}} \frac{P_{o4}}{P_{o3}} \frac{P_{o3}}{P_{o2}}}{\left. \frac{\dot{m}_5 \sqrt{T_{o5}}}{P_{o5}} \right)_{\text{des}} \frac{P_{o4}}{P_{o3}} \frac{P_{o3}}{P_{o2}}}_{\text{des}} \sqrt{\frac{1}{\phi_{\text{HP}}}} \sqrt{\frac{T_{o3}}{T_{o2}}}_{\text{des}} \quad \text{D.2.25}$$

$$\dot{m}_2 = \frac{\dot{m}_2 \sqrt{T_{o2}}}{P_{o2}} \frac{P_{o2}}{\sqrt{T_{o2}}} \quad \text{D.2.26}$$

For the LP compressor outlet,

$$P_{o3} = P_{o2} \frac{P_{o3}}{P_{o2}} \quad \text{D.2.27}$$

$$T_{o3} = T_{o2} \frac{T_{o3}}{T_{o2}} \quad \text{D.2.28}$$

$$\left. \frac{\dot{m}_3 \sqrt{T_{o3}}}{P_{o3}} = \frac{\dot{m}_3 \sqrt{T_{o3}}}{P_{o3}} \right)_{\text{des}} \left. \frac{\frac{\dot{m}_2 \sqrt{T_{o2}}}{P_{o2}} \frac{P_{o3}}{P_{o2}}}{\frac{\dot{m}_2 \sqrt{T_{o2}}}{P_{o2}}} \right)_{\text{des}} \frac{P_{o3}}{P_{o2}} \sqrt{\frac{T_{o3}}{T_{o2}}} \quad \text{D.2.29}$$

$$\dot{m}_3 = \frac{\dot{m}_3 \sqrt{T_{o3}}}{P_{o3}} \frac{P_{o3}}{\sqrt{T_{o3}}} \quad \text{D.2.30}$$

For the HP compressor outlet,

$$P_{o4} = P_{o3} \frac{P_{o4}}{P_{o3}} \quad \text{D.2.31}$$

$$T_{o4} = T_{o3} \frac{T_{o4}}{T_{o3}} \quad \text{D.2.32}$$

$$\dot{m}_4 = \dot{m}_3 \quad \text{D.2.33}$$

For the HP turbine inlet,

$$P_{o5} = P_{o4} \frac{P_{o5}}{P_{o4}} \Big)_{\text{des}} \quad \text{D.2.34}$$

$$T_{o5} = T_{o3} \left. \phi_{HP} \frac{T_{o5}}{T_{o3}} \right)_{des} \quad D.2.35$$

$$\dot{m}_f = \dot{m}_4 \frac{c_{pg} T_{o5} - c_{pa} T_{o4}}{\eta_B Q} \quad D.2.36$$

$$\dot{m}_5 = \dot{m}_4 + \dot{m}_f \text{ or } \dot{m}_5 = \frac{\dot{m}_5 \sqrt{T_{o5}}}{P_{o5}} \frac{P_{o5}}{\sqrt{T_{o5}}} \quad D.2.37$$

For the HP turbine outlet,

$$P_{o6} = P_{o5} \frac{P_{o6}}{P_{o5}} \quad D.2.38$$

$$T_{o6} = T_{o5} \frac{T_{o6}}{P_{o5}} \quad D.2.39$$

$$\dot{m}_6 = \dot{m}_5 \text{ or } \dot{m}_6 = \frac{\dot{m}_6 \sqrt{T_{o6}}}{P_{o6}} \frac{P_{o6}}{\sqrt{T_{o6}}} \quad D.2.40$$

For the LP turbine outlet,

$$P_{o7} = P_{o6} \frac{P_{o7}}{P_{o6}} \quad D.2.41$$

$$T_{o7} = T_{o6} \frac{T_{o7}}{P_{o6}} \quad D.2.42$$

$$\dot{m}_7 = \dot{m}_6 \text{ or } \dot{m}_7 = \frac{\dot{m}_7 \sqrt{T_{o7}}}{P_{o7}} \frac{P_{o7}}{\sqrt{T_{o7}}} \quad D.2.43$$

For the free power turbine outlet,

$$P_{o8} = P_{o7} \frac{P_{o8}}{P_{o7}} \quad \text{D.2.44}$$

$$T_{o8} = T_{o7} \frac{T_{o8}}{T_{o7}} \quad \text{D.2.45}$$

$$\dot{m}_8 = \dot{m}_7 \quad \text{D.2.46}$$

For the exhaust duct,

$$P_{o9} = P_{o8} \frac{P_{o9}}{P_{o8}} \approx P_o \quad \text{D.2.47}$$

$$T_{o9} \approx T_{o8} \quad \text{D.2.48}$$

$$\dot{m}_9 = \dot{m}_8 \quad \text{D.2.49}$$

If the gas turbine in question is a two-spool turbojet, its thrust can be calculated as per the theory discussed in the latter portion of Appendix D.1.5. If the power output, PWR, of the gas turbine is required, it can be calculated by,

$$\text{PWR} = \dot{m}_7 c_{pg} (T_{o7} - T_{o8}) \quad \text{D.2.50}$$

If the free power turbine was replaced by a power-turbine-equivalent converging nozzle, as done in pass-off performance test of the industrial RB211, only the exhaust gas power output, EGHP, can be calculated. This can be accomplished by,

$$\text{EGHP} = \dot{m}_7 c_{pg} T_{o7} \left[ 1 - \left( \frac{P_{o8}}{P_{o7}} \right)^{\frac{\gamma-1}{\gamma}} \right] \quad \text{D.2.51}$$

Finally, the specific fuel consumption, SFC, of the gas turbine can be calculated by,

$$\text{SFC} = \frac{\dot{m}_f}{\text{PWR}} \quad \text{D.2.52}$$

or,

$$\text{SFC} = \frac{\dot{m}_f}{\text{EGHP}} \quad \text{D.2.53}$$

This is the full solution process of the core control method for a two-spool gas generator with a free power turbine.

### D.3 Aerodynamic Coupling of the LP and HP Spools

The work balance between the LP compressor and LP turbine can be expressed by,

$$\dot{m}_2 c_{pa} (T_{o3} - T_{o2}) = \eta_m \dot{m}_6 c_{pg} (T_{o6} - T_{o7}) \quad \text{D.3.1}$$

which is then rearranged to determine the LP compressor temperature ratio,  $\frac{T_{o3}}{T_{o2}}$ , using the core control parameter,  $\phi_{HP}$ , through Equation 4.5.5.

However, Equation 4.5.4 can also be rearranged such that  $\frac{T_{o3}}{T_{o2}}$  is expressed as a

function of the LP spool temperature ratio,  $\phi_{LP}$ , as,

$$\frac{T_{o3}}{T_{o2}} = 1 + \phi_{LP} \left[ \left( \frac{T_{o3}}{T_{o2}} \right)_{des} - 1 \right] \frac{1 - \frac{T_{o7}}{T_{o6}}}{1 - \left( \frac{T_{o7}}{T_{o6}} \right)_{des}} \quad \text{D.3.2}$$

where,

$$\phi_{LP} = \frac{\frac{T_{o6}}{T_{o2}}}{\left( \frac{T_{o6}}{T_{o2}} \right)_{des}} \quad \text{D.3.3}$$

If the LP spool temperature ratio can be expressed by the HP spool temperature ratio, i.e.,  $\phi_{HP}$ , an equation that represents the aerodynamic coupling between the LP and HP spools can be obtained.

From the definition of  $\phi_{LP}$ , it can be shown that,

$$\phi_{LP} = \frac{\frac{T_{o6}}{T_{o5}}}{\left(\frac{T_{o6}}{T_{o5}}\right)_{des}} \frac{\frac{T_{o5}}{T_{o3}}}{\left(\frac{T_{o5}}{T_{o3}}\right)_{des}} \frac{\frac{T_{o3}}{T_{o2}}}{\left(\frac{T_{o3}}{T_{o2}}\right)_{des}} \quad D.3.4$$

or,

$$\phi_{LP} = \phi_{HP} \frac{\frac{T_{o6}}{T_{o5}}}{\left(\frac{T_{o6}}{T_{o5}}\right)_{des}} \frac{\frac{T_{o3}}{T_{o2}}}{\left(\frac{T_{o3}}{T_{o2}}\right)_{des}} \quad D.3.5$$

Therefore, Equation D.3.5 can be considered a representation of the aerodynamic coupling between the LP and HP spools.

## **D.4 Simulation of Bleed Flows in the Core Control Method**

### **D.4.1 Introduction**

This section discusses the theory and implementation of bleed flows in the core control method. Cooling bleed flows is first discussed, after which handling bleeds is discussed.

Figure D.5 contains a detailed schematic of a bleed system in a single-spool turbojet, which can be readily modified to suit a multi-spool gas turbine.

Although the theories of cooling and handling bleeds are discussed separately, the concatenated effect of these bleed flows can be obtained by simply combining the theories.

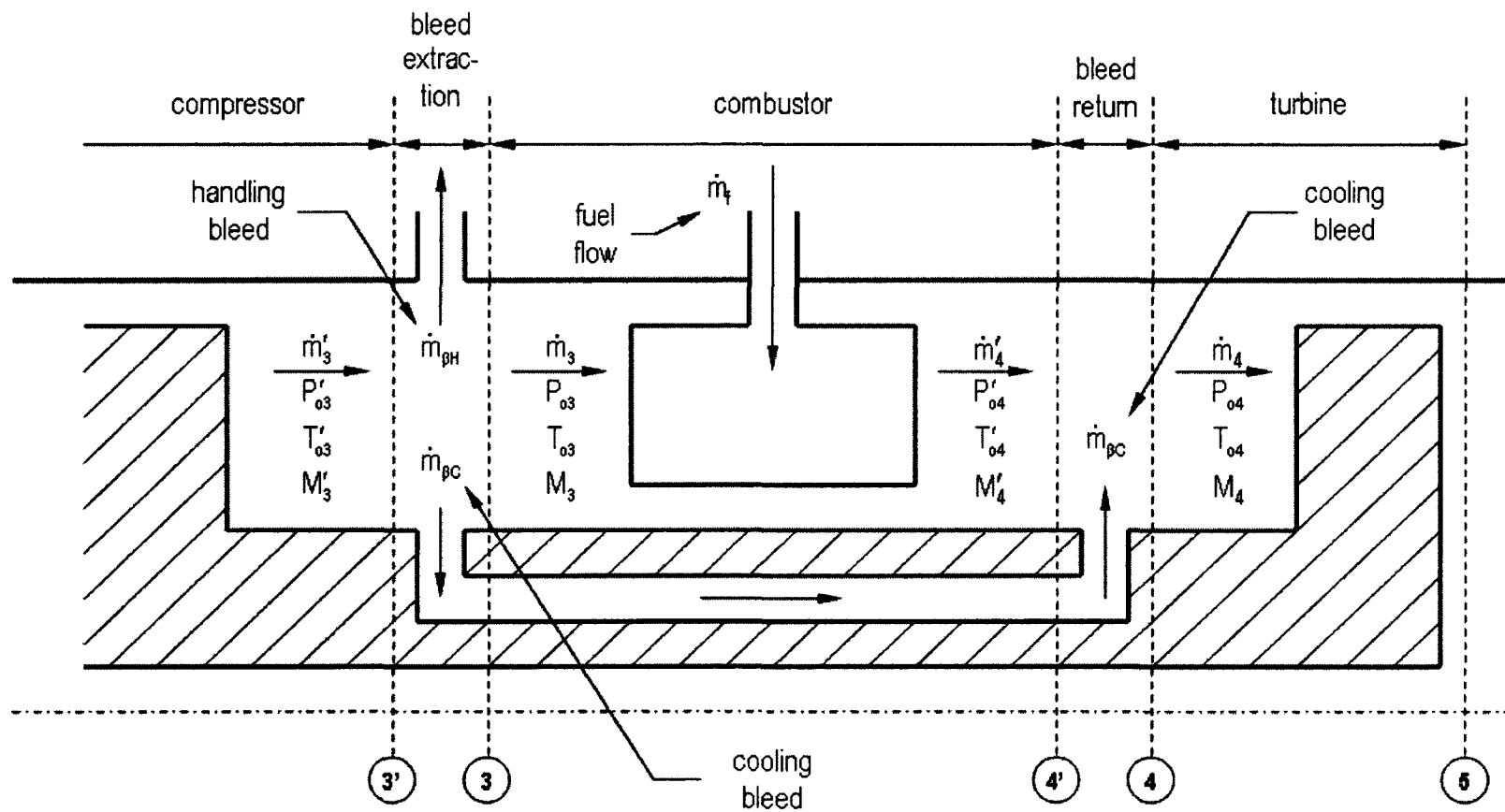


**Figure D.5** Bleed flows of a single-spool turbojet

#### D.4.2 Cooling Bleed Flows

The purpose of a cooling bleed flow is to protect the turbines from the exhaust gases. A cooling bleed flow rate,  $\dot{m}_{\beta C}$ , extracted from a compressor delivery flow rate,  $\dot{m}'_3$ , results in a combustor entry mass flow rate,  $\dot{m}_3$ , of,

$$\dot{m}_3 = \dot{m}'_3 - \dot{m}_{\beta C} \quad \text{D.4.1}$$

where  $\dot{m}_3 = \dot{m}_2$ , which is the compressor inlet mass flow rate (Figure D.5).

A bleed flow rate is typically expressed as a fraction with respect to the inlet mass flow rate of the respective compressor. Therefore, the cooling bleed fraction,  $\beta_C$ , can be expressed as,

$$\beta_C = \frac{\dot{m}_{\beta C}}{\dot{m}_2} \quad \text{D.4.2}$$

The combustor outlet temperature,  $T'_{o4}$ , can then be determined by,

$$T'_{o4} \approx \frac{c_{pg} T_{o4} - \beta_C c_{pa} T_{o3}}{(1 - \beta_C) c_{pg}} \quad \text{D.4.3}$$

Using which, the fuel flow rate,  $\dot{m}_f$ , can be then calculated by,

$$\dot{m}_f = \dot{m}_3 \frac{c_{pg} T'_{o4} - c_{pa} T_{o3}}{\eta_B Q} \quad \text{D.4.4}$$

### D.4.3 Handling Bleed Flows

Here, it is assumed that the handling bleed fraction,  $\beta_H$ , is extracted downstream of the compressor. The process of determining the effect of handling bleeds on engine performance is a two-tier process. The first step involves determining the performance change in the compressor as a result of the bleed extraction, where the second step involves determining the performance change due to the altered fuel consumption rate.

#### Performance Change in the Compressor

For a given iteration in the solution process,  $\frac{\dot{m}_2 \sqrt{T_{o2}}}{P_{o2}}$ ,  $\frac{P'_{o3}}{P_{o2}}$ , and  $\frac{T'_{o3}}{T_{o2}}$  are known. Here the prime (') is habitually omitted in normal engine performance calculations. Then, the compressor outlet mass flow rate,  $\dot{m}'_3$  is calculated by,

$$\dot{m}'_3 \equiv \frac{\dot{m}_2 \sqrt{T_{o2}}}{P_{o2}} \frac{P_{o2}}{\sqrt{T_{o2}}} \quad \text{D.4.5}$$

Next, a static compressor outlet temperature,  $T'_3$ , is assumed, using which the compressor outlet flow speed,  $V'_3$ , is calculated by,

$$V'_3 \equiv \sqrt{2 c_{pa} (T'_{o3} - T'_3)} \quad \text{D.4.6}$$

where

$$T'_{o3} = T_o \frac{T'_{o3}}{T_{o2}} \frac{T_{o2}}{T_{o1}} \frac{T_{o1}}{T_o} \quad \text{D.4.7}$$

Next, the compressor outlet static pressure,  $P'_3$ , is found by,

$$P'_3 = P'_{o3} \left( \frac{T'_3}{T'_{o3}} \right)^{\frac{\gamma}{\gamma-1}} \quad \text{D.4.8}$$

where

$$P'_{o3} = P_o \frac{P'_{o3} P_{o2} P_{o1}}{P_{o2} P_{o1} P_o} \quad \text{D.4.9}$$

Using the perfect gas law, the compressor outlet flow density,  $\rho'_3$ , can now be calculated by,

$$\rho'_3 = \frac{P'_3}{RT'_3} \quad \text{D.4.10}$$

using which, the compressor outlet mass flow rate can be recalculated from,

$$\dot{m}'_3 = \rho'_3 V'_3 A'_3 \quad \text{D.4.11}$$

where  $A'_3$  is the annulus area upstream of the handling bleed valve.

$T'_3$  is then iterated until Equation D.4.5 and Equation D.4.11 converge. Next, the mass flow rate downstream of the handling bleed valve,  $\dot{m}_3$ , can be determined by,

$$\dot{m}_3 = (1 - \beta_H) \dot{m}'_3 \quad \text{D.4.12}$$

This can then be expanded to give,

$$\rho_3 V_3 A_3 = (1 - \beta_H) \rho'_3 V'_3 A'_3 \quad \text{D.4.13}$$

where  $A_3$  is the annulus area downstream of the handling bleed valve.

Rearranging Equation D.4.13, the flow speed downstream of the handling bleed valve,  $V_3$ , can be expressed by,

$$V_3 = (1 - \beta_H) \left( \frac{T'_3}{T_3} \right)^{\frac{1}{\gamma-1}} \frac{A'_3}{A_3} V'_3 \quad \text{D.4.14}$$

where  $T_3$  is the only unknown, and it is assumed that  $\frac{A'_3}{A_3} \approx 1$ .

Therefore, for an assumed  $T_3$ , the Mach number downstream of the handling bleed valve,  $M_3$ , can be calculated by,

$$M_3 = \frac{V_3}{\sqrt{\gamma R T_3}} \quad \text{D.4.15}$$

and the total temperature,  $T_{o3}$ , by,

$$T_{o3} = T_3 + \frac{V_3^2}{2 c_{pa}} \quad \text{D.4.16}$$

Then, the static and total pressures can be calculated by,

$$P_3 = (1 - \beta_H) \frac{V'_3}{V_3} \frac{T_3}{T'_3} \frac{A'_3}{A_3} P'_3 \quad \text{D.4.17}$$

and,

$$P_{o3} = P'_{o3} \left( \frac{T_{o3}}{T'_{o3}} \right)^{\frac{\gamma}{\gamma-1}} \quad \text{D.4.18}$$

respectively. Using the compressible flow relationships,  $M_3$  can then be recalculated using,

$$M_3 = \sqrt{\frac{2}{\gamma-1} \left[ \left( \frac{P_{o3}}{P_3} \right)^{\frac{\gamma-1}{\gamma}} - 1 \right]} \quad \text{D.4.19}$$

$T_3$  is then iteratively searched until Equation D.4.15 and Equation D.4.19 converge. At the conclusion of this process, the total pressure and temperature downstream of the handling bleed valve is found, which is then used to calculate the updated compressor pressure and temperature ratio.

### Change in the Fuel Consumption

Due to the reduction of mass flow into the combustor as a result of the handling bleed extraction, the fuel-to-air ratio,  $f$ , of the combustor increases if the fuel flow rate is held constant since,

$$f = \frac{\dot{m}_f}{\dot{m}_3} \equiv \frac{\dot{m}_f}{\dot{m}_2 (1 - \beta_H)} \quad \text{D.4.20}$$

Here, note that Equation D.4.20 can also be expressed as,

$$\frac{\dot{m}_f}{\dot{m}_2} = (1 - \beta_H) \frac{c_{pg} T_{o4} - c_{pa} T_{o3}}{\eta_B Q} \quad \text{D.4.21}$$

With the increase in the fuel-to-air ratio, the combustor outlet temperature,  $T_{o4}$ , will increase as well. These variations in the fuel-to-air ratio and  $T_{o4}$  are of no consequence to the turbine corrected mass flow rate,  $\frac{\dot{m}_4 \sqrt{T_{o4}}}{P_{o4}}$ , as long as its magnitude is held constant prior to and after opening of the handling bleed valve at a given power setting. With  $\frac{\dot{m}_4 \sqrt{T_{o4}}}{P_{o4}}$  already known from the solution process (Appendix D.1 and Appendix D.2), the increase in  $f$  and  $T_{o4}$  can therefore be iteratively calculated by,

$$\frac{\dot{m}_4 \sqrt{T_{o4}}}{P_{o4}} = \frac{[\dot{m}_f + (1 - \beta_H) \dot{m}'_3] \sqrt{\frac{\dot{m}_f \eta_B Q (1 - \beta_H)}{\dot{m}'_3 c_{pg}} + \frac{c_{pa}}{c_{pg}} T_{o3}}}{P_{o4}} \quad \text{D.4.22}$$

**APPENDIX E      DETERIORATED ENGINE  
PERFORMANCE**

## E.1 Non-Dimensionalizing Predicted and Actual Performance

This section discusses the method by which the actual and predicted engine performance data are non-dimensionalized.

Let a performance parameter be expressed by  $X$ . Then, let  $X_{des}$  represent the design-point performance,  $X_{site}$  represent the performance at site, and  $X_{site})_{first}$  represent the first data point at site.

Then, the non-dimensionalized performance parameter,  $X_{ND}$ , is obtained by,

$$X_{ND} = 1 + \frac{X_{site} - X_{site})_{first}}{X_{des}} \quad \text{E.1.1}$$

Here, non-dimensionalization through  $\frac{X_{site}}{X_{des}}$  was not chosen since one may obtain the magnitude by which the power output and fuel flow rate of the industrial RB211 increase with respect to its operating life, whereas Equation E.1.1 simply translates the non-dimensionalized data to an initial value of unity while maintaining its original form.

## E.2 Predicted and Actual Performance Data at Site

This section contains the core control method predictions of the site performance data of GT1, GT2 and GT3.

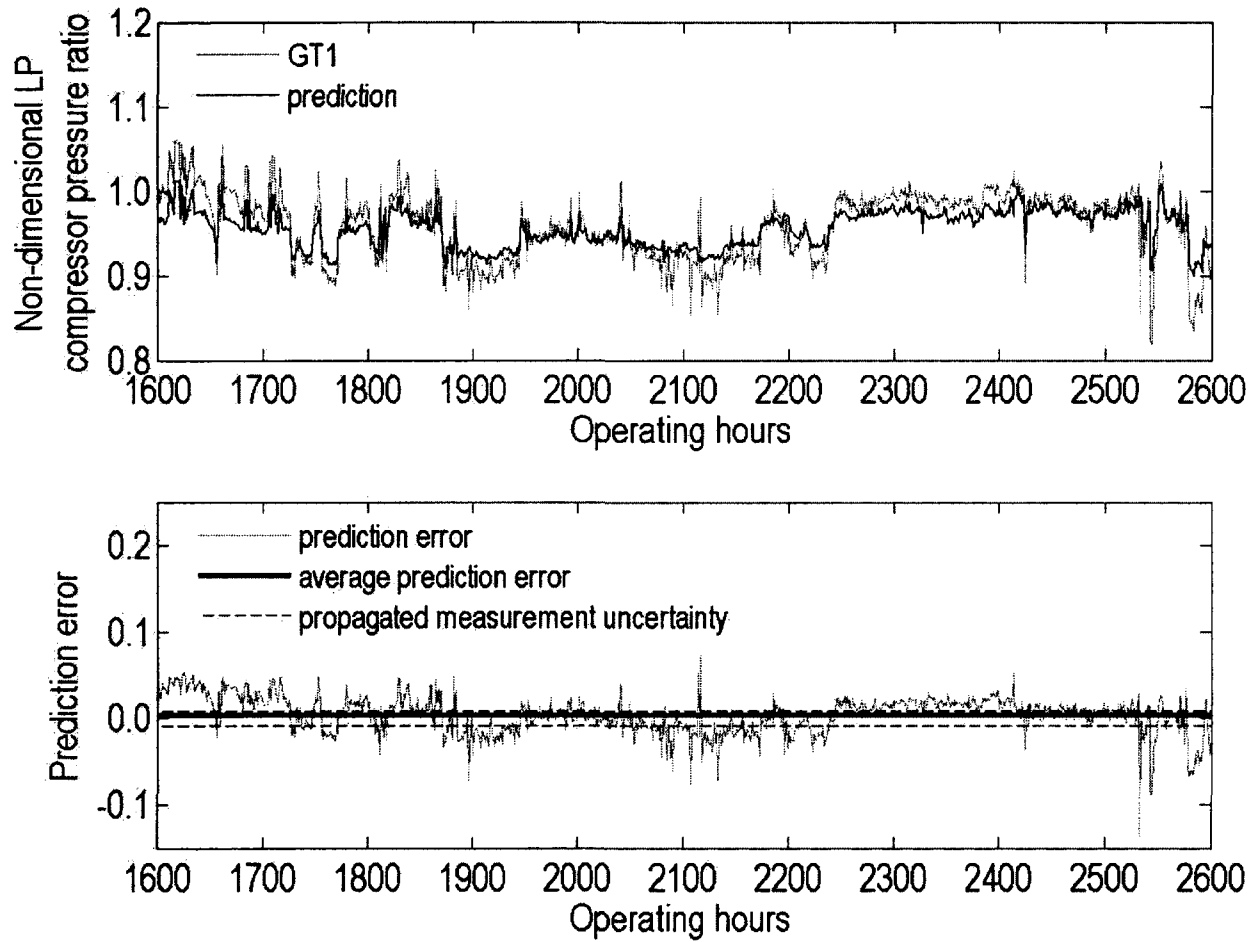


**Figure E.1** Non-dimensional LP compressor pressure ratio of GT1

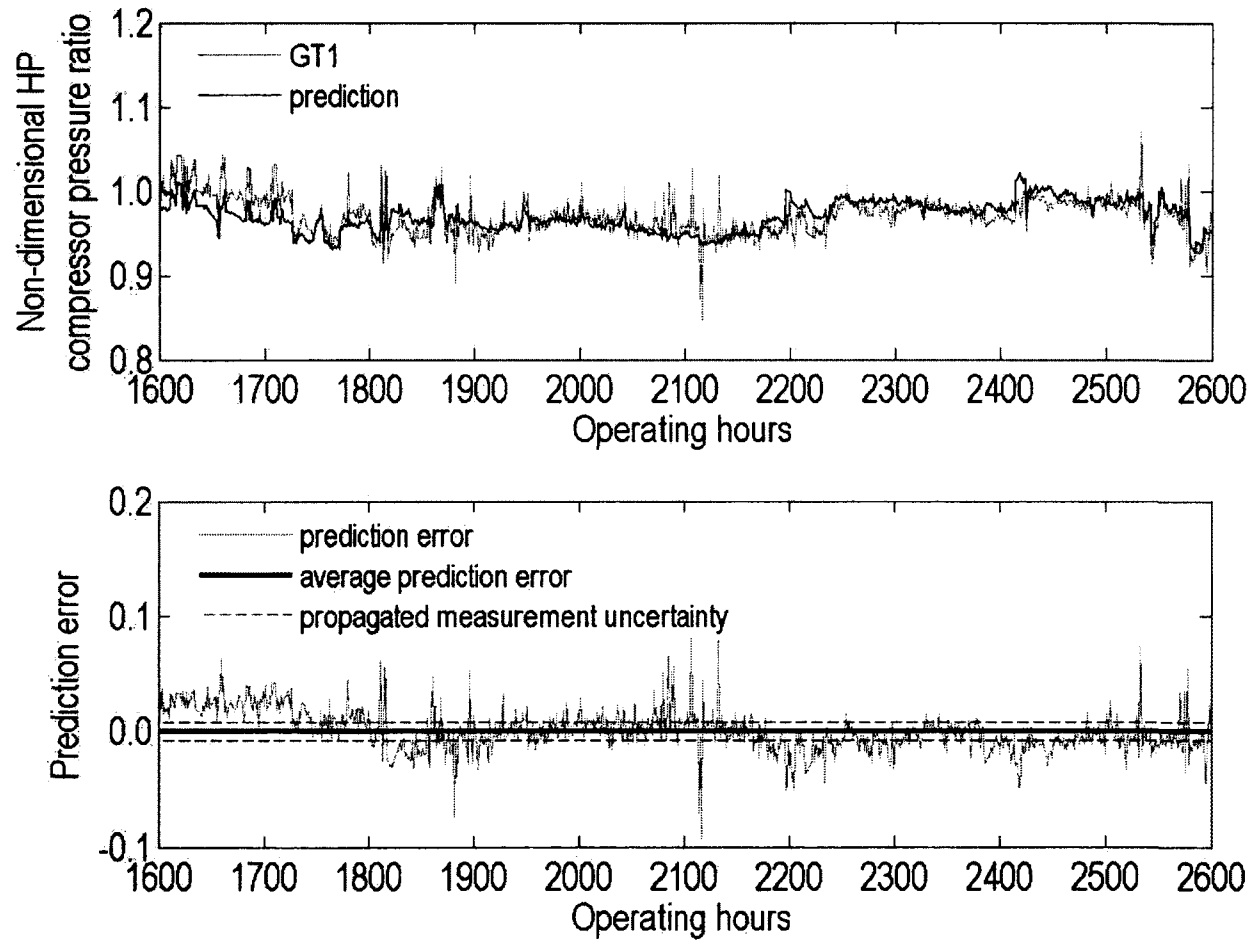


**Figure E.2** Non-dimensional HP compressor pressure ratio of GT1

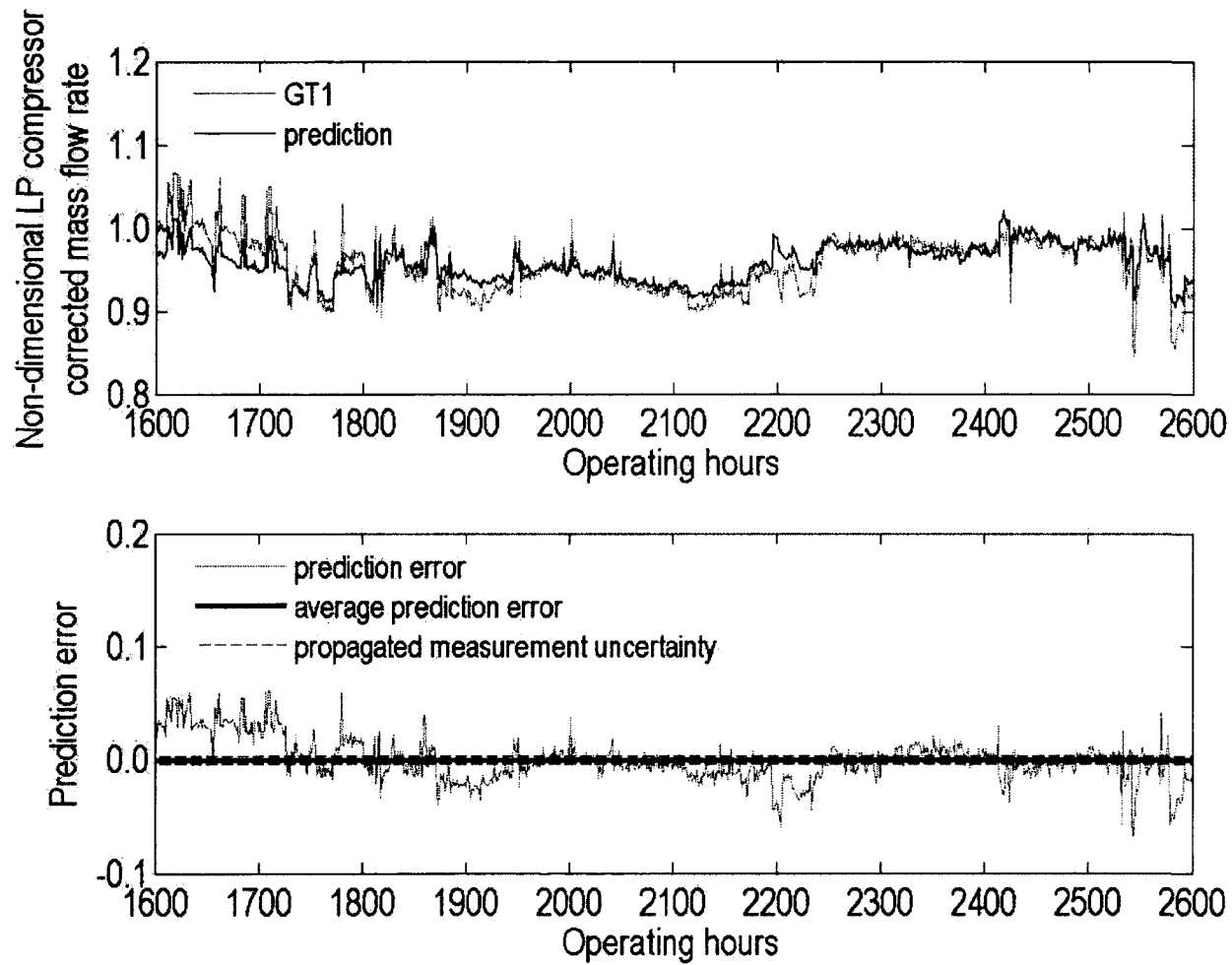


**Figure E.3** Non-dimensional LP compressor corrected mass flow rate of GT1

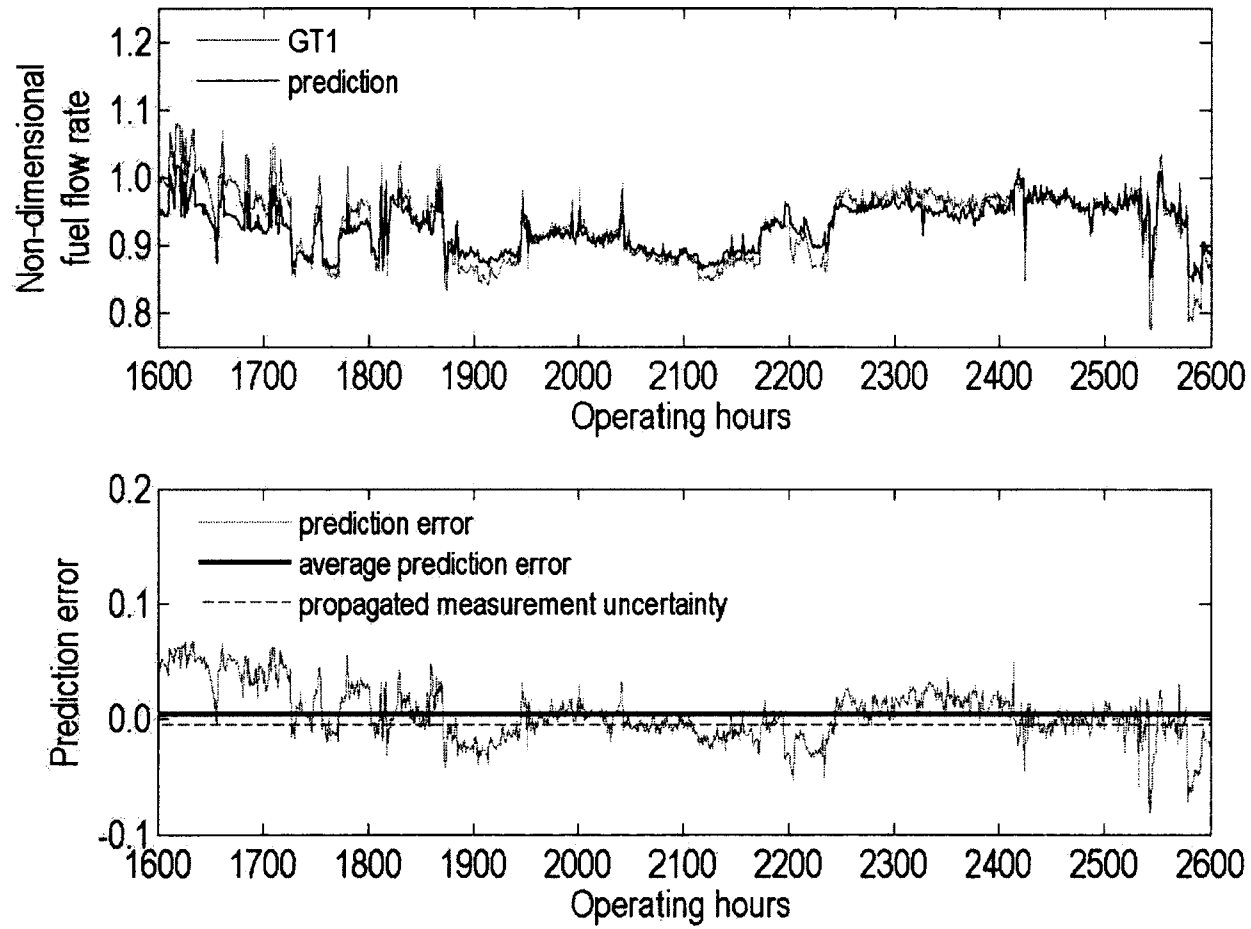


**Figure E.4** Non-dimensional fuel flow rate of GT1

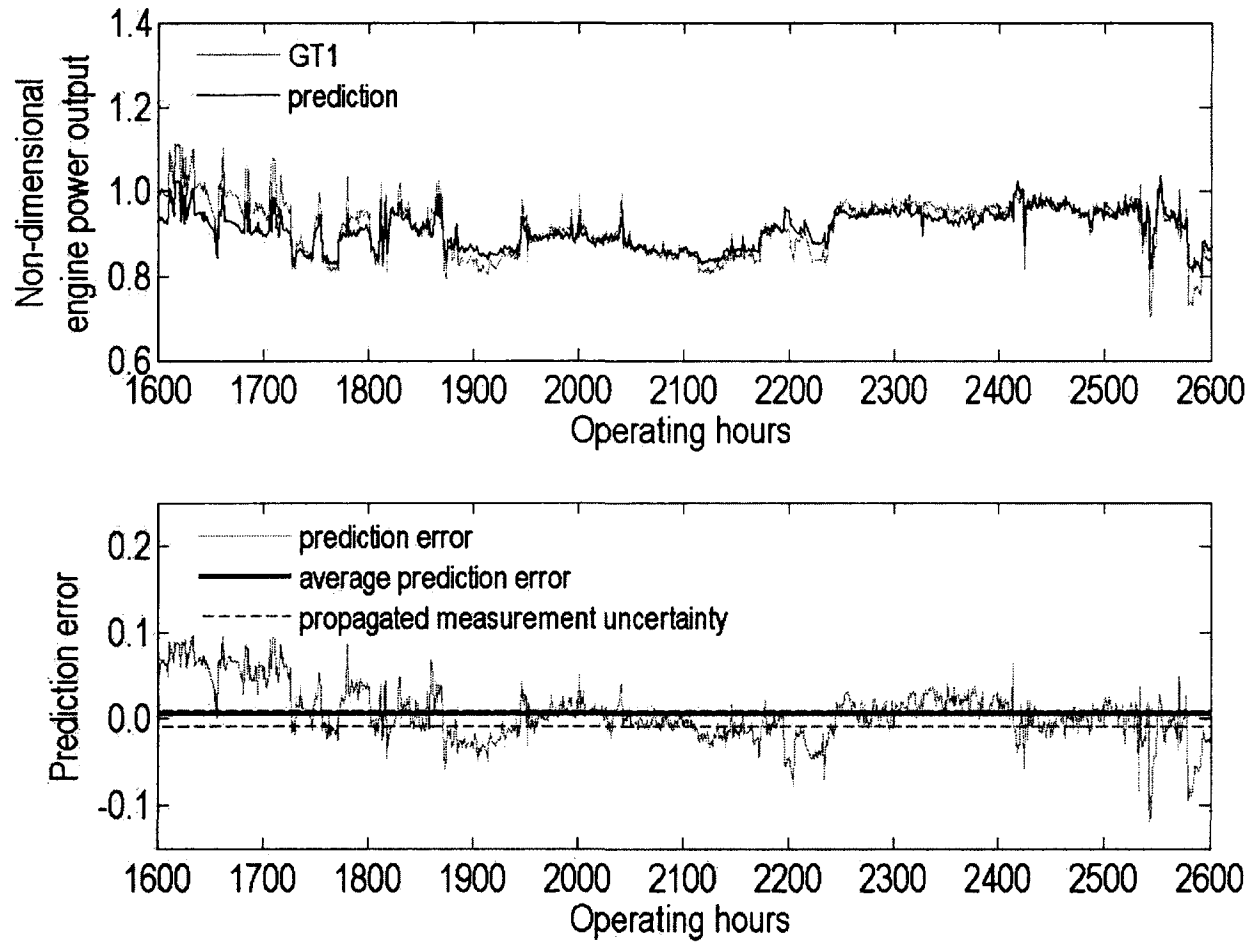


**Figure E.5** Non-dimensional power output of GT1

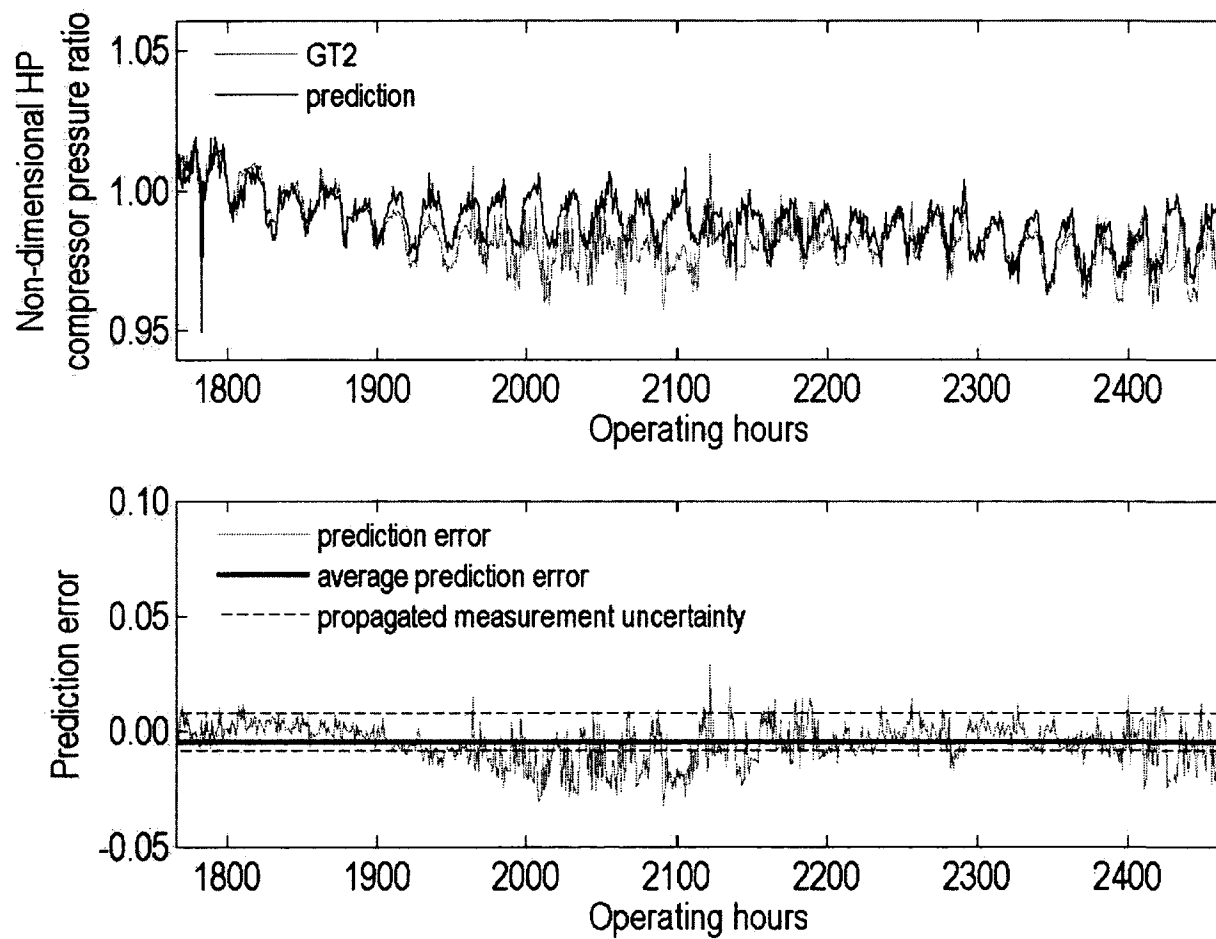


**Figure E.6** Non-dimensional HP compressor pressure ratio of GT2

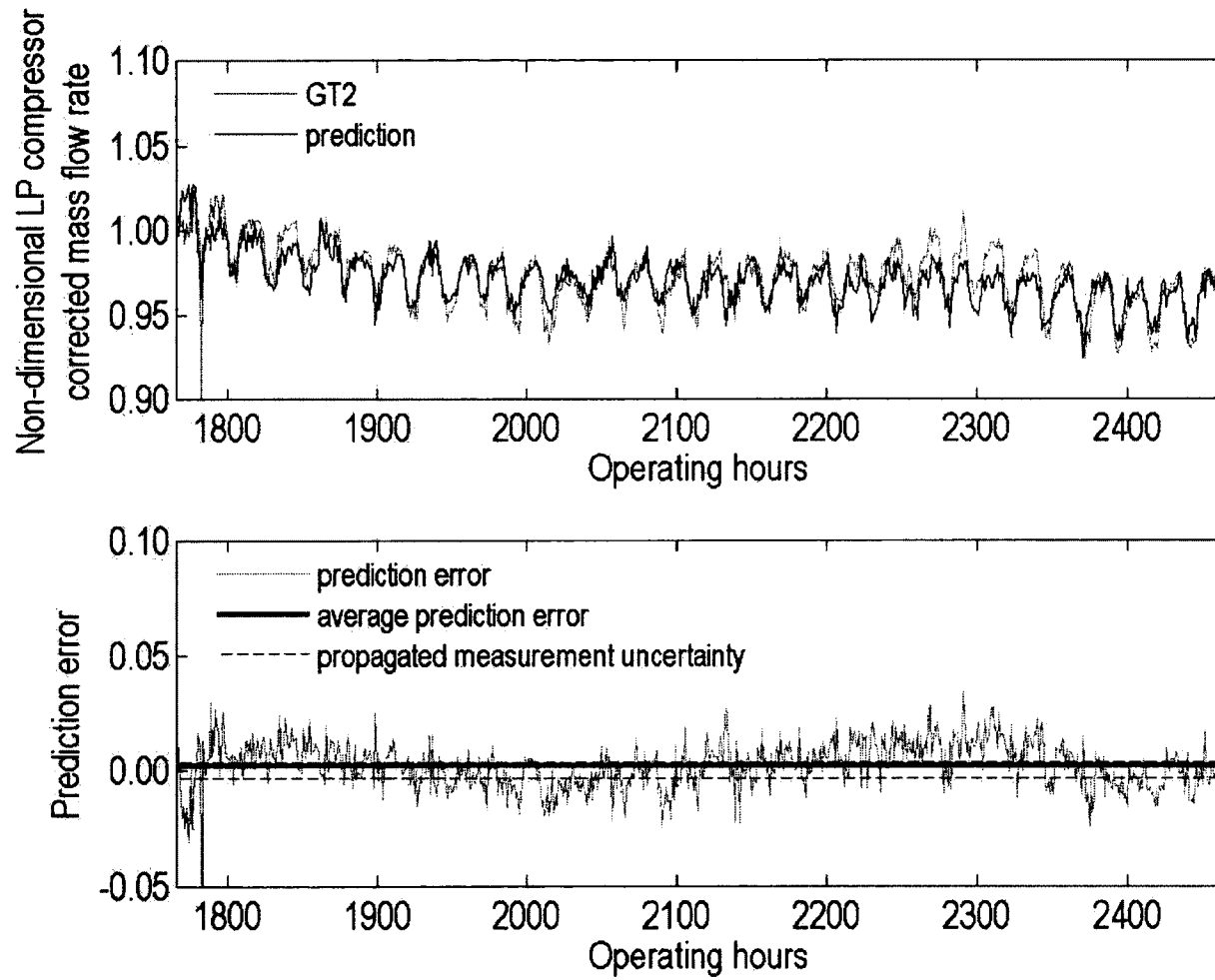


**Figure E.7** Non-dimensional LP compressor corrected mass flow rate of GT2

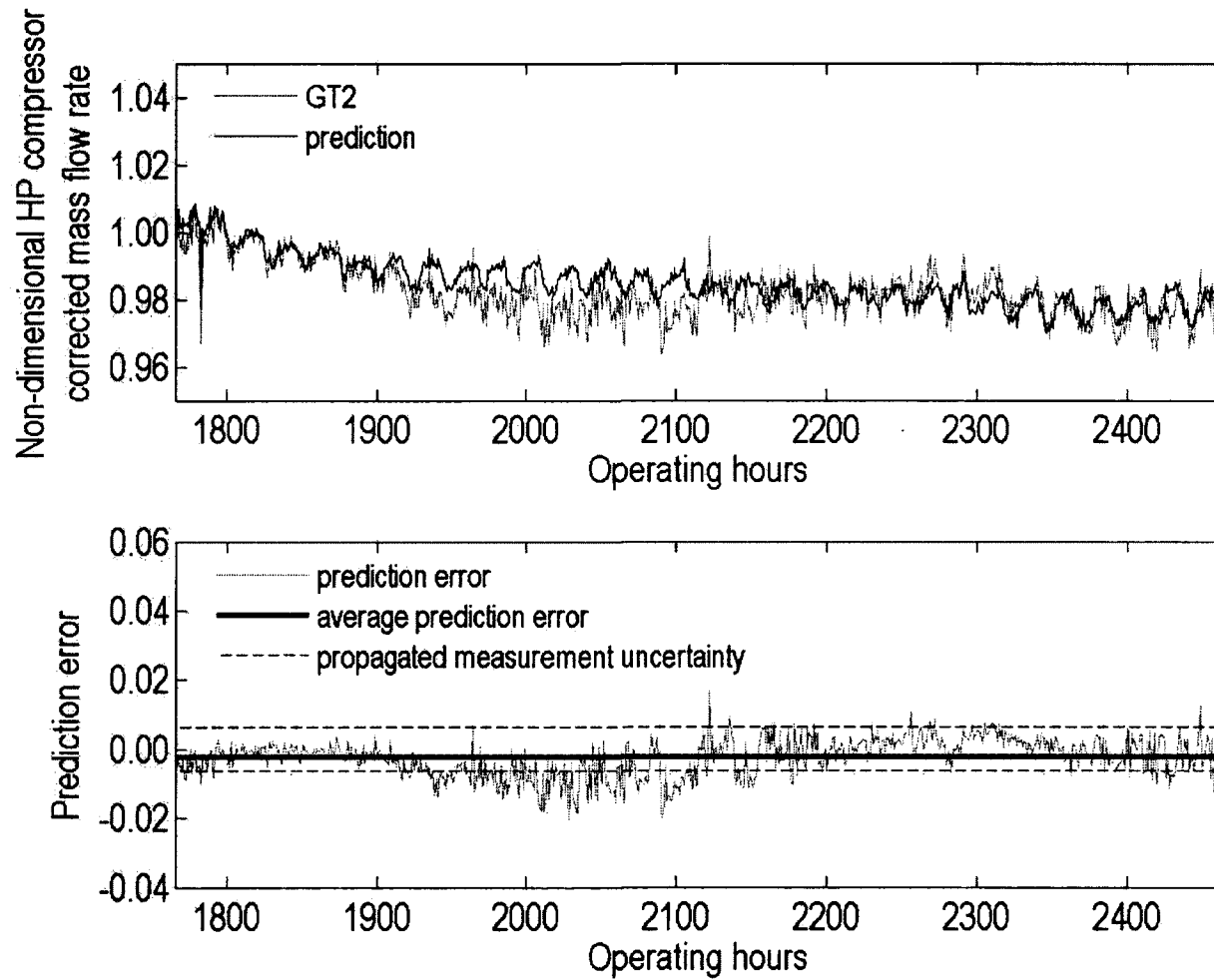


**Figure E.8** Non-dimensional HP compressor corrected mass flow rate of GT2

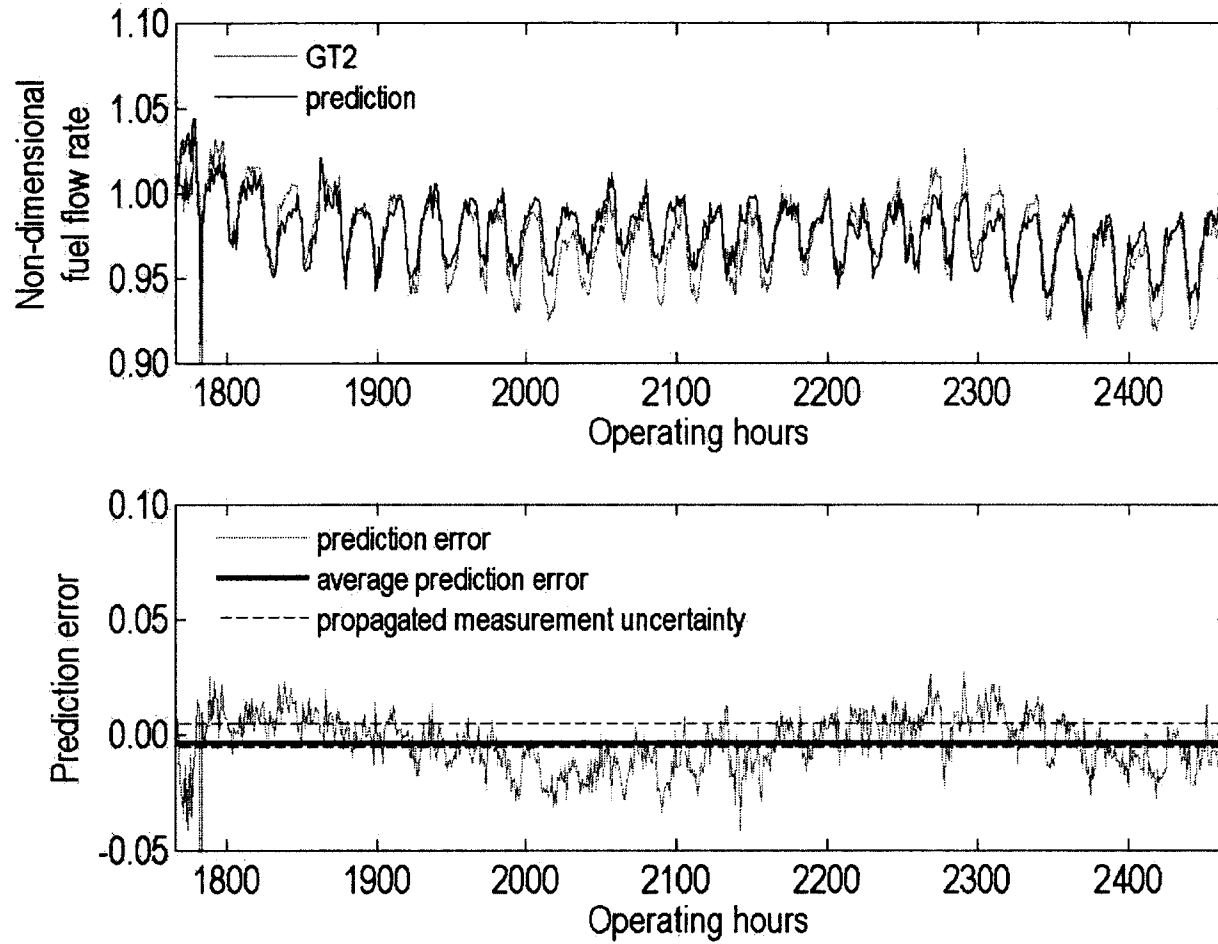


**Figure E.9** Non-dimensional fuel flow rate of GT2

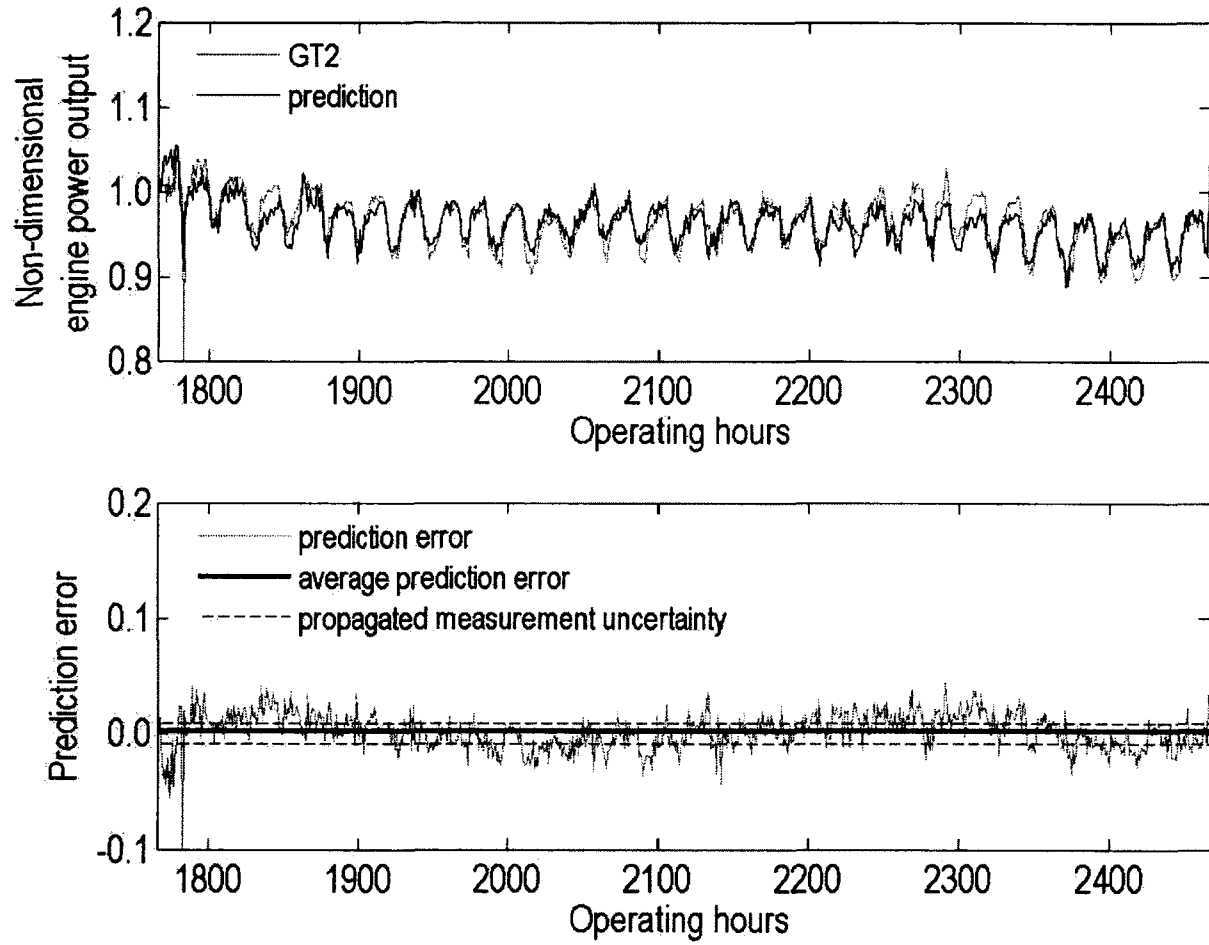
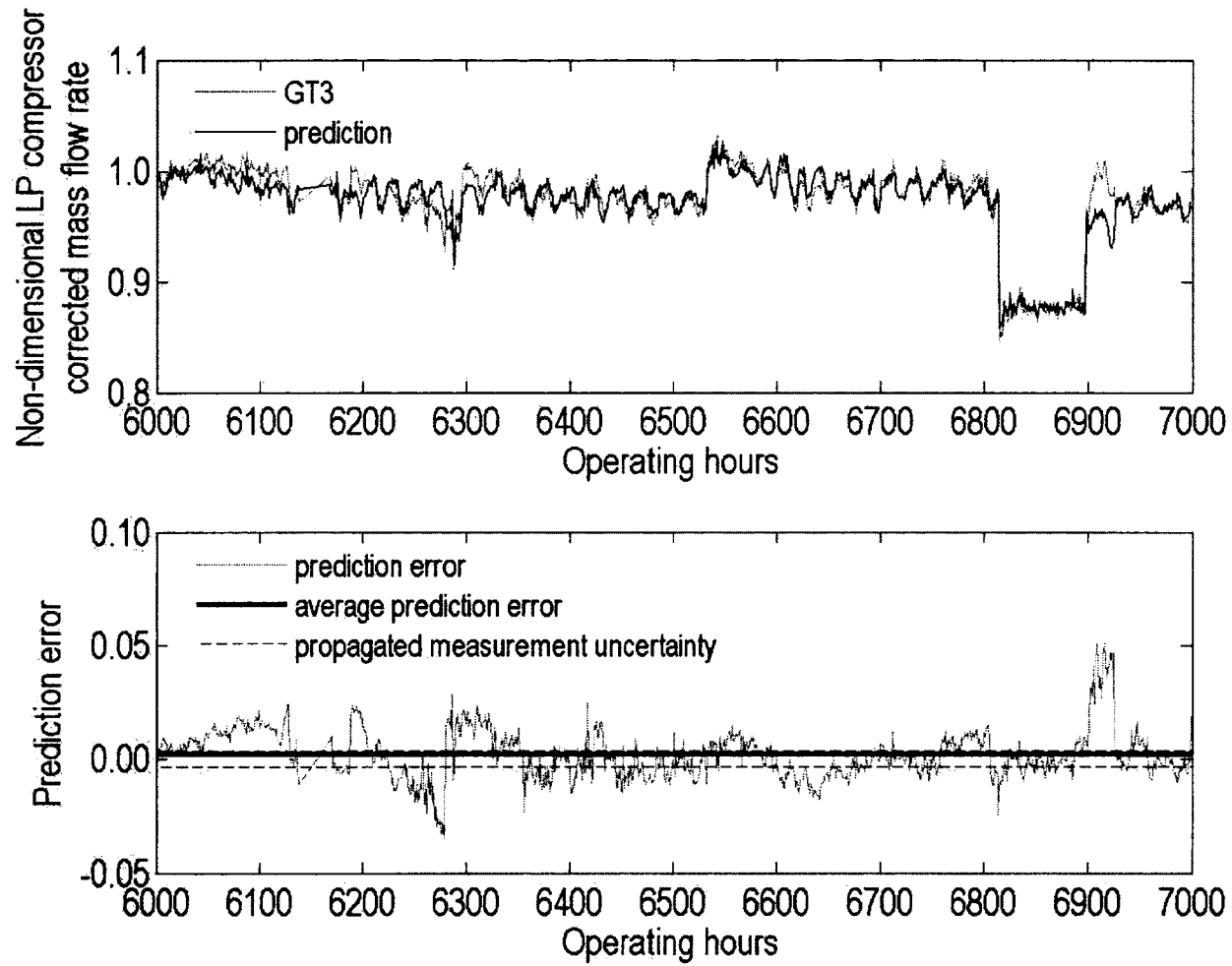
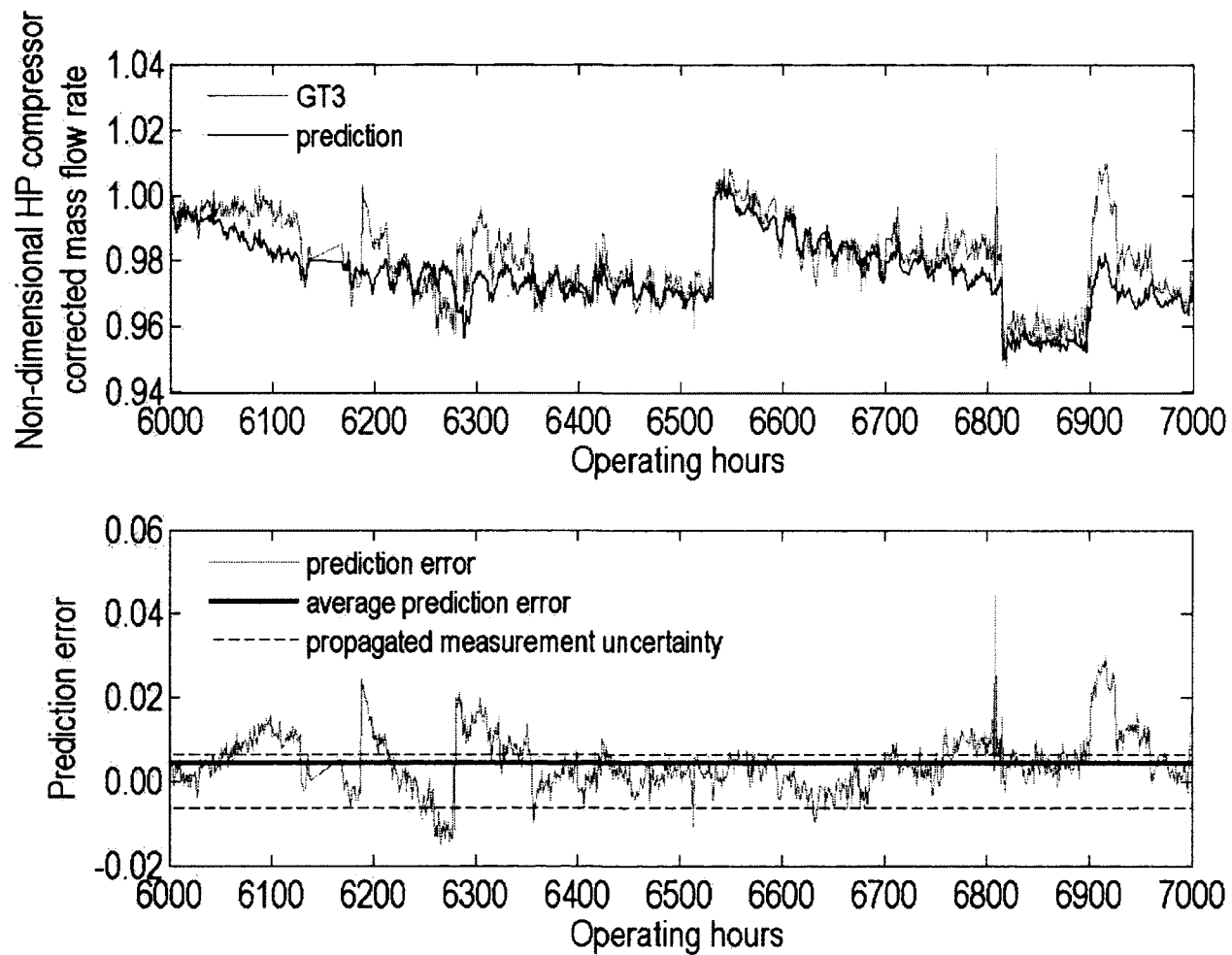


Figure E.10 Non-dimensional power output of GT2



**Figure E.11** Non-dimensional LP compressor corrected mass flow rate of GT3



**Figure E.12** Non-dimensional HP compressor corrected mass flow rate of GT3

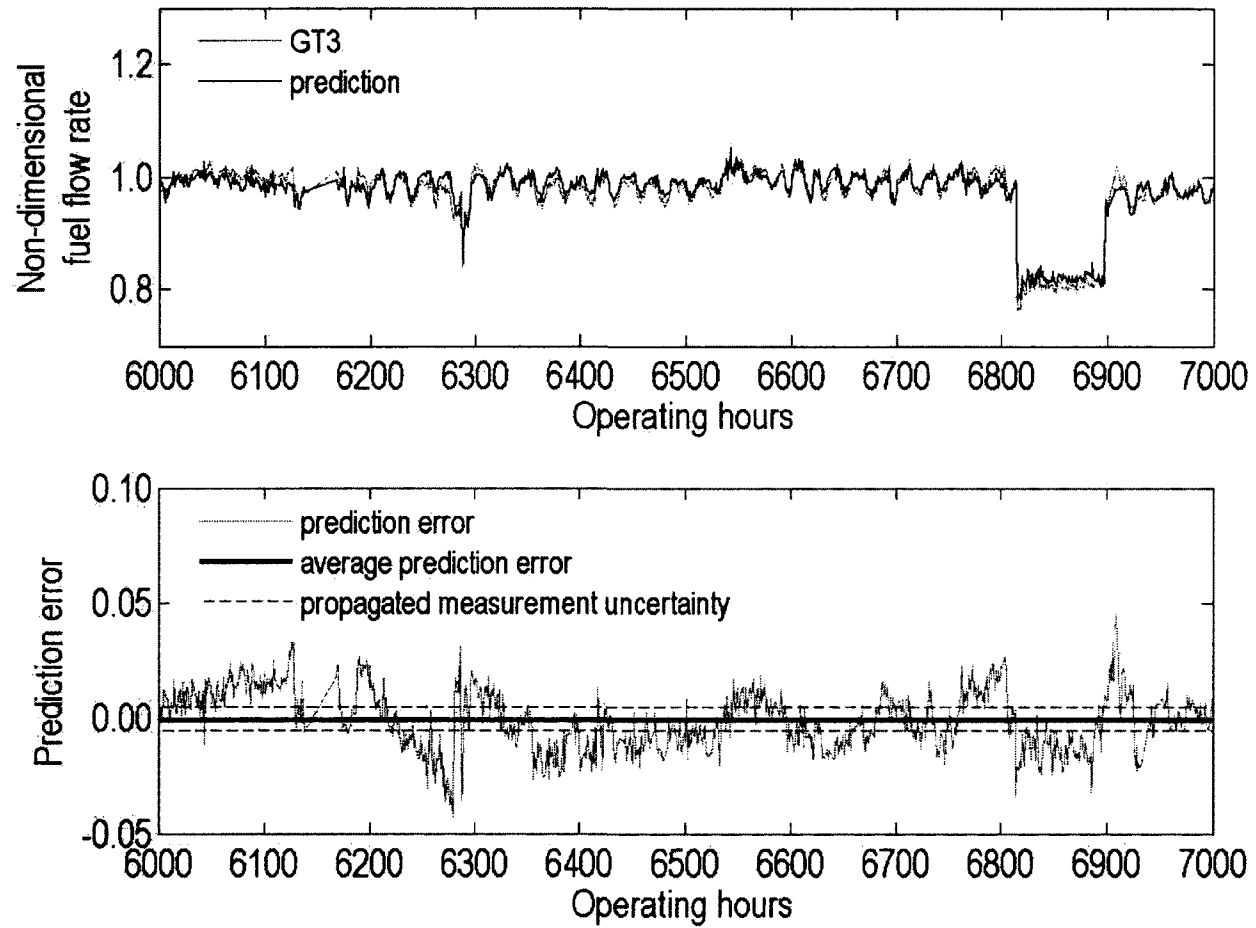


**Figure E.13** Non-dimensional fuel flow rate of GT3

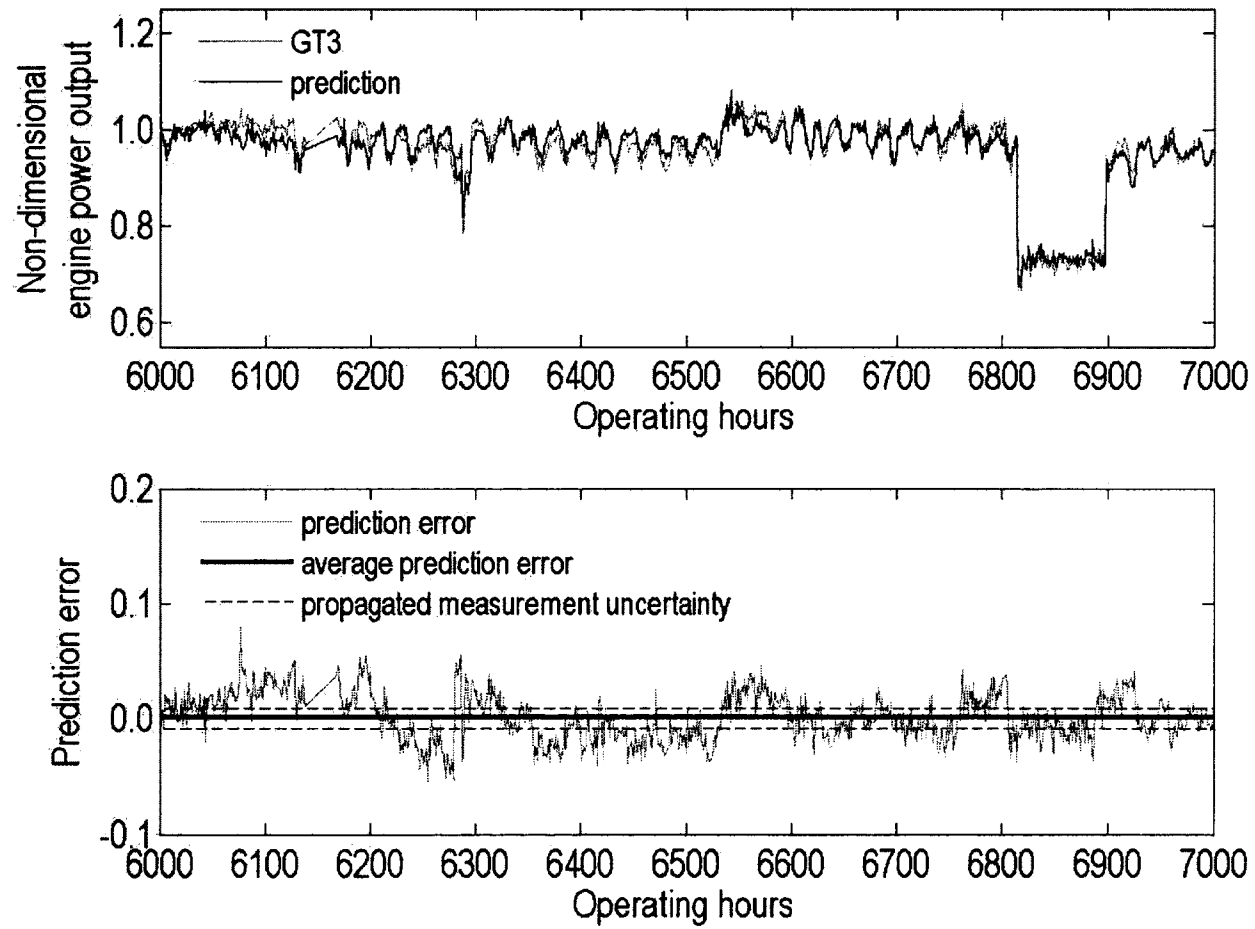


Figure E.14 Non-dimensional power output of GT3

## **APPENDIX F      MATLAB ALGORITHMS**



```

FCH4 = .8876;
FC2H6 = .04099;
FC3H8 = .006812;
FIC4H10 = .000849;
FNC4H10 = .001984;
FIC5H12 = .004004;
FNC5H12 = .00152;
FC6H14 = .001467;
FO2 = 0;
FN2 = .05402;
FCO2 = .000799;

molartotal = FCH4+FC2H6+FC3H8+FIC4H10+ ...
             FNC4H10+FIC5H12+FNC5H12+FC6H14+FO2+FN2+FCO2;

reality = 5555;

m = 250;
n = 400;
Q = zeros([n m]);

for j = 1:m
    for i = 1:n
        if reality == 5555
            UCH4 = leftU+rightU*rand;
            UC2H6 = leftU+rightU*rand;
            UC3H8 = leftU+rightU*rand;
            UIC4H10 = leftU+rightU*rand;
            UNC4H10 = leftU+rightU*rand;
            UIC5H12 = leftU+rightU*rand;
            UNC5H12 = leftU+rightU*rand;
            UC6H14 = leftU+rightU*rand;
            UO2 = leftU+rightU*rand;
            UN2 = leftU+rightU*rand;
            UCO2 = leftU+rightU*rand;
        else
            UCH4 = 0;
            UC2H6 = 0;
            UC3H8 = 0;
            UIC4H10 = 0;
            UNC4H10 = 0;
            UIC5H12 = 0;
            UNC5H12 = 0;
            UC6H14 = 0;
            UO2 = 0;
            UN2 = 0;
            UCO2 = 0;
        end
        FUCH4 = FCH4+UCH4;
        FUC2H6 = FC2H6+UC2H6;
        FUC3H8 = FC3H8+UC3H8;
        FUIC4H10 = FIC4H10+UIC4H10;
        FUNC4H10 = FNC4H10+UNC4H10;
        FUIC5H12 = FIC5H12+UIC5H12;
        FUNC5H12 = FNC5H12+UNC5H12;
        FUC6H14 = FC6H14+UC6H14;
    end
end

```

```

FUO2 = FO2+UO2;
FUN2 = FN2+UN2;
FUCO2 = FCO2+UCO2;
molartotalU = FUCH4+FUC2H6+FUC3H8+FUIC4H10+ ...
    FUNC4H10+FUIC5H12+FUNC5H12+FUC6H14+FUO2+FUN2+FUCO2;
% carbon
b = FUCH4+2*FUC2H6+3*FUC3H8+4*FUIC4H10+ ...
    4*FUNC4H10+5*FUIC5H12+5*FUNC5H12+6*FUC6H14+FUCO2;
% hydrogen
c = (4*FUCH4+6*FUC2H6+8*FUC3H8+10*FUIC4H10+ ...
    10*FUNC4H10+12*FUIC5H12+12*FUNC5H12+14*FUC6H14)/2;
% oxygen
a = (2*b+c-2*FUO2-2*FUCO2)/2;
% nitrogen
d = (2*FUN2+2*3.76*a)/2;
M = FUCH4*MCH4+FUC2H6*MC2H6+FUC3H8*MC3H8+FUIC4H10*MIC4H10+ ...
    FUNC4H10*MNC4H10+FUIC5H12*MIC5H12+FUNC5H12*MNC5H12+ ...
    FUC6H14*MC6H14+FUO2*MO2+FUN2*MN2+FUCO2*MCO2;
hRP = b*hCO2+c*hH2Og- ...
    (FUCH4*hCH4+FUC2H6*hC2H6+FUC3H8*hC3H8+FUIC4H10*hIC4H10+ ...
    FUNC4H10*hNC4H10+FUIC5H12*hIC5H12+FUNC5H12*hNC5H12+ ...
    FUC6H14*hC6H14+FUO2*ho2+FUN2*hn2+FUCO2*hCO2);
Q(i,j) = abs(hRP/M);
end
end

aQ = (sum(sum(Q)))/(n*m);

sigma = zeros([m 1]);
sigma95 = zeros([m 1]);
avQ = zeros([m 1]);

for i = 1:m
    sigma(i) = std(Q(:,i));
    sigma95(i) = tmat(length(1:i))* ...
        sqrt(sum(sigma(1:i).^2))/sqrt(length(1:i));
end

figure(1)
plot(1:m, (sigma95), 'k', 1:m, -(sigma95), 'k', [0 m], [0 0], '--k')
xlabel('Number of bundles', ...
    'FontSize',12,'FontName','Arial Narrow')
ylabel(['Fuel lower heating value uncertainty,', ...
    '\pmu_L_H_V_,_9_5_% [ kJ / kg ]'],'FontSize',12, ...
    'FontName','Arial Narrow')
text(m*.4,-100,[num2str(n),' sub-bundles per bundle'])
text(m*.4,-125,['calculated uncertainty = \pm', ...
    num2str(sigma95(m)),' kJ/kg'])
set(gca,'FontSize',12,'FontName','Arial Narrow')
axis([1 m -200 200])

```



```

T32des = To3/To2;
T42des = To4/To2;
T45des = To4/To5;

phi = [.566:.001:.57 .57:.01:1.15]'; % core control parameter

n = length(phi);

WRT2des = makes*sqrt(To2)/Po2;
WRT4des = (makes+mfdes)*sqrt(To4)/Po4;
WRT5des = (makes+mfdes)*sqrt(To5)/Po5;

% design-point polytropic efficiencies
ncdes = (.4/1.4)*log(P32des)/log(T32des);
ntdes = (1.333/.333)*log(T45des)/log(P45des);

% off-design efficiencies as a function of core control parameter
nc = 0.5715*phi.^5-3.2649*phi.^4+7.9788*phi.^3-10.0238*phi.^2+ ...
    6.1294*phi.^1-0.5060;
nt = -90.4862*phi.^5+441.4555*phi.^4-855.8122*phi.^3+823.1050*phi.^2-
    ...
    392.1914*phi.^1+74.7855;

nc(:) = ncdes;
nt(:) = ntdes;

% matrices initialization
P32 = zeros([n 1]);
P32calc = zeros([n 1]);
P45 = zeros([n 1]);
P50 = zeros([n 1]);
P3 = zeros([n 1]);
P4 = zeros([n 1]);
P5 = zeros([n 1]);
P6 = zeros([n 1]);
T32 = zeros([n 1]);
T45 = zeros([n 1]);
T3 = zeros([n 1]);
T4 = zeros([n 1]);
T5 = zeros([n 1]);
T6 = zeros([n 1]);
WRT2 = zeros([n 1]);
WRT4 = zeros([n 1]);
WRT5 = zeros([n 1]);
ma = zeros([n 1]);
mac = zeros([n 1]);
maf = zeros([n 1]);
macf = zeros([n 1]);
mg = zeros([n 1]);

% critical pressures
P45c = 1/(1-(y-1)/(y+1))^(y/(y-1));
P50c = 1/(1-(1/nnoz)*(y-1)/(y+1))^(y/(y-1));

```

```

% bleed flow
for i = 1:n
    if phi(i) >= 2.9/4.1
        loc = i;
        break
    end
end

B = .05;
beta = zeros([n 1]);
beta(1:loc) = linspace(B,0,loc);

pp = 0;
lim = 50;

for i = 1:n
    if phi(i) == 1
        nc(i) = ncdes;
        nt(i) = ntdes;
    end
    cond50 = 0;
    pip50 = 0;
    cond45 = 0;
    pip45 = 0;
    left45 = P45c*.57;
    right45 = P45des*1.0;
    P45(i) = .5*(left45+right45);
    count45 = 0;
    while pp < 1
        if abs(P45(i)-P45des) < 1e-2 % choked turbine
            P45(i) = P45des;
            T45(i) = T45des;
            WRT4(i) = WRT4des;
            WRT5(i) = WRT5des;
            left50 = P50c*.65;
            right50 = P50des*1.3;
            P50(i) = .5*(left50+right50);
            count50 = 0;
            while pp < 1
                T32(i) = 1+phi(i)*(T32des-1)*(1-1/T45(i))/(1-1/T45des);
                P32(i) = T32(i)^(nc(i)*ya/(ya-1));
                WRT2(i) = WRT2des*(WRT4(i)/WRT4des)* ...
                    (P32(i)/P32des)*sqrt(1/phi(i));
                if i <= loc % compensate for bleed flow
                    [P32(i) T32(i)] = ...
                        bleedeffect(beta(i),WRT2(i)/1000,P32(i), ...
                            Po2*1000,To2,ya,nc(i),.05,.05);
                end
                P32calc(i) = P50(i)*P45(i)/P43des;
                if abs(P32calc(i)-P32(i)) < 1e-3 % solution found
                    cond50 = 'NOZZLE CONVERGE'
                    break
                end
                % search for nozzle operating point
                if P32(i) > P32calc(i)
                    left50 = P50(i);

```

```

        else
            right50 = P50(i);
        end
        P50(i) = .5*(left50+right50);
        count50 = count50+1;
        if count50 > lim
            pip50 = 'NOZZLE LIM REACHED'
            break
        end
    end
end
% exit loop if equilibrium operating point was found
if cond50 == 'NOZZLE CONVERGE'
    break
elseif pip50 == 'NOZZLE LIM REACHED'
    break
end
% else, turbine is unchoked
T45(i) = P45(i)^(nt(i)*(y-1)/y);
T32(i) = 1+phi(i)*(T32des-1)*(1-1/T45(i))/(1-1/T45des);
P32(i) = T32(i)^(nc(i)*ya/(ya-1));
if P45(i) < P45c
    WRT4(i) = 1000*nozzleflow(1/P45(i),A4,WRT4des/1000,1,y,0);
else
    WRT4(i) = WRT4des;
end
WRT2(i) = WRT2des*(WRT4(i)/WRT4des)*(P32(i)/P32des)* ...
    sqrt(1/phi(i));
if i <= loc % compensate for bleed flow
    [P32(i) T32(i)] = bleedeffect(beta(i),WRT2(i)/1000, ...
        P32(i),Po2*1000,To2,ya,nc(i),.05,.05);
end
WRT5(i) = WRT5des*(WRT4(i)/WRT4des)*(P45(i)/P45des)* ...
    sqrt(T45des/T45(i));
P50(i) = nozzlepres(WRT5(i)/1000,A6,WRT5des/1000,nnoz,y,0);
P32calc(i) = P50(i)*P45(i)/P43des;
if abs(P32calc(i)-P32(i)) < 1e-3 % solution found
    cond45 = 'TURBINE CONVERGE'
    break
end
% search for turbine operating point
if P32(i) > P32calc(i)
    left45 = P45(i);
else
    right45 = P45(i);
end
P45(i) = .5*(left45+right45);
count45 = count45+1;
if count45 > lim
    pip45 = 'TURBINE LIM REACHED'
    break
end
end
end
end

```

```

% calculate off-design performance
for i = 1:n
    T3(i) = T32(i)*To2;
    P4(i) = P43des*P32(i)*Po2;
    P5(i) = P4(i)/P45(i);
    P6(i) = P5(i);
    ma(i) = WRT2(i)*Po2/sqrt(To2);
    mac(i) = ma(i)*(1-beta(i));
    macf(i) = bleedfuel(T3(i),P4(i)*1000,WRT4(i)/1000,mac(i),Q);
    mg(i) = mac(i)+macf(i);
    T4(i) = ((macf(i)/mac(i))*(.999*Q)+1.005*T3(i))/1.148;
    T5(i) = T4(i)/T45(i);
    T6(i) = T5(i);
end

% thrust and specific fuel consumption calculation
FN = zeros([n 1]);
FS = zeros([n 1]);
SFC = zeros([n 1]);

P6s = zeros([n 1]);
T6s = zeros([n 1]);
rho6 = zeros([n 1]);
V6 = zeros([n 1]);

for i = 1:n
    if WRT5(i) >= WRT5des
        P6s(i) = Po2*P32(i)*P43des/(P45(i)*P50c);
        T6s(i) = (2/(y+1))*T5(i);
        rho6(i) = P6s(i)/(R*T6s(i));
        V6(i) = sqrt(y*R*T6s(i));
    else
        [T6s(i) P6s(i) rho6(i) V6(i)] = ...
            staticinfo(mg(i),T6(i),P6(i)*1000,A6,y,1148);
        P6s(i) = P6s(i)/1000;
    end
    FN(i) = mg(i)*V6(i)/1000+A6*(P6s(i)-Po1);
    FS(i) = FN(i)/ma(i);
    SFC(i) = macf(i)/(1000*FN(i));
end

% outputs for plotting
[WRT2 P32 SFC*3600 FN T4/1000]

```



```

figure(2)
plot(1000*mat*14.696*.4536/101325,1000*sfc*3600,'^k')
hold on
plot(WRT21,1000*SFC1*3600,'-k','LineWidth',2)
plot(WRT22,1000*SFC2*3600,'--k','LineWidth',2)
plot([WRT2des WRT2des 0],1000*[0 sfcdes sfcdes]*3600,'--k')
hold off
text(WRT2des+.1,1000*(sfcdes*3600-.01),'design point', ...
     'FontName','Arial Narrow')
legend('Viper Mark 521','prediction', ...
      'prediction with overboard bleed neglected','Location','NW')
legend('boxoff')
set(gca,'FontSize',12,'FontName','Arial Narrow')
xlabel({'Compressor corrected mass flow rate, ', ...
       'm_2\surdT_o_2 / P_o_2 [ kg\surK / kPa\cdotsec ]'}, ...
       'FontSize',12,'FontName','Arial Narrow')
ylabel('Specific fuel consumption, SFC [ kg / hr\cdotkN ]', ...
       'FontSize',12,'FontName','Arial Narrow')
set(legend,'FontSize',10,'FontName','Arial Narrow')
set(gca,'XTickLabel',{'0','0.5','1.0','1.5','2.0','2.5', ...
                    '3.0','3.5','4.0','4.5','5.0'})
axis([0 5 0 400])

figure(3)
plot(1000*mat*14.696*.4536/101325,fn/1000,'^k')
hold on
plot(WRT21,FN1,'k','LineWidth',2)
plot(WRT22,FN2,'--k','LineWidth',2)
plot([WRT2des WRT2des 0],[0 fndes fndes]/1000,'--k')
hold off
text(WRT2des+.1,fndes/1000,'design point','FontName','Arial Narrow')
legend('Viper Mark 521','prediction', ...
      'prediction with overboard bleed neglected','Location','NW')
legend('boxoff')
set(gca,'FontSize',12,'FontName','Arial Narrow')
xlabel({'Compressor corrected mass flow rate, ', ...
       'm_2\surdT_o_2 / P_o_2', ...
       ' [ kg\surK / kPa\cdotsec ]'},'FontSize',12,'FontName', ...
       'Arial Narrow')
ylabel('Net thrust, F_N [ kN ]','FontSize',12, ...
       'FontName','Arial Narrow')
set(gca,'XTickLabel',{'0','0.5','1.0','1.5','2.0','2.5', ...
                    '3.0','3.5','4.0','4.5','5.0'})
set(legend,'FontSize',10,'FontName','Arial Narrow')
axis([0 5 0 20])

figure(4)
plot(testmass,testphi*T42des*288,'^k')
hold on
plot(WRT21,T41,'k','LineWidth',2)
plot(WRT22,T42,'--k','LineWidth',2)
plot([WRT2des WRT2des 0],[0 To4 To4],'--k')
hold off
text(WRT2des+.1,To4,'design point','FontName','Arial Narrow')
legend('Viper Mark 521','prediction', ...
      'prediction with overboard bleed neglected','Location','NW')

```

```

legend('boxoff')
set(gca,'FontSize',12,'FontName','Arial Narrow')
xlabel({'Compressor corrected mass flow rate, ', ...
    'm_2\surdT_o_2 / P_o_2 [ kg\surdK / kPa\cdotsec ]'}, ...
    'FontSize',12,'FontName','Arial Narrow')
ylabel({'Turbine inlet temperature, T_o_4 [ K ]'}, ...
    'FontSize',12,'FontName','Arial Narrow')
set(gca,'XTickLabel',{'0','0.5','1.0','1.5','2.0','2.5', ...
    '3.0','3.5','4.0','4.5','5.0'})
set(legend,'FontSize',10,'FontName','Arial Narrow')
axis([0 5 500 1500])

figure(5)
plot(testmass,testpr,'^k')
hold on
plot(WRT21,P321,'-k','LineWidth',2)
plot(WRT23,P323,'--k','LineWidth',2)
plot([WRT2des WRT2des 0],[0 P32des P32des],'--k')
hold off
text(WRT2des+.1,P32des,'design point','FontName','Arial Narrow')
legend('Viper Mark 521', ...
    'prediction with variable \eta_\infty_c', ...
    'prediction with constant \eta_\infty_c','Location','NW')
legend('boxoff')
xlabel({'Compressor corrected mass flow rate, ', ...
    'm_2\surdT_o_2 / P_o_2 [ kg\surdK / kPa\cdotsec ]'}, ...
    'FontSize',12,'FontName','Arial Narrow')
ylabel('Compressor pressure ratio, P_o_2 / P_o_1', ...
    'FontSize',12,'FontName','Arial Narrow')
set(gca,'XTickLabel',{'0','0.5','1.0','1.5','2.0','2.5', ...
    '3.0','3.5','4.0','4.5','5.0'})
set(gca,'FontSize',12,'FontName','Arial Narrow')
set(legend,'FontSize',10,'FontName','Arial Narrow')
axis([0 5 0 8])

figure(6)
plot(fn/1000,1000*sfc*3600,'^k')
hold on
plot(FN1,1000*SFC1*3600,'-k','LineWidth',2)
plot(FN3,1000*SFC3*3600,'--k','LineWidth',2)
plot([fndes fndes 0]/1000,1000*[0 sfcdes sfcdes]*3600,'--k')
hold off
text(fndes/1000+.1,1000*(sfcdes*3600+.015),'design point', ...
    'FontName','Arial Narrow')
legend('Viper Mark 521', ...
    'prediction with variable \eta_\infty_c', ...
    'prediction with constant \eta_\infty_c', ...
    'Location','NW')
set(gca,'FontSize',12,'FontName','Arial Narrow')
xlabel('Net thrust, F_N [ kN ]', ...
    'FontSize',12,'FontName','Arial Narrow')
ylabel('Specific fuel consumption, SFC [ kg / hr\cdotkN ]', ...
    'FontSize',12,'FontName','Arial Narrow')
legend('boxoff')
set(legend,'FontSize',10,'FontName','Arial Narrow')
axis([0 20 50 350])

```

```

figure(7)
plot(testmass,testphi*T42des*288,'^k')
hold on
plot(WRT21,T41,'k','LineWidth',2)
plot(WRT23,T43,'--k','LineWidth',2)
plot([WRT2des WRT2des 0],[0 To4 To4],'--k')
hold off
text(WRT2des+.1,To4,'design point','FontName','Arial Narrow')
legend('Viper Mark 521', ...
      'prediction with variable \eta_\infty_c', ...
      'prediction with constant \eta_\infty_c', ...
      'Location','NW')
legend('boxoff')
set(gca,'FontSize',12,'FontName','Arial Narrow')
xlabel({'Compressor corrected mass flow rate, ', ...
      'm_2\sqrt{T_o_2} / P_o_2 [ kg\sqrt{K} / kPa\cdotsec ]'}, ...
      'FontSize',12,'FontName','Arial Narrow')
ylabel({'Turbine inlet temperature, T_o_4 [ K ]'}, ...
      'FontSize',12,'FontName','Arial Narrow')
set(gca,'XTickLabel',{'0','0.5','1.0','1.5','2.0','2.5', ...
      '3.0','3.5','4.0','4.5','5.0'})
set(legend,'FontSize',10,'FontName','Arial Narrow')
axis([0 5 500 1500])

```



```

% mass flow rates at design-point
m2des = WRT2des*Po2/sqrt (To2) ;
m3des = WRT3des*Po3/sqrt (To3) ;
m5des = WRT5des*Po5/sqrt (To5) ;
m6des = WRT6des*Po6/sqrt (To6) ;
m7des = WRT7des*Po7/sqrt (To7) ;

% bleed flows at design-point
bHPT = (m6des-m5des)/m2des;
bLPT = (m7des-m6des)/m2des;

% pressure and temperature ratios at design-point
P21des = Po2/Po1;
P32des = Po3/Po2;
P43des = Po4/Po3;
P54des = Po5/Po4;
P56des = Po5/Po6;
P67des = Po6/Po7;
P78des = Po7/Po8;
P81des = Po8/Po1;
T32des = To3/To2;
T43des = To4/To3;
T56des = To5/To6;
T67des = To6/To7;
T53des = To5/To3;

R = 287;
Q = 43100;
y = 1.333;
ya = 1.4;

% turbine inlet areas
A5 = (WRT5des/1000)*sqrt (R/y)*((y+1)/2)^((y+1)/(2*(y-1)));
A6 = (WRT6des/1000)*sqrt (R/y)*((y+1)/2)^((y+1)/(2*(y-1)));
A7 = (WRT7des/1000)*sqrt (R/y)*((y+1)/2)^((y+1)/(2*(y-1)));

% design-point compressor and turbine polytropic efficiencies
nlpcdes = ((ya-1)/ya)*log (P32des)/log (T32des);
nhpcdes = ((ya-1)/ya)*log (P43des)/log (T43des);
nhptdes = (y/(y-1))*log (T56des)/log (P56des);
nlptdes = (y/(y-1))*log (T67des)/log (P67des);
nptdes = XXXX; % power turbine polytropic efficiency

% critical turbine pressure ratios
P56c = 1/(1-(y-1)/(y+1))^(y/(y-1));
P67c = 1/(1-(y-1)/(y+1))^(y/(y-1));
P78c = 1/(1-(y-1)/(y+1))^(y/(y-1));

% import control parameters from site data
q = length(datacon(:,1));
skipper = 1;
phiHP = datacon(1:skipper:q,1);
Po2 = datacon(1:skipper:q,2)*6.8947;
To2 = datacon(1:skipper:q,3);

```

```

n = length(phiHP);

% non-recoverable deterioration of compressors and turbines
nlpc(:) = nlpcdes+XXXX;
nhpc(:) = nhpcdes+XXXX;
nhpt = nhptdes+XXXX;
nlpt = nlptdes+XXXX;
npt = nptdes; % power turbine does not deteriorate

% recoverable deterioration of LP compressor
% polytropic efficiency
for i = 1:n
    nlpc(i) = nlpc(i)* ...
        (.0*(exp(-.006*datacon(1+(i-1)*skipper,5))-1)+1);
end

% recoverable deterioration of HP compressor
% polytropic efficiency
for i = 1:n
    nhpc(i) = nhpc(i)* ...
        (.02*(exp(-.006*datacon(1+(i-1)*skipper,5))-1)+1);
end

lpcap = zeros([n 1]);

% recoverable deterioration of LP compressor capacity
for i = 1:n
    lpcap(i) = .01*(exp(-.001*datacon(1+(i-1)*skipper,5))-1)+1;
end

% uncertainty margin of design-point polytropic efficiencies
kik = 0;
if kik == 1 % upper margin
    nlpc = nlpc+.0192;
    nhpc = nhpc+.02;
    nhpt = nhpt+.008;
    nlpt = nlpt+.01;
elseif kik == 2 % lower margin
    nlpc = nlpc-.0192;
    nhpc = nhpc-.02;
    nhpt = nhpt-.008;
    nlpt = nlpt-.01;
end

% initialize matrices
P32 = zeros([n 1]);
P32calc = zeros([n 1]);
P43 = zeros([n 1]);
P56 = zeros([n 1]);
P67 = zeros([n 1]);
P78 = zeros([n 1]);
T32 = zeros([n 1]);
T43 = zeros([n 1]);
T53 = zeros([n 1]);
T56 = zeros([n 1]);

```

```

T62 = zeros([n 1]);
T67 = zeros([n 1]);
T78 = zeros([n 1]);
WRT2 = zeros([n 1]);
WRT3 = zeros([n 1]);
WRT3n = zeros([n 1]);
WRT5 = zeros([n 1]);
WRT6 = zeros([n 1]);
WRT7 = zeros([n 1]);
P3 = zeros([n 1]);
P4 = zeros([n 1]);
P5 = zeros([n 1]);
P6 = zeros([n 1]);
P7 = zeros([n 1]);
P8 = zeros([n 1]);
T3 = zeros([n 1]);
T4 = zeros([n 1]);
T5 = zeros([n 1]);
T6 = zeros([n 1]);
T7 = zeros([n 1]);
T8 = zeros([n 1]);
m2 = zeros([n 1]);
m3 = zeros([n 1]);
m4 = zeros([n 1]);
m5 = zeros([n 1]);
m6 = zeros([n 1]);
m7 = zeros([n 1]);
m8 = zeros([n 1]);
mf = zeros([n 1]);
EGHP = zeros([n 1]);
HR = zeros([n 1]);

pp = 0;
lim = 30;

% LP compressor handling bleed schedule
locLPC = XXXX; % begin opening
locLPC0 = XXXX; % fully opened by
bLPC = XXXX; % bleed fraction
betaLPC = (-bLPC/(locLPC-locLPC0))*phiHP+bLPC*locLPC/ ...
    (locLPC-locLPC0);
for i = 1:n
    if phiHP(i) >= locLPC
        betaLPC(i) = 0;
    elseif phiHP(i) <= locLPC0
        betaLPC(i) = bLPC;
    end
    if locLPC0 == locLPC
        betaLPC(i) = bLPC;
    end
end
end

% LP compressor handling bleed malfunction for GT3
anstart = 6816;
anend = 6897;
bLPCmalfun = .025;

```

```

for i = 1:n
    cond56 = 0;
    cond67 = 0;
    cond78 = 0;
    pip56 = 0;
    pip67 = 0;
    pip78 = 0;
    left56 = P56c*.6;
    right56 = P56des*1.0;
    P56(i) = .5*(left56+right56);
    count56 = 0;
    % unchoked HP turbine
    while pp < 1
        if abs(P56(i)-P56des) < 1e-4 % choked HP turbine
            P56(i) = P56des;
            WRT5(i) = WRT5des;
            left67 = P67c*.6;
            right67 = P67des*1.0;
            P67(i) = .5*(left67+right67);
            count67 = 0;
            while pp < 1
                if abs(P67(i)-P67des) < 1e-4
                    % choked LP turbine
                    P56(i) = P56des;
                    WRT5(i) = WRT5des;
                    P67(i) = P67des;
                    WRT6(i) = WRT6des;
                    left78 = P78c*.7;
                    right78 = P78des*1.5;
                    P78(i) = .5*(left78+right78);
                    count78 = 0;
                    % choked power turbine
                    while pp < 1
                        T56(i) = P56(i)^(nhpt*(y-1)/y);
                        T67(i) = P67(i)^(nlpt*(y-1)/y);
                        T78(i) = P78(i)^((y-1)/y);
                        T43(i) = 1+phiHP(i)*(T43des-1)* ...
                            (1-1/T56(i))/(1-1/T56des);
                        P43(i) = T43(i)^(nhpc(i)*ya/(ya-1));
                        T32(i) = (1-phiHP(i)*(1-1/T32des)* ...
                            (T56des/T56(i))* ...
                            (1-1/T67(i))/(1-1/T67des))^-1;
                        T3(i) = T32(i)*To2(i);
                        T5(i) = phiHP(i)*T53des*T3(i);
                        T6(i) = T5(i)/T56(i);
                        T7(i) = T6(i)/T67(i);
                        if T7(i) >= T7max % To7 limiter
                            T7(i) = T7max;
                            T6(i) = T7(i)*T67(i);
                            T5(i) = T6(i)*T56(i);
                            T3(i) = T5(i)/(phiHP(i)*T53des);
                            T32(i) = T3(i)/To2(i);
                        end
                        P32(i) = T32(i)^(nlpc(i)*ya/(ya-1));
                        % *****
                        % GT3 LP compressor handling bleed
                        % valve malfunction
                    end
                end
            end
        end
    end
end

```

```

if anstart <= datacon(1+(i-1)*skipper,4) ...
    && datacon(1+(i-1)*skipper,4) <= anend
    WRT2(i) = lpcap(i)*WRT2des* ...
        (WRT5(i)/WRT5des)*(P43(i)/P43des)* ...
        (P32(i)/P32des)*sqrt(1/phiHP(i))* ...
        sqrt(T32des/T32(i));
    [P32(i) T32(i)] = ...
        bleedeffect((1-lpcap(i))* ...
            bLPCmalfun),WRT2(i)/1000, ...
            P32(i),Po2(i)*1000,To2(i),ya, ...
            nlpc(i),.05,.05);
end
% *****
WRT2(i) = WRT2des*(WRT5(i)/WRT5des)* ...
    (P43(i)/P43des)*(P32(i)/P32des)* ...
    sqrt(1/phiHP(i))* ...
    sqrt(T32des/T32(i));
% LP compressor handling bleed schedule
if phiHP(i) <= locLPC
    [P32(i) T32(i)] = ...
        bleedeffect(betaLPC(i), ...
            WRT2(i)/1000,P32(i),Po2(i)*1000, ...
            To2(i),ya,nlpc(i),.05,.05);
end
P7(i) = P54des*P43(i)*P32(i)*Po2(i)/ ...
    (P56(i)*P67(i));
T8(i) = T7(i)*(Po8/P7(i))^(npt*(y-1)/y);
m7(i) = m6(i);
EGHP(i) = m7(i)*1.148*(T7(i)-T8(i));
if EGHP(i) > EGHPmax % power limiter
    break
end
P32calc(i) = P81des*P78(i)*P67(i)*P56(i)/ ...
    (P54des*P43(i)*P21des);
if abs(P32calc(i)-P32(i)) < 1e-4
    cond78 = 'NOZZLE CONVERGE'
    break
end
if P32(i) > P32calc(i)
    left78 = P78(i);
else
    right78 = P78(i);
end
P78(i) = .5*(left78+right78);
count78 = count78+1;
if count78 > lim
    pip78 = 'NOZZLE LIM REACHED'
    break
end
end
end
if cond78 == 'NOZZLE CONVERGE'
    break
elseif pip78 == 'NOZZLE LIM REACHED'
    break
end
T67(i) = P67(i)^(nlpt*(y-1)/y);

```

```

if P67(i) < P67c
    WRT6(i) = 1000*nozzleflow(1/P67(i),A6, ...
        WRT6des/1000,1,y,0);
else
    WRT6(i) = WRT6des;
end
WRT7(i) = WRT7des*(WRT6(i)/WRT6des)* ...
    (P67(i)/P67des)*sqrt(T67des/T67(i));
P78(i) = nozzlepres(WRT7(i)/1000,A7, ...
    WRT7des/1000,1,y,0);
T78(i) = P78(i)^(y-1)/y;
T43(i) = 1+phiHP(i)*(T43des-1)*(1-1/T56(i))/ ...
    (1-1/T56des);
P43(i) = T43(i)^(nhpc(i)*ya/(ya-1));
T32(i) = (1-phiHP(i))*(1-1/T32des)* ...
    (T56des/T56(i))*(1-1/T67(i))/(1-1/T67des))^-1;
T3(i) = T32(i)*To2(i);
T5(i) = phiHP(i)*T53des*T3(i);
T6(i) = T5(i)/T56(i);
T7(i) = T6(i)/T67(i);
if T7(i) >= T7max % To7 limiter
    T7(i) = T7max;
    T6(i) = T7(i)*T67(i);
    T5(i) = T6(i)*T56(i);
    T3(i) = T5(i)/(phiHP(i)*T53des);
    T32(i) = T3(i)/To2(i);
end
P32(i) = T32(i)^(nlpc(i)*ya/(ya-1));
% *****
% GT3 LP compressor handling bleed valve malfunction
if anstart <= datacon(1+(i-1)*skipper,4) && ...
    datacon(1+(i-1)*skipper,4) <= anend
    WRT2(i) = lpcap(i)*WRT2des*(WRT5(i)/WRT5des)* ...
        (P43(i)/P43des)* ...
        (P32(i)/P32des)*sqrt(1/phiHP(i))* ...
        sqrt(T32des/T32(i));
    [P32(i) T32(i)] = ...
        bleedeffect((1-lpcap(i))*bLPCmalfun, ...
            WRT2(i)/1000,P32(i),Po2(i)*1000,To2(i), ...
            ya,nlpc(i),.05,.05);
end
% *****
WRT2(i) = WRT2des*(WRT5(i)/WRT5des)* ...
    (P43(i)/P43des)*(P32(i)/P32des)* ...
    sqrt(1/phiHP(i))*sqrt(T32des/T32(i));
% LP compressor handling bleed schedule
if phiHP(i) <= locLPC
    [P32(i) T32(i)] = ...
        bleedeffect(betaLPC(i),WRT2(i)/1000, ...
            P32(i),Po2(i)*1000,To2(i),ya,nlpc(i),.05,.05);
end
P7(i) = P54des*P43(i)*P32(i)*Po2(i)/(P56(i)*P67(i));
T8(i) = T7(i)*(Po8/P7(i))^(npt*(y-1)/y);
m7(i) = m6(i);
EGHP(i) = m7(i)*1.148*(T7(i)-T8(i));
if EGHP(i) > EGHPmax % power limiter
    break

```

```

end
P32calc(i) = P81des*P78(i)*P67(i)*P56(i)/ ...
(P54des*P43(i)*P21des);
if abs(P32calc(i)-P32(i)) < 1e-4
cond67 = 'LPT CONVERGE'
break
end
if P32(i) > P32calc(i)
left67 = P67(i);
else
right67 = P67(i);
end
P67(i) = .5*(left67+right67);
count67 = count67+1;
if count67 > lim
pip67 = 'LPT LIM REACHED'
break
end
end
end
if cond78 == 'NOZZLE CONVERGE'
break
elseif pip78 == 'NOZZLE LIM REACHED'
break
elseif cond67 == 'LPT CONVERGE'
break
elseif pip67 == 'LPT LIM REACHED'
break
end
T56(i) = P56(i)^(nhpt*(y-1)/y);
if P56(i) < P56c
WRT5(i) = 1000* ...
nozzleflow(1/P56(i),A5,WRT5des/1000,1,y,0);
else
WRT5(i) = WRT5des;
end
WRT6(i) = WRT6des*(WRT5(i)/WRT5des)*(P56(i)/P56des)* ...
sqrt(T56des/T56(i));
P67(i) = nozzlepres(WRT6(i)/1000,A6,WRT6des/1000,1,y,0);
T67(i) = P67(i)^(nlpt*(y-1)/y);
WRT7(i) = WRT7des*(WRT6(i)/WRT6des)*(P67(i)/P67des)* ...
sqrt(T67des/T67(i));
P78(i) = nozzlepres(WRT7(i)/1000,A7,WRT7des/1000,1,y,0);
T78(i) = P78(i)^((y-1)/y);
T43(i) = 1+phiHP(i)*(T43des-1)*(1-1/T56(i))/(1-1/T56des);
P43(i) = T43(i)^(nhpc(i)*ya/(ya-1));
T32(i) = (1-phiHP(i)*(1-1/T32des)*(T56des/T56(i))* ...
(1-1/T67(i))/(1-1/T67des))^-1;
T3(i) = T32(i)*To2(i);
T5(i) = phiHP(i)*T53des*T3(i);
T6(i) = T5(i)/T56(i);
T7(i) = T6(i)/T67(i);
if T7(i) >= T7max % To7 limiter
T7(i) = T7max;
T6(i) = T7(i)*T67(i);
T5(i) = T6(i)*T56(i);
T3(i) = T5(i)/(phiHP(i)*T53des);

```

```

        T32(i) = T3(i)/To2(i);
    end
    P32(i) = T32(i)^(nlpc(i)*ya/(ya-1));
    % *****
    % GT3 LP compressor handling bleed malfunction
    if anstart <= datacon(1+(i-1)*skipper,4) && ...
        datacon(1+(i-1)*skipper,4) <= anend
        WRT2(i) = lpcap(i)*WRT2des*(WRT5(i)/WRT5des)* ...
            (P43(i)/P43des)* ...
            (P32(i)/P32des)*sqrt(1/phiHP(i))*sqrt(T32des/T32(i));
        [P32(i) T32(i)] = ...
            bleedeffect((1-lpcap(i)*bLPCmalfun),WRT2(i)/1000, ...
                P32(i),Po2(i)*1000,To2(i),ya,nlpc(i),.05,.05);
    end
    % *****
    WRT2(i) = WRT2des*(WRT5(i)/WRT5des)* ...
        (P43(i)/P43des)*(P32(i)/P32des)*sqrt(1/phiHP(i))* ...
        sqrt(T32des/T32(i));
    % LP compressor handling bleed schedule
    if phiHP(i) <= locLPC
        [P32(i) T32(i)] = bleedeffect(betaLPC(i),WRT2(i)/1000, ...
            P32(i),Po2(i)*1000,To2(i),ya,nlpc(i),.05,.05);
    end
    P7(i) = P54des*P43(i)*P32(i)*Po2(i)/(P56(i)*P67(i));
    T8(i) = T7(i)*(Po8/P7(i))^(npt*(y-1)/y);
    m7(i) = m6(i);
    EGHP(i) = m7(i)*1.148*(T7(i)-T8(i));
    if EGHP(i) > EGHPmax % power limiter
        break
    end
    P32calc(i) = P81des*P78(i)*P67(i)*P56(i)/ ...
        (P54des*P43(i)*P21des);
    if abs(P32calc(i)-P32(i)) < 1e-4
        cond56 = 'HPT CONVERGE'
        break
    end
    if P32(i) > P32calc(i)
        left56 = P56(i);
    else
        right56 = P56(i);
    end
    P56(i) = .5*(left56+right56);
    count56 = count56+1;
    if count56 > lim
        pip56 = 'HPT LIM REACHED'
        break
    end
end
end
end

```

```

% post-solution process calculations
T5c = zeros([n 1]);
T6c = zeros([n 1]);
Cpm = zeros([n 1]);
Cp6 = zeros([n 1]);
FAR = zeros([n 1]);
m5c = zeros([n 1]);
y6 = zeros([n 1]);

for i = 1:n
    WRT2(i) = lpcap(i)*WRT2des*(WRT5(i)/WRT5des)*(P43(i)/P43des)* ...
        (P32(i)/P32des)*sqrt(1/phiHP(i))*sqrt(T32des/T32(i));
    WRT3(i) = WRT3des*(WRT2(i)/WRT2des)*(P32des/P32(i))* ...
        sqrt(T32(i)/T32des);
    P3(i) = Po2(i)*P32(i);
    P4(i) = P3(i)*P43(i);
    P5(i) = P4(i)*P54des;
    P6(i) = P5(i)/P56(i);
    P7(i) = P6(i)/P67(i);
    P8(i) = P7(i)/P78(i);
    T3(i) = To2(i)*T32(i);
    T4(i) = T3(i)*T43(i);
    T5(i) = phiHP(i)*T53des*T3(i);
    m2(i) = WRT2(i)*Po2(i)/sqrt(To2(i));
    m3(i) = WRT3(i)*P3(i)/sqrt(T3(i));
    m4(i) = m3(i)-bHPT*m2(i);
    T5c(i) = (1.148*T5(i)-bHPT*1.005*T4(i))/((1-bHPT)*1.148);
    mf(i) = m4(i)*(1.148*T5c(i)-1.005*T4(i))/(.999*Q);
    m5c(i) = m4(i)+mf(i);
    m5(i) = m5c(i)+bHPT*m2(i);
    T6c(i) = T5(i)/T56(i);
    m6(i) = m5(i);
    T6(i) = T6c(i);
    T7(i) = T6(i)/T67(i);
    T8(i) = T7(i)*(Po8/P7(i))^(npt*(y-1)/y);
    m7(i) = m6(i);
    EGHP(i) = m7(i)*1.148*(T7(i)-T8(i));
    HR(i) = 3600*mf(i)/EGHP(i);
end

% output to be used for plotting by X_2TJ_PLOTS
[phiHP P32 T32 P43 T43 P56 T56 P67 T67 P78 T78 T7/1000 ...
    WRT2 WRT3 WRT5 WRT6 WRT7 HR EGHP/1000]

```



```

legend('boxoff')
xlabel('Operating hours', ...
      'FontSize',12,'FontName','Arial Narrow')
ylabel('Prediction error', ...
      'FontSize',12,'FontName','Arial Narrow')
set(gca,'YTickLabel',{'-0.02','0.00','0.02','0.04'})
set(gca,'FontSize',12,'FontName','Arial Narrow')
set(legend,'FontSize',10,'FontName','Arial Narrow')
axis([min(datacore(:,1)) max(datacore(:,1)) -.02 .04])

figure(6)
subplot(2,1,1)
plot(datacore(:,1),(dataeng(:,8)/mfdes)+ ...
      1-(dataeng(1,8)/mfdes), ...
      '-','Color',.6*[1 1 1])
hold on
plot(datacore(:,1),(datacore(:,8)/mfdes)+ ...
      1-(dataeng(1,8)/mfdes),'k')
hold off
legend('GT3','prediction','Location','NW')
legend('boxoff')
xlabel('Operating hours', ...
      'FontSize',12,'FontName','Arial Narrow')
ylabel({'Non-dimensional','fuel flow rate'}, ...
      'FontSize',12,'FontName','Arial Narrow')
set(gca,'YTickLabel',{'0.8','1.0','1.2'})
set(gca,'FontSize',12,'FontName','Arial Narrow')
set(legend,'FontSize',10,'FontName','Arial Narrow')
axis([min(datacore(:,1)) max(datacore(:,1)) .7 1.3])
avman = sum((dataeng(:,8)/mfdes)- ...
            (datacore(:,8)/mfdes))/length(datacore(:,1));
subplot(2,1,2)
plot(datacore(:,1),(dataeng(:,8)/mfdes)- ...
      (datacore(:,8)/mfdes),'-', ...
      'Color',.6*[1 1 1])
hold on
plot([min(datacore(:,1)) max(datacore(:,1))], ...
      [avman avman],'-k','LineWidth',2)
plot([min(datacore(:,1)) max(datacore(:,1))], ...
      [.00513 .00513], '--k')
plot([min(datacore(:,1)) max(datacore(:,1))], ...
      -1* [.00513 .00513], '--k')
hold off
legend({'prediction error','average prediction error', ...
      'propagated measurement uncertainty'},'Location','NW')
legend('boxoff')
xlabel('Operating hours', ...
      'FontSize',12,'FontName','Arial Narrow')
ylabel('Prediction error', ...
      'FontSize',12,'FontName','Arial Narrow')
set(gca,'YTickLabel',{'-0.05','0.00','0.05','0.10'})
set(gca,'FontSize',12,'FontName','Arial Narrow')
set(legend,'FontSize',10,'FontName','Arial Narrow')
axis([min(datacore(:,1)) max(datacore(:,1)) -.05 .1])

```

```

figure(5)
subplot(2,1,1)
plot(datacore(:,1), (dataeng(:,7)/PWRdes)+ ...
      1-(dataeng(1,7)/PWRdes), ...
      '-','Color',.6*[1 1 1])
hold on
plot(datacore(:,1), (datacore(:,7)/PWRdes)+ ...
      1-(dataeng(1,7)/PWRdes), 'k')
hold off
legend('GT3', 'prediction', 'Location', 'NW')
legend('boxoff')
xlabel('Operating hours', ...
       'FontSize',12, 'FontName', 'Arial Narrow')
ylabel({'Non-dimensional', 'engine power output'}, ...
       'FontSize',12, 'FontName', 'Arial Narrow')
set(gca, 'YTick', .6:.2:1.2)
set(gca, 'YTickLabel', {'0.6', '0.8', '1.0', '1.2'})
set(gca, 'FontSize',12, 'FontName', 'Arial Narrow')
set(legend, 'FontSize',10, 'FontName', 'Arial Narrow')
axis([min(datacore(:,1)) max(datacore(:,1)) .55 1.25])
avman = sum((dataeng(:,7)/PWRdes)- ...
            (datacore(:,7)/PWRdes))/length(datacore(:,1));
subplot(2,1,2)
plot(datacore(:,1), (dataeng(:,7)/PWRdes)- ...
      (datacore(:,7)/PWRdes), '- ', ...
      'Color',.6*[1 1 1])
hold on
plot([min(datacore(:,1)) max(datacore(:,1))], ...
      [avman avman], '-k', 'LineWidth',2)
plot([min(datacore(:,1)) max(datacore(:,1))], ...
      [.00902 .00902], '--k')
plot([min(datacore(:,1)) max(datacore(:,1))], ...
      -1* [.00902 .00902], '--k')
hold off
legend({'prediction error', 'average prediction error', ...
       'propagated measurement uncertainty'}, 'Location', 'NW')
legend('boxoff')
xlabel('Operating hours', ...
       'FontSize',12, 'FontName', 'Arial Narrow')
ylabel('Prediction error', ...
       'FontSize',12, 'FontName', 'Arial Narrow')
set(gca, 'FontSize',12, 'FontName', 'Arial Narrow')
set(legend, 'FontSize',10, 'FontName', 'Arial Narrow')
set(gca, 'YTickLabel', {'-0.1', '0.0', '0.1', '0.2'})
axis([min(datacore(:,1)) max(datacore(:,1)) -.1 .2])

figure(4)
subplot(2,1,1)
plot(datacore(:,1), (dataeng(:,5)/WRT3des)+ ...
      1-(dataeng(1,5)/WRT3des), ...
      '-','Color',.6*[1 1 1])
hold on
plot(datacore(:,1), (datacore(:,5)/WRT3des)+ ...
      1-(dataeng(1,5)/WRT3des), 'k')
hold off
legend('GT3', 'prediction', 'Location', 'NW')
legend('boxoff')

```

```

xlabel('Operating hours', ...
       'FontSize',12,'FontName','Arial Narrow')
ylabel({'Non-dimensional HP compressor', ...
       'corrected mass flow rate'}, ...
       'FontSize',12,'FontName','Arial Narrow')
set(gca,'YTickLabel',{'0.94','0.96','0.98', ...
       '1.00','1.02','1.04'})
set(gca,'FontSize',12,'FontName','Arial Narrow')
set(legend,'FontSize',10,'FontName','Arial Narrow')
axis([min(datacore(:,1)) max(datacore(:,1)) .94 1.04])
avman = sum((dataeng(:,5)/WRT3des)- ...
       (datacore(:,5)/WRT3des))/length(datacore(:,1));
subplot(2,1,2)
plot(datacore(:,1), (dataeng(:,5)/WRT3des)- ...
       (datacore(:,5)/WRT3des),'-', ...
       'Color',.6*[1 1 1])
hold on
plot([min(datacore(:,1)) max(datacore(:,1))], ...
       [avman avman], '-k','LineWidth',2)
plot([min(datacore(:,1)) max(datacore(:,1))], ...
       [.00633 .00633], '--k')
plot([min(datacore(:,1)) max(datacore(:,1))], ...
       -1* [.00633 .00633], '--k')
hold off
legend({'prediction error','average prediction error', ...
       'propagated measurement uncertainty'}, 'Location','NW')
legend('boxoff')
xlabel('Operating hours', ...
       'FontSize',12,'FontName','Arial Narrow')
ylabel('Prediction error', ...
       'FontSize',12,'FontName','Arial Narrow')
set(gca,'FontSize',12,'FontName','Arial Narrow')
set(legend,'FontSize',10,'FontName','Arial Narrow')
set(gca,'YTickLabel',{'-0.02','0.00','0.02','0.04','0.06'})
axis([min(datacore(:,1)) max(datacore(:,1)) -.02 .06])

figure(3)
subplot(2,1,1)
plot(datacore(:,1), (dataeng(:,4)/WRT2des)+ ...
       1- (dataeng(1,4)/WRT2des), ...
       '-', 'Color',.6*[1 1 1])
hold on
plot(datacore(:,1), (datacore(:,4)/WRT2des)+ ...
       1- (dataeng(1,4)/WRT2des), 'k')
hold off
legend('GT3','prediction','Location','NW')
legend('boxoff')
xlabel('Operating hours', ...
       'FontSize',12,'FontName','Arial Narrow')
ylabel({'Non-dimensional LP compressor', ...
       'corrected mass flow rate'}, ...
       'FontSize',12,'FontName','Arial Narrow')
set(gca,'YTick',.8:.1:1.2)
set(gca,'YTickLabel',{'0.8','0.9','1.0','1.1'})
set(gca,'FontSize',12,'FontName','Arial Narrow')
set(legend,'FontSize',10,'FontName','Arial Narrow')
axis([min(datacore(:,1)) max(datacore(:,1)) .8 1.1])

```

```

avman = sum((dataeng(:,4)/WRT2des)- ...
    (datacore(:,4)/WRT2des))/length(datacore(:,1));
subplot(2,1,2)
plot(datacore(:,1), (dataeng(:,4)/WRT2des)- ...
    (datacore(:,4)/WRT2des), '- ', ...
    'Color', .6*[1 1 1])
hold on
plot([min(datacore(:,1)) max(datacore(:,1))], ...
    [avman avman], '-k', 'LineWidth', 2)
plot([min(datacore(:,1)) max(datacore(:,1))], ...
    [.00333 .00333], '--k')
plot([min(datacore(:,1)) max(datacore(:,1))], ...
    -1* [.00333 .00333], '--k')
hold off
legend({'prediction error', 'average prediction error', ...
    'propagated measurement uncertainty'}, 'Location', 'NW')
legend('boxoff')
xlabel('Operating hours', ...
    'FontSize', 12, 'FontName', 'Arial Narrow')
ylabel('Prediction error', ...
    'FontSize', 12, 'FontName', 'Arial Narrow')
set(gca, 'YTickLabel', {'-0.05', '0.00', '0.05', '0.10'})
set(gca, 'FontSize', 12, 'FontName', 'Arial Narrow')
set(legend, 'FontSize', 10, 'FontName', 'Arial Narrow')
axis([min(datacore(:,1)) max(datacore(:,1)) -.05 .1])

figure(2)
subplot(2,1,1)
plot(datacore(:,1), ((dataeng(:,3)-1)/(P43des-1))+ ...
    1-((dataeng(1,3)-1)/(P43des-1)), ...
    '- ', 'Color', .6*[1 1 1])
hold on
plot(datacore(:,1), ((datacore(:,3)-1)/(P43des-1))+ ...
    1-((dataeng(1,3)-1)/(P43des-1)), 'k')
hold off
legend('GT3', 'prediction', 'Location', 'NW')
legend('boxoff')
xlabel('Operating hours', ...
    'FontSize', 12, 'FontName', 'Arial Narrow')
ylabel({'Non-dimensional HP', 'compressor pressure ratio'}, ...
    'FontSize', 12, 'FontName', 'Arial Narrow')
set(gca, 'YTickLabel', {'0.90', '0.95', '1.00', '1.05'})
set(gca, 'FontSize', 12, 'FontName', 'Arial Narrow')
set(legend, 'FontSize', 10, 'FontName', 'Arial Narrow')
axis([min(datacore(:,1)) max(datacore(:,1)) .9 1.05])
avman = sum(((dataeng(:,3)-1)/(P43des-1))- ...
    ((datacore(:,3)-1)/(P43des-1)))/length(datacore(:,1));
subplot(2,1,2)
plot(datacore(:,1), ((dataeng(:,3)-1)/(P43des-1))- ...
    ((datacore(:,3)-1)/(P43des-1)), '- ', ...
    'Color', .6*[1 1 1])
hold on
plot([min(datacore(:,1)) max(datacore(:,1))], ...
    [avman avman], '-k', 'LineWidth', 2)
plot([min(datacore(:,1)) max(datacore(:,1))], ...
    [.00807 .00807], '--k')
plot([min(datacore(:,1)) max(datacore(:,1))], ...

```

```

-1* [.00807 .00807], '--k')
hold off
legend({'prediction error', 'average prediction error', ...
       'propagated measurement uncertainty'}, 'Location', 'NW')
legend('boxoff')
xlabel('Operating hours', ...
       'FontSize', 12, 'FontName', 'Arial Narrow')
ylabel('Prediction error', ...
       'FontSize', 12, 'FontName', 'Arial Narrow')
set(gca, 'YTickLabel', {'-0.05', '0.00', '0.05', '0.10'})
set(gca, 'FontSize', 12, 'FontName', 'Arial Narrow')
set(legend, 'FontSize', 10, 'FontName', 'Arial Narrow')
axis([min(datacore(:,1)) max(datacore(:,1)) -.05 .1])

figure(1)
subplot(2,1,1)
plot(datacore(:,1), ((dataeng(:,2)-1)/(P32des-1))+ ...
      1-((dataeng(1,2)-1)/(P32des-1)), ...
      '-', 'Color', .6*[1 1 1])
hold on
plot(datacore(:,1), ((datacore(:,2)-1)/(P32des-1))+ ...
      1-((dataeng(1,2)-1)/(P32des-1)), 'k')
hold off
legend('GT3', 'prediction', 'Location', 'NW')
legend('boxoff')
xlabel('Operating hours', 'FontSize', 12, 'FontName', 'Arial Narrow')
ylabel({'Non-dimensional LP', 'compressor pressure ratio'}, ...
       'FontSize', 12, 'FontName', 'Arial Narrow')
set(gca, 'YTickLabel', {'0.8', '0.9', '1.0', '1.1'})
set(gca, 'FontSize', 12, 'FontName', 'Arial Narrow')
set(legend, 'FontSize', 10, 'FontName', 'Arial Narrow')
axis([min(datacore(:,1)) max(datacore(:,1)) .75 1.15])
avman = sum(((dataeng(:,2)-1)/(P32des-1))- ...
           ((datacore(:,2)-1)/(P32des-1)))/length(datacore(:,1));
subplot(2,1,2)
plot(datacore(:,1), ((dataeng(:,2)-1)/(P32des-1))- ...
      ((datacore(:,2)-1)/(P32des-1)), '-', ...
      'Color', .6*[1 1 1])
hold on
plot([min(datacore(:,1)) max(datacore(:,1))], ...
     [avman avman], '-k', 'LineWidth', 2)
plot([min(datacore(:,1)) max(datacore(:,1))], ...
     [.00872 .00872], '--k')
plot([min(datacore(:,1)) max(datacore(:,1))], ...
     -1* [.00872 .00872], '--k')
hold off
legend({'prediction error', 'average prediction error', ...
       'propagated measurement uncertainty'}, 'Location', 'NW')
legend('boxoff')
xlabel('Operating hours', ...
       'FontSize', 12, 'FontName', 'Arial Narrow')
ylabel('Prediction error', ...
       'FontSize', 12, 'FontName', 'Arial Narrow')
set(gca, 'YTickLabel', {'-0.05', '0.00', '0.05', '0.10'})
set(gca, 'FontSize', 12, 'FontName', 'Arial Narrow')
set(legend, 'FontSize', 10, 'FontName', 'Arial Narrow')
axis([min(datacore(:,1)) max(datacore(:,1)) -.08 .12])

```



```

end

M = v3/(sqrt(y*R*T3));

rside = m2;

m4 = m3*(1-B);

left = .7*To3;
right = To3;
T4 = .5*(left+right);

count = 0;

% calculate flow conditions downstream of the bleed valve
for i = 1:xx
    v4 = (1-B)*v3*(T4/T3)^(1-(y-1)/y)*(Ain/Aout);
    To4 = T4+v4^2/(2*1005);
    M4 = v4/sqrt(y*R*T4);
    m4 = (1-B)*m3;
    rho4 = m4/(v4*Aout);
    P4 = rho4*R*T4;
    Po4 = Po3*(To4/To3)^(y/(y-1));
    M4c = sqrt((((Po4/P4)^(y/(y-1)))-1)*2/(y-1));
    if abs(M4-M4c) < 1e-3
        break
    end
    if M4 > M4c
        left = T4;
    else
        right = T4;
    end
    T4 = .5*(left+right);
end

% calculate new compressor pressure and temperature ratios
pr = Po4/Po2;
tr = To4/To2;

```







```
        if count > 100
            break
        end
    end
end

% plot turbine characteristic is requested
if figureon == 5555
    hold on
    plot(guess,1000*mass,'ok',[guess guess 1],[0 1000*mass ...
1000*mass],'--k')
    text(guess+.1,1000*mass*.15,['\leftarrow Operating', ...
        ['pressure ratio']])
    hold off
elseif figureon == 0
end
```